Cooperative Behavior in Cavity-cooled, Parametrically-pumped Electron Oscillators

A thesis presented

by

Joseph Ngai Tan

to

The Department of Physics

in partial fulfillment of the requirements

for the degree of

Doctor of Philosophy

in the subject of

Physics

Harvard University

Cambridge, Massachusetts

September 1992

Abstract

Stochastic motions of parametrically-pumped electron oscillators synchronize abruptly when the pump strength is increased through a sharp threshold and internal motions are radiatively cooled via coupling to a mode of a cold, microwave cavity. The collective motion is characterized by an instability which is approximated by a rigid model. Hysteresis is observed when either pump frequency or pump strength is swept. Time translation invariance requires that any coherent response be phase bistable, with the two degenerate phase states differing only in phase by 180 degrees. The collective behavior in this system is self-organized insofar as the choice between these bistable phase states is determined by internal motions. Parametrically-pumped electron oscillators are only partially synchronized, with a coherent component which is observed to be very sensitive to radiative cooling of the internal motions, providing a new technique for probing the standing-wave modes of a Penning trap cavity, *in situ* at 4K, without a microwave drive. Measured resonant frequencies of a specially designed cylindrical Penning trap agree very well with the eigenfrequencies of an ideal microwave cavity, typically to a percent or better. This cylindrical trap is of such high quality that one isolated electron in its cavity is observed with good signal-to-noise. For the first time, cavity modes of a Penning trap are clearly observed and identified with familiar field configurations. Among over 100 observed modes are some which are suited for cyclotron excitations, rapid change of cyclotron damping, sideband cooling of an electron to very low (mK) temperatures and directly driven spin flips. The extraordinary control over a wide range of parameters in this well-characterized system opens the way to a new generation of electron magnetic-moment measurements and other radiative studies, as well as experiments on collective behaviors and fluctuation phenomena.

Contents

Abstract i

1 Introduction 3

1.1 Cooperative Phenomena 3

1.2 Eliminating Cavity Shifts 5

2 Electron Oscillators in a Cylindrical Cavity 9

2.1 Sweeping the Cyclotron Frequency 14

2.2 Cylindrical Penning Trap 19

2.3 Observing A One Electron Oscillator 21

2.3.1 Minimizing Anharmonicity 23

2.3.2 Orthogonalized Electrodes 26

2.3.3 Displacing the Axial Position 28

2.4 Counting Electron Oscillators 30

2.5 Detection and Damping of Axial Motion 31

2.5.1 Interaction with a Tuned Circuit 33

2.5.2 Signal Amplification 36

2.5.3 Phase-sensitive Detection 37

2.5.4 Center-of-mass Energy Detection 39

2.6 Forced Excitation 39

2.7 Parametric Excitation 43

2.8 Summary 45

3 Parametric Resonance 47

3.1 Transition to Coherent Oscillations 48

3.2 Hysteresis and Lineshapes 53

3.3 A Rigid Model 57

3.3.1 Steady State Amplitudes 60

3.3.2 Phase Bistability 61

3.3.3 Instability of $Z = 0$ State 62

3.3.4 Hysteresis 63

3.4 Full Equations of Motion 64

3.5 Summary 68

4 Interaction with Cavity Standing Waves 70

4.1 Observing Microwave Cavity Modes Below 166 GHz 70

4.1.1 Motional Effects 76

4.1.2 Comparison with Ideal Cavity 77

4.1.3 Strong Coupling 79

4.2 New Generation of g-2 measurements 84

4.2.1 Magnetic Moments Without Cavity Shifts 86

4.2.2 Rapid Control of Electron-Cavity Coupling 88

4.2.3 Sideband Cooling of Axial Motion 90

4.3 Calibrating the Monitored Currents 91

4.4 Electron-Cavity Interactions 93

4.5 Full Spectrum Below 166 GHz 99

4.6 Summary 114

5 Fluctuations and Related Phenomena 115

5.1 Transitions between Phase Bistable States 117

5.2 Partial Synchronization 125

5.3 Internal Motions: Slow Relaxations 132

5.4 Summary 136

6 Conclusion 138

A Self-shielding Superconducting Solenoids 141

A.1 Ambient Fluctuations in the Magnetic Field 142

A.2 Single Superconducting Solenoid Circuit 143

A.3 Coupled Superconducting Circuits 149

A.4 Commercial Solenoid Circuits 152

A.5 Measured Shielding 155

A.6 Field Homogeneity of Shielded Region 157

A.7 Shielding for Nonhomogeneous Fields 159

B Linear Coupled Oscillators with Thermal Noise 162

B.1 Detection Circuit: Harmonic Oscillator 163

B.2 Coupled oscillators 165

B.3 Electron Cooling of Trapped Antiprotons 169

B.4 Bolometric model 172

References 176

Acknowledgements

I am grateful to my advisor, Gerald Gabrielse, for a fruitful Ph.D. study at Harvard, which has been challenging and pleasurable. This study has drawn upon contributions and insight gained from many earlier works. In particular, theoretical analyses done in collaboration with L.S. Brown, K.C. Chan, G. Gabrielse, and K. Helmerson provided some insight into cavity electrodynamics of trapped electrons which are observed. I wish to thank co-workers in our laboratory: X. Fei, R. Tjoelker, L. Haarsma, D. Phillips, A. Khabbaz, D.G. Reisenfeld, D. Hall, L. Lapidus for their assistance; and in particular, C.H. Tseng for experimental support. This work has benefitted from stimulating conversations with D. Fisher, T.M. O'Neil, D. Wineland, R. Jensen, S. Strogatz, and J. Wurtle. I have had the fortune of interacting with L. Orozco, S. Rolston, B. Brown, W. Jhe, W. Quint, R. Kaiser and K. Abdullah. I am grateful to my father, Tiong-Han Tan, and mother, Kam-Chu Ngai, for their support. Initial stages of this work were done in part at the University of Washington. Funding support came from the National Science Foundation and the Office of Naval Research.

Publications during Ph.D. study

1. "Cyclotron Motion in a Microwave Cavity: Possible Shifts of the Measured Electron g Factor";
   L.S. Brown, G. Gabrielse, K. Helmerson, and J. Tan,
   Phys. Rev. Lett. **55**, 44 (1985).

2. "Cyclotron Motion in a Microwave Cavity: Lifetime and Frequency Shifts";
   L.S. Brown, G. Gabrielse, K. Helmerson, and J. Tan,
   Phys. Rev. A **32**, 3204 (1985).

3. "Cyclotron Motion in a Spherical Microwave Cavity";
   L.S. Brown, K. Helmerson, and J. Tan,
   Phys. Rev. A **34**, 2638 (1986).

4. "Cyclotron Motion in a Penning Trap Microwave Cavity";
   L.S. Brown, G. Gabrielse, J. Tan, and K.C.D. Chan,
   Phys. Rev. A **37**, 4163 (1988).

5. "Self-shielding Superconducting Solenoid Systems";
   G. Gabrielse and J. Tan,
   J. Appl. Phys. **63**, 5143 (1988); U.S. Patent # 4,974,113.

6. "One Electron in an Orthogonalized Cylindrical Penning Trap";
   J. Tan and G. Gabrielse,
   Appl. Phys. Lett. **55**, 2144 (1989).

7. "Cavity Shifts of Measured Electron Magnetic Moments";
G. Gabrielse, J. Tan, and L.S. Brown,
in **Quantum Electrodynamics**, p. 389 ff, edited by T. Kinoshita
(World, Singapore, 1990).

8. "A Superconducting Solenoid System Which Cancels Fluctuations
in the Ambient Magnetic Field";
G. Gabrielse, J. Tan, P. Clateman, L.A. Orozco,
S.L. Rolston, C.H.Tseng, and R. Tjoelker,
J. Magnetic Resonance, **91**, 564 (1991).

9. "Synchronization of Parametrically-pumped Electron Oscillators with
Phase Bistability";
J. Tan and G. Gabrielse,
Phys. Rev. Lett. **67**, 3090 (1991).

10. "One Electron in a Cavity";
G. Gabrielse and J. Tan,
to appear in **Cavity Quantum Electrodynamics**,
edited by P. Berman (Academic, New York, 1992).

11. "Parametrically-pumped Electron Oscillators";
J. Tan and G. Gabrielse,
to be published in Phys. Rev. A.

List of Figures

1.1 Characteristic dependence of an oscillator's damping rate γ in (a) and frequency shift $\Delta\omega$ in (b), as a function of its detuning δ from the resonant frequency of a coupled cavity mode (or LCr circuit). . 7

2.1 Orthogonalized cylindrical trap cavity (to scale with $z_0 = 0.3838(6)$ cm and $\rho_0 = 0.4559(6)$ cm at 4 K). A spatially uniform magnetic field ($\Delta B/B < 10^{-6}$ over $z_0/10$) is along the vertical axis. Choke flanges ($\lambda/4$ at 164 GHz) are incorporated to minimize losses. . . . 10

2.2 Ideal cylindrical cavity. 11

2.3 Representation of the transverse electric field for TE_{1np} modes: (a) in the midplane for odd p and (b) along the z-axis for even p. . . . 12

2.4 Model circuit for ramping the magnetic field in a superconducting solenoid. 15

2.5 Simplified circuit representation of a Nalorac superconducting solenoid system, connected to a highly-regulated power supply. 16

2.6 Measured current $I(t)$ versus time (dots) as the field in a superconducting solenoid system is ramped, and a linear fit (line). 18

2.7 Motions of one electron confined in a Penning trap formed from a pure electrostatic quadrupole and a uniform magnetic field. "Guiding center" of fast cyclotron motion (at ω_c) oscillates along trap axis (at ω_z) and slowly drifts around the trap center (at ω_m). 22

2.8 Driven axial resonance of one electron in a cylindrical Penning trap. [77] 23

2.9 Simplified diagram of orthogonalized cylindrical trap. For the trap used, $\Delta z_c/z_o = 0.2$, and $\rho_o/z_o = 1.186$, $z_o = 0.3838(6)$ cm . The z-axis is aligned with a spatially uniform magnetic field. 25
2.10 Driven axial resonance for one electron in the orthogonalized cylindrical trap. The middle curve (b) is the symmetric lineshape for a well-tuned trap ($C_4 \approx 0$). The characteristic lineshapes for an anharmonic oscillator are obtained when the potential V_c is adjusted so that $C_4 > 0$ in (a) and $C_4 < 0$ in (c). [77] 27
2.11 Detection of 7 electron oscillators loaded into a cylindrical Penning trap cavity sequentially. 30
2.12 Driven resonance for an electron cloud observed using phase-sensitve detection, with in-phase component in (a) and quadrature component in (b). 32
2.13 Electromechanical representation of a harmonically-bound electron coupled to a tuned circuit. 34
2.14 A dualgate MOSFET pre-amplifier monitors induced voltage across tuned circuit. 36
2.15 Schematic diagram of electrical set-up for processing observed signal. 38
2.16 Lorentzian form fits well to measured damping width of driven resonance versus oscillation frequency ν_z near the resonance frequency ν_M of tuned circuit. 41
2.17 Simplified diagram showing detection electronics used in observing parametrically-pumped electron oscillators (modeled as massive, charged balls attached to springs). 43

3.1 Observation of abrupt transition from weak, disordered motions to large, coherent CM oscillation at a pump strength threshold (a). Measured threshold varies linearly with damping rate (b) and with the number of electrons (c). 48

3.2 Parametric resonance with characteristic exponential growth of harmonic oscillation (dashed line). Periodic variation results as anharmonicity arrests growth (dotted line) but damping causes relaxation to steady state (solid line). 49

3.3 Region of $n = 1$ Mathieu instability (shaded) . For $h \ll 1$, a hyperbola divides the neighborhood (h, ω_d) into regions having different sets of stable steady states. For negative C_4 or C_6, region I has 3 stable states; region II, 2 phase bistable exited states; regions III and O, 1 quiescent state. 51

3.4 Calculated rigid model lineshapes, showing hysteresis of CM energy versus pump frequency ν_d . CM energy is a linear function of pump frequency ν_d for $C_4 < 0$ with $C_6 = 0$ (a), and a parabolic function of ν_d for $C_4 = 0$ with $C_6 < 0$ (b). 54

3.5 Observed resonance lineshapes with hysteresis. Maximum CM energy is limited by cavity-cooling but lineshapes (a) for large C_4 and (b) for negligible C_4 agree qualitatively with rigid model. 55

3.6 (a) Observed hysteresis loops of CM energy versus pump strength in 4 consecutive cycles [O $\longrightarrow$ I $\longrightarrow$ II $\longrightarrow$ I $\longrightarrow$ O]. (b) Histograms of transition points showing that the quiescent state is less stable against fluctuations. 57

3.7 Observed frequency range of instability (a) increases with h . Increasing ω_d at fixed h values as illustrated in (b) generates a family of parametric resonances (a). Measured corner frequencies $\nu_+(h)$ and $\nu_-(h)$ fit well to a hyperbola (c) when plotted versus h. 58

3.8 Basins of attraction for the two phase states. Quiescent state at the center is a saddle-point. 61

4.1 (a) Cavity resonance observed by monitoring the axial CM energy while slowly sweeping the magnetic field to vary ω_c', with pump frequency at $\omega_d = 2\omega_z$ and pump strength $h = 1.3h_T$. (b) Parametric axial resonances for indicated cyclotron frequencies. 71
4.2 Simplified diagram of the experimental apparatus for cavity mode detection. 72
4.3 Observed cavity modes between 70 and 120 GHz. 74
4.4 Lorentzian lineshapes (solid lines) fit to observed cavity modes (dots) which are well separated from other modes. 75
4.5 Motional splitting of singlet modes TE_{0np}. The best fit (center dashed line) is consistent with $2\nu_z$ (solid line) within its uncertainty (dashed lines above and below). 76
4.6 (a) Motional doublet for a mode with p even has separation of $2\nu_z$. (b) Motional sidebands for a mode with odd p are separated from the strong central peak by $2\nu_z$. 78
4.7 Fit of measured TE_{0np} mode eigenfrequencies to those calculated for an ideal cylinder , in situ at 4K, determines effective dimensions of the trap cavity to within 6 μm. 79
4.8 Comparison of observed and calculated eigenfrequencies for series of cavity modes of particular experimental interest. 81
4.9 The Lorentzian lineshape (a) is modified to the strongly coupled lineshapes in (b) and (c) as the number of electrons N is increased to increase the electron-cavity coupling. 82
4.10 Observed cavity modes in a 10 GHz spectrum (a). Calculated frequency shifts (b) and damping rates (c) for one electron at the cavity center. The dashed line in (b) accounts for the two nearest modes that couple, TM_{123} and TE_{115}. The solid line also includes the effect of nearby coupled modes not in this span. 87

4.11 (a) Antisymmetric potential across endcaps displaces electrons along the z-axis. (b) Representation of transverse electric field component near the z-axis for a p=3 mode. 89
4.12 (a) Observed resonance for TE_{027} ($\lambda/4 = 550\mu$m) with a centered electron cloud. (b) Motional doublet observed when the electrons are displaced from the center by $\Delta z = 510\mu$m. 90
4.13 (a) Cavity mode resonance for field calibration. (b) Measurement of offset constant τ_o 93
4.14 Observed cavity modes below 166 GHz. 99

5.1 Sampled IF signal (5 MHz) illustrates (a) incoherent response for $h < h_T$ and (b) long-term coherence for $h > h_T$. Dotted lines in (b) show maximum deviations from mean coherent motion. 116
5.2 Random transitions between phase-bistable states (a)-(b) . Disordered motions (c) result if cyclotron cooling is weak. Residence time τ, illustrated in (a), on average becomes shorter (b) with increasing detuning between cyclotron and cavity mode frequencies. 118
5.3 (a) Distribution of residence times, and (b) good fit to an exponential form. 119
5.4 Examples of phase jump "trajectories" observed with 600 electrons parametrically driven at $h = 1.4h_T$ ($C_4 \sim -6 \times 10^{-4}$ and $N\gamma_z/\omega_z = 1.2 \times 10^{-5}$). 121
5.5 Distribution of jump times and variation with control parameters. 122
5.6 Dependences of mean residence time $\bar{\tau}$ on control parameters. Mean time between phase flips versus (a) number of electrons, (b) anharmonicity coefficient $|C_4|$, (c) pump strength h and (d) detuning between cyclotron frequency and a cavity mode eigenfrequency. . . 124
5.7 CM Energy versus pump strength for various detunings between cyclotron frequency and TE_{115} eigenfrequency. Saturation level is clearly limited by cyclotron cooling of internal motions. 125

5.8 Fourier spectra of responses for various detunings from a cavity mode. Coherent response (peak) diminishes as cyclotron frequency is detuned from cavity mode eigenfrequency, but fluctuation spectrum broadens. Other system parameters are given in preceding figure. 127

5.9 Fourier spectra for various pump strengths. A sharp peak emerges as pump strength exceeds threshold (a), with only broadband spectrum appearing below threshold. Fluctuation spectrum continues to broaden with increasing pump strength (b), becoming skewed for very strong pumping. 128

5.10 Comparison of power in the peak (square) with the integrated power in the fluctuation spectrum (circle) for the data set shown in preceding figure. 129

5.11 Decrease in coherent response to parametric excitation when cyclotron motions are heated with a microwave drive. Measured energy in axial CM energy with parametric drive at lower corner frequency $\nu_d = 2\nu_-$, is plotted versus normalized microwave drive power (dots). A simple form (solid) fits well to it. 130

5.12 Scaling of rms induced current with number of electrons (a) above threshold and (b) below threshold. 131

5.13 Characteristic responses to pulsed parametric pumping (a) below threshold and (b) above threshold. Averaging over 256 pulses improves the S/N below threshold (a), but only a single pulse is used above threshold (b). Slow relaxation (b) follows initial rapid growth, above threshold. 134

5.14 Pulsed cyclotron excitation. Slow growth and fast decay indicates temperature dependence of equilibration process. 135

A.1 Typical fluctuations in the magnetic field in our laboratory as measured using a fluxgate magnetometer and a detection bandwidth of 0.01 Hz. The quiet window during the night occurs when the MBTA (Cambridge) subway is shut down. 144
A.2 Simple, single-layer solenoid. 146
A.3 Shielding of a densely would, single-layer solenoid as a function of its aspect ratio, the ratio of its half length l to its radius a. 149
A.4 Large solenoid to illustrate typical properties of high-field persistent solenoids. 150
A.5 Cross section of the windings of the high-field solenoid which produces a vertical magnetic field. The innermost solenoid was added to make the solenoid system cancel external fluctuations. 154
A.6 Change in the magnetic field measured within the solenoid (deduced from the change in NMR frequency of an acetone sample) as a function of the external magnetic field applied over the solenoid, without (a) and with (b) the added inner solenoid. 158
A.7 Examples of larger than expected shielding factors due to gradients in the applied magnetic field. 160

B.1 Harmonic oscillators: (a) series LCr network, (b) damped, ideal spring-mass system, (c) parallel LCR network 163
B.2 Observed "noise resonance" of the tuned circuit obtained by sweeping the center frequency of bandpass filter (a) when the trap is empty and (b) when the trap has a small electron cloud with the same resonant frequency. 166
B.3 Simplified representation of a tuned circuit coupled to an charged particle oscillating in a background gas. 167
B.4 Calculated noise power from tuned circuit coupled to (a) no electron, (b) small electron cloud at $\omega_z = \omega_M$, and (c) small electron cloud at $\omega_z > \omega_M$ 170

B.5 The bolometric model 174

Chapter 1

Introduction

Isolated elementary particles and ions in electromagnetic traps have made possible a growing variety of experiments, ranging from the most stringent tests of renormalized QED with the measured electron magnetic moment [88] and tests of CPT in the proton/antiproton system [36], to trapping large numbers of cryogenic positrons and anti-protons for synthesis of anti-hydrogen, to studies of pure electron plasmas [61,68] and spatially ordered structures in laser-cooled, trapped ions [21,95,47,40,16]. This work presents the first study of recently discovered [78,79] self-organized [65] collective behaviors in a system of cavity-cooled, parametrically-pumped electron oscillators which are isolated in a new cylindrical Penning trap cavity.

1.1 Cooperative Phenomena

Centuries ago, Huygens observed that pendula of two clocks on a wall tend to synchronize [81]. More recent efforts to characterize large dynamical systems have generated increased interest in larger systems of coupled oscillators. Extensive studies of cooperative behavior in the laser, for example, revealed strong similarity in this nonequilibrium system to critical phenomena in a ferromagnet, developing concepts and techniques analogous to those of phase transition theory. [42,17] Also, arrays of Josephson junction oscillators synchronize when they produce high frequency microwaves, being coupled via a common load of passive circuit elements

[43,60]. Large systems of well-characterized, coupled oscillators are difficult to realize under good control in the laboratory and no unified theoretical approach has yet emerged for collective behavior far from thermal equilibrium. Nonetheless, an increasing number of works studying a few simple systems of coupled limit cycle oscillators are revealing recognizable cooperative phenomena such as oscillator synchronization, "clustering" and "attractor crowding" [91,25]. Examples include Van der Pol oscillators [96] and an "active rotator" model [58] which are studied using various techniques: solutions of coupled differential equations [96,66,62], coupled iterative maps [74,91,25], generalized mean field approaches [58], as well as renormalization-group analysis [15].

Parametrically-pumped electron oscillators are far from thermal equilibrium insofar as they are strongly driven and they continuously dissipate energy. A unique feature is that the oscillators synchronize to produce an observable, coherent motion of their center-of-mass (CM) at half the frequency of the pump. Time translation symmetry requires that any such response be bistable in phase relative to a subharmonic of the parametric pump. The collective motion is self-organized insofar as the choice between the bistable phases depends upon the internal motions of the electrons (not upon the external pumping field) and characteristically requires sufficient energy dissipation [65]. Transitions between the bistable phase states depend upon the internal energy of the oscillators (relative to their CM), reminiscent of a two state system coupled to a thermal bath. This energy is varied by tuning the radiative dissipation to the cold microwave cavity formed by electrodes of a specially designed, cylindrical Penning trap. The collective motion is characterized by an instability which is well approximated by a rigid model, with hysteresis occurring when either pump frequency or pump strength is swept back and forth through a region of instability. Partial synchronization is manifested by interesting effects, such as the broadening of fluctuation spectra, saturation of the coherent component as pump power is increased above a threshold, slow relaxation to steady level in pulsed excitation, etc..

Likely applications of the newly developed techniques include a thousand-fold

reduction in the axial temperature of a trapped elementary particle, radiative cooling of cryogenic electron plasmas and internal motions of molecular ions at adjustable rates, and a new generation of measurements of the electron magnetic moment which are no longer limited by cavity frequency shifts or by damping linewidths.

1.2 Eliminating Cavity Shifts

Although the observed nonlinear dynamics and collective behaviors in parametrically-pumped electron oscillators are of interest in themselves, the development of a high quality cylindrical Penning trap which has made this study possible was originally motivated by the goal of starting a new generation of electron magnetic moment measurements in well-characterized radiation fields. The discovery of synchronized motions in parametrically-pumped oscillators has allowed us, for the first time, to clearly observe and identify microwave standing wave modes in a trap cavity, greatly accelerating progress towards this goal.

Measurements of the anomalous magnetic moment of the electron a provide the most stringent test of quantum electrodynamics (QED) [52]. This theory predicts corrections to the simplest Dirac theory due to the interaction of an electron with the fluctuating radiation modes of the electromagnetic vacuum. It relates a to an asymptotic series in powers of the fine structure constant α,

$$a = C_1\left(\frac{\alpha}{\pi}\right) + C_2\left(\frac{\alpha}{\pi}\right)^2 + C_3\left(\frac{\alpha}{\pi}\right)^3 + C_4\left(\frac{\alpha}{\pi}\right)^4 + \ldots \quad . \tag{1.1}$$

Over four decades, measurements of a [14,88,89] and α were greatly improved, as were QED calculations [52,53] of the expansion coefficients C_i. The highest accuracy measurements [88,89] of a employ a single electron in a Penning trap [10] to obtain an accuracy $\Delta a/a < 4 \times 10^{-9}$. This unrivaled comparison of a measured and calculated property of an elementary particle, reveals an agreement $\Delta a/a < 4 \times 10^{-8}$ which would have astounded those who were struggling to formulate renormalized QED.

A few years ago, experimental progress in measuring the anomalous magnetic moment a was seriously interrupted. The electromagnetic vacuum in which the electron was located was discovered to be significantly modified by the metal electrodes of the Penning trap [32]. Electron cyclotron motion around a vertical magnetic field $B = 6$ Tesla is at frequency

$$\omega_c = \frac{eB}{mc} = 2\pi \text{ (164 GHz)}. \tag{1.2}$$

Cyclotron motion in free space would would damp via synchrotron radiation at a rate

$$\gamma_c = \frac{4e^2\omega_c^2}{3mc^3} = (0.1 \text{ sec})^{-1}. \tag{1.3}$$

Instead, the decay of cyclotron energy [32] for a single electron in the trap was shown to be decidedly less by a factor of 3, the first observation of inhibited spontaneous emission within a microwave cavity [22]. Corresponding cavity shifts of measured frequencies, calculated [8,9,12] but not yet observed, were estimated to be the largest experimental uncertainty [88,89] based upon the calculations. To complicate this serious problem, so little was known about the radiation field within trap cavities that the uncertainty estimate is itself rather suspect. Also, the traditional hyperbolic electrode geometries do not allow easy calculation [12] or even a ready classification of the standing-wave fields in cavity radiation modes. Even if mode eigenfrequencies were known, the field configuration and hence the coupling of a centered electron to any particular cavity mode (if any) would not be known.

Although the importance of cavity shifts for measurements of the electron magnetic moment was demonstrated only recently, the basic notion that the couplings of two oscillators can shift both the damping rate and oscillation frequency of the oscillations (Fig. 1.1) is certainly very familiar. (The electron cyclotron motion and an electromagnetic cavity mode are the coupled oscillators here.) Long ago, for example, it was mentioned that the spontaneous emission of an atom placed in a cavity could be inhibited [70]. Further discussions of cavity-induced modifications to atom damping rates came later [55], with clear realization of the problems

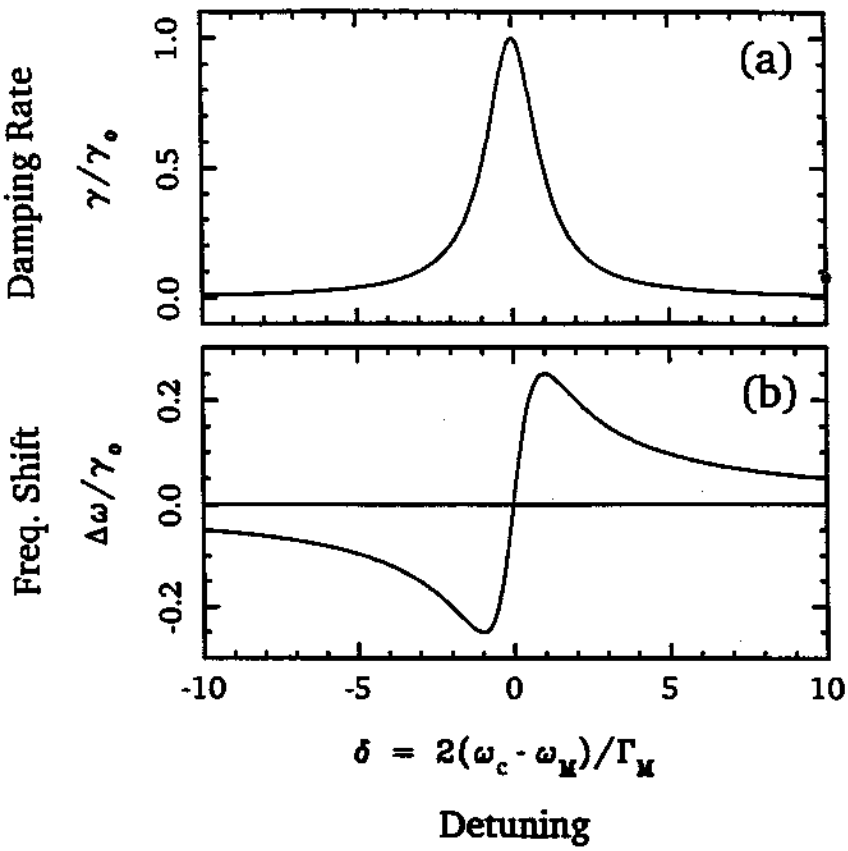

Figure 1.1: Characteristic dependence of an oscillator's damping rate γ in (a) and frequency shift $\Delta\omega$ in (b), as a function of its detuning δ from the resonant frequency of a coupled cavity mode (or LCr circuit).

that the frequency shifts would present for precise measurements of resonance frequencies [54]. In fact, soon after the observation of inhibited spontaneous emission in a trap cavity, similar effects were observed with Rydberg atoms traveling between parallel conducting plates [48] and in another Penning trap [88,89]. Related studies with Rydberg atoms continue [44,46]. Some additional evidence for the presence of cavity modes in a hyperbolic trap has also been observed [87] but remains difficult to interpret since signal-to-noise was poor, no Lorentzian lineshapes

were established and no information about the standing wave field configurations (and hence the coupling to a trapped electron) could be deduced.

The new experiments made possible by the synchronized motions of parametrically-pumped electron oscillators in a high quality cylindrical trap and described here show how to change the cavity-modified vacuum from a serious interruption into an advantage. The well-characterized, standing wave fields of the cylindrical trap cavity revives interest in cavity-shifts of an electron's spin precession frequency. Theoretical studies first suggested that the cavity modified vacuum could be responsible for shifts large enough to be observable [26]. Brown and Boulware [4] contradicted the initial claim. Many other theoretical papers were written [27,5,76,56,80,57,2]. The latest work seems to support the contradiction of the initial claims, even though opposing conclusions have never been resolved as completely as might be desired. The theoretical studies share the common difficulty of making a calculable model (eg. a spin near a conducting plate or plates) which is also a reasonable approximation to an electron in a trap cavity. It remains to theoretically study the resonant interaction of a spin with one of the high Q modes of the cylindrical trap cavity which couple most strongly to a spin. If it is experimentally demonstrated that cavity shifts of the cyclotron frequency are well understood, cavity shifts of the spin frequency could then be investigated experimentally as well.

Chapter 2

Electron Oscillators in a Cylindrical Cavity

This study of the collective behavior of parametrically pumped electron oscillators is made possible by a cylindrical Penning trap (Fig. 2.1) which is constructed to be the best possible approximation to an ideal microwave cavity. As we shall see, trapped electrons can be used to clearly observe the radiation modes of the cylindrical trap cavity. The observed resonance frequencies correspond extremely well to the familiar eigenfrequencies ν_{mnp} of an ideal cylinder (Fig. 2.2). We can thus classify and identify the electromagnetic standing wave fields in a familiar way as either transverse magnetic or transverse electric modes. With some effort, sections of the cavity walls are made to be the electrodes of a Penning trap. Trapped electrons are thereby localized within well-characterized standing wave fields and the interaction of the electrons with the surrounding radiation field is under precise control.

The familiar eigenfrequencies for a cylindrical microwave cavity of height $2z_0$ and radius ρ_0 (Fig. 2.2) are given by [49]

$$2\pi\nu_{mnp} = c\sqrt{\left(\frac{\chi_{mn}}{\rho_o}\right)^2 + \left(\frac{p\pi}{2z_o}\right)^2}, \tag{2.1}$$

where c is the speed of light. For transverse magnetic modes TM_{mnp}, the χ_{mn} is the nth zero of the mth order Bessel function $J_m(x)$ and $p = 0, 1, 2, \ldots$. For

transverse electric modes TE_{mnp}, the χ_{mn} is the nth zero of the Bessel function derivative $J'_m(x)$ and $p = 1, 2, \ldots$. In both cases, $m = 0, 1, \ldots$ and $n = 1, 2, \ldots$. The electromagnetic fields for each of the standing wave modes are simple analytic functions [49]. Great care was taken to make a cylindrical trap cavity which closely approximates an ideal cylindrical microwave cavity. This makes it possible to thoroughly analyze the interaction of particular cavity radiation modes with a single electron localized in the trap cavity (summarized in Sec. 4.4).

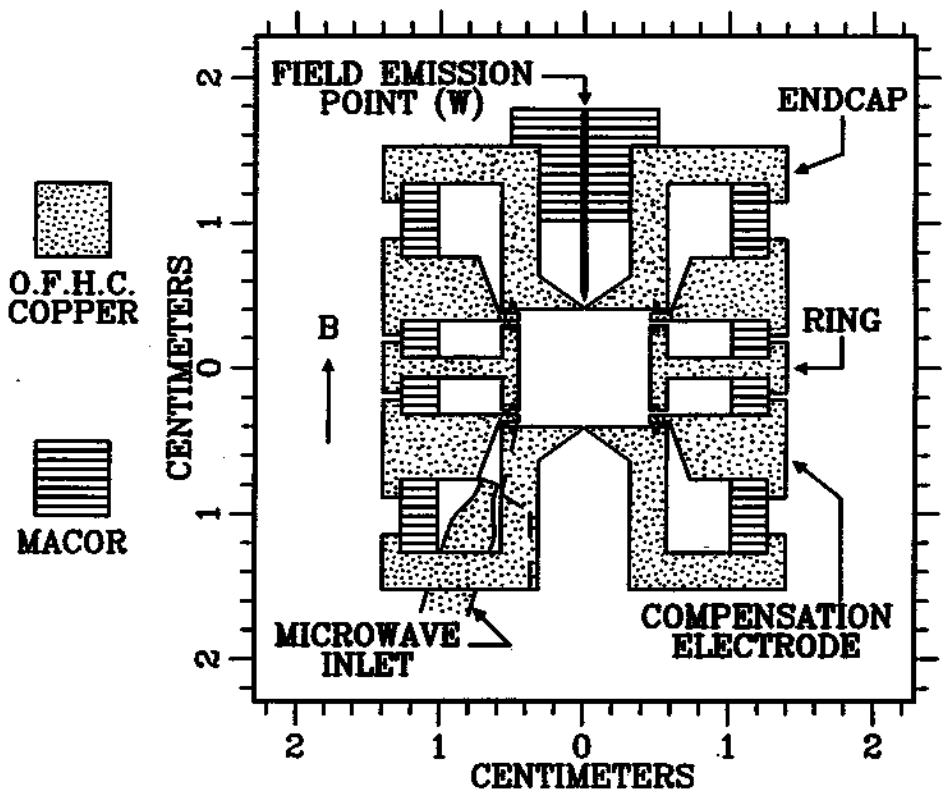

Figure 2.1: Orthogonalized cylindrical trap cavity (to scale with $z_0 = 0.3838(6)$ cm and $\rho_0 = 0.4559(6)$ cm at 4 K). A spatially uniform magnetic field ($\Delta B/B < 10^{-6}$ over $z_0/10$) is along the vertical axis. Choke flanges ($\lambda/4$ at 164 GHz) are incorporated to minimize losses.

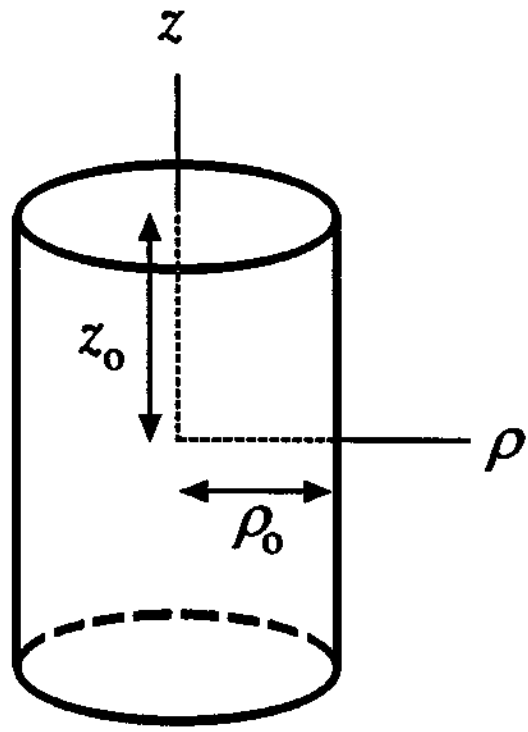

Figure 2.2: Ideal cylindrical cavity.

Of particular interest are the standing wave modes which couple to electron cyclotron motion which is perpendicular to the axis of the cylinder and typically near to it. Such coupling requires an electric field perpendicular to the cylinder axis. This is provided by either TE_{1np} or TM_{1np} standing wave modes, provided that the electron is not localized in an axial standing wave minimum. To illustrate, the transverse electric fields of TE_{1np} modes near the symmetry axis of the cavity are simple sine and cosine functions of the z-coordinate (relative to the center of the cavity). The quantum number p indicates the number of standing wave maxima (anti-nodes) which fit between the two endcaps. For modes with odd p,

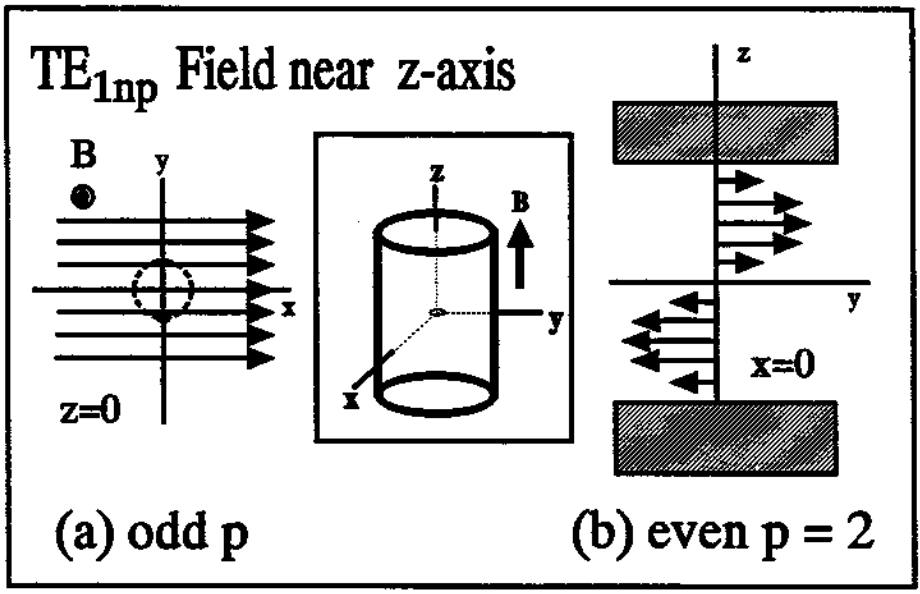

Figure 2.3: Representation of the transverse electric field for TE_{1np} modes: (a) in the midplane for odd p and (b) along the z-axis for even p.

components of the transverse electric field,

$$E_\perp = E_o \cos\left(\frac{\pi p z}{2z_0}\right) e^{-i\omega t}, \tag{2.2}$$

have a maximum in the midplane as illustrated in Fig. 2.3a. These odd p modes, with their electric field maxima near the trap center, couple strongly to electron cyclotron motion at the center of the trap. These modes are thus particularly suited for driving a centered cyclotron oscillator with an external microwave source. They provide efficient damping of electron cyclotron motion, as well, but also cause associated frequency shifts, as we shall see. For the related modes with p even,

the electric field vanishes in the midplane (Fig. 2.3b)

$$E_\perp = E_o \sin\left(\frac{\pi p z}{2 z_0}\right) e^{-i\omega t}. \tag{2.3}$$

The even p modes thus do not couple to the cyclotron motion of an electron at the center of the cavity. However, spatially displacing the electron from node to antinode provides a way to rapidly couple and uncouple the electron and cavity, turning the cyclotron damping from on to off. Moreover, the spatial gradients near the nodes are suited for sideband cooling thermal motions of the electron along the cavity axis.

Anywhere from 1 to more than 10^5 electrons can be localized within the cylindrical microwave cavity when the cavity walls are split to allow them to also serve as the electrodes of a Penning trap. A strong magnetic field confines the electrons radially, producing cyclotron oscillations. For precision experiments with the cyclotron motion, the magnetic field is required to be very uniform spatially and very stable in time [33]. This is provided by a specially designed superconducting solenoid system (Appendix A). In addition, an electrostatic restoring force along the z-axis (parallel to the magnetic field) keeps the electrons oscillating near the midplane of the cavity. Oscillations of the electrons along the magnetic field generate an observable current in a detection circuit connected to the trap electrodes.

Isolated electrons are confined in an ultra-high vacuum cavity attained by enclosing the trap in an evacuated envelope which is cryopumped because the envelope is kept at 4 K via thermal contact with a LHe bath. (A Long storage time limit, $\tau > 3.4$ months, of $\sim 10^3$ anti-protons in an open-access cylindrical trap used at CERN indicates that the vacuum in a cryopumped trap cavity can be better than 5×10^{-17} Torr. [36]) A field emission point is used to load electrons into the cavity. Electrons are stripped from the background gas by the $\sim$ 1keV electron beam from the field emission point entering along the trap axis through a 25 μm hole. (The field emission current strikes an electrode surface, removing adsorbed atoms into the cavity.) These secondary electrons are trapped as they dissipate energy via radiation into the cavity and via Joule heating of a detection

resistor. A good vacuum is restored after the field emission current is turned off. One electron has been continuously confined and studied in the cylindrical trap depicted in Fig. 2.1 for over two months before being ejected deliberately. (A 10-month confinement of one electron has been demonstrated in a hyperbolic trap. [31])

2.1 Sweeping the Cyclotron Frequency

In free space, the cyclotron oscillation of an electron decays due to synchrotron radiation. A microwave cavity formed by the metallic trap electrodes modifies the electromagnetic vacuum coupled to the electron oscillator, enhancing or suppressing radiation depending on the proximity of standing wave eigenfrequencies to the cyclotron oscillation frequency. Isolated electrons in a Penning trap cavity are well suited for radiative studies since the cyclotron frequency

$$2\pi\ \nu_c = \frac{eB}{mc} \tag{2.4}$$

is readily changed using the precisely controlled magnetic field. The coherent motions of parametrically-pumped electron oscillators studied here provide a new way to observe these cavity radiation modes by sweeping the magnetic field so that the electron oscillators are brought into resonance with the cavity modes. A magnetic field which is varying linearly in time is desirable.

Precise control of the cyclotron frequency is facilitated by the properties of a superconducting solenoid which provides the magnetic field. The current $J(t)$ in a superconducting solenoid of inductance L changes at a rate given by

$$\frac{dJ}{dt} = \frac{V}{L} \tag{2.5}$$

when a voltage source V is connected in series with the solenoid, according to Faraday's law. A model circuit is shown in Fig. 2.4 with a pure inductor representing a superconducting solenoid. Shunt resistor R has the combined resistance of a superconductive switch (present only when the switch is open) and a protection

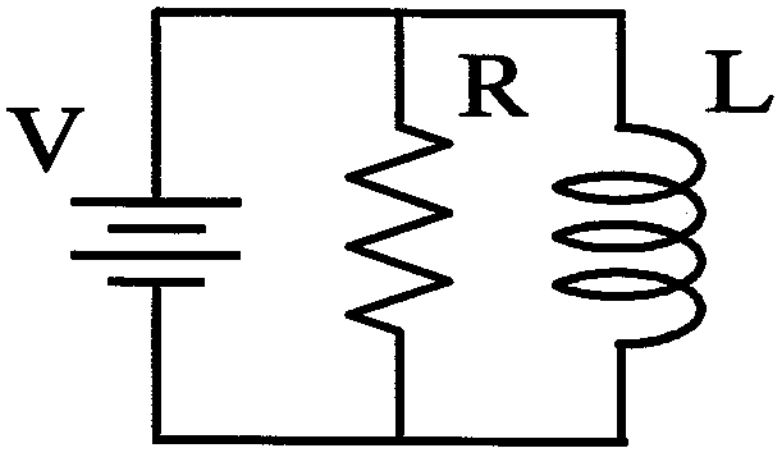

Figure 2.4: Model circuit for ramping the magnetic field in a superconducting solenoid.

resistor. The ideal voltage source must supply a current I(t) given by

$$I = \frac{V}{R} + J(t) \,, \tag{2.6}$$

where integration of Eq.(2.5) gives

$$J(t) = J(0) + \frac{V}{L}t \,. \tag{2.7}$$

Thus, electrons localized at the center of the solenoid experience a magnetic field varying linearly in time

$$B_z(t) = g\left(J(0) + \frac{V}{L}t\right) \tag{2.8}$$

where the coefficient g is calculable from the geometry and winding characteristics of the solenoid (Appendix A). Experimentally, the net current output I of the power supply is more readily monitored than the solenoid current J. The field $B_z(t)$ can be determined from the current supplied by the voltage source provided the "offset" current V/R drawn by resistor R is taken into account. It is convenient to introduce a time constant τ_o defined by

$$\frac{V}{R} = \frac{V}{L}\tau_o \tag{2.9}$$

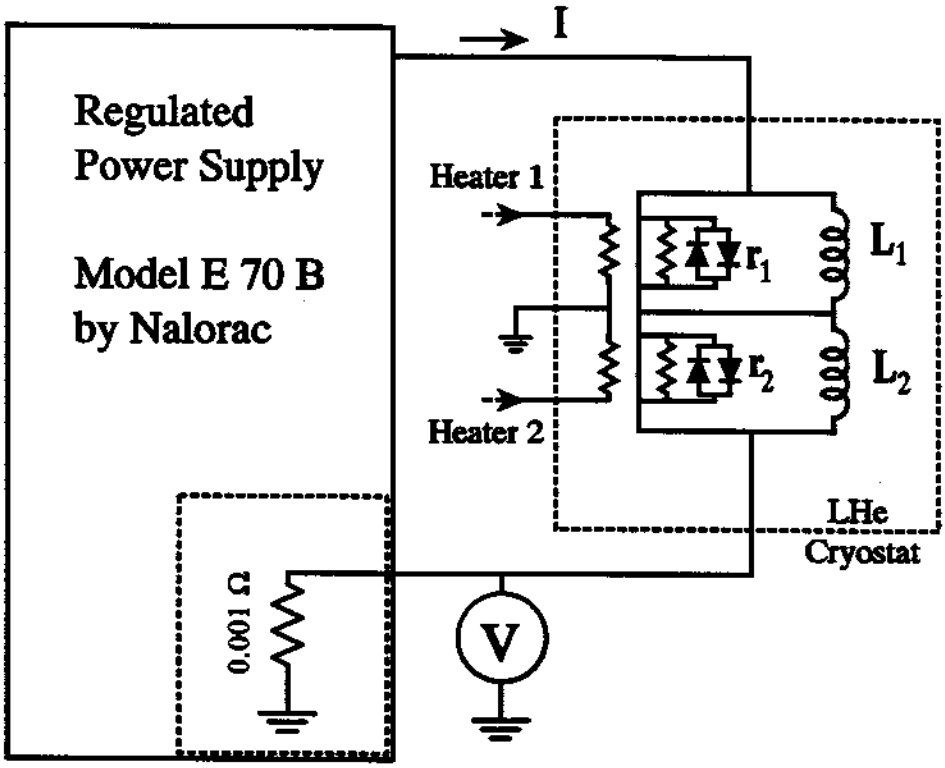

Figure 2.5: Simplified circuit representation of a Nalorac superconducting solenoid system, connected to a highly-regulated power supply.

so that the magnetic field is given by

$$B_z(t) = g\left[I(0) + \frac{V}{L}(t - \tau_o)\right], \tag{2.10}$$

in terms of measurable quantities. Alternatively, the cyclotron frequency is related to the current by

$$\nu_c(t) = \frac{\Delta\nu_c}{\Delta I}\left[I(0) + \frac{V}{L}(t - \tau_o)\right] \tag{2.11}$$

where the conversion factor $\Delta\nu_c/\Delta I$ is measured using a precision frequency synthesizer to drive a cyclotron resonance at a known current $I(0)$ with $V = 0$.

To attain high spatial homogeneity, some commercial superconductive magnets are constructed with circuits of more than one solenoid (Appendix A). Our

Parameter	Value	Unit
r_1	0.37 (7)	Ω
r_2	1.55 (2)	Ω
$L_1 + L_2 + 2M$	214 (2)	H
$\Delta\nu_c/\Delta I$	4.1854 (2)	GHz/A
τ_o	101 (1)	s
S	-4.1 (1)	—

Table 2.1: Measured properties of a traditional Nalorac superconductive magnet (JOB43).

Parameter	Value	Unit
$L_1 + L_2 + 2M$	207 (2)	H
$\Delta\nu_c/\Delta I$	4.1388 (2)	GHz/A
τ_o	102 (3)	s
S	-156(6)	—

Table 2.2: Measured properties of a new Nalorac superconductive magnet redesigned to be self-shielding (JOB51).

studies employed superconductive magnets (constructed by Nalorac Cryogenics Corp.) consisting of two solenoids to provide the high magnetic field. With appropriate generalization described below, the results for the simple solenoid also apply to a system with two solenoids. Fig. 2.5 shows a simplified circuit representation of a Nalorac superconductive magnet. To ramp the current in one solenoid, a small segment of the superconducting wire (a superconductive switch) can be turned normal (with a heater) if a matching current is provided by an external source. A highly-regulated power supply (model E70B by Nalorac) provides the matching current, monitors the charging voltage V across the system by remote sensing and maintains this voltage at a desired value. The net current output I of

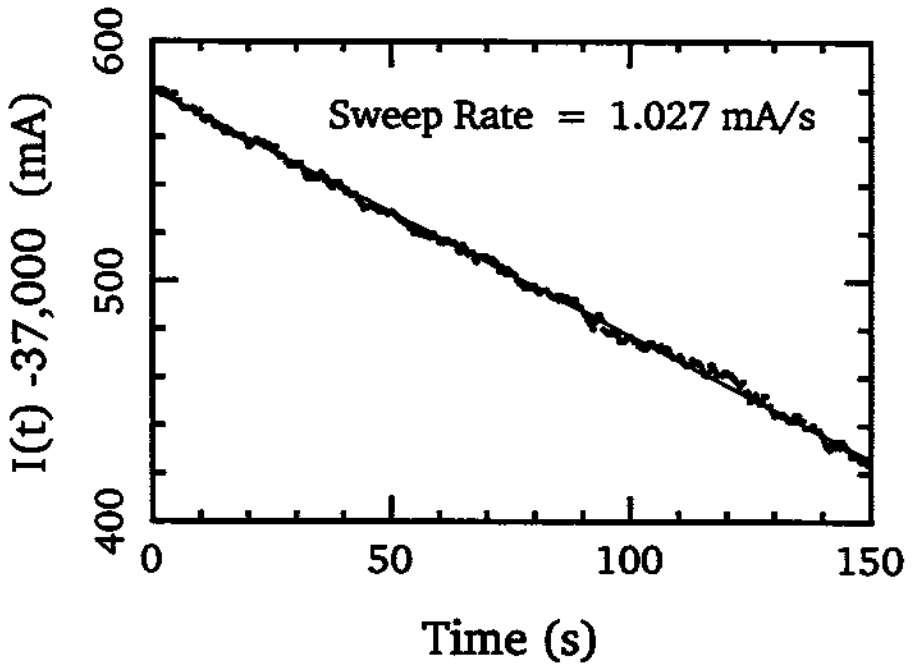

Figure 2.6: Measured current $I(t)$ versus time (dots) as the field in a superconducting solenoid system is ramped, and a linear fit (line).

the power supply is monitored on the return line using a precision resistor (0.001 Ω). The monitored current is digitized and stored in a computer to record the current continuously. As an example, Fig. 2.6 plots the return line current I versus time as the solenoid is discharged at a rate of $V/L = 1.0\text{mA/s}$. Measurement of the offset constant τ_o involves observation of a high-Q cavity mode for various charging rates V and will be discussed in Chapter 4. Measured characteristics for the superconductive magnets employed in our study are summarized in Table 2.1 and Table 2.2. Other characteristics calculated for these systems are tabulated in Appendix A.

In more detail, electrons localized near the center of a two-solenoid system (Fig. 2.5) experience

$$B_z(t) = g_1 J_1 + g_2 J_2 \quad , \tag{2.12}$$

which is a sum of contributions from current J_1 in solenoid L_1 with coefficient g_1

and from current J_2 in solenoid L_2 with coefficient g_2. Shortly after the heaters are activated, the currents J_1 and J_2 maintain a small difference proportional to the applied voltage V. When the currents in the two sections are equal (which occurs when $V = 0$), we have

$$B_z(t) = gJ_1 = gJ_2 \quad , \tag{2.13}$$

where $g = g_1 + g_2$. Relaxing within $\sim$ 3s after a voltage V is applied across the system, the currents J_1 and J_2 vary at the same constant rate V/L, where $L = L_1 + L_2 + 2M$ is the net inductance of the system with two solenoids (L_1 and L_2) having mutual inductance M. The offset current drawn by resistors r_1 and r_2 (Fig. 2.4b) is characterized by the time constant

$$\tau_o = \frac{1}{g}\left(\frac{g_1(L_1 + M)}{r_1} + \frac{g_2(L_2 + M)}{r_2}\right) \quad . \tag{2.14}$$

With these generalized definitions, Eq. (2.10) and Eq. (2.11) hold for two-solenoid systems. The case of a simple solenoid corresponds to $L_2 = M = g_2 = 0$.

2.2 Cylindrical Penning Trap

One electron experiments, in fact, require that the axial restoring force be nearly linear, as would be obtained from a high quality electrostatic quadrupole potential when appropriate voltages are applied to the trap electrodes. This results in harmonic oscillations of the trapped particle at well defined and precisely measurable frequencies, independent of small amplitude variations. For more trapped electrons, it is also convenient to use an electrostatic potential which can be precisely controlled and which is primarily an electrostatic quadrupole. In more detail, the desired electrostatic quadrupole potential can be written as

$$V = V_0 \frac{z^2 - \rho^2/2}{2d^2}[1 + C_2] \quad , \tag{2.15}$$

where V_0 is the the potential applied to the electrodes, d is an appropriate trap dimension (defined presently), and C_2 is a dimensionless constant which can be calculated from the electrode geometry. The axial dimension z is the distance from

the center of the trap along the magnetic field direction, ρ is the corresponding radial coordinate. A trapped particle of charge q and mass m oscillates harmonically in this potential, along the magnetic field direction, at axial frequency ω_z given by

$$\omega_z^2 = \frac{qV_0}{md^2}[1 + C_2] \ . \tag{2.16}$$

Typically the axial oscillation frequency is monitored precisely, with small shifts in this frequency used to derive information about the cyclotron and spin motions of the isolated electron.

Traditionally, such a potential was produced using Penning traps with metal electrodes painstakingly shaped along the hyperbolic contours which are the equipotentials of the desired electrostatic quadrupole. The microwave properties of a hyperbolic cavity, however, are not well understood. Our goal is to use the cylindrical trap cavity for controlling the radiation field. Hence, to approximate an ideal cylindrical cavity, the trap cavity in Fig. 2.1 was precisely constructed with small slits (0.013 cm) that incorporate choke flanges ($\lambda/4$ at 164 GHz). Although this cylindrical geometry is a much better way to understand and control the radiation field configurations in the trap cavity, it is a much less straightforward way to produce the high quality electrostatic quadrupole potential.

The trap cavity has its symmetry axis coincident with the vertical axis $\hat{z}$ parallel to a 6-T magnetic field from a superconducting solenoid. Small slits perpendicular to the magnetic field divide the oxygen-free high-conductivity copper cavity walls into two end-cap electrodes (at z_o above and below the trap center), a ring electrode (with radius ρ_o), and two compensation ring electrodes (with height Δz_c). A judicious choice of the ratio ρ_0/z_0 yields a crucial orthogonalization property [30]. Leading deviations which are unavoidably added to the desired electrostatic quadrupole potential in Eq. (2.15)

$$\begin{aligned} \Delta V \ = \ & \frac{1}{2}C_4V_0\frac{1}{d^4}\left(z^4 - 3z^2\rho^2 + \frac{3}{8}\rho^4\right) \\ & + \frac{1}{2}C_6V_0\frac{1}{d^6}\left(z^6 - \frac{15}{2}z^4\rho^2 + \frac{45}{8}z^2\rho^4 - \frac{5}{16}\rho^6\right) \end{aligned} \tag{2.17}$$

can be tuned (by adjusting potentials on the compensation electrodes [82]), with negligible change in the strength of the desired electrostatic quadrupole. More specifically, C_4 can be tuned over the range

$$10^{-5} < |C_4| < 10^{-1}, \tag{2.18}$$

while C_6 remains relatively constant at the large value [30]

$$C_6 \approx -10^{-1}. \tag{2.19}$$

Potentials on the trap electrodes are tuned to make the oscillation more harmonic, thus improving the observed signal-to-noise to the point that a resonant signal from just one trapped electron can be easily observed.

2.3 Observing A One Electron Oscillator

Once the potential is tuned, the motions of an isolated electron in a cylindrical trap are the same as in a hyperbolic trap. In the absence of damping, the exact equations of motions for one electron in a pure electrostatic quadrupole and uniform magnetic field are given by [10]

$$\ddot{z} + \omega_z^2 z = 0\,, \tag{2.20}$$

$$\ddot{\vec{\rho}} - \vec{\omega}_c \times \dot{\vec{\rho}} - \frac{1}{2}\omega_z^2 \vec{\rho} = 0\,, \tag{2.21}$$

where $\vec{\rho}(t) = x(t)\,\hat{x} + y(t)\,\hat{y}$ and a dot denotes the time derivative. The three familiar motions [10] include a cyclotron orbit around magnetic-field lines (at frequency $\omega_c'/2\pi < 170$ GHz), a harmonic axial oscillation along the magnetic field direction $\hat{z}$ (at frequency $\omega_z/2\pi = 63$ MHz) and a circular magnetron motion (at a much lower 12 kHz frequency) which is not important for the cavity electrodynamics. These harmonic motions are illustrated in Fig. 2.7. Cyclotron motion is damped because of its coupling to the radiation modes of a trap cavity. Axial oscillation is damped by a detection circuit connected to the electrodes. Fig. 2.8 shows a forced resonance of the damped axial motion for a single trapped electron, with

a linewidth which is less than 4 Hz. With this signal-to-noise ratio, a shift in the axial resonance frequency of 1 Hz out of 64 MHz is easily resolved, a resolution which is comparable with that obtained in hyperbolic traps [88,84,10]. Such high accuracy is needed in precision tests of fundamental physics, high-resolution mass spectroscopy, studies of single elementary particles and radiative studies. Specific examples which illustrate the sensitivity involved include the measurements of the anomalous magnetic moments $(g-2)$ of the electron and positron [88,84], the proton/electron mass ratio [85], observation of relativistic hysteresis and bistability

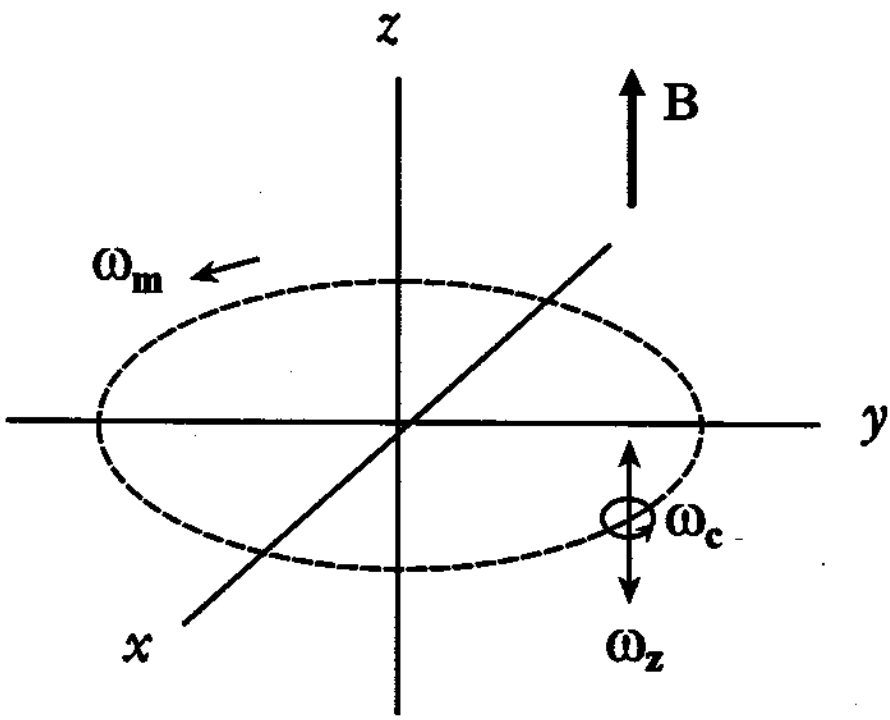

Figure 2.7: Motions of one electron confined in a Penning trap formed from a pure electrostatic quadrupole and a uniform magnetic field. "Guiding center" of fast cyclotron motion (at ω_c) oscillates along trap axis (at ω_z) and slowly drifts around the trap center (at ω_m).

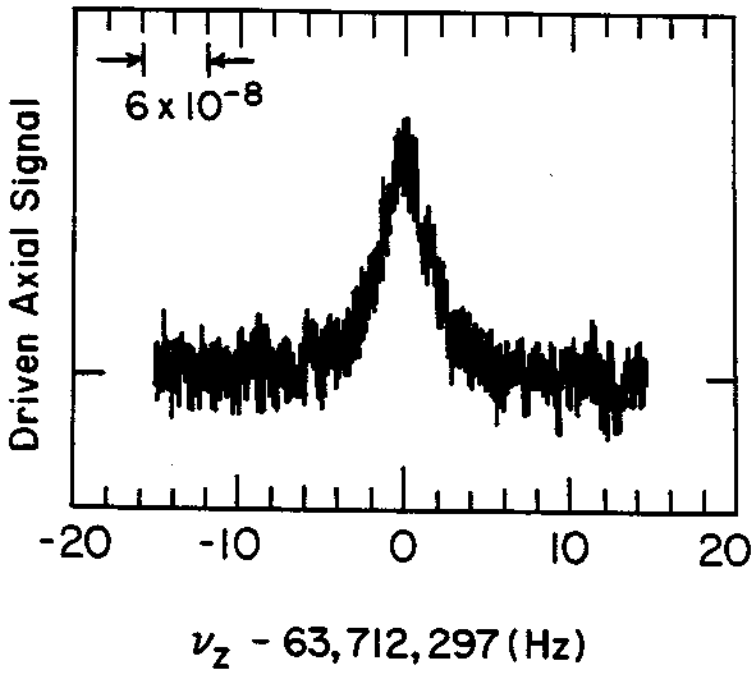

Figure 2.8: Driven axial resonance of one electron in a cylindrical Penning trap. [77]

of a single electron [31], and inhibition of spontaneous emission [32].

2.3.1 Minimizing Anharmonicity

Potentials $+\frac{1}{2}V_o$ on the flat endplates and $-\frac{1}{2}V_o$ on the center ring produce the electrostatic restoring force. Nonlinearity in restoring force causes amplitude-dependent frequency shifts and linewidth broadening in the resulting anharmonic particle oscillations. A potential V_c on the pair of compensation rings (Fig.2.9) must be adjusted [82] to minimize deviations from the electric quadrupole potential and thus make the axial restoring force as linear as possible. The height of these

electrodes

$$\Delta z_c/z_o = 0.2 \tag{2.22}$$

is sufficient to avoid an unacceptable sensitivity to the mechanical tolerances. A corresponding choice of radius [30]

$$\rho_o/z_o = 1.186 \tag{2.23}$$

was calculated to minimize the undesired frequency shifts which have been mentioned. We find it convenient to specify the size of the trap with a characteristic dimension $d = 0.355$ cm where d is defined by

$$d^2 = \frac{1}{2}\left({z_o}^2 + \frac{1}{2}{\rho_o}^2\right) \tag{2.24}$$

and $z_o = 0.3838(6)$ cm. Gaps between the electrodes (so different potentials can be applied to different electrodes) were made as small as practicable at 0.013 cm. The gaps were not expected to have major consequences [34].

For any axially symmetric trap, the electric potential near the trap center may be written as a series expansion given by

$$V(\mathbf{r}) = V_o\left(\frac{z^2 - \frac{1}{2}\rho^2}{2d^2}\right) + \frac{1}{2}V_o\sum_{\substack{n=0\\ \text{even}}}^{\infty} C_k\left(\frac{r}{d}\right)^k \mathrm{P}_k(\cos\theta) \tag{2.25}$$

where d is the characteristic length for this trap and the sum is over even n because of symmetry under reflections, $z \to -z$. The first term on the right is the desired electric quadrupole potential in cylindrical coordinates (ρ,z). The second term represents undesired additions in an imperfect trap, expanded in spherical coordinates (r,θ) and Legendre polynomials P_k. The expansion coefficients are linear in the compensation potential V_c

$$C_k = C_k^{(0)} + D_k\frac{V_c}{V_o} \tag{2.26}$$

with $C_k^{(0)}$ and D_k exactly calculable [30] using standard techniques [50] for perfectly aligned and cleaned conducting electrodes. The expansion converges rapidly for

particles near the center of the trap where $(r/d) \leq 10^{-2}$, so we only consider lowest order coefficients C_2 and C_4 (C_0 having no observable consequences for particles confined in the traps).

The compensation potential V_c is tuned to make $C_4 = 0$, thereby eliminating the leading deviation from a quadrupole potential. This occurs when $V_c/V_o = -C_4^{(0)}/D_4$ from Eq. (2.26). In practice, we tune V_c while monitoring the coherent

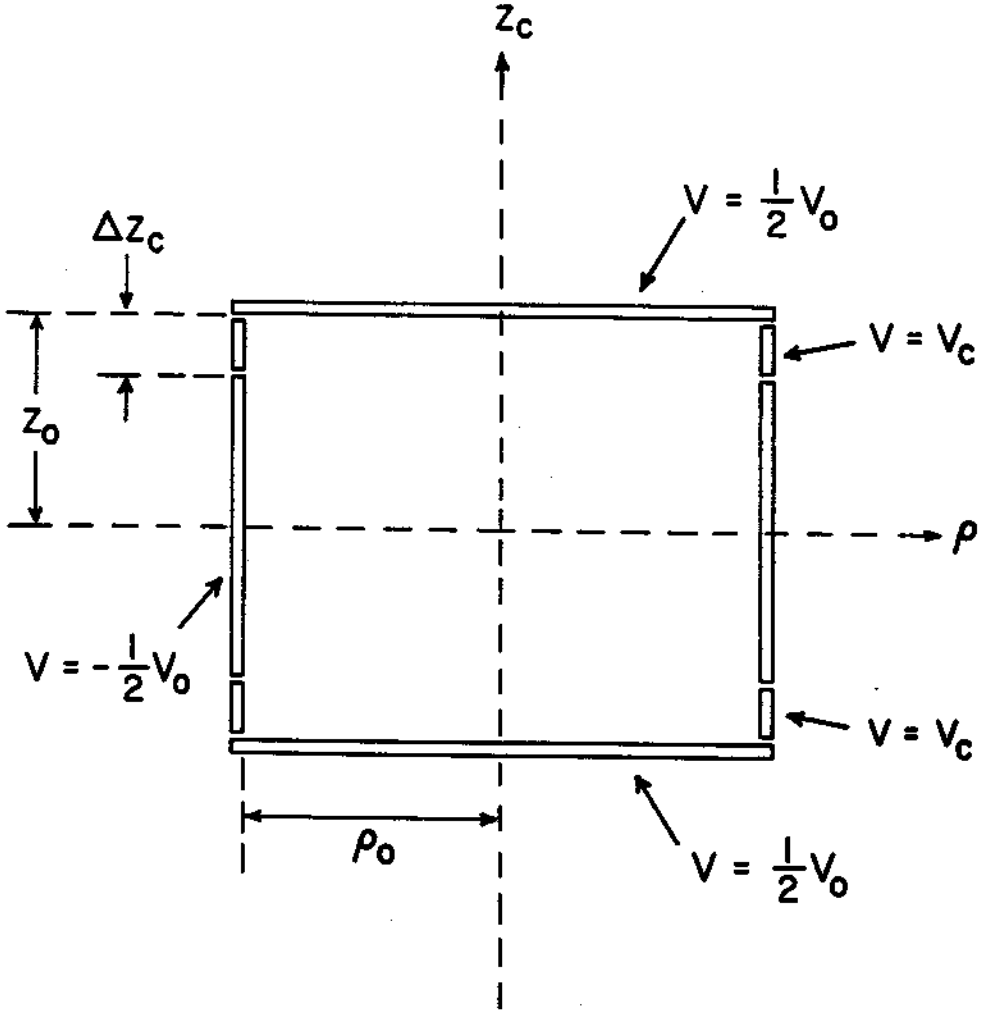

Figure 2.9: Simplified diagram of orthogonalized cylindrical trap. For the trap used, $\Delta z_c/z_o = 0.2$, and $\rho_o/z_o = 1.186$, $z_o = 0.3838(6)$ cm . The z-axis is aligned with a spatially uniform magnetic field.

response of a single trapped electron whose oscillatory axial motion along the magnetic field axis is being driven. For the trapping potential in this experiment ($V_o = 10.193\ V$) we must tune $V_c = 3.574\ V$ to get a symmetric resonance lineshape as shown in Fig. 2.8 and Fig. 2.10b. Thus, we get an experimental value of $V_c/V_o = -0.350(1)$ in good agreement with calculated value $V_c/V_o = -0.34(2)$, the uncertainty being due to the estimated mechanical tolerance of 8×10^{-4}cm in the dimensions and due to thermal contractions when the apparatus is submerged in liquid helium. The good agreement verifies the calculated value of $D_4 = -0.066(1)$. Detuning V_c to either side of this optimal value produces the characteristic skewed lineshape of an anharmonic oscillator. This is illustrated in Fig. 2.10a and Fig. 2.10c where V_c is +20mV and −20mV from the optimum, respectively. Since the compensation voltage must be tuned to within 1 mV of the optimal value to avoid an observable skewing of the resonance lineshape (e.g., Fig. 2.10), we use the calculated value of D_4 to conclude that we are able to tune $|C_4| < 10^{-5}$ in this trap.

2.3.2 Orthogonalized Electrodes

The adjustments to minimize deviations from the electrostatic quadrupole are generally attended by very inconvenient shifts in the resonant frequency of oscillation when the particles are driven along the magnetic field axis. In general, the axial resonance frequency ω_z will be shifted when V_c is changed since

$$\omega_z^2 = \frac{qV_o}{md^2}\left[1 + C_2^{(0)} + D_2\left(\frac{V_c}{Vo}\right)\right] \tag{2.27}$$

for the oscillation of a particle with charge q and mass m. Ideal electrode proportions would make $D_2 = 0$ so adjustments in the compensation potential leaves ω_z unchanged. A compensated Penning trap whose dimensions are selected to make $D_2 = 0$ is said to be "orthogonalized." Differentiating Eq. (2.27) and neglecting the small $C_2^{(0)} \sim 0.1$ we get

$$D_2 \approx \left(\frac{\partial\omega_z}{\partial V_c}\right) / \left(\frac{\partial\omega_z}{\partial V_o}\right) \ . \tag{2.28}$$

Using Eq.(2.28), we measure $D_2 \approx 2 \times 10^{-5}$ for this cylindrical trap, which is substantially smaller in magnitude than $D_2 \approx -5 \times 10^{-3}$ for the first generation hyperbolic traps used in so many precision experiments [88,31]. Fig. 2.10 illustrates how little ω_z shifts when a substantial adjustment of V_c to either side of the optimal tuning point, where the anharmonic distortions are clearly visible.

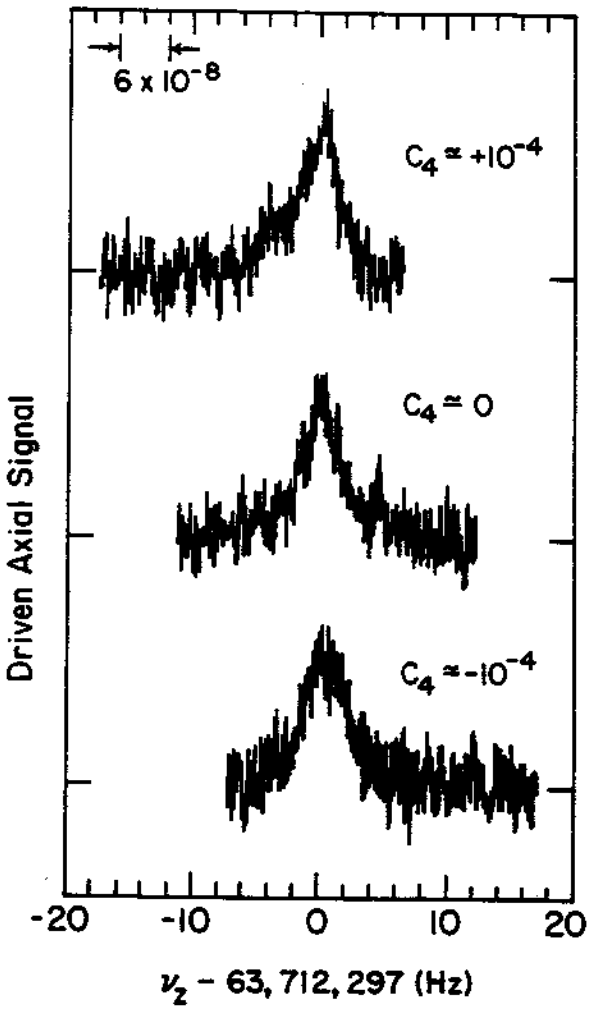

Figure 2.10: Driven axial resonance for one electron in the orthogonalized cylindrical trap. The middle curve (b) is the symmetric lineshape for a well-tuned trap ($C_4 \approx 0$). The characteristic lineshapes for an anharmonic oscillator are obtained when the potential V_c is adjusted so that $C_4 > 0$ in (a) and $C_4 < 0$ in (c). [77]

Comparable changes in the original hyperbolic traps would be accompanied by a frequency shift of about 500 linewidths.

A measure of the quality of an orthogonalized trap is how little the axial frequency ω_z changes for a given change in C_4. To quantify this a quality factor

$$\gamma_D \equiv D_2/D_4 \tag{2.29}$$

has been defined [28,30] with $\gamma_D = 0$ representing a perfectly orthogonalized trap. Using the measured value of D_2 and the calculated value of D_4 we obtained $\gamma_D \simeq 3\times10^{-4}$ which is a substantial improvement over $\gamma_D \simeq 0.56$ for the first generation hyperbolic traps.

2.3.3 Displacing the Axial Position

The potential within the trap when $\frac{1}{2}V_A$ and $-\frac{1}{2}V_A$ are applied to the upper and lower endcaps, with all the other electrodes grounded, is important for damping, driving and shifting the center of oscillation for the axial motion of trapped particles [29]. Near the center

$$V(\mathbf{r}) = \frac{1}{2}V_A \sum_{\substack{n=1\\ odd}}^{\infty} c_k \left(\frac{r}{d}\right)^k \mathrm{P}_k(\cos\theta) \tag{2.30}$$

with $c_1 = 0.784$ and $c_3 = 0.320$ calculated [30]. The product c_1c_3 can be easily measured [10] from the resulting frequency shift given by

$$\frac{\Delta\omega_z}{\omega_z} = -\frac{3}{4}\left(\frac{\mathrm{d}}{z_o}\right)^4 \frac{c_1c_3}{(1+C_2)^2}\left(\frac{V_A}{V_o}\right)^2. \tag{2.31}$$

We obtained $c_1c_3 = 0.26(1)$ which agrees with the calculated value. (These values for the cylindrical trap depicted in Fig. 2.1 provide neither advantages nor disadvantages relative to the hyperbolic traps.)

In chapter 4, rapid electronic control of electron-cavity interaction is demonstrated by shifting the axial positions of trapped electrons in a standing wave of the cavity. With the potential of Eq. (2.30), electrons near the trap center are shifted along the z-axis by

$$z_e = \frac{1}{2}\frac{c_1}{1+C_2}\left(\frac{V_A}{V_o}\right)d\,. \tag{2.32}$$

For the trap of Fig. 2.1 ($C_2 = 0.128$ and $d = 3550\mu$m), a trapping potential of $V_o = 10.2$ Volts yields

$$z_e = \left(121\frac{\mu\text{m}}{V}\right) V_A \ . \tag{2.33}$$

Thus, applying $V_A = 4.55$ Volts should shift electrons from anti-node to node (or vice-versa) of a standing wave with 550 μm quarter-wavelength along the z-axis (such as TE_{027}).

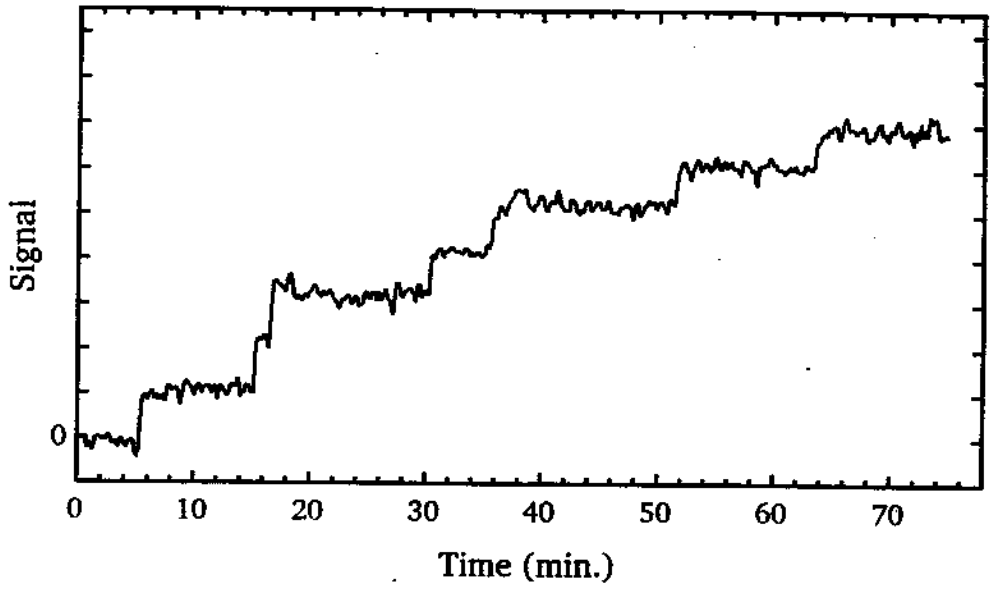

Figure 2.11: Detection of 7 electron oscillators loaded into a cylindrical Penning trap cavity sequentially.

2.4 Counting Electron Oscillators

Electrons confined in the trap cavity can be counted in non-destructive ways. This allows collective behavior to be studied in a wide range of electron numbers, ranging from small dynamical systems with as few as two electrons to "microplasmas" with as many as 10^5 electrons. Fig. 2.11 shows a signal changing in discrete increments as 7 electrons are loaded in sequence into the cavity. The signal is derived from the induced current through a resistor when the electrons are forced at a frequency ω_f fixed at a large detuning below the resonance frequency ω_z. Forced

axial CM motion of N electrons (each of mass m and charge q) satisfies

$$m\left[\frac{d^2}{dt^2} + N\gamma_z\frac{d}{dt} + (\omega_z)^2\right] z(t) = \kappa\frac{qV_d}{d}\sin(\omega_f t + \phi) \tag{2.34}$$

where γ_z is the damping for one electron and V_d is the drive strength. A commercial lock-in amplifier is used for phase-sensitive detection of the driven response, with the in-phase component of the signal given by

$$S_I = \alpha V_d \frac{(N\gamma_z/2)^2}{(N\gamma_z/2)^2 + \Delta\omega^2} \tag{2.35}$$

and the quadrature component of the signal given by

$$S_Q = \alpha V_d \frac{(N\gamma_z/2)\ \Delta\omega}{(N\gamma_z/2)^2 + \Delta\omega^2} \tag{2.36}$$

where $\Delta\omega = \omega_f - \omega_z$. For large detuning ($|\Delta\omega| >> N\gamma_z$), the quadrature component is proportional to the number of particles and thus generates the step structure shown in Fig. 2.11 as a low field emission current slowly loads electrons into the cavity. The number of particles in a large system is more readily determined from the linewidth of the forced resonance. Fig. 2.12 shows the in-phase (a) and quadrature (b) signals as the drive frequency is swept through resonance. Comparison of the linewidth from either component with that of a single electron (Fig. 2.8) indicates that $N = 10^3$. For systems so large that the CM motion couples strongly to the detection circuit, the number of particles can be determined from the Fourier spectrum of the noise-driven coupled system, as discussed in Appendix B.

2.5 Detection and Damping of Axial Motion

An electron near the center of the cavity executes simple harmonic motion along the magnetic field. Axial oscillation plays an important role in many experiments because a shift in its resonance frequency can be used to observe the states of the other motions. To detect the axial motion, an inductor is connected to one endcap and AC grounded with the remaining electrodes. The voltage across the inductor

is monitored. The resonance frequency of the resulting tank circuit (formed by trap electrodes and the coil) is typically tuned to the oscillation frequency of the axial motion. Under this condition, the capacitive reactance of the electrodes is cancelled by the inductive reactance of the coil and the tuned circuit is effectively a resistor R. The current induced through the resistor R by axial motion produces

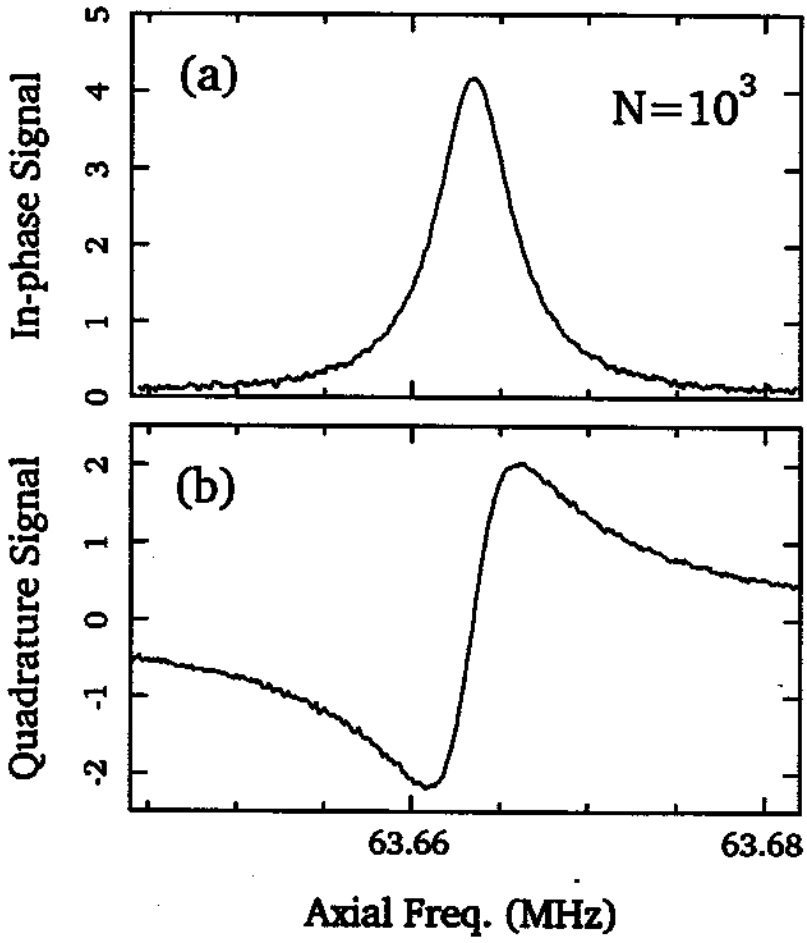

Figure 2.12: Driven resonance for an electron cloud observed using phase-sensitve detection, with in-phase component in (a) and quadrature component in (b).

a voltage given by [73,29]

$$V(t) = -\left[\frac{\kappa q}{2z_o}\right] \dot{z}(t)\ R\ . \tag{2.37}$$

The induced RF current ($V/R \propto \dot{z}$) dissipates energy in the resistor and thus damps the axial motion as indicated earlier in Eq. (2.34). A resonant force is applied using RF fields to excite the damped oscillator. The observed voltage across the resistor is monitored with a dual-gate, GaAs MOSFET pre-amplifier which is submerged in LHe to minimize thermal noise. After further amplification, various electronics are used to extract amplitude and phase information about the electron motions from the processed signal.

2.5.1 Interaction with a Tuned Circuit

Interaction of the electron axial oscillator with an LCr circuit allows the axial oscillation to be observed and the damping rate to be precisely controlled. Axial oscillation $z(t)$ induces a current in an LCr circuit formed by a helical resonator (with inductance L) connected across an endcap and ring electrodes of the trap (with effective capacitance C). The oscillating current $\dot{Q}(t)$ in the tuned circuit, in turn, produces an RF electric field which acts back on the electron. This electromechanical system is represented in Fig. 2.13 and the coupling between the two oscillators is described by the interaction potential

$$V_{int} = -\left[\frac{\kappa q}{2z_o C}\right]\ z(t)\ Q(t). \tag{2.38}$$

The dimensionless coupling constant κ has value $\kappa = 1$ for a capacitor with infinite parallel plates (separated by $2z_o$). (For our actual trap electrodes $\kappa = c_1 = 0.784$ has been calculated [30].) The equations of motion are

$$L\left[\frac{d^2}{dt^2} + \Gamma_M \frac{d}{dt} + (\omega_M)^2\right] Q(t) + \left[\frac{\kappa q}{2z_o C}\right] z(t) = 0 \tag{2.39}$$

$$m\left[\frac{d^2}{dt^2} + (\omega_z)^2\right] z(t) + \left[\frac{\kappa q}{2z_o C}\right] Q(t) = F(t) \tag{2.40}$$

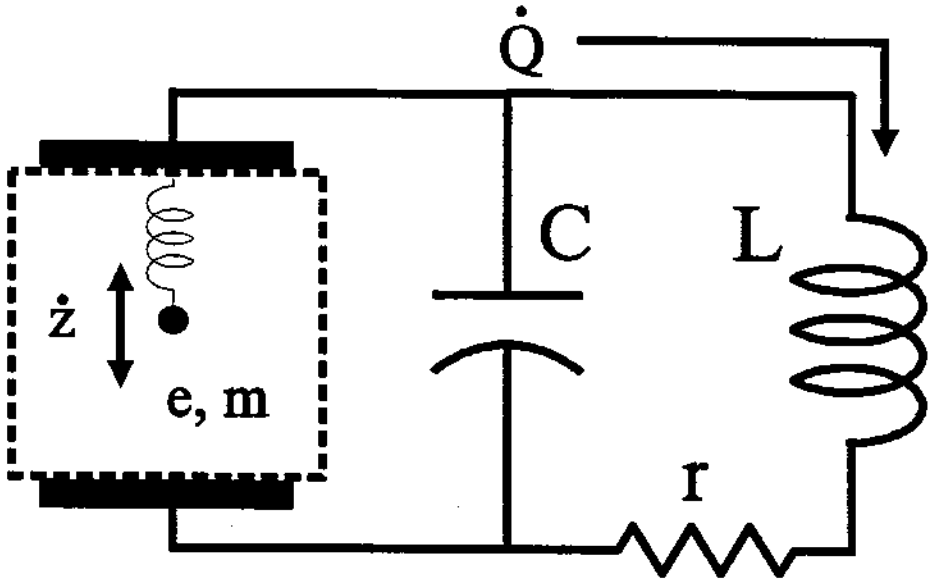

Figure 2.13: Electromechanical representation of a harmonically-bound electron coupled to a tuned circuit.

The resonance frequencies of the tuned circuit and electron oscillator are ω_M and ω_z, respectively, when the interaction is turned off. The right hand side of Eq.(2.39) is set to zero since we are neglecting the Johnson noise (Appendix B) due to the resistor. This coupled system also serves as a simple model for electron-cavity interaction (Chapter 4).

The tuned circuit, as indicated by Eq. (2.39), is a damped, harmonic oscillator which is driven by the electron oscillation. The oscillating current $\dot{Q}(t)$ in the helical resonator damps out at a rate $\Gamma_M = r/L$. Observed signal is derived from the voltage across the inductor

$$V_L = L\ddot{Q}(t) \; . \tag{2.41}$$

When $\omega_z = \omega_M$, this voltage is given by Eq. (2.37) in terms of the the effective

parallel resistance

$$R = \frac{L}{rC}. \tag{2.42}$$

We will often find it convenient to use this simplification.

2.5.2 Signal Amplification

The signal generated by driven electrons is generally very weak. For example, the response from a single electron dissipates only 10^{-20} Watt of power in the tuned circuit. To provide enough power to drive the low input impedance of the

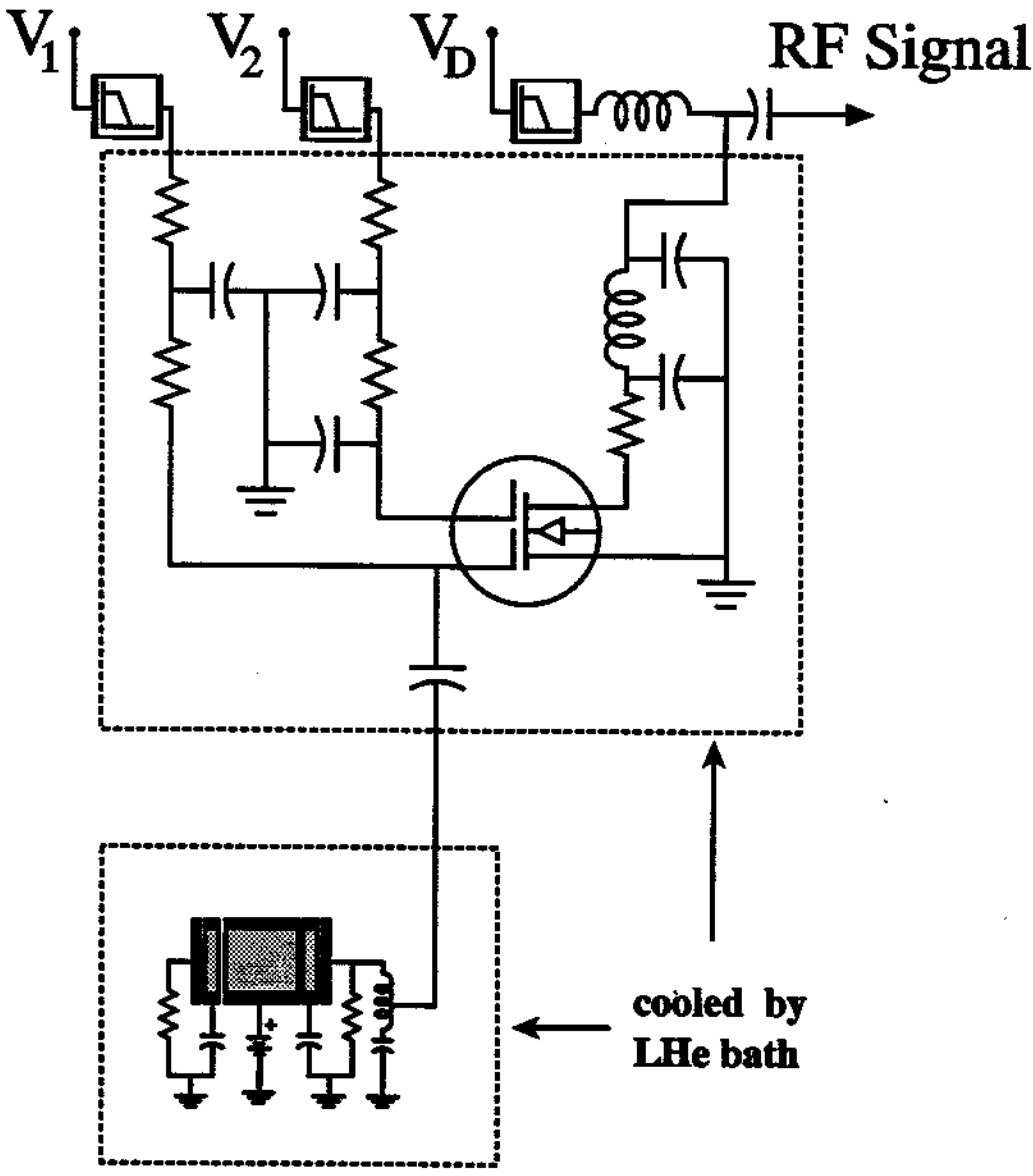

Figure 2.14: A dualgate MOSFET pre-amplifier monitors induced voltage across tuned circuit.

amplifier chain, a dualgate gallium arsenide MOSFET circuit (Fig. 2.14) serves as a pre-amplifier for the weak induced voltage across the helical resonator. This FET pre-amplifier is cooled by thermal contact with a LHe bath to reduce thermal noise. The size of signal and time scale of interest span many orders of magnitude in our study of collective behavior, requiring some important modifications (Fig. 2.15) which have been made to optimize an otherwise traditional electrical set-up [18,93,94,87]. Wideband amplifiers increase the signal from the FET pre-amplifier by a gain of 34 dB. This signal is mixed down to an intermediate frequency (5 MHz), passed through a crystal filter (6 kHz bandpass centered at 5 MHz) and amplified further with a gain of 40 dB. The amplified signal at this frequency can be further processed in various ways using, for example, a storage oscilloscope, a lock-in amplifier and square-law circuits. A splitter sends the signal simultaneously to these devices.

2.5.3 Phase-sensitive Detection

A lock-in amplifier converts the IF signal (5 MHz) into a DC output which is a function of the relative phase between the local oscillator and the forced response [10]

$$S_D = V_d \frac{(\Gamma_z/2)^2 \cos\phi + (\Gamma_z/2)\,\delta\omega_d \sin\phi}{(\delta\omega_d)^2 + (\Gamma_z/2)^2} \quad . \tag{2.43}$$

The relative phase ϕ is varied with the phase-shifter in the lock-in amplifier. This phase-sensitive signal S_D (output A in Fig. 2.15) also depends on the damping rate $\Gamma_z = N\gamma_z$, on the drive strength V_d and on the detuning $\delta\omega_d$ between the drive frequency and the electron oscillator frequency. Fig. 2.12a shows the absorptive signal ($\phi = 0$), and Fig. 2.12b shows the dispersive signal ($\phi = 90°$) for $N = 10^3$ electrons, obtained by sweeping the drive frequency. The full width at half maximum of the Lorentzian lineshape gives the axial damping rate Γ_z, which is used to determine the number of electrons, as already shown.

As we have mentioned, the resonant response to parametric excitation can have one of two steady-state phases which differ by 180° . Since $S_D \rightarrow -S_D$ when

$\phi \rightarrow \phi \pm \pi$, a transition between the phase-bistable states of a parametrically-driven electron can be detected. However, the shortest integration time constant available in our commercial lock-in amplifiers is 10 ms. Hence, to observe the fastest transitions which occur in parametrically-pumped electrons, we bypass this lock-in amplifier, mix the signal with a local oscillator to produce "baseband"

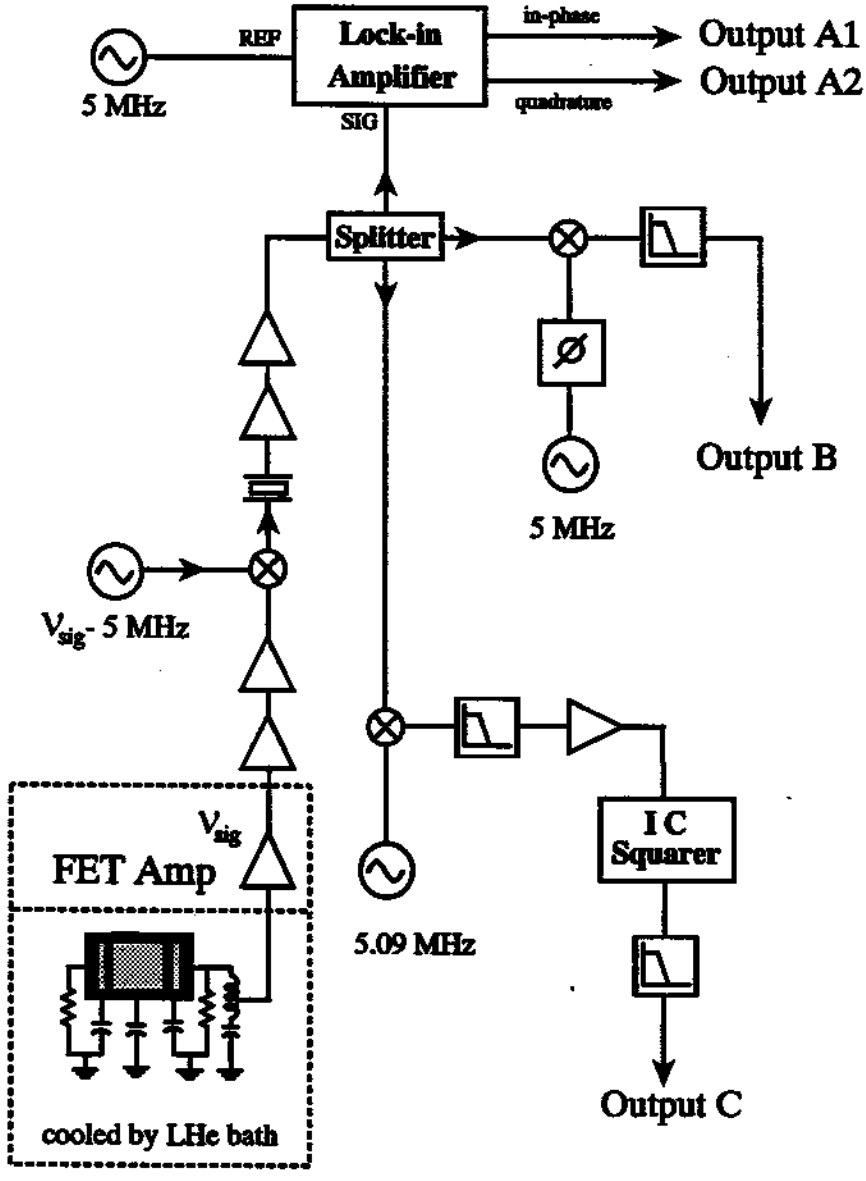

Figure 2.15: Schematic diagram of electrical set-up for processing observed signal.

output and use a storage scope (output B in Fig. 2.15).

2.5.4 Center-of-mass Energy Detection

In some experiments, the amplitude or energy in the axial CM motion is of interest. To measure energy in the CM motion, the response signal is squared and a low-pass filter removes the AC component to obtain a baseband signal which is proportional to the squared amplitude (or energy) of the CM motion (output C in Fig. 2.15). We use a multiplier chip (Analog Devices AD532K) designed for precision instruments to implement

$$V_{out} = \frac{(V_{in})^2}{10} , \tag{2.44}$$

where V_{in} and V_{out} are given in Volts. The accuracy is better than 10% for output in the range of 9 mV to 14V and is better than 5% for output in the range of 25 mV to 10 V. Traditionally, passive diode square-law circuits have been used for this purpose but with narrower operating voltage range (typically 10 times narrower). Unlike the typically weak stochastic signal which these passive diode circuits have been constructed to observe, the coherent response of parametrically-pumped electrons can vary by many orders of magnitude. The better performance of the IC squarer is very useful in establishing the lineshapes of cavity mode resonances which are clearly observed using the coherent motions of parametrically-pumped electron oscillators.

2.6 Forced Excitation

To excite the axial motion which is damped by the tuned circuit, a sinusoidal force $F(t) = F_o \sin(\omega t + \phi)$ can be applied using precision frequency synthesizers. If the rate of energy exchange between the two coupled oscillators is much slower than the rate of resistive dissipation in the tuned circuit (weak-coupling regime), then the differential equation for the axial motion, Eq.(2.40), can be simplified

into one describing a forced, damped, harmonic oscillator

$$m\left[\frac{d^2}{dt^2} + \gamma_z\frac{d}{dt} + (\tilde{\omega}_z)^2\right] z(t) = F_o \sin(\omega t + \phi) \ , \tag{2.45}$$

with a damping rate γ_z. The resonance frequency ω_z of the oscillator is shifted ($\omega_z \longrightarrow \tilde{\omega}_z$) due to interaction with the tuned circuit. The shift $\Delta\omega = \tilde{\omega}_z - \omega_z$ does not exceed one fourth of the maximum linewidth, but must be taken into account to be within range of parametric resonance. Helical resonators using silver-coated or superconducting wire have high quality factor at LHe temperature ($Q > 600$), allowing a further simplification of the damping and frequency shift due to the tuned circuit

$$\gamma_z = \gamma_{zo}\frac{1}{1+\delta^2} \ , \tag{2.46}$$

$$\tilde{\omega}_z - \omega_z = \frac{1}{2}\gamma_{zo}\frac{\delta}{1+\delta^2} \ . \tag{2.47}$$

These forms are illustrated in Fig. 1.1. The detuning δ is defined by $\delta = 2(\omega_z - \omega_M)/\Gamma_M$. The maximum damping rate, given by [18,93]

$$\gamma_{zo} = \left[\frac{\kappa q}{2z_o}\right]\frac{R}{m}, \tag{2.48}$$

with effective parallel resistance $R = L/rC$, is obtained when electron and helical resonator are tuned to the same frequency ($\delta = 0$). Damping can be reduced by adjusting the detuning δ. Control of resistive damping is important for studying parametrically-pumped electron oscillators. Interestingly enough, the electromechanical system of Fig. 2.13 also provides a model for understanding electron-cavity coupling. The frequency shift, which is maximum at $\delta = \pm 1$, has serious implications for some precision experiments (Sec. 4.4).

The description given above for one electron also applies to a system of N electrons provided $z(t) \longrightarrow Z(t)$ to represent the axial center-of-mass (CM) coordinate; $m \longrightarrow Nm$, the total mass; and $q \longrightarrow Nq$, the total charge of the cloud. The damping rate for the axial CM motion is proportional to N

$$\Gamma_z = N\gamma_z \tag{2.49}$$

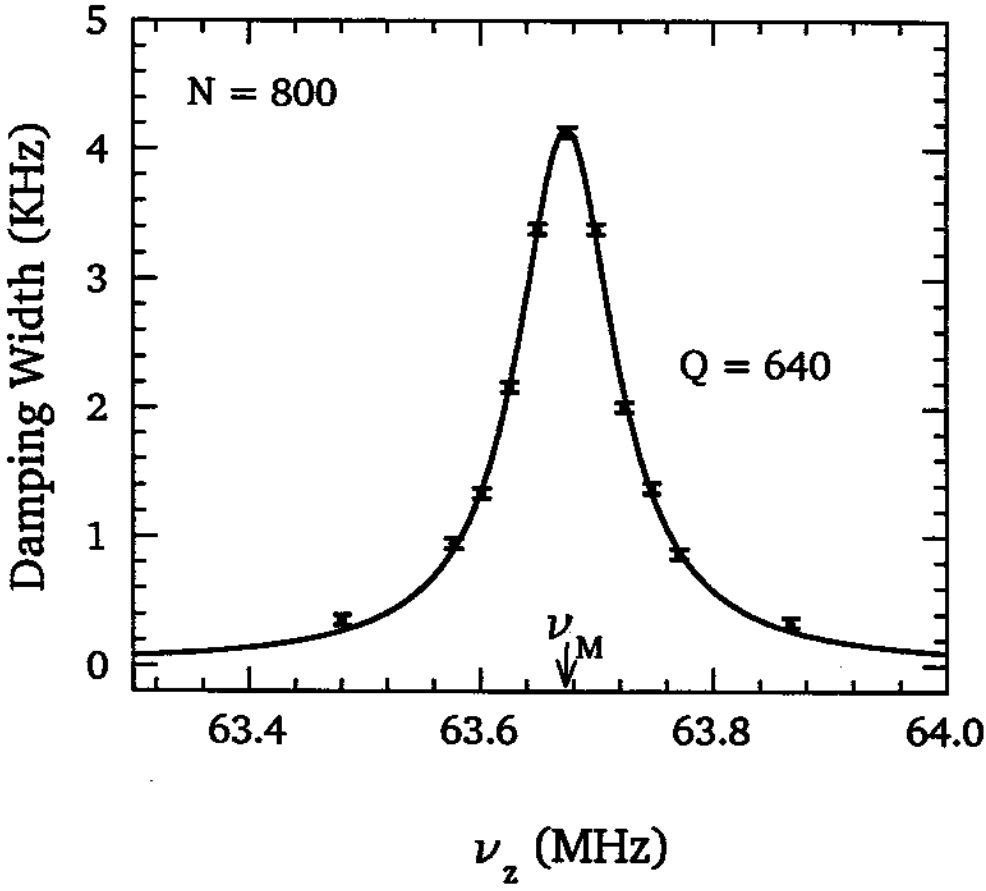

Figure 2.16: Lorentzian form fits well to measured damping width of driven resonance versus oscillation frequency ν_z near the resonance frequency ν_M of tuned circuit.

where γ_z is $(30\ \text{ms})^{-1}$ at maximum for one electron. The damping width can be measured from the FWHM width of the Lorentzian lineshape (Fig. 2.12) of the in-phase signal from a phase-sensitive detector, as already mentioned. Fig. 2.16 plots the measured resonance linewidth as a function of detuning from the tuned circuit for $N = 800$ electrons. Variation of observed linewidths with detuning δ fits well to a Lorentzian lineshape, as expected from Eq. (2.46). Quality factor of the helical

resonator measured from Fig. 2.16 is in good agreement with that obtained from Johnson-noise-driven resonance of the tuned circuit (Appendix B). As already shown, Eq. (2.49) allows N to be determined by comparison with the driven resonance linewidth for one electron γ_z. For large number of electrons ($N \gg 10^3$), the axial frequency must be sufficiently detuned from the LCr frequency in order for Eq. (2.49) and for weak-coupling approximations to be valid. When coupling between the tuned circuit and a very large number of electrons is too strong, the noise-driven Fourier spectrum of the resonantly coupled system can be used to measure N (discussed in Appendix B).

Forced excitation, Eq. (2.45), can be accomplished by applying a single RF electric field near to resonance with the electron axial frequency. This method is not used in practice because a direct, resonant drive will saturate the high-gain chain of amplifiers used to observe the small signal of driven electrons ($V_L \sim 20$nV for one electron). To avoid stray coupling (such as capacitive coupling) between the drive and detection electrodes with a resonant RF field, two RF fields of lower frequencies are used to drive the electrons. We briefly summarize the essential features since the mechanism has been treated in detail elsewhere [10]. The spring constant of the axial oscillator is modulated at a fixed frequency ω_1 which is much lower than the resonant frequency $\tilde{\omega}_z$ (shifted by tuned circuit). Another frequency synthesizer drives the electron at a frequency ω_d which can be varied, so that

$$F_o \sin(\omega_d t + \phi) = m\left[\frac{d^2}{dt^2} + \Gamma_z \frac{d}{dt} + (\tilde{\omega}_z)^2 (1 + \epsilon \cos(\omega_1 t))\right] z(t) \quad , \qquad (2.50)$$

where $\epsilon \ll 1$ is the ratio of the modulation amplitude to the static trapping potential. An observable response is obtained by sweeping the drive frequency ω_d so that

$$\omega_d = (\tilde{\omega}_z - \omega_1) + \delta\omega_d \qquad (2.51)$$

where $\delta\omega_d$ is a drive detuning from resonance. The effective force produced in this manner is the same as the direct drive in Eq.(2.45), with the exception that the effective force is smaller in amplitude by a factor $\beta/2$. The "modulation index" β

is given by [10]

$$\beta = \frac{\epsilon}{2}\frac{\tilde{\omega}_z}{\omega_1} \ . \tag{2.52}$$

2.7 Parametric Excitation

Throughout this study, the cooperative phenomena of interest are observed when trapped electrons are pumped parametrically at a frequency $\omega_d \approx 2\omega_z$ which is approximately twice the axial oscillation frequency. To accomplish this, the otherwise static potential in Eq. (2.15) is modulated using a precision frequency synthesizer. The resulting axial restoring force has a spring "constant" with a small periodic component, i.e.,

$$m\omega_z^2 \longrightarrow m\omega_z^2\left[1 + h\cos(\omega_d t)\right] . \tag{2.53}$$

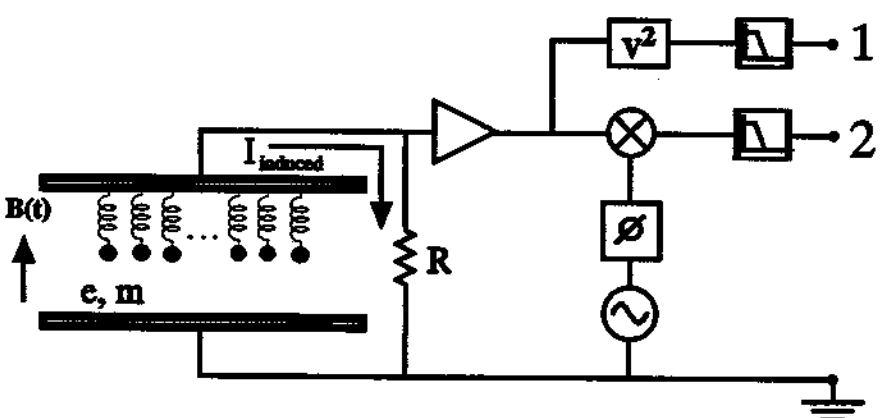

Figure 2.17: Simplified diagram showing detection electronics used in observing parametrically-pumped electron oscillators (modeled as massive, charged balls attached to springs).

Both the strength of the parametric drive, h, and its frequency ω_d are varied as part of these studies. A simplified model which gives the important features of the system under study is presented in Fig. 2.17. A trapped electron is modeled as a ball of charge q and mass m suspended from an axial spring whose spring constant has just been discussed. The trap electrodes are involved in the detection of the axial motion of the center of mass of the trapped electrons in a way that can be represented by the parallel plates in the figure. We observe the current induced through the resistor R connected across the parallel plates. (For simplicity, the axial oscillation frequency is tuned to the resonant frequency of the LCr circuit so that it can be effectively replaced by a resistor R.) Power dissipated in the resistor is responsible for the axial damping which has been mentioned. The voltage across resistor R (proportional to the velocity of the CM motion) is amplified and electronically processed to give the CM energy (output 1 in Fig. 2.17) and the phase of the CM motion (output 2 in Fig. 2.17) relative to the parametric pump. Because the pump is at twice the response frequency, any coherent (steady-state) response of the electron cloud (not previously observed) must have either of bistable phases that differ by 180°. Transitions between these phase-bistable states can be observed via output 2 in Fig. 2.17. This simplified picture omits several features that are important. First, the perpendicular motions of the electrons are important, with the fast cyclotron motions of the electrons about the strong magnetic field radiating into the surrounding microwave cavity to cool the system. Inter-particle Coulomb repulsion couples the oscillators and is crucial for collective motions. Further, energy exchange occurs between the axial and perpendicular motions.

Instead of applying an RF potential (at $\omega_d \approx 2\tilde{\omega}_z$) between the ring electrode and both endcaps to produce the desired modulation

$$V_o \longrightarrow V(t) = V_o\,[1 + h\ cos(\omega_d t)]\,, \tag{2.54}$$

it is experimentally convenient to apply the RF drive between one endcap and the ring electrode. The resulting RF field at the trap center has a symmetric and

anti-symmetric component. Only the symmetric field contributes significantly to parametric excitation, with effective modulation strength which is smaller by 6 dB. The anti-symmetric component, in principle [59], can produce parametric resonance if the trapping potential has a cubic anharmonicity of the form

$$\Delta V = \frac{1}{2} c_3 \left(\frac{Z}{z_o}\right)^3 V_A \tag{2.55}$$

where $V_A < 10^{-4} V_o$ is a very small imbalance in the applied trapping potential. The relative modulation strength of the anti-symmetric component compared to the symmetric component is given by

$$\frac{h_{anti}}{h_{sym}} = \frac{1}{2} \frac{c_1 c_3}{(1+C_2)^2} \left(\frac{d}{z_o}\right)^4 \left(\frac{V_A}{V_o}\right). \tag{2.56}$$

The coefficients $c_1 c_3$, and C_2 have been measured (mentioned earlier). In practice, this ratio is negligibly small ($\sim 10^{-5}$) and hence only the symmetric modulation of the trapping potential contributes to parametric resonance.

2.8 Summary

Electrons isolated in a cylindrical cavity provide a new system for radiative experiments with standing wave modes having well-known field configurations. Anywhere from one to over 10^5 electron oscillators can be confined in a cylindrical Penning trap which is constructed to be the best approximation to an ideal microwave cavity. The electrons can be displaced along trap axis to probe the standing wave patterns. The cyclotron frequency is readily varied to selectively couple with a cavity mode of interest. A cylindrical Penning trap thus allows precise control of electron-cavity interaction (Chapter 4). On the other hand, it requires a large correction potential V_c to minimize deviations from a pure electric quadrupole (which insures harmonic axial oscillation at well-defined frequency needed for precise experiments with one electron). Traditionally, necessary corrections are reduced by employing trap electrodes shaped along hyperbolic contours, but residual anharmonicity is unavoidable due to imperfections and misalignments

as well as holes and slits. Analysis [28,29] of the electrostatic properties of hyperbolic traps suggested that the need for hyperbolic electrodes may not be as strong as had been assumed. Fortunately, the electrostatic properties for cylindrical traps can be calculated analytically, greatly facilitating the design of an "orthogonalized" set of cylindrical electrodes [30] which allows large adjustments to be made to restore a high quality electric quadrupole. Cylindrical electrodes can be machined to higher accuracy in less time. We have now demonstrated that the simpler, cylindrical traps can be utilized even for the precise measurements with one electron (already mentioned), with the added advantages of a well-characterized microwave cavity. [77] A single electron has been observed with a signal-to-noise ratio which compares favorably with that obtained in hyperbolic traps [88,84,10]. Parametric excitation of isolated electron oscillators in such a well characterized environment is ideal for studying collective behaviors, cavity electrodynamics, and fluctuation phenomena.

Chapter 3

Parametric Resonance

Emergence of long-term temporal order in a system of parametrically-pumped electron oscillators may be regarded as a dissipative structure [65] (whose coherent behaviors can only be maintained with sufficient flow of energy). Familiar dissipative structures include the Rayleigh-Benard instability in convection cells and the laser instability [17]. For example, it is well-known that the laser behaves like an ordinary lamp if the pump is weak, and hence the output is low and incoherent. But when the pump power exceeds a threshold, the power and coherence time of the laser output increase by many orders of magnitude.

Parametric excitation, except in an experiment with one electron [92], has been used to increase the disordered internal motions of stored ions or electrons [18,93]. In the new regime which is studied here, parametrically-pumped electron oscillators respond stochastically at a low level until the electrons are cooled via radiation into the microwave cavity whereupon strong coherent oscillations are observed. Cooling by the LCr circuit does not suffice. However, electron-electron collisions transfer some internal energy to the cyclotron motions of the electrons. This energy is removed by coupling the cyclotron oscillators to a resonant mode of the cold, cylindrical cavity (Chapter 4). Throughout this chapter, radiative cooling of the electron oscillators has been maximized by tuning the cyclotron frequency into resonance with the eigenfrequency of a cavity mode, such as TE_{115}. Later chapters will discuss what happens when the electrons are not resonantly

cooled by the microwave cavity.

3.1 Transition to Coherent Oscillations

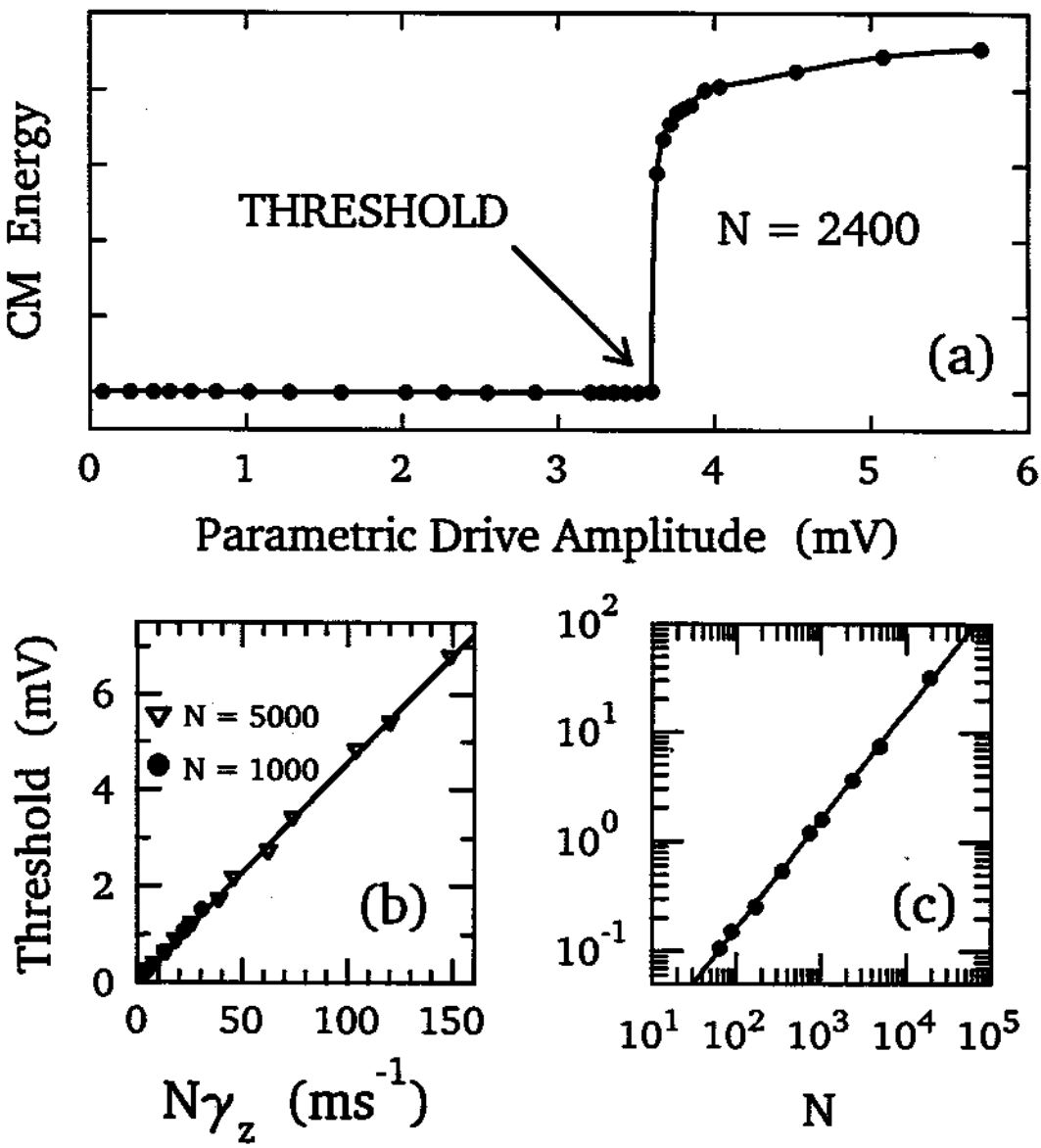

Figure 3.1: Observation of abrupt transition from weak, disordered motions to large, coherent CM oscillation at a pump strength threshold (a). Measured threshold varies linearly with damping rate (b) and with the number of electrons (c).

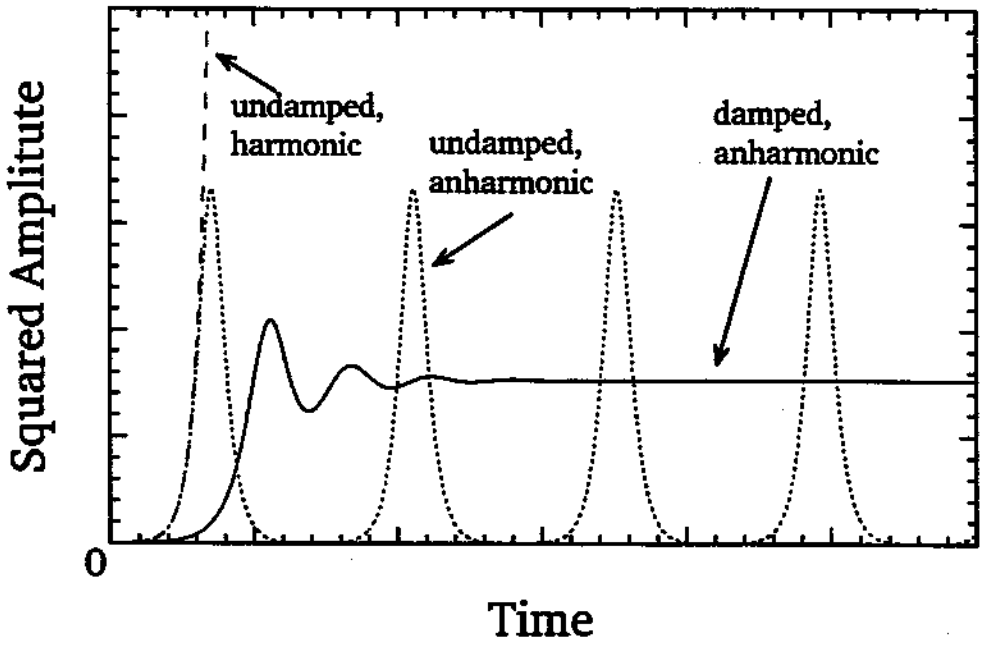

Figure 3.2: Parametric resonance with characteristic exponential growth of harmonic oscillation (dashed line). Periodic variation results as anharmonicity arrests growth (dotted line) but damping causes relaxation to steady state (solid line).

Cooled electrons switch abruptly from independent, stochastic motions to a highly synchronized motion with a greatly increased center-of-mass (CM) amplitude (Fig. 3.1a) as the strength of the parametric pump at $\omega_d = 2\omega_z$ is increased by less than 0.5 dB across the threshold $h = h_T$. The amplitude of the CM motion increases by orders of magnitude and this motion is phase coherent with the subharmonic of the drive at $\omega_d/2$ (coherence time $> 1000s$ for $N > 2000$ electrons). Fig. 3.1b shows that $h_T \propto N\gamma_z$ by detuning ω_z from resonance with the LCR circuit to change γ_z (as illustrated earlier in Fig. 2.16) and by varying the electron number between $N = 60$ and $N = 18,000$ (Fig. 3.1c). Logarithmic scales are used in Fig. 3.1c to show the linear dependence over many orders of magnitude.

These observations suggest that the parametric drive is exciting an insta-

bility in the collective motion of the N electron oscillators. The full equations of motions are described in Sec. 3.4. To examine some features of the motions, we use a dimensionless CM coordinate $Z = \sum z_i/(Nd)$ where z_i/d is the axial position of the ith electron scaled by a suitable trap dimension. In the limit of vanishing internal energy, the collective motions approach those of a rigid model. A rigid axial motion of N electrons near the trap center has the same differential equation as that for a single particle on axis except with N times larger damping,

$$\begin{aligned} \ddot{Z} + (N\gamma_z)\dot{Z} &+ \tilde{\omega}_z^2[\,1 + h\cos(\omega_d t)\,]Z \\ &+ \frac{2C_4}{1+C_2}\omega_z^2 Z^3 + \frac{3C_6}{1+C_2}\omega_z^2 Z^5 = 0, \end{aligned} \tag{3.1}$$

where h is the pump strength and ω_d is the pump frequency. The nonlinear (anharmonic) terms, with strengths C_4 and C_6, arise from unavoidable or deliberate distortions of the pure electrostatic quadrupole potential [10]. Hence, confined in a pure electrostatic quadrupole, undamped rigid motion would satisfy Mathieu's equation (which is regained from Eq. (3.1) by setting $\gamma_z = C_4 = C_6 = 0$). Mathieu's equation should be a good approximation for small oscillations near the center of actual traps where the restoring force is essentially linear.

It is well-known that the bound solution $Z = 0$ to Mathieu's equation is unstable in some regions of the space (h,ω_d) formed from the pump strength and frequency [1,63]. For small pump strength, $h << 1$, the regions of instability are located near

$$\omega_d = \frac{2\tilde{\omega}_z}{n}. \tag{3.2}$$

We focus only on the $n = 1$ region since higher order instability regions are very narrow and much harder to excite [59]. For pump frequency sufficiently close to $2\omega_z$, any small oscillation grows exponentially without bound (dashed line in Fig. 3.2). In actual Penning traps, however, the residual anharmonicities shift the resonant frequency as the amplitude increases, arresting the rapid growth and causing periodic variation in the amplitude (dotted line in Fig.3.2). With damping

taken into account, the $n = 1$ region of the Mathieu instability is given by

$$-\frac{1}{2}\omega_z\sqrt{h^2 - h_T^2} < \omega_d - 2\tilde{\omega}_z < \frac{1}{2}\omega_z\sqrt{h^2 - h_T^2}\,, \tag{3.3}$$

which has a hyperbolic boundary (Fig. 3.3). This region is smaller for increased damping since the pump must compete with energy dissipation (dashed hyperbola in Fig. 3.3). Inside the hyperbolic region, any small symmetry-breaking fluctuation in the CM location ($Z \neq 0$) increases exponentially but with reduced exponent as the parametric drive overcomes the resistive damping. With the rapid growth arrested by anharmonicities, the damped oscillator relaxes to a steady-state amplitude (Fig.3.2, solid line). Nontrivial steady-state solutions to Eq. (3.1), therefore,

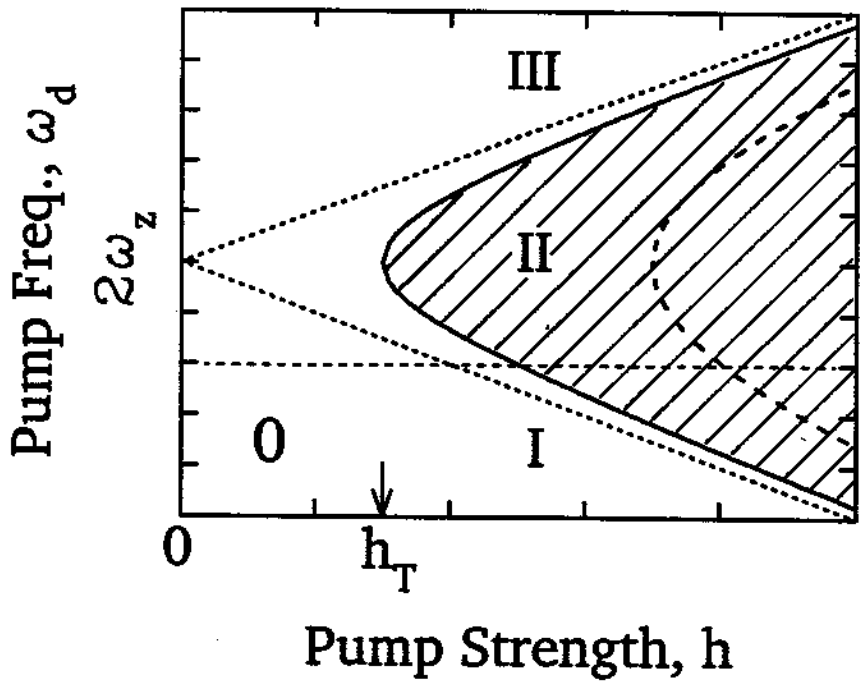

Figure 3.3: Region of $n = 1$ Mathieu instability (shaded) . For $h \ll 1$, a hyperbola divides the neighborhood (h, ω_d) into regions having different sets of stable steady states. For negative C_4 or C_6, region I has 3 stable states; region II, 2 phase bistable exited states; regions III and O, 1 quiescent state.

are limit cycle oscillations [64,59] and

$$h_T \equiv 2N\gamma_z/\omega_z \tag{3.4}$$

is the drive strength h at which there is an abrupt threshold. The observed threshold in Fig. 3.1 corresponds to this vertex of the hyperbolic boundary of the Mathieu instability, which shifts outward with increasing $N\gamma_z$. The measured proportionality constant agrees with Eq. (3.4) within 40% uncertainty.

For an isolated electron ($N = 1$), Eq. (3.1) is an exact description of the unavoidable rigid motion which has been observed [92]. The generalization of Eq. (3.1) which describes the general, nonrigid motion of N electrons has anharmonic terms which depend upon the axial and radial coordinates of the individual electrons (z_i and ρ_i), rather than upon Z alone. For example (see Sec. 3.4), Z^3 becomes $\sum_i (z_i^3 - 3z_i\rho_i^2/2)/N$. Rigid motion of many electrons is typically prevented by the large, stochastically changing coordinates (z_i, ρ_i) of the individual electrons.

Below threshold (i.e. $h < h_T$), $Z = 0$ is the only steady-state solution to Eq.(3.1), and hence is absolutely stable. For the electron cloud, only internal motions (relative to the CM) can therefore be excited by the parametric driving force. Such excitations are occurring, perhaps because the resonant frequencies of internal motions are broadly distributed by the Coulomb repulsion of the electrons, or perhaps because resonant modes of the electron cloud are excited [23], but the exact mechanism is still not understood. Energy coupled into the CM motion by the anharmonic nonlinearities is observed in the form of incoherent transients since such fluctuations (Chapter 5) are damped by the LCR circuit at a rate of order $N\gamma_z$. The coherence time for the detected CM motion is less than 1 ms. This regime is well described by a "bolometric model" which treats the electron cloud as a gas which comes into thermal equilibrium via collisions between electrons [18,93]. However, no synchronized, coherent motion is anticipated or can be accounted for in this model.

Region in (h, ω_d) Space	Stable States	Multiplicity
Region O $(h < h_T)$	1 Quiescent	1
Region I $(h > h_T)$	1 Quiescent + 2 Excited (phase-bistable)	3
Region II $(h > h_T)$	2 Excited (phase-bistable)	2
Region III $(h > h_T)$	1 Quiescent	1

Table 3.1: Multiplicity of stable steady states near $n = 1$ threshold of Mathieu instability. Negative C_4 or C_6 is assumed. For positive C_4 or C_6, regions I and III are interchanged.

3.2 Hysteresis and Lineshapes

In the new regime with $h > h_T$, history-dependent behavior is observed, indicating that the system has more than one stable, collective state above threshold. A hyperbola, Eq.(3.3), divides the parameter space of the pump into 3 distinct regions in the neighborhood of the $n = 1$ instability, according to the multiplicity of stable states which exist above threshold. For simplicity, we discuss the case for $C_4 \leq 0$ and $C_6 \leq 0$ but not both equal zero (Table 3.1 and Fig. 3.3). Below threshold (region O), only the quiescent state ($Z = 0$) is stable. Region I (below the lower branch of the hyperbola in Fig. 3.3)has two degenerate excited states which differ only in phase by 180°, in addition to the quiescent state. Region II (inside the hyperbola in Fig. 3.3) has only the two phase-bistable states because the quiescent state is a saddle-point. As in region O, the quiescent state is the only stable state in Region III (above the upper branch of the the hyperbola in Fig. 3.3). For $C_4 > 0$ or $C_6 > 0$, regions I and III are interchanged.

The "lineshape" of parametric resonance (frequency dependence of the CM energy) varies with anharmonicity and the order in which the pump frequency is swept through these three regions above threshold. Expected lineshapes for the rigid model are shown in Fig. 3.4. Increasing the pump frequency in the order

(I $\longrightarrow$ II $\longrightarrow$ III), the CM energy jumps to a large value as the initial quiescent state becomes unstable in region II. On the other hand, if the pump frequency is decreasing in the order (III $\longrightarrow$ II $\longrightarrow$ I), the system remains in an excited state even though the pump frequency is in Region I. Fluctuations would cause the excited state to collapse to the quiescent state eventually. Different characteristic dependencies of the steady-state amplitude upon the pump frequency is obtained by tuning the trap potentials to make either the C_4 or the C_6 term dominant. For a very anharmonic trap (when C_4 term dominates), the CM energy in the excited

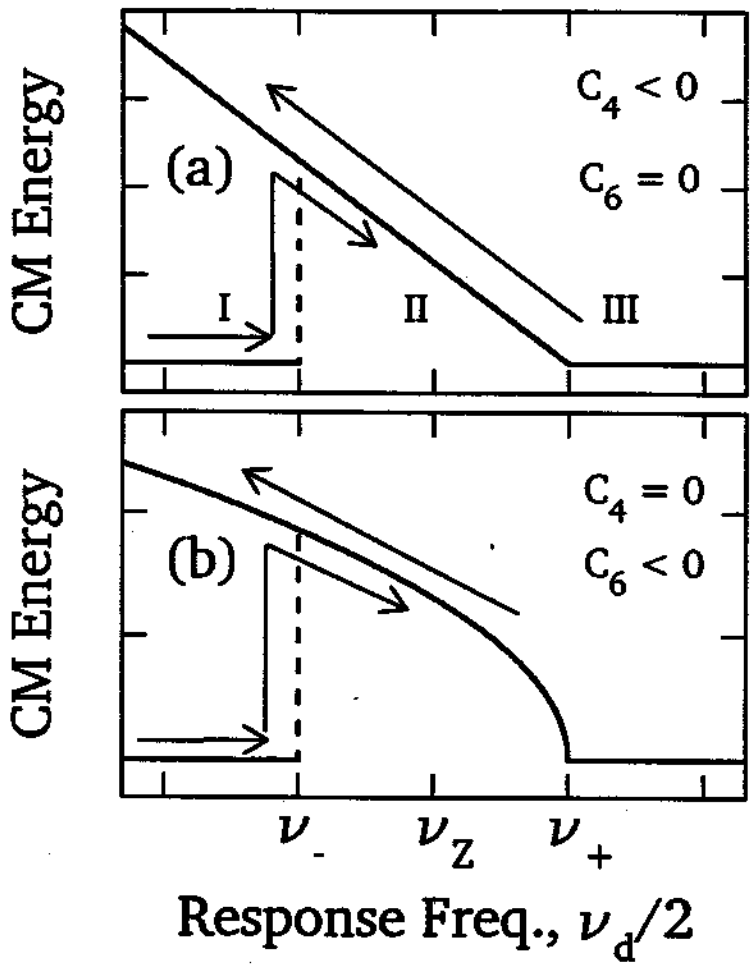

Figure 3.4: Calculated rigid model lineshapes, showing hysteresis of CM energy versus pump frequency ν_d . CM energy is a linear function of pump frequency ν_d for $C_4 < 0$ with $C_6 = 0$ (a), and a parabolic function of ν_d for $C_4 = 0$ with $C_6 < 0$ (b).

state is a linear function of the the pump frequency (Fig. 3.4a). On the other hand, for a well-tuned trap (when $C_4 \approx 0$ and C_6 term dominates), the CM energy for the rigid model is a parabolic function of the pump frequency (Fig. 3.4b). Hysteresis is indeed observed (Fig. 3.5) with resonance "lineshapes" which agrees qualitatively with the rigid model, even though the size of the signal is limited by cavity cooling, an interesting and useful feature which is studied in Chapter 4.

Another type of hysteresis but with fixed pump frequency, is observed when the

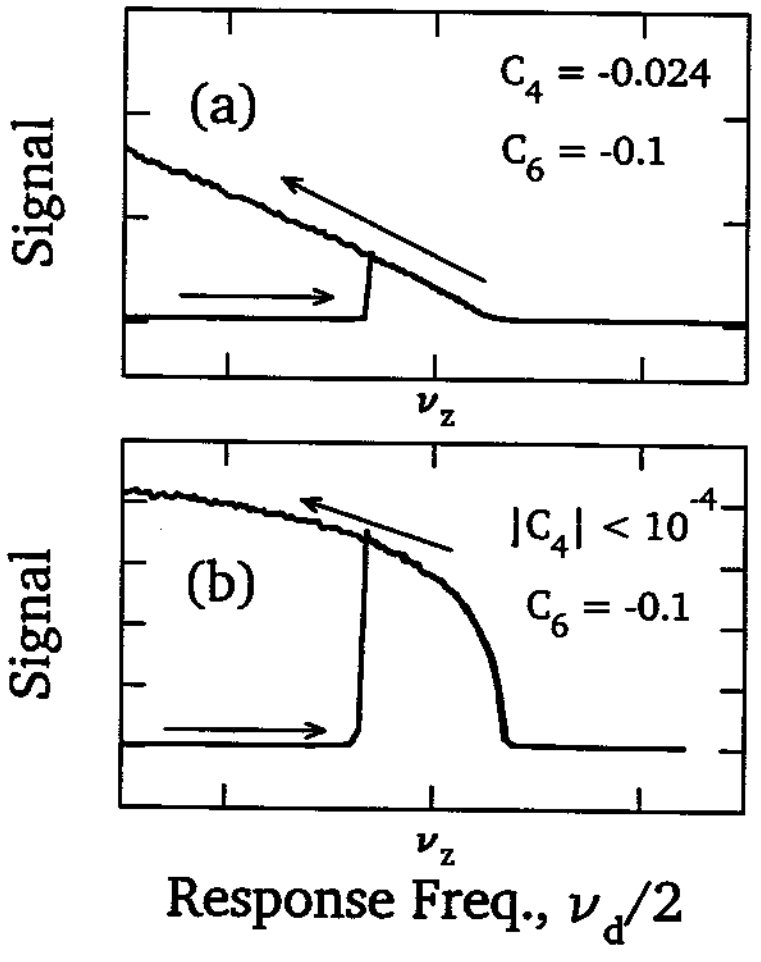

Figure 3.5: Observed resonance lineshapes with hysteresis. Maximum CM energy is limited by cavity-cooling but lineshapes (a) for large C_4 and (b) for negligible C_4 agree qualitatively with rigid model.

pump strength is swept through Regions I and II (e.g., Fig. 3.3, dashed horizontal line). In a rigid model without fluctuations, the system remains in the quiescent state as the pump strength is increased into Region I. It abruptly jumps to an excited state as the pump strength increases across the boundary between Regions I and II. If the pump strength is subsequently decreased into Region I, the excited state remains stable until the pump goes below threshold h_T. Fig.(3.6 a) shows the hysteresis loops observed with synchronized electron oscillators, taken from 4 consecutive sweep cycles (O $\longrightarrow$ I $\longrightarrow$ II $\longrightarrow$ I $\longrightarrow$ O) of the pump strength. Transitions between quiescent and excited states are random due to fluctuations (Chapter 5). The observed distribution (Fig. 3.6 b) of downward transition points (excited to quiescent) shows a narrow spread with small deviations from the threshold h_T in most cases. On the other hand, the observed distribution (Fig. 3.6 b) of upward transition points (quiescent to excited) shows a broader spread with larger deviations from h_U, the boundary point between regions I and II. This seems to suggest that the quiescent state is less stable against fluctuations than the excited states.

The boundary in (h,ω_d) space wherein $Z = 0$ becomes unstable is observed by obtaining a family of resonances at fixed pump strengths above threshold (Fig. 3.7a). The electron oscillators start in the quiescent state in region I. As the pump frequency is increased, the signal jumps abruptly to a large value as $Z = 0$ becomes unstable upon crossing into region II, defining a lower corner frequency $\nu_-(h)$ in Fig. 3.7a. As the pump frequency is increased further, the large signal falls abruptly upon crossing into region III, defining an upper corner frequency $\nu_+(h)$ in Fig. 3.7a. This is repeated for a sequence of fixed pump strengths (illustrated in Fig. 3.7b). The observed range of parametric resonance $[\nu_-(h), \nu_+(h)]$ increases with pump strength h. In agreement with Eq.(3.3) for a rigid model, measured corner frequencies (Fig. 3.7c) lie on a hyperbola when plotted versus pump strength h, with a vertex corresponding to a threshold h_T.

3.3 A Rigid Model

A rigid model neglects many interesting features in order to provide a simple picture. Many important observations which are presented in subsequent chapters can not be described in a rigid model. Nevertheless, it is a useful approximation for some features of the observed coherent motions. Main features of a rigid model have been presented above for comparison with the observed coherent behavior in parametrically-pumped electron oscillators. An exact analysis is difficult but

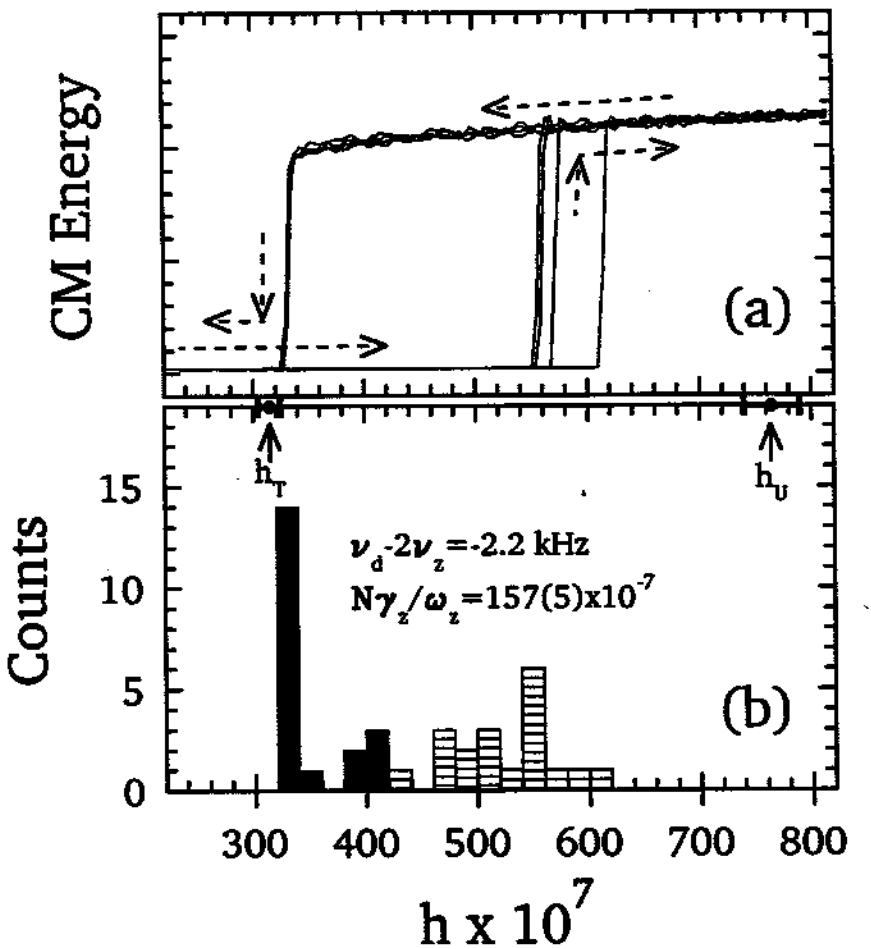

Figure 3.6: (a) Observed hysteresis loops of CM energy versus pump strength in 4 consecutive cycles [O $\longrightarrow$ I $\longrightarrow$ II $\longrightarrow$ I $\longrightarrow$ O]. (b) Histograms of transition points showing that the quiescent state is less stable against fluctuations.

fortunately good approximations are available when the system is weakly damped. This allows the steady state properties to be studied analytically and transient responses to be simulated efficiently. The approximate equations of motion are

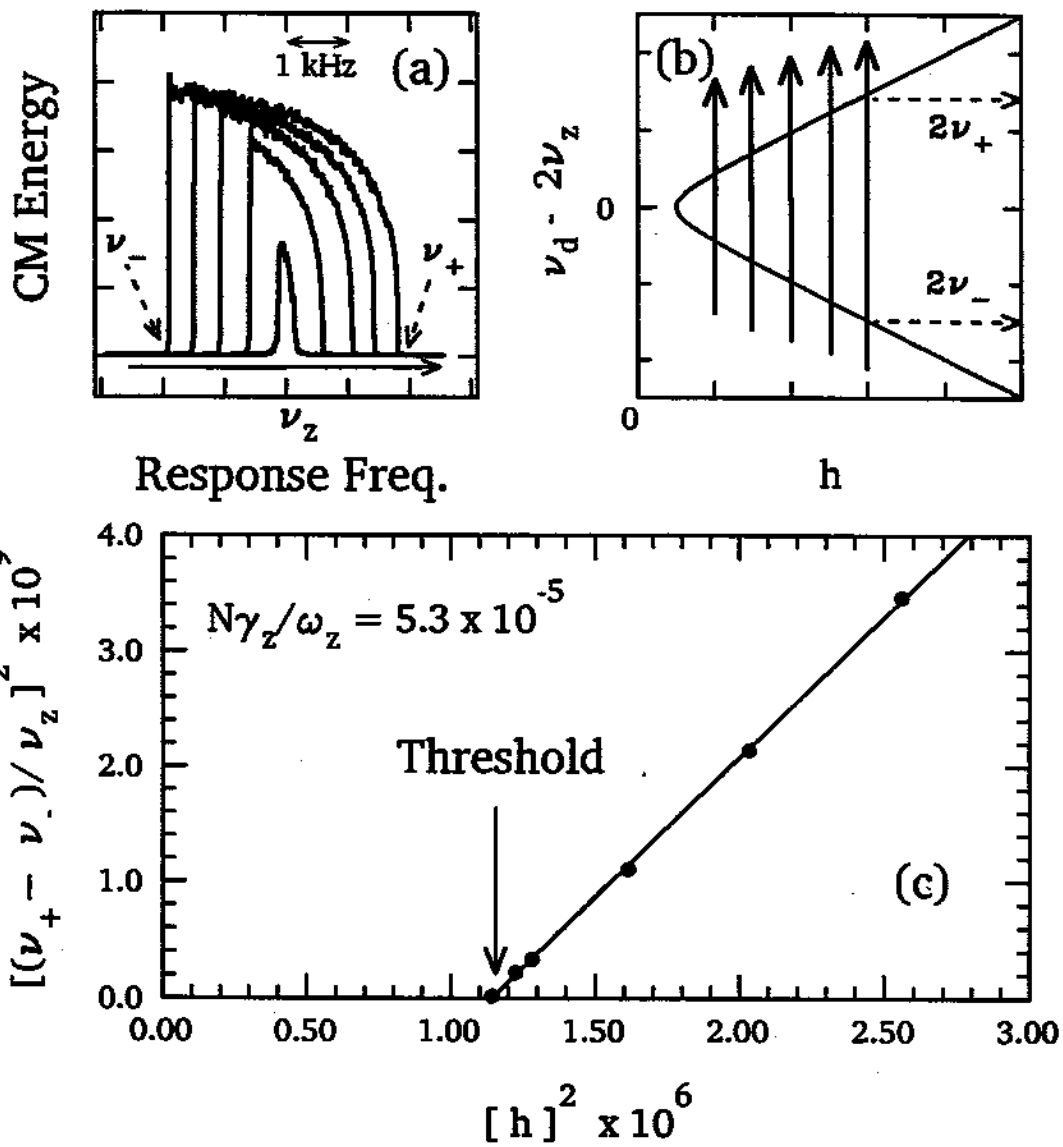

Figure 3.7: Observed frequency range of instability (a) increases with h . Increasing ω_d at fixed h values as illustrated in (b) generates a family of parametric resonances (a). Measured corner frequencies $\nu_+(h)$ and $\nu_-(h)$ fit well to a hyperbola (c) when plotted versus h.

presented in this section with a generalized treatment of the trap anharmonicity and a possible interesting application to one electron (Sec. 3.3.4). The equation of motion Eq. 3.1 is rewritten as

$$0 = \left[\frac{d^2}{dt^2} + N\gamma_z\frac{d}{dt} + (\tilde{\omega}_z)^2(1 + h\cos(2\Omega t))\right] Z(t) + (\omega_z)^2 G(Z) \ , \qquad (3.5)$$

where h is the strength of the parametric drive and 2Ω ($\equiv \omega_d$) is the drive frequency. As before, the coordinate Z is made dimensionless by scaling to the trap size d. To include all orders of deviations (deliberate and unavoidable) from a pure electrostatic quadrupole, the anharmonicity function $G(Z)$ is written as an infinite power series

$$G(Z) = \sigma_4 Z^3 + \sigma_6 Z^5 + \sigma_8 Z^7 + ..., \qquad (3.6)$$

with dimensionless coefficients σ_n which are related to the expansion coefficients C_n of the trapping potential by

$$\sigma_n = \frac{n}{2}\frac{C_n}{1 + C_2}. \qquad (3.7)$$

In compensated Penning traps, C_4 can be made negligibly small using potentials on a set of compensation electrodes (as already discussed). Hence, the two leading terms in the series are used in Eq. (3.1). Since the electron oscillators are weakly damped ($N\gamma_z \ll \omega_z$), a method of multiple time scale [64] may be employed to study Eq.(3.5) in the parameter range of experimental interest. To lowest order in the small parameter $h \ll 1$, we seek solutions at half the frequency of the parametric pump

$$Z(t) = A(t)\ cos[\Omega t + \Psi(t)] + O(h) \ . \qquad (3.8)$$

In this approximation, the slowly varying amplitude $A(t)$ and phase $\Psi(t)$ satisfy a set of coupled first order differential equations

$$\frac{d}{dt}A = -\frac{1}{2}N\gamma_z\left[1 - \frac{h}{h_T}\sin(2\Psi)\right]A, \qquad (3.9)$$

$$\frac{d}{dt}\Psi = (\tilde{\omega}_z - \Omega) + \frac{1}{4}\tilde{\omega}_z h\cos(2\Psi) + J(\{\sigma_i\}, A), \qquad (3.10)$$

derived using a method of multiple time scale [64]. The trap anharmonicity enters these approximate equations of motion through the function

$$J(\{\sigma_i\}, A) = \frac{\omega_z^2}{A\tilde{\omega}_z} \int_0^{2\pi} \frac{d\phi}{2\pi} \cos\phi \; G(A\cos\phi) \quad . \tag{3.11}$$

For example, if $G(Z) = \sigma_4 Z^3$ then

$$J(\sigma_4, A) = \frac{3}{8}\sigma_4 \frac{\omega_z^2}{\tilde{\omega}_z \Omega} A^2. \tag{3.12}$$

We shall use this specific case to illustrate some of the calculations. For example, calculation of growth and relaxation to steady state as shown in Fig. 3.2 is faster using the approximate equations of motion, with results which agree with a direct numerical integration of the exact equation to better than 0.3%.

3.3.1 Steady State Amplitudes

The amplitude of oscillation $A(t)$ will decay for $h < h_T$ because $A^{-1}\dot{A}$ is negative definite, from Eq.(3.9). Hence, below the threshold

$$h_T = 2N\frac{\gamma_z}{\tilde{\omega}_z} \quad , \tag{3.13}$$

the only steady state solution ($\dot{A} = \dot{\Psi} = 0$) is

$$Z(t) = 0. \tag{3.14}$$

For a drive strength above h_T, there are two additional equilibrium amplitudes

$$(A_\pm)^2 \;=\; \frac{4}{3}\frac{1}{\sigma_4}\left[\frac{2(\Omega - \tilde{\omega}_z)}{\tilde{\omega}_z} \pm \frac{1}{2}\sqrt{h^2 - h_T^2}\right]. \tag{3.15}$$

It can be shown that only one choice of the sign gives stable steady-state solutions. Assuming $\sigma_4 < 0$ the negative sign gives stable solutions (Fig. 3.4a). For a well-tuned trap, higher order anharmonicity must be considered. If $G(Z) = \sigma_6 Z^5$ (to approximate a well-tuned trap) then the non-trivial steady states have amplitude given by

$$(A_\pm)^4 \;=\; \frac{8}{5}\frac{1}{\sigma_6}\left[\frac{2(\Omega - \tilde{\omega}_z)}{\tilde{\omega}_z} \pm \frac{1}{2}\sqrt{h^2 - h_T^2}\right], \tag{3.16}$$

with the same sign selection rule (Fig. 3.4b).

3.3.2 Phase Bistability

Resonantly-excited solutions are degenerate because the steady-state phase is determined by the pump only up to $\pm\pi$. This is reflected by the invariance of Eq.(3.9) and Eq.(3.10) under the transformation

$$\Psi \longrightarrow \Psi \pm \pi. \tag{3.17}$$

On the other hand, the phase of steady-state solutions Ψ is given by the condition ($\dot{A} = 0$)

$$\sin(2\Psi_s) \;=\; h_T/h. \tag{3.18}$$

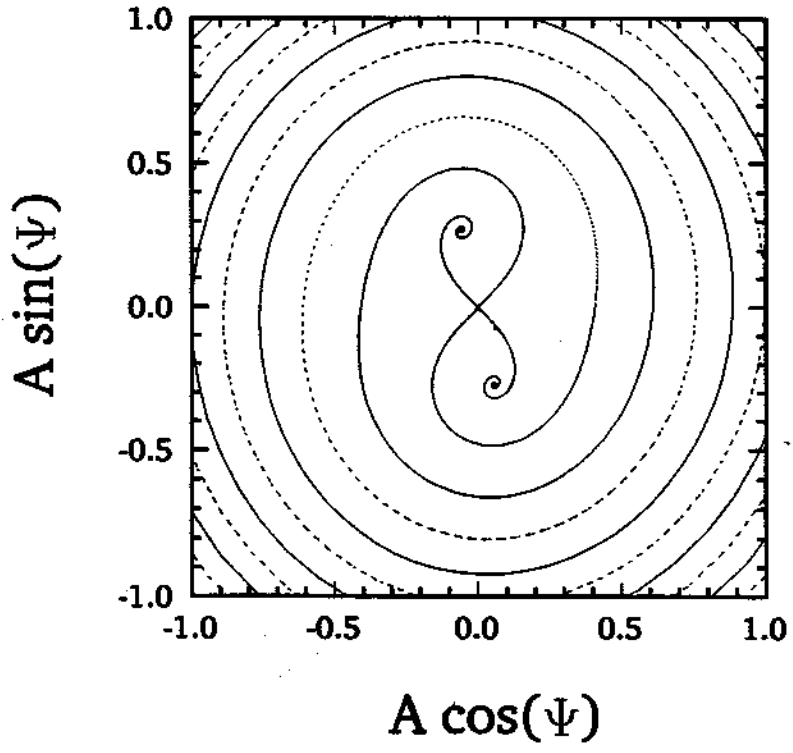

Figure 3.8: Basins of attraction for the two phase states. Quiescent state at the center is a saddle-point.

This is graphically illustrated in Fig. 3.8 which shows the basins of attraction of the two phase states. The saddle-point at the origin is the quiescent state. Phase bistability is manifested by parametrically pumped electron oscillators in interesting ways involving fluctuation phenomena (Chapter 5).

3.3.3 Instability of $Z = 0$ State

As already shown, the quiescent state $Z(t) = 0$ is unstable for some range of system parameters. Without anharmonicity $G(Z)$, the electrons would be ejected from the trap. In actual traps, residual anharmonicity keeps the electrons confined but is not important at the onset of instability which involves only small oscillations. The importance of the tuned circuit is discussed here in some detail. In the absence of the tuned circuit, the rapid exponential growth ($\sim e^{Kt}$) at the onset of the instability is characterized by an exponent given by[59]

$$K = \frac{1}{2}\sqrt{\left(\frac{1}{2}h\omega_z\right)^2 - 4\left(\Omega - \omega_z\right)^2} \tag{3.19}$$

provided that the pump frequency 2Ω is sufficiently near to $2\tilde{\omega}_z$

$$-\frac{1}{2}h\tilde{\omega}_z < 2\Omega - 2\tilde{\omega}_z < \frac{1}{2}h\tilde{\omega}_z \tag{3.20}$$

(region between two dotted lines which intersect at $h = 0$ in Fig. 3.3). However, when the tuned circuit is used for detection, the resonance frequency

$$\omega_z^2 = \frac{qV_o}{md^2}(1 + C_2) \tag{3.21}$$

given in terms of the trapping potential, is shifted slightly ($\omega_z \longrightarrow \tilde{\omega}_z$) because the axial CM motion of the electron oscillators is coupled to a tuned (LCr) circuit. As mentioned earlier, this coupling also damps the CM energy at the rate $N\gamma_z$. If the coupling is not too strong, γ_z and $\tilde{\omega}_z$ are well approximated by simple analytic functions of the detuning between the tuned circuit and electron resonance frequencies, as given in Eq. (2.46) and Eq. (2.47), respectively. Frequency shifts are undesirable in high precision experiments (as discussed in Sec. 4.4). Fortunately, they present a minor inconvenience to our studies because the shifted frequency

and damping rate are determined from a forced resonance of the CM motion as already illustrated in Fig. 2.12. The frequency and strength of the parametric drive are then set using these measured values. In fact, control of the damping rate, according to

$$\gamma_z = \frac{\gamma_{zo}}{1+\delta^2}, \tag{3.22}$$

by changing the detuning δ has been very useful in demonstrating Mathieu instability. Damping stabilizes the quiescent state somewhat as amplification of fluctuations competes with energy dissipation in the tuned circuit, reducing growth in amplitude to $e^{(K-N\gamma_z/2)t}$ (slower initial growth is shown in solid line in Fig. 3.2). The region of parametric resonance ($K - N\gamma_z/2 > 0$) is therefore narrower with a hyperbolic boundary given by Eq. (3.3). As already mentioned, variation of damping rate γ_z using the tuned circuit shows that observed threshold corresponds to the vertex of a hyperbolic boundary.

3.3.4 Hysteresis

When system parameters are changing gradually, hysteresis can occur in nonlinear systems which have multiple stable states with instability under some conditions. The stability of steady states in various ranges of pump strength and frequency (labeled in Fig. 3.3 as O, I, II and III) is summarized in Table 3.1 (for negative σ_k). A sharp transition from one steady state to another occurs when the system parameters are swept slowly into a region wherein the former state becomes unstable. After the transition, if the system is restored to its original conditions by sweeping the parameters through the same path in reverse, the system may remain in the new state or make a transition to the former state under very different conditions. For parametrically-pumped electron oscillators, hysteresis is observed when sweeping the pump frequency with pump strength fixed above threshold (Fig. 3.5) or when sweeping the pump strength with pump frequency fixed below $2\omega_z$ (Fig. 3.6).

Hysteresis can also occur when the pump frequency and strength are fixed

but the oscillator resonance frequency is changing. We illustrate with a possible application for detecting the excitation of a relativistic, mono-electron cyclotron oscillator [31]. The axial resonance frequency

$$\omega_z^2 = \frac{eV_o}{md^2}(1 + C_2) \tag{3.23}$$

is shifted down by an observable amount [31] when the cyclotron oscillator is excited with a microwave drive. This is due to relativistic effects which effectively increase the mass of the electron according to

$$m = \frac{m_o}{\sqrt{1 - (v/c)^2}} \tag{3.24}$$

where m_o is the "rest mass," and v is the velocity of the cyclotron oscillator. Some experiments require knowing if the energy in the cyclotron motion has exceeded a given level within/after a certain period. To detect the corresponding frequency shift $\delta\omega_z$, a parametrically-driven electron is prepared initially in the quiescent state in region I (see Fig. 3.4 and Table 3.1) with the pump frequency fixed at $2\omega_- - 2\delta\omega_z$. As the microwave drive increases the energy in the cyclotron oscillation, region II (wherein $Z = 0$ is unstable) in Fig. 3.4 shifts down toward the drive frequency. When the driven cyclotron oscillator reaches the desired energy level, the quiescent state becomes unstable and the ensuing parametric resonance generates a signal. The signal would persist even if the cyclotron oscillation is subsequently allowed to decay (shifting region II up again). Amplifiers can be turned off to minimize thermal fluctuations during crucial stages of the experiments, and no resonant response to the parametric drive is incurred until the desired level of cyclotron excitation is reached. Briefly, one parametrically-pumped electron oscillator effectively has 1 bit of memory which can be used for detection "in the dark."

3.4 Full Equations of Motion

The rigid model is an accurate description of one electron oscillating along the symmetry axis of the trap. We have demonstrated here that it also provides a

good approximation for many observed features of the coherent CM motions when parametrically-pumped electron oscillators are radiatively cooled by a cold cavity. This rigid model is an oversimplification, however, because it neglects internal and transverse motions entirely, which have important, observable consequences (discussed in following chapters). Without transverse motions, radiative cooling of the internal motions would not be possible. Further, even at 4K (undriven) the thermal motions are more energetic than the average inter-particle Coulomb potential and thus the electrons do not form rigid structures [61]. To understand other interesting observed phenomena which are decidedly non-rigid, a more detailed treatment is required.

Although a thorough analysis of coupled, parametrically-pumped electron oscillators is not yet available, this system is so well-characterized that the full equations of motions of N electrons coupled to 1 cavity mode can be written down. The wide range of experimental control over system parameters allows some simplifications to be made. The k^{th} electron has 3 degrees of freedom $\mathbf{r}_k = (x_k, y_k, z_k)$, which are made dimensionless by scaling to the size of the trap, d. The coupled oscillations parallel to the symmetry axis of the trap (or to the magnetic field) satisfy

$$\begin{aligned} \ddot{z}_k + \quad \gamma_z \textstyle\sum_{i=1}^{N} \quad \dot{z}_i \; + \; \omega_z^2 \, z_k \; + \; \tilde{C}_4 \, \omega_z^2 \, (2z_k^2 - 3\rho_k^2) \, z_k \\ + \quad \tilde{C}_6 \, \omega_z^2 \, (3z_k^4 - 15 z_k^2 \rho_k^4 + \frac{45}{8} \rho_k^4) \, z_k \\ = \; \omega_{ce}^2 \sum_{i \neq k}^{N} \frac{(z_k - z_i)}{|\mathbf{r}_{ik}|^3} \, . \end{aligned} \tag{3.25}$$

Terms with coefficients $\tilde{C}_4$ and $\tilde{C}_6$ are due to deviations from an electric quadrupole potential. To be precise,

$$\tilde{C}_k = \frac{C_k}{1 + C_2} \approx C_k \tag{3.26}$$

since $C_2 \approx 0.13$ for the cylindrical trap used in our study. The series on the right hand side describes the inter-particle Coulomb repulsion. We assume that the axial frequency ω_z is tuned into resonance with the detection (LCr) circuit. Thus,

the damping term, proportional to the center-of-mass velocity, is due to energy dissipation in the resistor representing the detection circuit.

For the (transverse) motions in the xy-plane, we have

$$\begin{aligned}\ddot{x}_k \;-\; \omega_c\,\dot{y}_k \;&-\; \frac{1}{2}\,\omega_z^2\,x_k \;-\; 3\,\tilde{C}_4\,\omega_z^2\,(z_k^2-\rho_k^2/4)\,x_k \\ &-\; \frac{15}{2}\,\tilde{C}_6\,\omega_z^2\,(z_k^4-\frac{3}{2}z_k^2\rho_k^2+\frac{1}{8}\rho_k^4)\,x_k \\ &+\; \sqrt{\frac{r_e}{z_o}}\,\omega_M\,\Lambda_M(\mathbf{r}_k)\,\dot{f}_x \;=\; \omega_{ee}^2\sum_{i\neq k}^{N}\frac{(x_k-x_i)}{|\mathbf{r}_{ik}|^3}\,, \qquad (3.27)\end{aligned}$$

where $\mathbf{r}_{ik}=\mathbf{r}_i-\mathbf{r}_k$ and $\rho_k^2=x_k^2+y_k^2$; and

$$\begin{aligned}\ddot{y}_k \;+\; \omega_c\,\dot{x}_k \;&-\; \frac{1}{2}\,\omega_z^2\,y_k \;-\; 3\,\tilde{C}_4\,\omega_z^2\,(z_k^2-\rho_k^2/4)\,y_k \\ &-\; \frac{15}{2}\,\tilde{C}_6\,\omega_z^2\,(z_k^4-\frac{3}{2}z_k^2\rho_k^2+\frac{1}{8}\rho_k^4)\,y_k \\ &+\; \sqrt{\frac{r_e}{z_o}}\,\omega_M\,\Lambda_M(\mathbf{r}_k)\,\dot{f}_y \;=\; \omega_{ee}^2\sum_{i\neq k}^{N}\frac{(y_k-y_i)}{|\mathbf{r}_{ik}|^3}\,. \qquad (3.28)\end{aligned}$$

Coupling terms due to anharmonicity and Coulomb interaction are similar to those for the axial motions. Analogous to interaction with a tuned circuit, the cyclotron oscillations are coupled to a standing wave mode of the cavity. For simplicity, we have assumed the electrons are interacting with an $m=1$ cavity mode near the trap symmetry axis. Then the dimensionless field components (f_x, f_y) are governed by [8,9] :

$$\begin{aligned}\begin{pmatrix}\ddot{f}_x\\ \ddot{f}_y\end{pmatrix} \;+\; \Gamma_M\begin{pmatrix}\dot{f}_x\\ \dot{f}_y\end{pmatrix} \;+\; \omega_M^2\begin{pmatrix}f_x\\ f_y\end{pmatrix} \\ -\;\sqrt{\frac{r_e}{z_o}}\,\omega_M\sum_{k=1}^{N}\Lambda_M(\mathbf{r}_k)\begin{pmatrix}\dot{x}_k\\ \dot{y}_k\end{pmatrix} \;=\; 0, \qquad (3.29)\end{aligned}$$

where $\sqrt{r_e/z_o}\;=\;8.56\times10^{-7}$. The couplings Λ_M are related to those calculated and tabulated for regular geometries of interest [37]. The typical values of frequencies in these equations are provided in Table 3.2.

The standing wave configurations in a cylindrical cavity are described by known analytic functions, allowing us to characterize the electron-cavity coupling

Axial damping width	$\gamma_z/(2\pi)$	(max.) 5 Hz
Collision constant	$\omega_{ee}/(2\pi)$	12×10^3 Hz
Axial frequency	$\omega_z/(2\pi)$	63×10^6 Hz
Cyclotron frequency (swept)	$\omega_c/(2\pi)$	$\sim 100 \times 10^9$ Hz

Table 3.2: Typical values of frequency parameters in the equations of motion.

by the simple functions $\Lambda_M(\mathbf{r}_k)$. For the modes of greatest interest, near the trap symmetry axis, the electron-cavity coupling is given by

$$\Lambda_{1np}(\mathbf{r}_k) \;=\; \Lambda_{1np}\,\sin\left(\frac{p\pi d}{2z_o}z_k + \frac{p\pi}{2}\right). \tag{3.30}$$

The first of two important cases is for an antinode at the midplane, eg. TE_{115}, with

$$\Lambda_{115}(\mathbf{r}_k) \;=\; \Lambda_{115}\,\cos\left(\frac{5\pi d}{2z_o}z_k\right) \quad . \tag{3.31}$$

For a small axial oscillation amplitude, the electron-cavity coupling is a simple constant in this case. The other important case produces cavity mode resonances of a different type (Chapter 4), namely, the case for a node at the midplane, eg. TE_{132}, with

$$\Lambda_{132}(\mathbf{r}_k) \;=\; -\Lambda_{132}\,\sin\left(\frac{\pi d}{z_o}z_k\right) \quad . \tag{3.32}$$

For our apparatus, $d/z_o \;=\; 0.923$. Since these examples are of experimental interest, we provide the values of their parameters in Table 3.3.

The system is parametrically excited by modulating the axial spring constant $m\omega_z^2$, so that the above equations are modified by the substitution

$$\omega_z^2 \longrightarrow \omega_z^2\left[1 + h\cos(\omega_d t)\right]. \tag{3.33}$$

The observed signal is obtained from the voltage induced across the effective detection resistor R

$$V = -\frac{1}{2}\kappa N q\left(\frac{d}{z_o}\right)\dot{Z} \tag{3.34}$$

	TE_{115}	TE_{132}
Λ_M	0.31	0.56
$\Gamma_M/(2\pi)$	144×10^6 Hz	3.8×10^6 Hz
$\omega_M/(2\pi)$	99.513×10^9 Hz	97.525×10^9 Hz

Table 3.3: Parameters for two modes of experimental interest.

which is proportional to the CM oscillation

$$\dot{Z} = \frac{1}{N}\sum_{i=1}^{N} \dot{z}_i. \tag{3.35}$$

A phase-sensitive detector monitors the phase of the coherent response with respect to the pump (Sec. 5.1). For CM energy measurements, this signal is amplified, squared and filtered, giving an output proportional to $\langle \dot{Z}^2 \rangle$.

3.5 Summary

Resonantly cooled by a cavity mode, parametrically-pumped electron oscillators switch abruptly from disordered motions to long-term, coherent CM oscillations as the pump strength exceeds a sharp threshold. Observed collective behavior exhibits Mathieu instability and shares many features characteristic of the nonlinear dynamics in a rigid model. A hyperbolic region of instability in the (h,ω_d) space of the pump is established. Phase degeneracy and hysteresis due to multiplicity of stable states are also observed. Observed maximum CM energy is limited by cavity cooling of internal motions. Nevertheless, dependences of observed parametric resonance lineshapes on anharmonicity are in qualitative agreement with the rigid model.

So far, radiative cooling has been maximized to reveal the collective behaviors of parametrically-pumped electron oscillators. Notwithstanding good agreement with many observed features of the collective motions, the rigid model suffers

from serious over-simplifications. The electron oscillators do not form a rigid structure even at 4K (undriven) because they are "weakly correlated" [67], with the energy in thermal motions being comparable to or exceeding the inter-particle Coulomb energy. Omission of the internal and transverse motions greatly reduces the usefulness of the model in understanding other interesting, non-rigid behaviors. Fortunately, a system of collisionally-coupled, parametrically-pumped electron oscillators is so well-characterized that the full equations of motions can be written down, although not as easily analyzed. We refer to the observed coherent motions in this system as "synchronized motions," to distinguish them from the rigid motions expected of crystal structures. An interesting non-rigid feature, for example, is the extreme sensitivity of the CM energy in synchronized motion to radiative cooling by cavity modes, which opens the way to new experiments involving electron-cavity interaction, as we shall see.

Chapter 4

Interaction with Cavity Standing Waves

As mentioned in Chapter 1, the electromagnetic fields form simple standing wave patterns within a cylindrical cavity, which are ideal for radiative studies. Splitting the metallic walls of a cylindrical cavity to form the electrodes of a Penning trap allows electrons to be confined in a region smaller than the characteristic wavelength of a cavity standing wave. Radiative cooling of localized electrons in a resonant cavity mode, in fact, is crucial for demonstrating many of the collective behaviors in parametrically-pumped electron oscillators, presented in Chapter 3. The extreme sensitivity of synchronized motions to radiative cooling provides a new technique for probing the standing wave modes of a Penning trap cavity, *in situ* at 4 K without any microwave drive. We now discuss the interesting effects which are observed, and important applications which are possible, when electrons interact with well-characterized radiation fields.

4.1 Observing Microwave Cavity Modes Below 166 GHz

Despite great attention to making a cylindrical Penning trap cavity which is a good approximation to an ideal cylindrical cavity, the small slits, holes and uncontrolled imperfections unavoidably shift the radiation eigenfrequencies of the

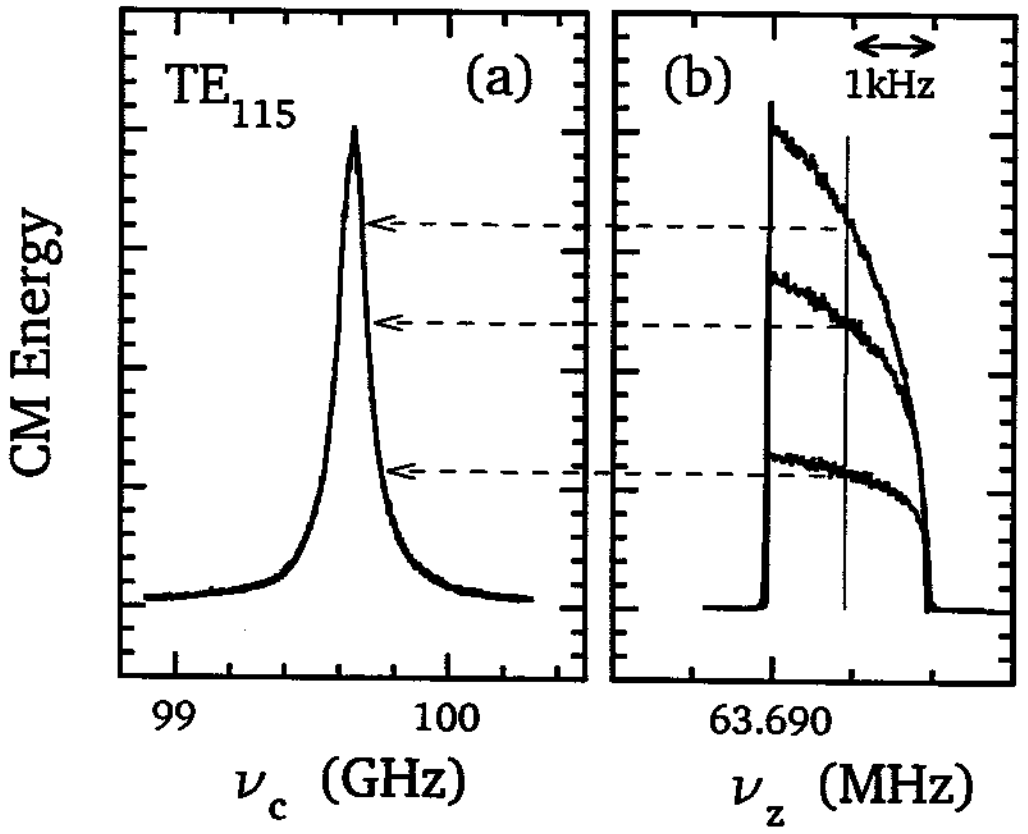

Figure 4.1: (a) Cavity resonance observed by monitoring the axial CM energy while slowly sweeping the magnetic field to vary ω_c', with pump frequency at $\omega_d = 2\omega_z$ and pump strength $h = 1.3h_T$. (b) Parametric axial resonances for indicated cyclotron frequencies.

trap cavity from those of an ideal cylindrical cavity. The hope is that the shifts are small, so that measured eigenfrequencies can still be used to identify the modes. Furthermore, small shifts would indicate that the standing wave fields in the trap cavity are essentially the simple analytic forms discussed above.

A simplified diagram of the system with detection electronics is depicted in Fig. 2.17. To insure that parametric resonance is sustained during mode detection, the parametric pump is prepared in the region of (Mathieu's) instability in (h, ω_d) space, in which the quiescent state is unstable. This region is cross-hatched in

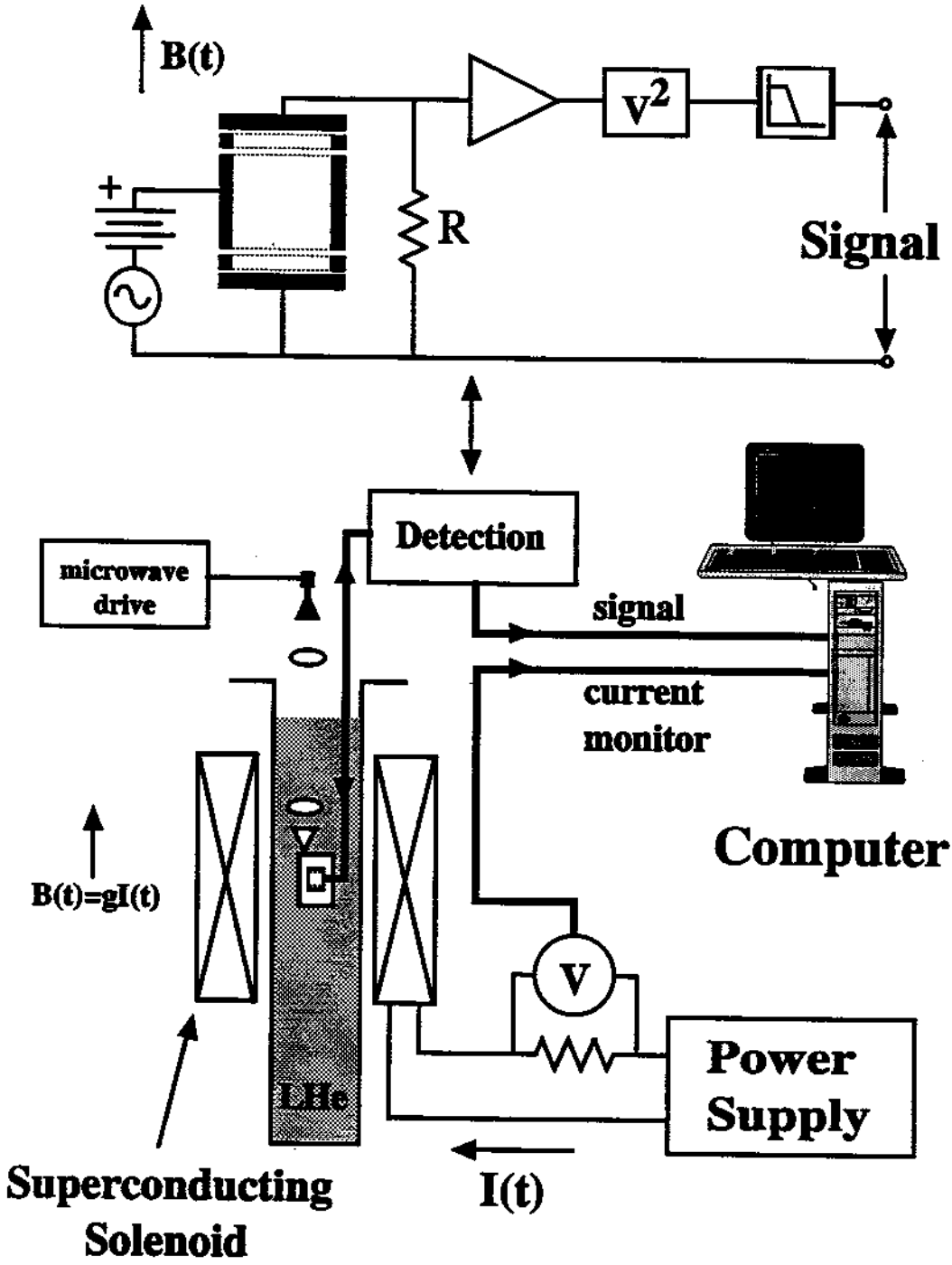

Figure 4.2: Simplified diagram of the experimental apparatus for cavity mode detection.

Fig. 3.3. Fig. 4.1b shows the measured frequency response with the pump strength held fixed at a value above the threshold. This family of superimposed resonances is obtained by varying the detuning between the cavity mode frequency and the electron cyclotron frequency. It clearly shows that the signal grows with increasing radiative cooling and reaches a maximum when the cyclotron frequency is swept into resonance with the cavity mode. Cavity modes are thus conveniently detected by fixing the pump frequency at $\omega_d = 2\omega_z$ and monitoring the axial CM energy, while the cyclotron frequency is being swept, as illustrated in Fig. 4.1a. A simplified overview of the full apparatus is shown in Fig. 4.2. The trap is sealed in a high-vacuum envelope, which is cryopumped via thermal contact with a liquid helium bath. The magnetic field is generated by a superconducting solenoid designed for precise studies with nuclear magnetic resonance. Since the cyclotron frequency is proportional to the magnetic field, we sweep the current in the superconducting solenoid up to 5.9 Tesla (slowly, because the solenoid inductance is 200 Henries) in order to tune the cyclotron oscillators into resonance with one cavity mode after another. A measure of the current in the solenoid and the signal from the electron oscillators are digitized simultaneously and stored in a computer. (A conversion from measured solenoid current to cyclotron frequency is obtained by exciting an electron cyclotron resonance with a microwave source.) A 50 GHz wide spectrum is shown in Fig. 4.3 (without any microwave drive). The full spectrum of observed cavity modes between 0 to 166 GHz is presented in Fig. 4.14 and takes about 10 hrs to obtain. The extraordinary sensitivity of the synchronized motion of the electron oscillators to radiative cooling via energy transfer to the modes of the trap cavity allows us to observe even weakly coupled cavity modes (e.g., those with nodes in the midplane), presumably because the electrons occupy a volume extending slightly away from the center of the trap. Isolated resonances have Lorentzian lineshapes, as illustrated by the data points and Lorentzian fits for the two modes in Fig. 4.4. Thermal cycling of the trap apparatus up to 300 K and back to 4.2 K changes the observed resonance frequencies by less than 0.1%.

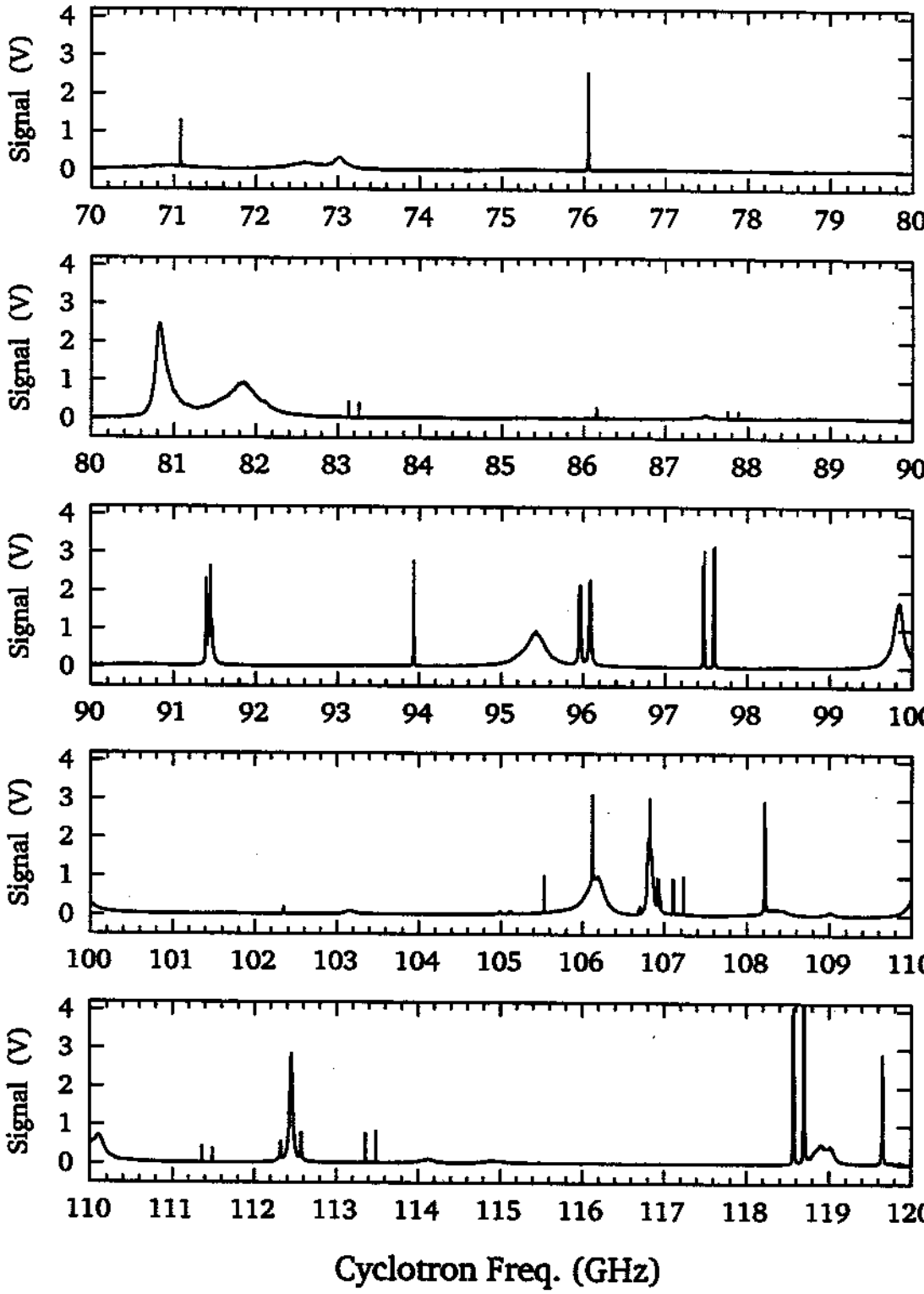

Figure 4.3: Observed cavity modes between 70 and 120 GHz.

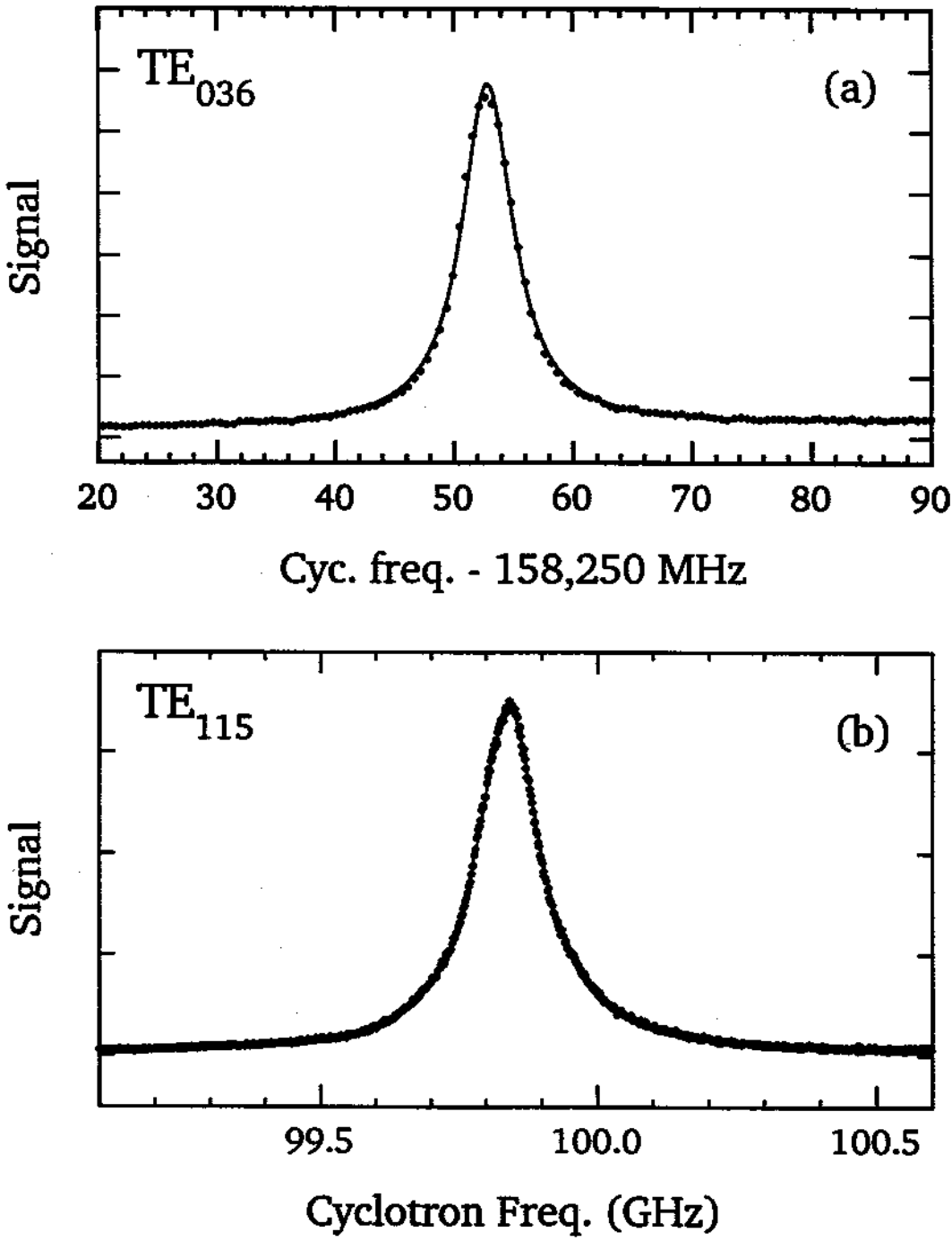

Figure 4.4: Lorentzian lineshapes (solid lines) fit to observed cavity modes (dots) which are well separated from other modes.

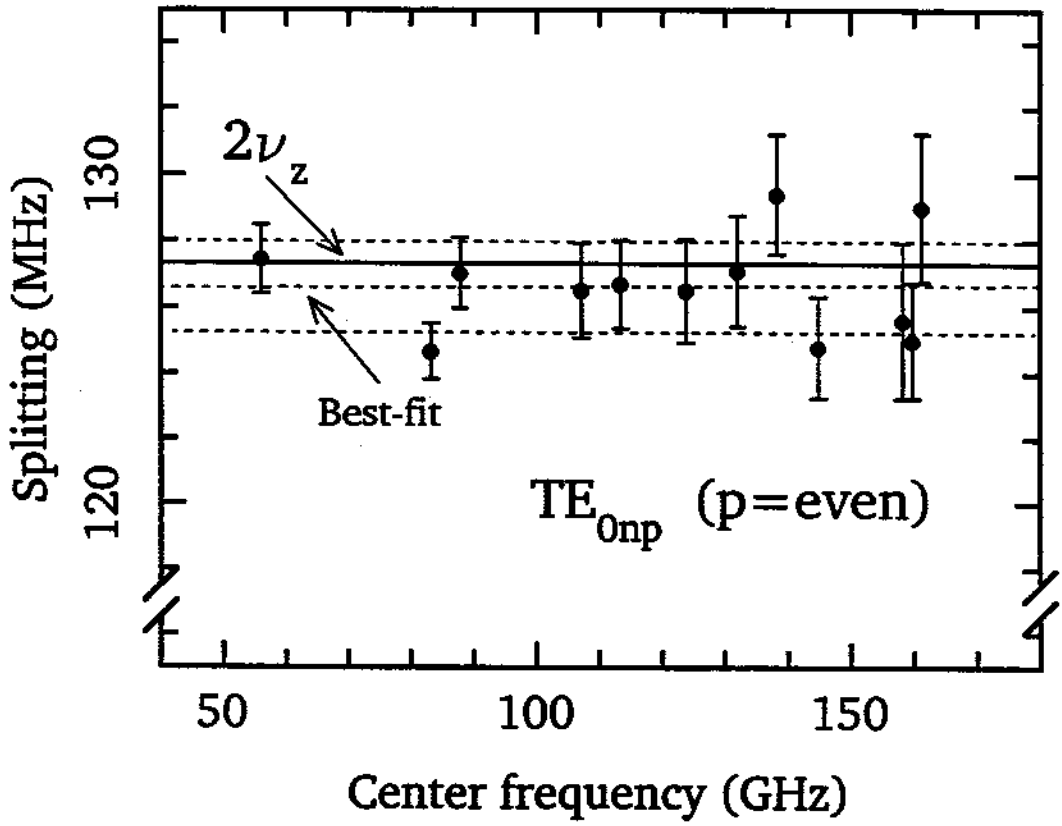

Figure 4.5: Motional splitting of singlet modes TE_{0np}. The best fit (center dashed line) is consistent with $2\nu_z$ (solid line) within its uncertainty (dashed lines above and below).

4.1.1 Motional Effects

The TE_{0np} modes are unusual in that these azimuthally symmetric modes are singlets, unlike $m > 0$ modes which are doubly degenerate. In the observed spectrum, however, TE_{0np} resonances with even p appear near the frequencies expected for an ideal cylinder in Eq. (2.1), but they appear as doublets. Modes with p even have a node in the midplane of the trap and are thus decoupled from the cyclotron motion of electrons located exactly at the center of the trap. The periodic axial motion of the electrons, driven by the parametric pump, makes the electrons sample the standing wave field away from the node at the center of the trap. The

microwave field experienced by the oscillating electrons is thus amplitude modulated, which produces the observed sidebands. Plotting the frequency separations for the doublets (Fig. 4.5) shows clearly that the splittings are twice the axial oscillation frequency as would be expected. All even p modes, regardless of m value, give similar motional splitting in the spectrum, as illustrated in Fig. 4.6a. The motional effect is different (and typically smaller) for odd p modes since these have a maximum of the standing wave field at the center of the trap. Nevertheless, for sufficiently large oscillations and for large p, small sidebands are observed at $2\nu_z$ to either side of the strong central peak as illustrated in Fig. 4.6b.

4.1.2 Comparison with Ideal Cavity

With motional sidebands understood, the measured frequencies correspond well to those for a perfect cylindrical cavity, offering the possibility of identifying resonant modes of a trap cavity for the first time. The azimuthally-symmetric TE modes with $m = 0$ have high Q values and are not shifted much by the slits because induced surface currents flow parallel to the slits, allowing the effective trap dimensions to be determined *in situ* at 4 K to within 6 μm, as shown in Fig. 4.7. A best fit of Eq. (2.1) to 12 measured eigenfrequencies for such modes yields a rms frequency deviation of 0.08% and dimensions $\rho_0 = 0.4559(6)$ cm and $z_0 = 0.3838(6)$ cm, in good agreement with our expectations based upon machining tolerances and expected thermal contraction. Taking the observed width at half maximum divided by the resonant frequency to be Q^{-1}, the mean Q is 20,000 with an rms spread of 6500.

For other field symmetries of experimental interest, Fig. 4.8 shows percentage deviations of measured and calculated resonant frequencies. There is good agreement. The most important modes [9,10,37], those with p odd and $m = 1$, have nonvanishing transverse electric fields at the cavity center and hence couple directly to the small cyclotron orbit of an electron. The strong coupling results in the largest observed resonance signals (i.e. largest peak area in Fig. 4.3) for the 29

of these modes which we observe. Frequency deviations are typically 1%, which is larger than for the TE_{0np} modes above as expected. Nonetheless, the shifts are still typically 5 times smaller than the average mode spacing, though mode overlap gets more likely as the mode density increases at higher frequencies. The mean Q is 1300, with a spread of 1100 and a highest Q of 3700.

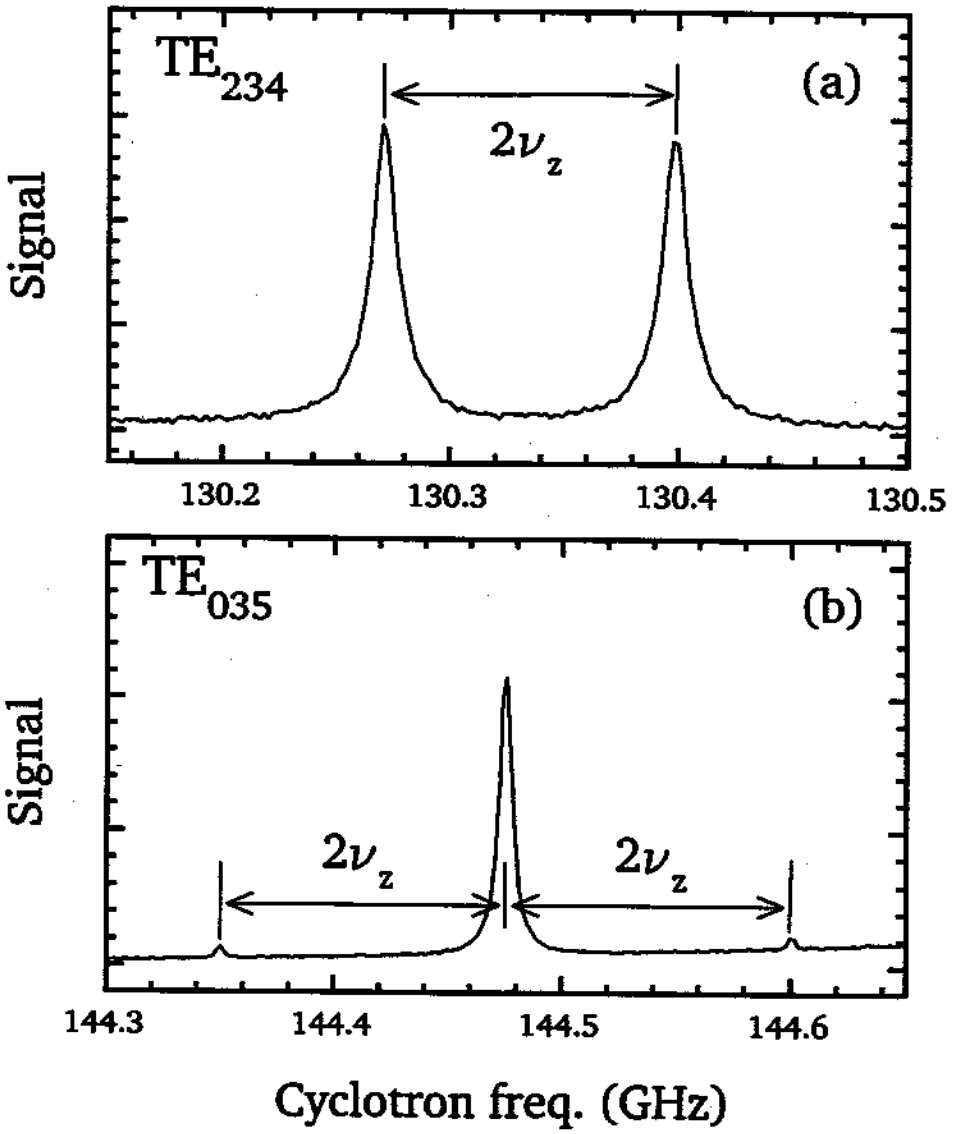

Figure 4.6: (a) Motional doublet for a mode with p even has separation of $2\nu_z$. (b) Motional sidebands for a mode with odd p are separated from the strong central peak by $2\nu_z$.

4.1.3 Strong Coupling

Isolated modes fit well to Lorentzian lineshapes, as has been illustrated. Fig. 4.9 illustrates the lineshape modification which occurs when an electron cloud and a cavity mode are strongly coupled. A Lorentzian lineshape (Fig. 4.9a) is observed with small number of electrons. For weak coupling, the decay rate of one electron cyclotron oscillator coupled to the Mth cavity mode is, as we shall see later, given

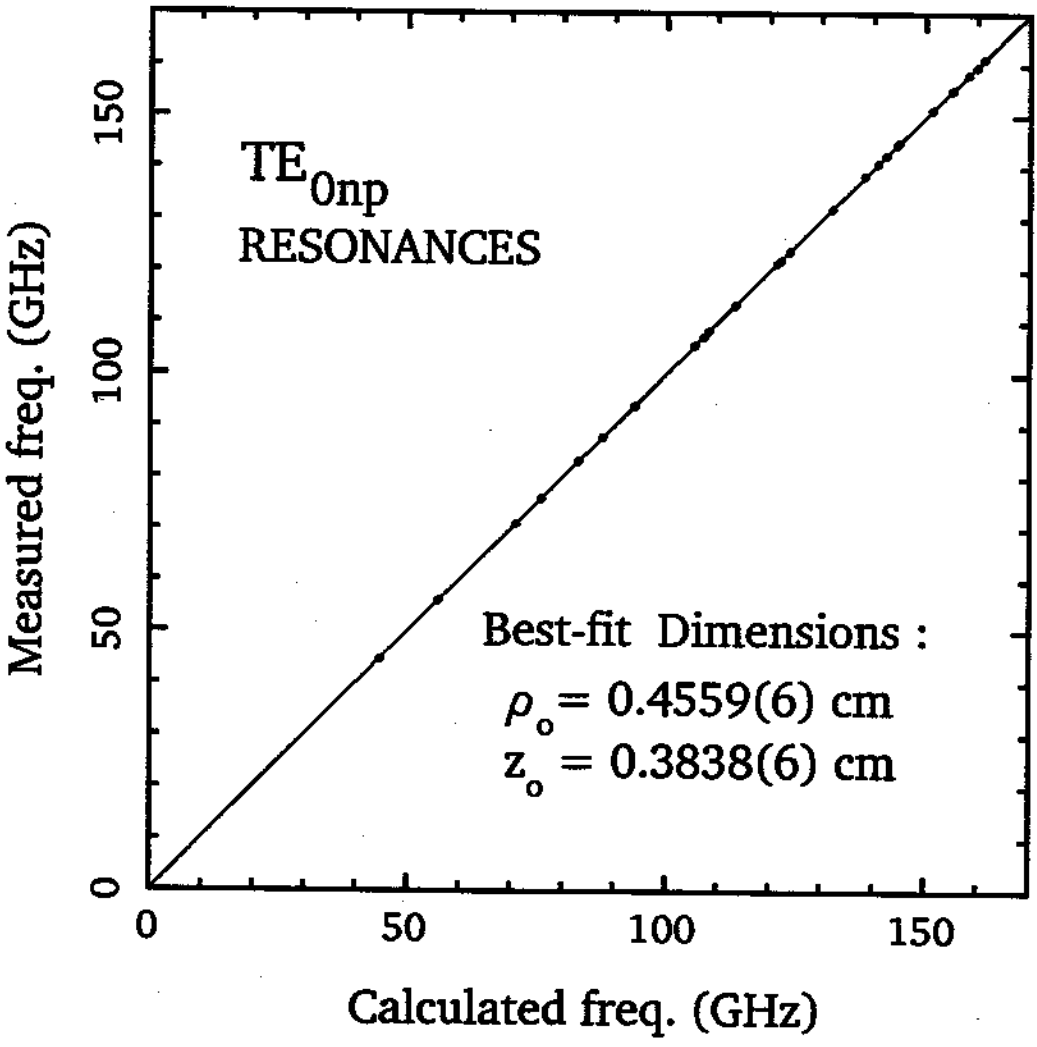

Figure 4.7: Fit of measured TE_{0np} mode eigenfrequencies to those calculated for an ideal cylinder , in situ at 4K, determines effective dimensions of the trap cavity to within 6 μm.

Mode	Eigenfrequency (GHz)	$\gamma_M/Q_M\gamma_c$
TE_{111}	27.435	0.8295
TM_{111}	44.608	0.0542
TE_{121}	59.124	0.1709
TE_{113}	61.667	0.0732
TM_{113}	70.993	0.0480
TM_{121}	75.986	0.0068
TE_{123}	80.905	0.0668
TE_{131}	91.461	0.0724
TM_{123}	93.936	0.0213
TE_{115}	99.513	0.0174
TM_{115}	105.547	0.0184
TE_{133}	106.842	0.0455
TM_{131}	108.265	0.0017
TE_{125}	112.454	0.0249
TM_{133}	121.538	0.0085
TM_{125}	122.165	0.0159
TE_{141}	124.077	0.0395
TE_{135}	132.346	0.0239
TE_{143}	135.813	0.0302
TE_{117}	138.033	0.0065
TM_{141}	140.824	0.0006
TM_{117}	142.444	0.0080
TM_{135}	144.470	0.0099
TE_{127}	147.635	0.0110
TM_{143}	151.267	0.0037
TM_{127}	155.159	0.0094
TE_{145}	156.670	0.0197
TE_{151}	156.803	0.0248
TE_{137}	163.296	0.0128
TE_{153}	166.245	0.0208

Table 4.1: Calculated properties of $m = 1$, p odd modes below 170 GHz for an ideal cavity which has the best-fit dimensions of the trap cavity ($\rho_o/z_o = 1.186$).

by

$$\gamma = \frac{\gamma_M}{1+\delta^2}, \tag{4.1}$$

where γ_M is the maximum damping rate which occurs when the detuning δ (between the cyclotron and cavity mode resonance frequencies) is zero. The electron-

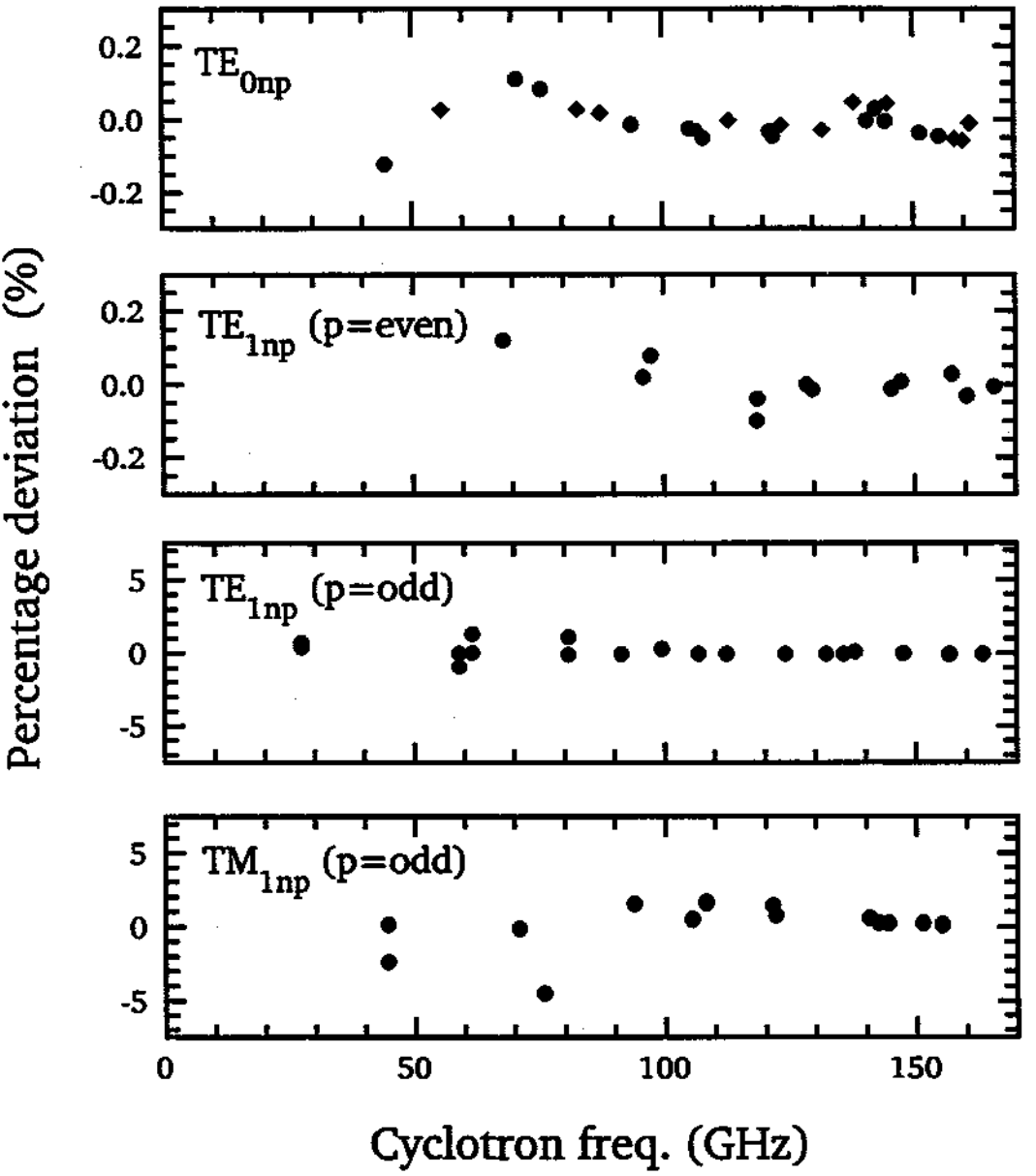

Figure 4.8: Comparison of observed and calculated eigenfrequencies for series of cavity modes of particular experimental interest.

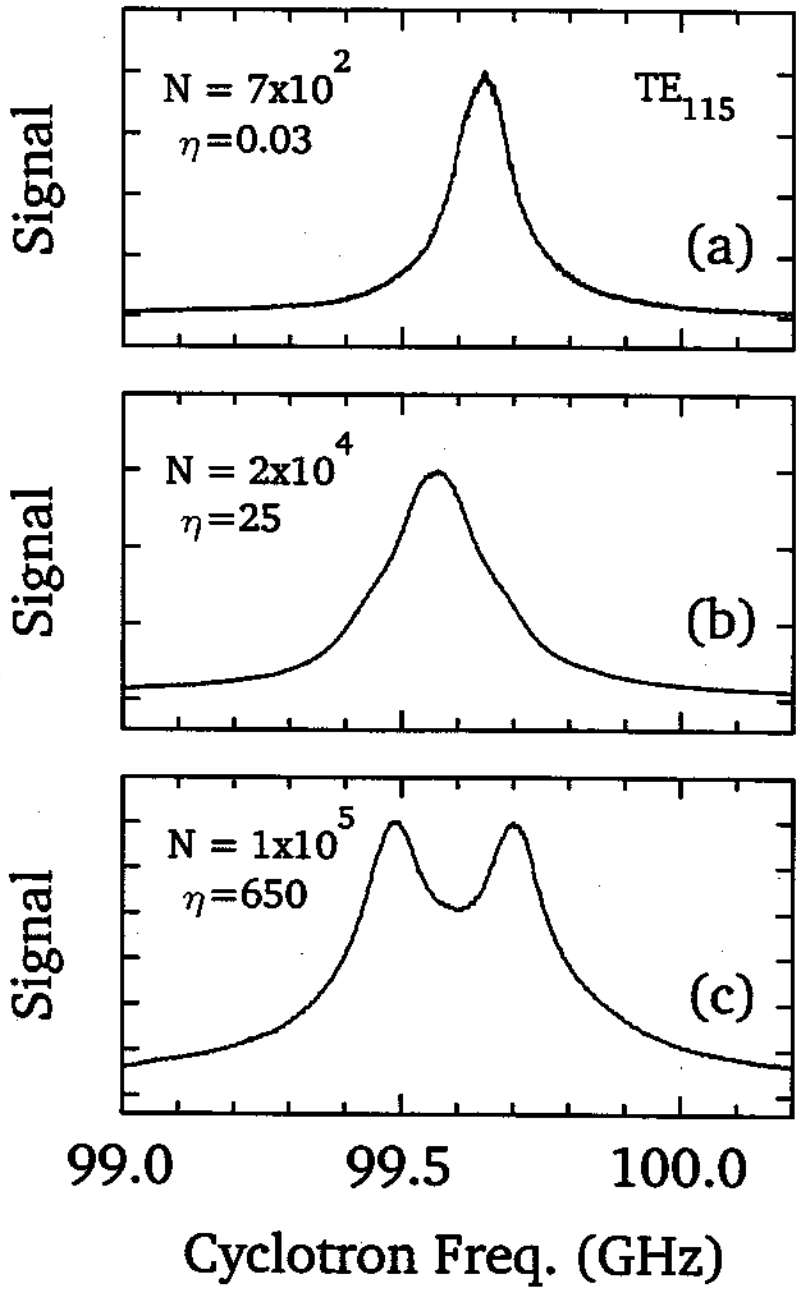

Figure 4.9: The Lorentzian lineshape (a) is modified to the strongly coupled lineshapes in (b) and (c) as the number of electrons N is increased to increase the electron-cavity coupling.

cavity interaction is weak if the energy coupled into a cavity standing wave is dissipated in the cavity walls in a time shorter than is required for the cyclotron oscillator to re-absorb the energy. A useful parameter for comparing the coupling time between the CM cyclotron motion of N electrons and a cavity mode, on the one hand, to the decay rate of the standing wave itself due to losses in the cavity walls, on the other hand, is defined by

$$\eta = \frac{N^2 \gamma_M}{\Gamma_M}, \tag{4.2}$$

where the numerator gives the rate of energy transfer from the CM cyclotron motion to the Mth cavity mode, and is proportional to N^2 because this rate depends on the square of the charge of the oscillator. The denominator Γ_M gives the decay rate of energy in the cavity mode due to losses in the cavity walls. The weak coupling approximation which provides Eq. (4.1) is good for $\eta \ll 1$. Since the decay rate of one electron in free space is given by Eq. (1.3) and the quality factor Q_M of the cavity mode is given by $\Gamma_M = \omega_M / Q_M$, we can rewrite η defined in Eq. (4.2) as

$$\eta = \frac{4}{3}\left[\frac{\gamma_M}{Q_M \gamma_c}\right] N^2 Q_M^2 \left(\frac{r_e \omega_M}{c}\right), \tag{4.3}$$

in terms of known quantities (from calculations and measurements), with r_e being the classical electron radius. The factor in square brackets is calculable, depending only on the geometry of the cavity, and is tabulated in Table 4.1.

We can make this coupling parameter η rather large by either increasing N or selecting a cavity mode with very high quality factor Q_M. The weak coupling approximation breaks down when N or Q_M is so large that the coupling time between an electron cloud and a cavity mode becomes shorter than the decay time for the energy in the cavity mode itself. Under this condition, the CM cyclotron oscillator and the cavity mode can form normal modes. For TE_{115}, we observe that $\nu_M = 99.84 GHz$ and $Q_M = 690$ in the weak coupling limit, and therefore

$$\eta = 6.51 \times 10^{-8}\ N^2. \tag{4.4}$$

With 700 electrons, $\eta = 0.03$ and a Lorentzian lineshape is observed, consistent

with Eq. (4.1). Broadening of the lineshape is observed (Fig. 4.9b, especially at its base) when $N = 2 \times 10^4$, which corresponds to $\eta = 25$. Evidence of normal-mode splitting is obtained (Fig. 4.9c) when the number of electrons is increased to $N = 10^5$, corresponding to $\eta = 650$. Normal-mode splitting has been observed recently in other systems with atoms coupled to a cavity mode as an atomic beam passes through a high-finesse optical cavity [71,97].

4.2 New Generation of g-2 measurements

As discussed in Sec. 1.2, the observation of inhibited spontaneous emission [32] and subsequent calculation of related shifts of the cyclotron frequency (See review in Ref. [37]) provided a serious obstacle to measurement of the magnetic moment of the electron and positron. Cavity shifts presently limit the precision of the measured magnetic moments of the electron and positron [88,89]. Inhibited spontaneous emission in the cyclotron motion has been observed in these experiments, with cyclotron decay time longer than in free space. The corresponding frequency shift which must be present (illustrated in Fig. 1.1b), however, has not been determined because the microwave properties of the hyperbolic trap are virtually unknown experimentally and are difficult to deal with even in principle. Consequently, latest measurements of the magnetic moment for the electron and positron

$$a(e^-) = 0.001\ 159\ 652\ 188\ 4\ (14)\ (40) \tag{4.5}$$

$$a(e^+) = 0.001\ 159\ 652\ 187\ 9\ (14)\ (44) \tag{4.6}$$

are reported with the largest uncertainty (40) due to cavity shifts [88,89]. This uncertainty, called the "most probable" cavity shift in the cyclotron frequency [88], was crudely estimated using our calculations for a cylindrical cavity model which is not a very satisfying approximation to a hyperbolic trap cavity.

QED calculations of the electron's anomalous magnetic moment have been pushed to nearly the same precision [53]. As mentioned earlier, however, QED relates measured a values to measured values of the fine structure constant α. For comparison to the measured a values, the QED calculation and the measured fine structure constant together give an anomalous magnetic moment

$$a = 0.001\ 159\ 652\ 140\ 0\ (53)\ (41)\ (271). \tag{4.7}$$

The largest uncertainty (271) comes from uncertainty in the fine structure constant as measured using the quantum Hall effect. The uncertainties of (53) and (41) come from numerical calculations of the expansion coefficients C_3 and C_4 (not related to λ_i), respectively.

More precise tests of QED require improved precision for the measured fine structure constant first (this is expected), then improved measurements of a and an improved QED calculation. It was pointed out to us by B.N. Taylor that

$$\alpha^2 = \frac{2R_\infty}{c}\frac{m(Na)}{m_p}\frac{m_p}{m_e}\frac{h}{m(Na)}. \tag{4.8}$$

The Rydberg constant R_∞ is now known to within an uncertainty of $\sim 2 \times 10^{-10}$. Thus, an improved value of α can be obtained from precision measurements of the proton-electron mass ratio m_p/m_e and the sodium-proton mass ratio $m(Na)/m_p$ in Penning traps, in combination with a proposed determination of $h/m(Na)$ (Planck's constant over mass of a sodium atom) using atomic interferometry[51]. The latest adjustment of fundamental constants is based in part on a somewhat more precise determination of α obtained by combining the QED calculation (assuming the exact validity of QED) with the measurement of a to obtain

$$\alpha^{-1}(QED) = 137.\ 035\ 992\ 22\ (94). \tag{4.9}$$

The uncertainty in this QED determination of the fine structure constant is 7×10^{-9} if the shift estimate turns out to be accurate.

4.2.1 Magnetic Moments Without Cavity Shifts

Controlling the interaction of an electron cyclotron oscillator with the cavity-modified vacuum will be crucial for higher precision tests of QED. Better a measurements in trap cavities of unknown microwave properties appear difficult and unlikely. For example, using lossy materials as electrodes would make a hyperbolic trap cavity approximate the free-space vacuum (and thus avoid shifts due to unknown standing-wave fields). However, the cyclotron damping linewidth would also be as large as in free space, making precise frequency measurements more difficult. To relate the uncertainty $\Delta\omega_c$ in measuring the cyclotron frequency to the resulting uncertainty Δa in the measured anomalous magnetic moment a, we note that

$$a = \frac{\omega_s - \omega_c}{\omega_c} \tag{4.10}$$

can be regarded as a definition of a, where ω_s is the electron's spin precession frequency. Since $a \approx 10^{-3}$ is small,

$$\frac{\Delta a}{a} \approx \frac{1}{a}\frac{\Delta\omega_c}{\omega_c}. \tag{4.11}$$

For $B = 5.9$ Tesla, without line splitting, the cyclotron frequency could therefore (in principle) be measured to 8×10^{-12}, from substitution of Eqs. (1.2) and (1.3) into Eq.(4.10). Setting $\Delta\omega_c$ equal to the free space line width yields $\Delta a/a \approx 8 \times 10^{-9}$. The experimental error currently quoted [88,89] is already much smaller than this free space linewidth.

The cylindrical cavity, with identified p odd, $m = 1$ modes, is a greatly improved environment for experiments with a centered, one-electron cyclotron oscillator. To illustrate, a 10 GHz span of experimental interest is displayed in Fig. 4.10. Of the modes in this span, only TM_{123} and TE_{115} couple to the cyclotron motion of one electron at the center of the trap. TE_{124}, and TE_{132} do not couple to one centered electron but are suited for sideband cooling of the axial motion. Both the damping rate γ for an electron's cyclotron motion (for small enough damping

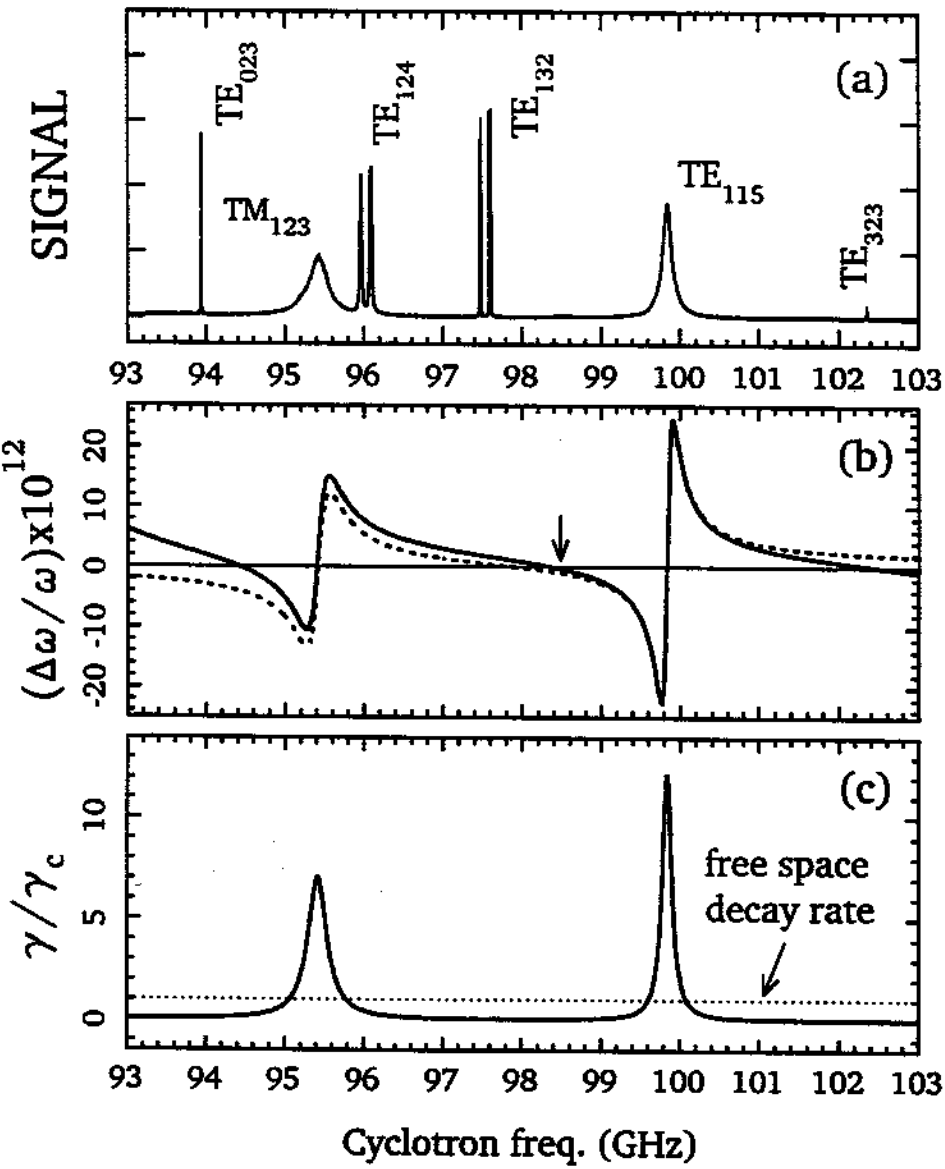

Figure 4.10: Observed cavity modes in a 10 GHz spectrum (a). Calculated frequency shifts (b) and damping rates (c) for one electron at the cavity center. The dashed line in (b) accounts for the two nearest modes that couple, TM_{123} and TE_{115}. The solid line also includes the effect of nearby coupled modes not in this span.

[32]), and the cavity shift of its frequency $\Delta\nu$, could be measured as a function of ν_c' with one trapped electron, but this would take a very long time. However, to a good approximation, coupling to the Mth of these cavity modes (with resonant frequency ν_M) yields the explicit forms [37]

$$\gamma = A_M \frac{Q_M}{1+(Q_M\delta_M)^2} \tag{4.12}$$

$$2\pi\Delta\nu = \frac{1}{2}A_M\frac{(Q_M)^2\delta_M}{1+(Q_M\delta_M)^2} = \frac{1}{2}\gamma Q_M\delta_M. \tag{4.13}$$

The constants A_M are precisely known (equivalent to those tabulated [37] as elaborated in Sec. 4.4) because the field configurations of these modes are known. Both γ and $\Delta\nu$ are functions of the "detuning" $\delta_M = 2(\nu_c' - \nu_M)/\nu_M$ (which is accurately controlled and measured) and the quality factor for the mode Q_M. These explicit forms, with ν_M and Q_M from the measurements described earlier (summing over nearby modes as necessary and including manageable renormalization corrections neglected here [37]) can be used to compute the frequency shift (Fig. 4.10b) and damping rate (Fig. 4.10c) for a centered electron. The hope is to compare with several specific measurements with one electron and then to deduce the cyclotron frequency (i.e. the magnetic field) at which the electron's cyclotron frequency is not shifted by the cavity (arrow in Fig. 4.10b). The damping width is 50 times narrower than in free space at this unshifted cyclotron frequency. The likelihood for thereby improving the measurement accuracy is very high.

4.2.2 Rapid Control of Electron-Cavity Coupling

The simple standing wave pattern of $m = 1$ modes can be used to change the cyclotron damping rate rapidly without changing the magnetic field (which would take months to restabilize sufficiently for high precision experiments). This is possible because the coupling between the cyclotron oscillator and a cavity mode vanishes at a node of the standing wave. An electron can be moved up and down by by adding an anti-symmetric electric potential V_A across the endcaps

(Fig. 4.11a). Fig. 4.11b represents the magnitude of a component of the transverse electric field of a TE_{1n3} mode along the z-axis. If an electron is displaced from the center of the trap (where its coupling with the cavity mode is strongest) along the z-axis by a quarter wavelength to the nearest node, then its interaction with the standing-wave is switched off.

Electronic control of the electron-cavity coupling is demonstrated in Fig. 4.12. The peak in Fig. 4.12a is due to coupling of TE_{027} to an electron cloud near the trap center. TE_{027} has 7 anti-nodes between the endcaps, with $\lambda/4 = 550\ \mu$m. For Fig. 4.12b, the electron cloud is displaced by 510 μm from the trap center along its axis. Proximity to the node causes the resonant peak in Fig. 4.12a to disappear. Instead, a pair of peaks separated by $2\omega_z$ appear in the spectrum because the

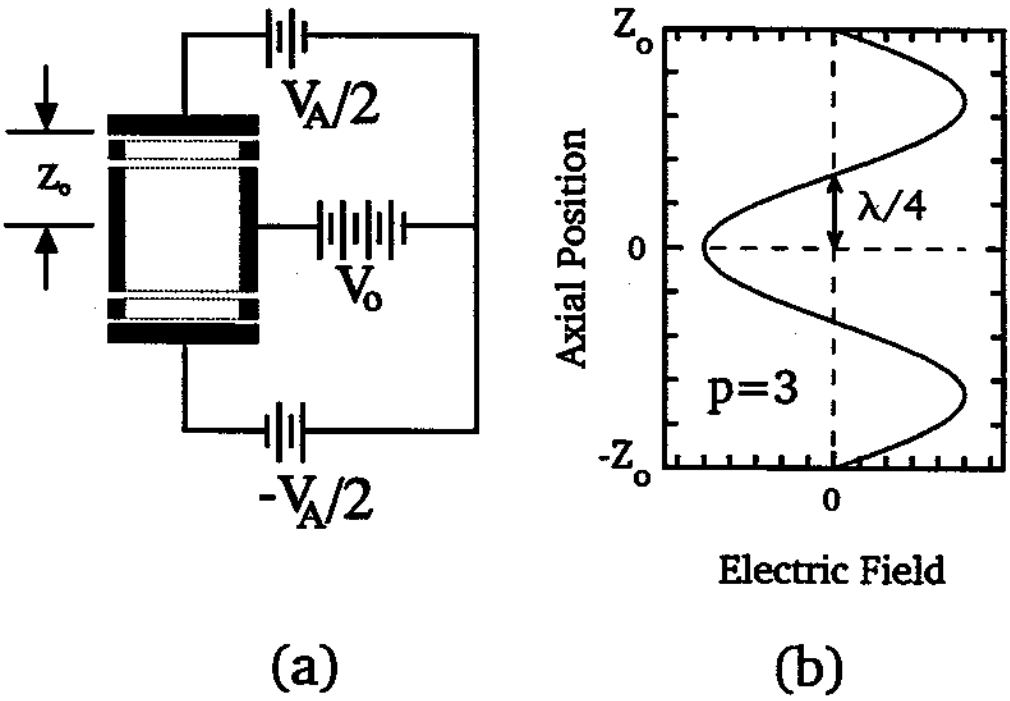

Figure 4.11: (a) Antisymmetric potential across endcaps displaces electrons along the z-axis. (b) Representation of transverse electric field component near the z-axis for a p=3 mode.

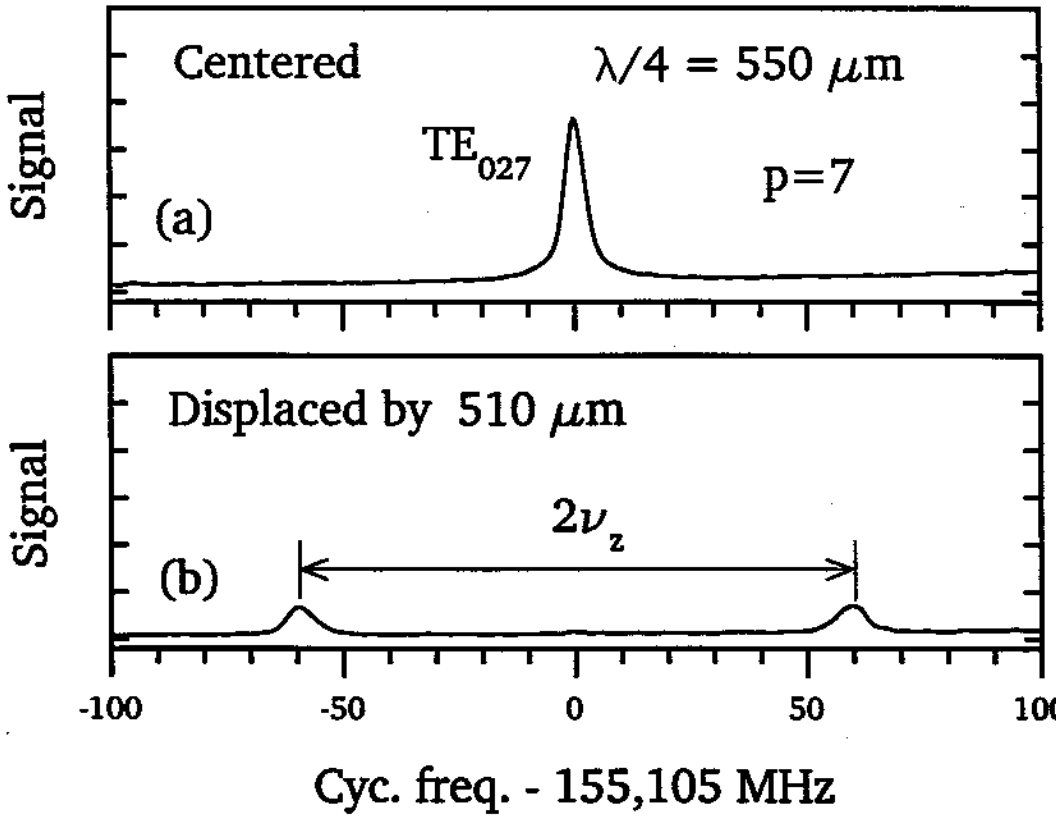

Figure 4.12: (a) Observed resonance for TE_{027} ($\lambda/4 = 550\mu$m) with a centered electron cloud. (b) Motional doublet observed when the electrons are displaced from the center by $\Delta z = 510\mu$m.

electrons are oscillating at frequency ω_z through the node plane at $z \approx \lambda/4$.

4.2.3 Sideband Cooling of Axial Motion

The axial motion of a trapped electron is dissipated as Joule heating in a resistor connected between appropriate electrodes, cooling the axial motion into thermal equilibrium with the resistor. Even at 4 K, thermal axial motions are highly undesirable in efforts to study the relativistic, quantum structure of the cyclotron

oscillator because the thermal energy is coupled into the cyclotron motion via several mechanisms.

To bring the axial motion to a much lower temperature, the electron would be decoupled from the resistor and a sideband cooling technique [94,10] would be employed. Modes with even p and $m = 1$ (eg. in Fig. 4.10), when driven at $\nu_c' - \nu_z$, produce the proper oscillatory spatial gradients required to transfer the axial energy into the cyclotron motion. The cyclotron excitation, in turn, dissipates the transferred thermal energy into the cavity via modes with odd p and $m = 1$. It should be possible to cool the undamped axial motion to an extremely low temperature limit [10]

$$T_z = (\nu_z/\nu_c')T_c. \tag{4.14}$$

With the frequencies used here, this would be an unprecedented (and extremely useful) axial temperature of 2 mK for $T_c = 4.2K$. Because the field intensity builds up within the high Q cavity, much less drive power should be required than was estimated for propagating plane-waves [10]. These same modes have a transverse magnetic field at the cavity center and could thus be used to directly flip an electron spin (when driven at ω_s). Off-resonance cyclotron excitations by the strong spin flip drive are suppressed because these modes do not couple directly to the cyclotron motion.

4.3 Calibrating the Monitored Currents

The cyclotron frequency is swept by ramping the current in a superconducting solenoid which provides the magnetic field, as already described. The current I supplied to the superconducting magnet by a regulated power supply is monitored, digitized and stored in a computer at a rate of ~ 3 data points per second. The frequency of the cyclotron oscillator at any time is, using Eq. (2.10),

$$\nu_c = \frac{e}{m}B_z(t) = \frac{e}{m}g\left(I - \frac{V}{L}\tau_o\right), \tag{4.15}$$

where e/m is the charge-to-mass ratio of an electron. The constant τ_o takes into account the current drawn by the protection resistor shunting the superconducting solenoid. By sweeping the current from 0 to 40 Amperes, the cyclotron oscillation frequency is varied between 0 and 167 GHz. This maximum frequency corresponds to the maximum field for the superconducting solenoid. The conversion from monitored current to the cyclotron frequency is measured accurately by using a high precision microwave source to drive the cyclotron oscillator. For the superconducting solenoid used to obtain Fig. 4.3, the driven resonant frequency ν_c at a known current I gives

$$\frac{\nu_c}{I} = 4.1854(2)\text{GHz/A} \quad . \tag{4.16}$$

The uncertainty is due to the statistical error in current measurement. This is in good agreement with the theoretical value calculated from the windings of the solenoid, within the tolerance of the solenoid and the calibration error of the metering resistor.

To measure the offset constant τ_o, we choose a high Q cavity mode. The axial CM energy of a synchronized electron cloud is maximum when the cyclotron oscillation is in resonance with the cavity mode, shown in Fig. 4.13(a). The current corresponding to the cavity mode resonance, I_N, is measured for various sweep rates. The sweep rate V/L is measured from the time-stamped, digitized record of current readings (see, e.g., Fig. 2.6). The linear variation of the resonant current, I_N, with the sweep rate V/L is shown in Fig. 4.13(b). The slope directly gives

$$\tau_o = 101(1)\text{s} \quad , \tag{4.17}$$

which characterizes the shunt resistor across the superconducting solenoid mentioned earlier.

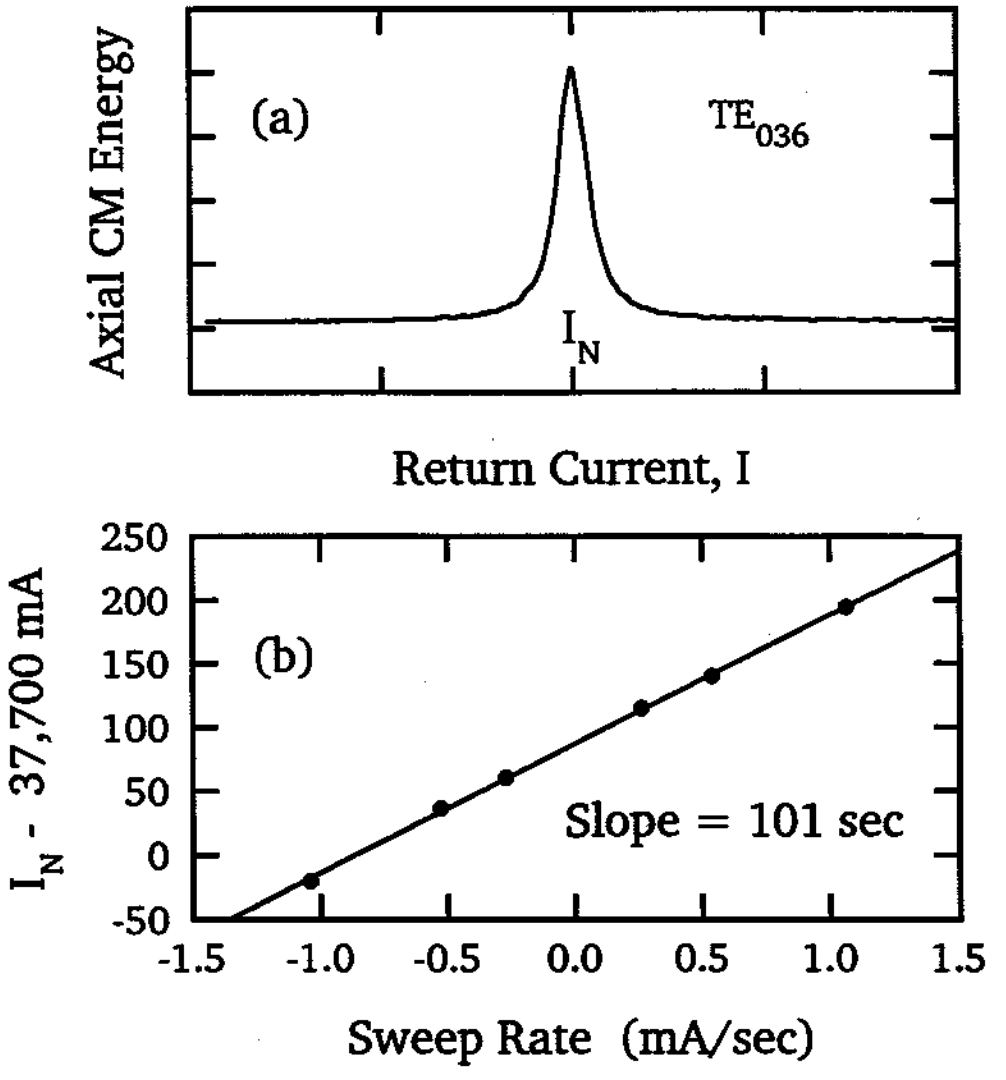

Figure 4.13: (a) Cavity mode resonance for field calibration. (b) Measurement of offset constant τ_o

4.4 Electron-Cavity Interactions

The dynamics of one cyclotron oscillator localized in the midplane (near the center) of a cylindrical, microwave cavity is governed by [8,9]

$$m\dot{\mathbf{v}} - (e/c)\mathbf{B} \times \mathbf{v} = e\mathbf{E}^T \quad , \tag{4.18}$$

where $\mathbf{v} = \dot{\rho}$ is the velocity in the midplane. The transverse electric field $\mathbf{E}^T$, in the dipole approximation, is due to radiation standing-wave modes with $m = 1$ (i.e., TE_{1np} and TM_{1np}), generated as the accelerating electron radiates into the

cavity. Thus Eq. (4.18) indicates that the cavity standing waves act back upon the cyclotron oscillator. The calculations are classical since it has been shown that within a high level of accuracy, the exact apparatus of quantum electrodynamics yields the classical results [4].

The essential features of this interaction are also contained in a simpler electromechanical model (Fig. 2.13) appropriate when one cavity mode is considered [3]. In this model, the selected M^{th} cavity mode is represented by a series LCr tuned circuit. Such a tank circuit is resonant at angular frequency $\omega_M = (LC)^{-1/2}$ with damping width $\Gamma_M = r/L$. The electron oscillator is represented as a charge e and mass m on a spring with spring constant $m(\omega_c')^2$. The electron oscillation $z(t)$ excites a current $\dot{Q}(t)$ in the tuned circuit. The oscillating current in the tuned circuit, in turn, produces an RF electric field which acts back on the electron. The interaction potential for these two coupled oscillators is given by

$$V_{int} = -\left[\frac{\kappa q}{2z_o C}\right] z(t)\, Q(t), \tag{4.19}$$

where the dimensionless coupling $\kappa = 1$ for a capacitor with infinite parallel plates (separated by $2z_o$). Using familiar Lagrangian equations, we find that, analogous to Eq. (4.18),

$$m\left[\frac{d^2}{dt^2} + (\omega_c')^2\right] z(t) = -\left[\frac{\kappa q}{2z_o C}\right] Q(t). \tag{4.20}$$

The excitation of the tuned circuit is described by

$$L\left[\frac{d^2}{dt^2} + \Gamma_M \frac{d}{dt} + (\omega_M)^2\right] Q(t) = -\left[\frac{\kappa q}{2z_o C}\right] z(t). \tag{4.21}$$

We can neglect Johnson noise (which represents the 4 K radiation of the cavity in thermal contact with the liquid helium bath).

In the weak-coupling regime (wherein the cavity field decays due to wall losses in a time shorter than required for the electron to re-absorb the radiation), the tuned circuit effectively damps the electron oscillation $z(t)$ at rate γ and shifts its resonant frequency to $\tilde{\omega}_c'$. Since the cavity modes typically have high quality

factors ($Q \sim 10^3$ or higher), the damping and frequency shift take the simple forms

$$\gamma = \gamma_M \frac{1}{1+\delta^2} , \tag{4.22}$$

$$\tilde{\omega}_c' - \omega_c' = \frac{1}{2}\gamma_M \frac{\delta}{1+\delta^2} . \tag{4.23}$$

In terms of the effective resistance $R = L/(rC)$, the maximum damping rate γ_M is given by

$$\gamma_M = \left[\frac{\kappa q}{2z_o}\right]\frac{R}{m}. \tag{4.24}$$

The resonant frequencies of the tuned circuit and electron motion are ω_M and ω_c, respectively, when the interaction is turned off. The unperturbed resonance frequency of the two oscillators are related by a detuning δ defined by

$$\omega_c' = \omega_M + \frac{1}{2}\Gamma_M\delta. \tag{4.25}$$

If the electron oscillator and the LCr circuit are tuned to the same unperturbed resonance frequency (i.e. $\delta = 0$) there is no frequency shift, but the damping rate is maximum. When $\delta \neq 0$, the damping rate is reduced but the resonant frequency of the electron oscillator is shifted. The maximum frequency shifts $\pm\gamma_M/4$ occur near resonance, at detunings $\delta = \pm 1$. The characteristic shapes for γ and $\Delta\omega$ are shown in Fig. 1.1 and are clearly evident in more detailed calculations.

Since $\gamma_M \sim R \sim Q_M$, the maximum damping and maximum frequency shift are larger when the quality factor $Q_M = \omega_M/\Gamma_M$ is larger. To display the Q dependence explicitly we write

$$\frac{\gamma_M}{\omega_M} = 2Q_M\left(\frac{\lambda_M}{\omega_M}\right)^2 \tag{4.26}$$

thereby defining the coupling strength λ_M [98]. This definition also allows the use of a simple form for the electron's frequency shift and damping rate

$$\Delta\omega - i\frac{\gamma}{2} = \frac{\omega(\lambda_M)^2}{\omega^2 + i\omega\Gamma_M - \omega_M^2} , \tag{4.27}$$

which can be generalized to include interactions with more than one cavity mode by summing the right hand side over the mode index M.

For Eq. (4.27) and its generalization to be quantitatively useful, the coupling constants $\lambda_M^2 = \lambda_{n,l}^2$ have been calculated for regular cavities of interest [37]. In particular, for the cylindrical cavity, the mode index M is identified here with the two quantum numbers $n = 0, 1, 2, ...$ and $l = 1, 2, 3, ...$ When the magnetic field is along the symmetry axis of the cavity, these two indices identify the subset of cavity modes which couple to a cyclotron oscillator located at the center of the cavity. Two types of modes couple to the cyclotron motion and for both it is convenient to use $k_n = (n + 1/2)\pi/z_o$. For TE (transverse electric) modes

$$\lambda_{n,l}^2 = \frac{r_e c^2}{z_o \rho_o^2} \frac{2}{\alpha_l^2 - 1} \frac{\alpha_l^2}{J_1(\alpha_l)^2} \tag{4.28}$$

$$\omega_{n,l}^2 = \left(k_n^2 + \frac{\alpha_l^2}{\rho_o^2} \right) c^2 \tag{4.29}$$

where α_l (defined by $J_1'(\alpha_l) = 0$) is the l^{th} zero of the derivative of the first-order Bessel function. For TM (transverse magnetic) modes which couple to electron cyclotron motion

$$\lambda_{n,l}^2 = \frac{r_e c^2}{z_o \rho_o^2} \frac{2 k_n^2 c^2}{\omega_{n,l}^2} \frac{1}{J_0(\beta_l)} \tag{4.30}$$

$$\omega_{n,l}^2 = \left(k_n^2 + \frac{\beta_l^2}{\rho_o^2} \right) c^2 \tag{4.31}$$

where β_l (given by $J_1(\beta_l) = 0$) is the l^{th} zero of the first order Bessel function. The quantum numbers n and l which we use to label the cavity modes which couple to the electron are simply related to common conventions for labeling all the modes of a cylindrical cavity. For example, in the textbook by Jackson [49] the origin of the coordinate system is translated to the center of the bottom endcap , and the TE and TM modes identified above are labeled as $TE_{1,l,2n+1}$ and the $TM_{1,l,2n+1}$, respectively. Couplings for other cavity geometries of interest are found in an earlier work [37].

Unfortunately, the simple theory is afflicted with problems arising from self-field interaction. To see this, we note that the standing wave field is actually composed of two contributions

$$\mathbf{E}^T = \mathbf{E}_{self} + \mathbf{E}', \tag{4.32}$$

the self-field $\mathbf{E}_{self}$ radiated directly by the oscillator (as if into free space) and the reflected field $\mathbf{E}'$ which is reflected from the cavity walls. The back reaction of a self-field upon the accelerating charge which is radiating, is well known to lead to difficulties and divergences in classical electricity and magnetism [69] (inherited by QED in addition to divergences of its own). In our particular situation, the real part of the mode sum

$$\Delta\omega - i\frac{\gamma}{2} = \omega - \omega_c - i\frac{\gamma_c}{2} = \omega \sum_M \frac{\lambda_M^2}{\omega^2 + i\omega\Gamma_M - \omega_M^2}, \tag{4.33}$$

diverges when the sum includes all the cavity modes. For a correctly renormalized calculation, the self-field term is replaced by a radiation damping term for radiation into free space (with damping rate γ_c) and only the transverse reflected field $\mathbf{E}'$ acts back upon the cyclotron oscillator, so that Eq.4.18) is rewritten as

$$\dot{\mathbf{v}} - \omega_c \times \mathbf{v} + (\gamma_c/2)\mathbf{v} = (e/m)\mathbf{E}'. \tag{4.34}$$

Only in special cases is it possible to separate the reflected field and the self-field which together make up the standing wave. The high degree of symmetry for a spherical cavity [11,20] makes the removal of the self-field relatively simple because the free-space radiation from the oscillator at the center contains only outgoing spherical waves, easily distinguished from the reflected waves. A cylindrical cavity [8,9] has less symmetry, but the separation can still be accomplished by using image charges to satisfy the cavity boundary conditions. The reflected field is thus clearly distinguished as the field of the images. For a hyperbolic cavity (which corresponds to the trap within which the electron's magnetic moment was measured) a separation of self and reflected fields is completely intractable. Finite mode sums as done in the simple model are the only possibility. Comparisons of a modified mode sum and a complete calculation for the cylindrical cavity are used to estimate the optimal number of terms to be included in the finite mode sum, even though the mode density is significantly higher in a hyperbolic cavity.

The usefulness of the simple theory is limited especially when the electron cyclotron oscillator is not near to resonance with a high Q cavity mode. A detailed discussion of how the divergences arise and can be partially circumvented

in this model has been presented [12,37]. In general, the contribution from any off-resonant (M^{th}) mode to the frequency shift $\Delta\omega$ of the electron oscillator, going as $\frac{1}{2}(\lambda_M)^2/(\omega_c - \omega_M)$, independent of Q_M is overstated slightly due to self-field in the standing wave. The overstated contributions add up as the contributions from many modes are included. Optimal use of the simple, mode sum model thus requires a careful choice of the number of cavity modes included in the sum. Beyond a certain number of terms, the real part of the mode sum will start to diverge. Eventually, the mode sum over an infinite number of such small contributions diverges. It is difficult to establish the optimum number of terms or the accuracy of the truncated mode sum except by comparison to a calculation which avoids the divergences entirely [12]. A modified mode sum formula was obtained [12] which converges for the case of a cylindrical cavity and can be used to obtain the unshifted cyclotron frequency to 1 part in 10^9.

4.5 Full Spectrum Below 166 GHz

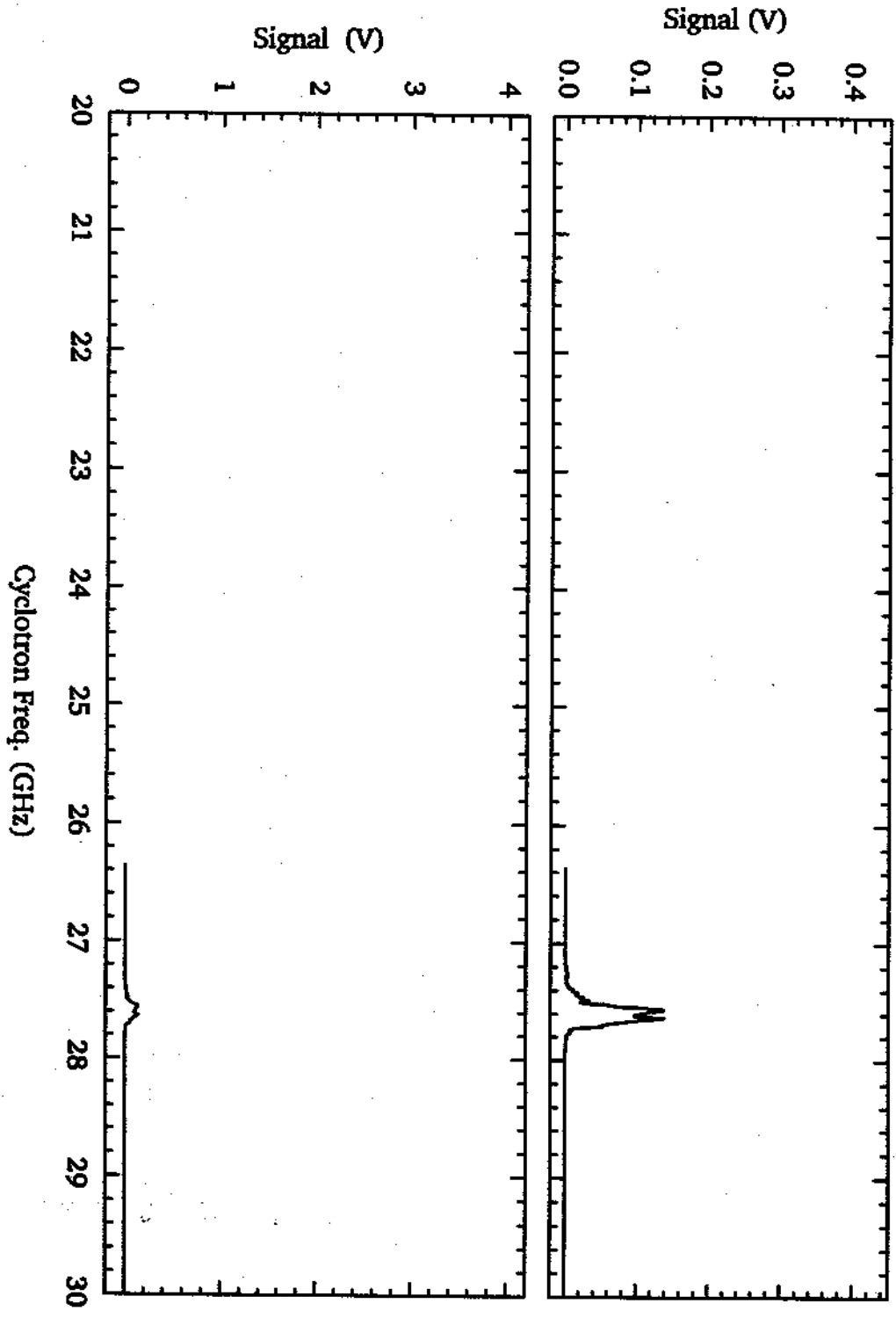

Figure 4.14: Observed cavity modes below 166 GHz.

4.5 Full Spectrum Below 166 GHz

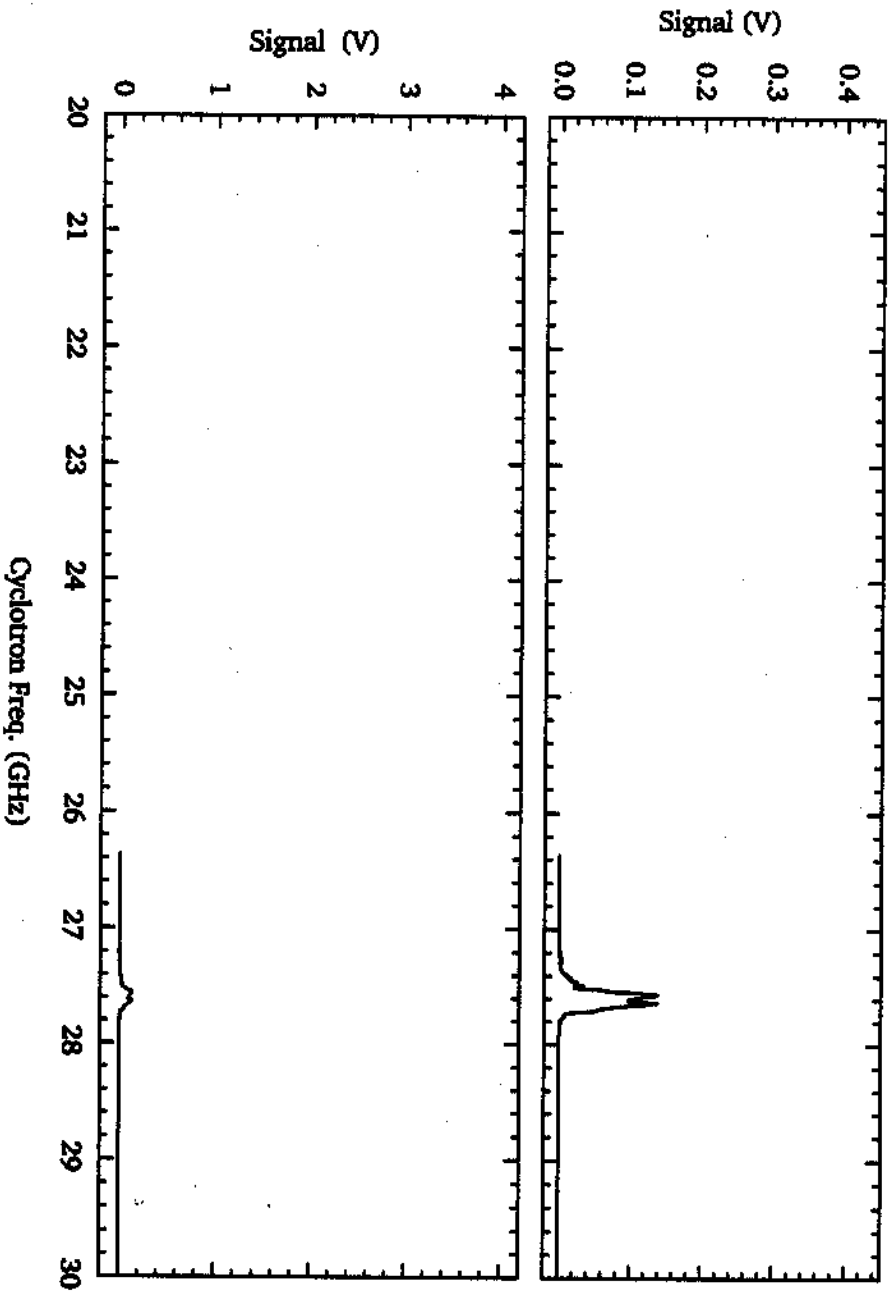

Figure 4.14: Observed cavity modes below 166 GHz.

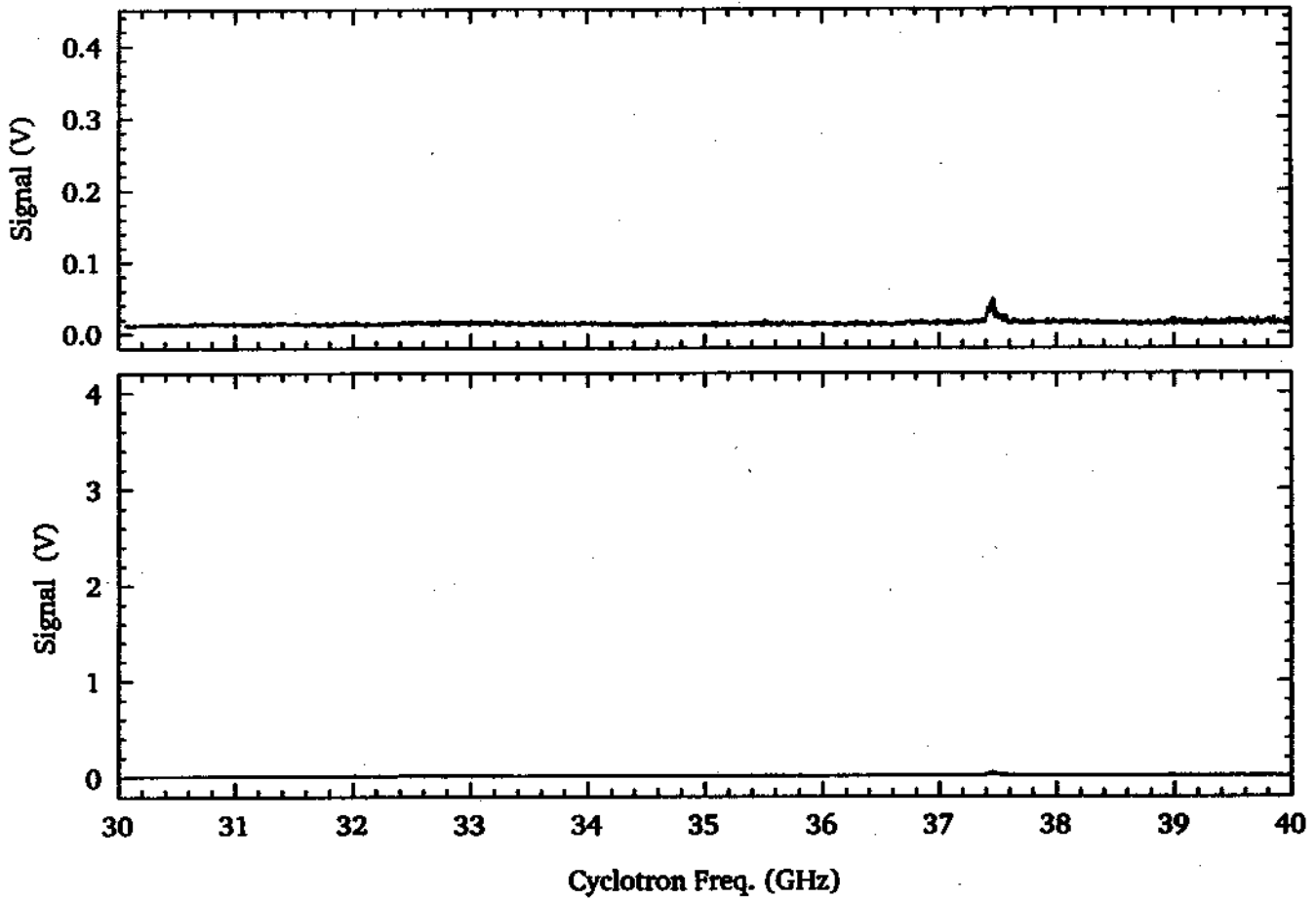
Signal (V)
0.4
0.3
0.2
0.1
0.0
Signal (V)
4
3
2
1
0
30
31
32
33
34
35
36
37
38
39
40
Cyclotron Freq. (GHz)

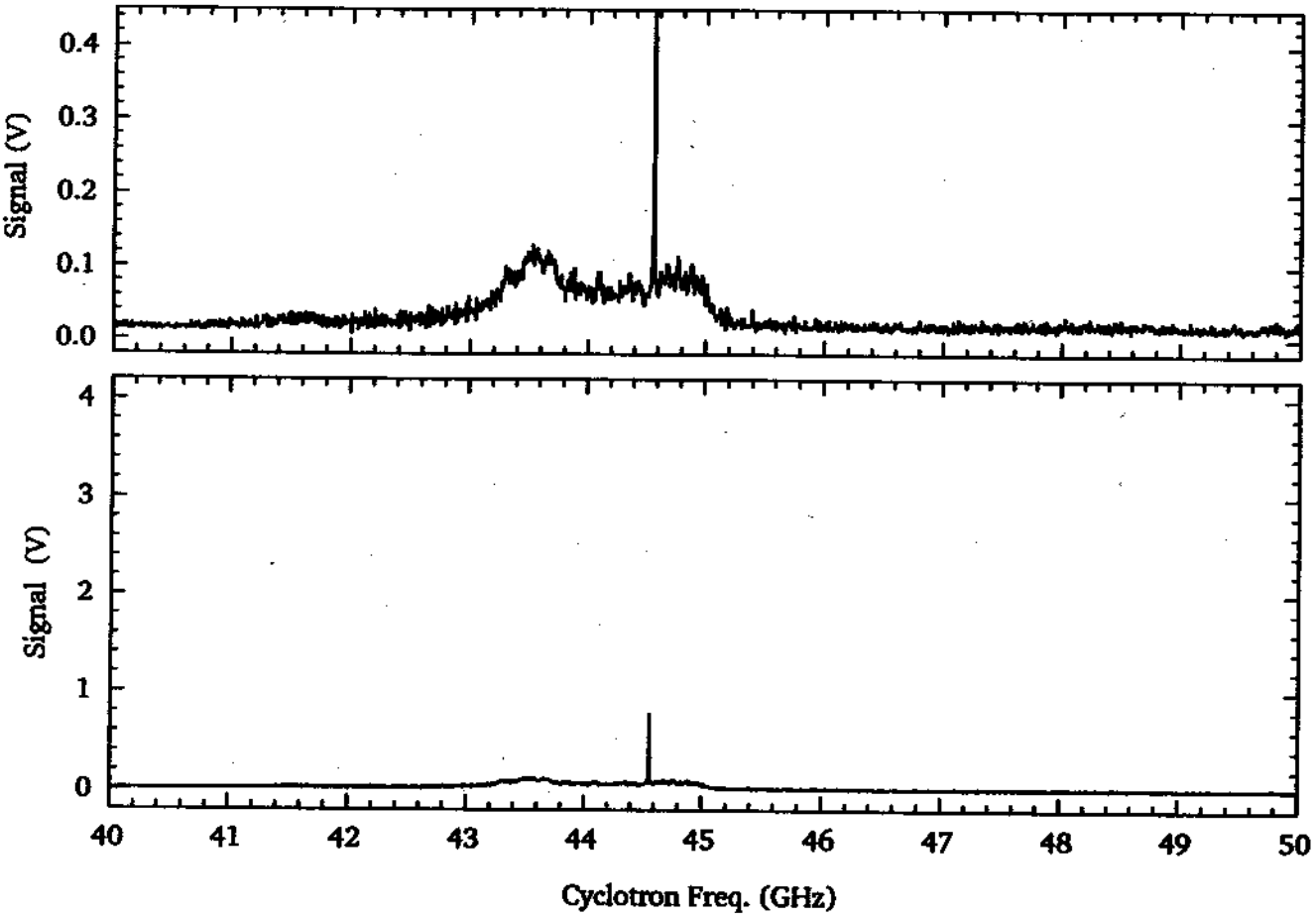
0.4
0.3
0.2
0.1
0.0
Signal (V)
4
3
2
1
0
Signal (V)
40
41
42
43
44
45
46
47
48
49
50
Cyclotron Freq. (GHz)

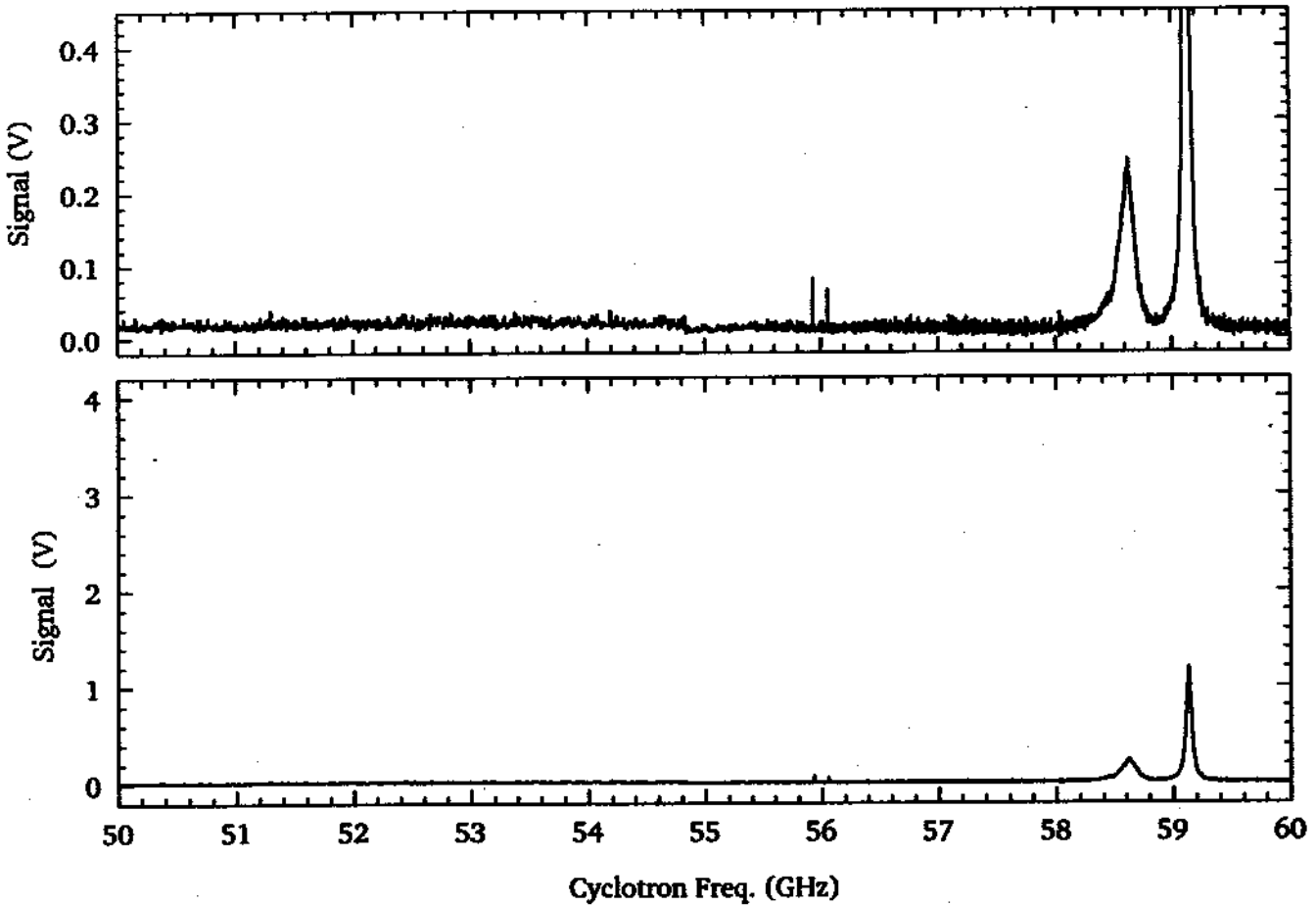
Signal (V)
0.4
0.3
0.2
0.1
0.0
Signal (V)
4
3
2
1
0
50
51
52
53
54
55
56
57
58
59
60
Cyclotron Freq. (GHz)

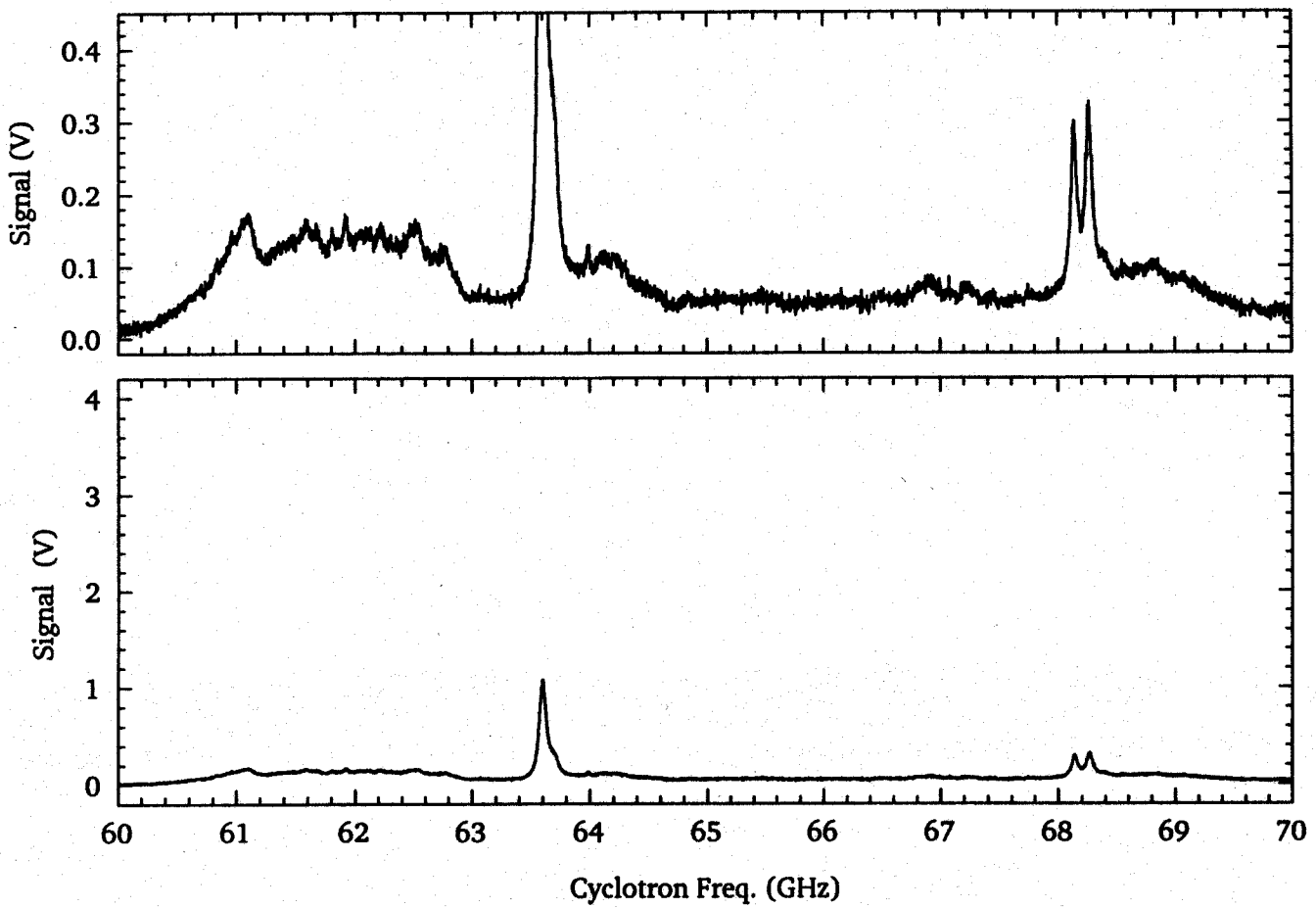
Signal (V)
0.4
0.3
0.2
0.1
0.0
Signal (V)
4
3
2
1
0
60
61
62
63
64
65
66
67
68
69
70
Cyclotron Freq. (GHz)

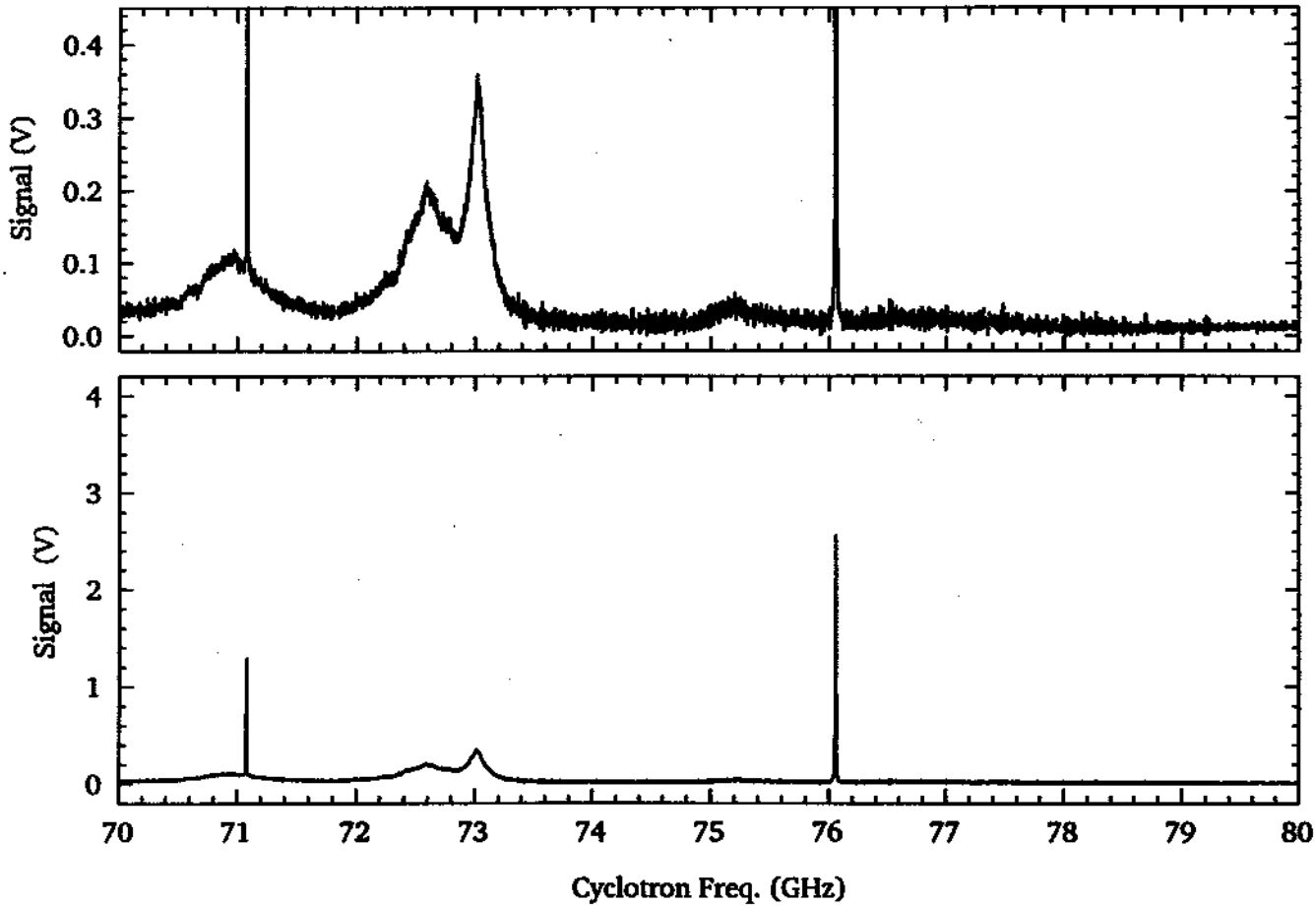
Signal (V)
0.4
0.3
0.2
0.1
0.0
Signal (V)
4
3
2
1
0
70
71
72
73
74
75
76
77
78
79
80
Cyclotron Freq. (GHz)

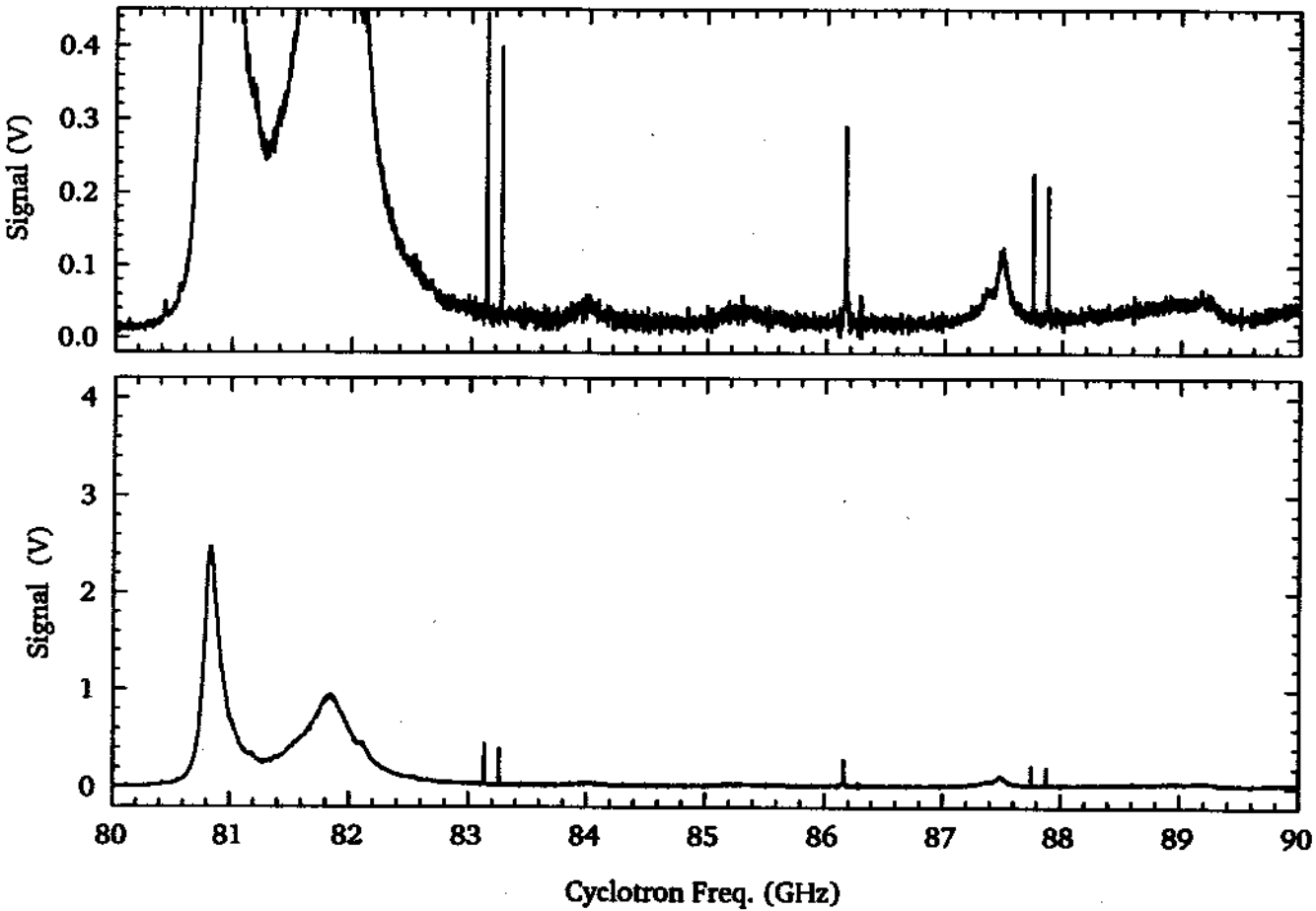
Signal (V)
0.4
0.3
0.2
0.1
0.0
Signal (V)
4
3
2
1
0
80
81
82
83
84
85
86
87
88
89
90
Cyclotron Freq. (GHz)

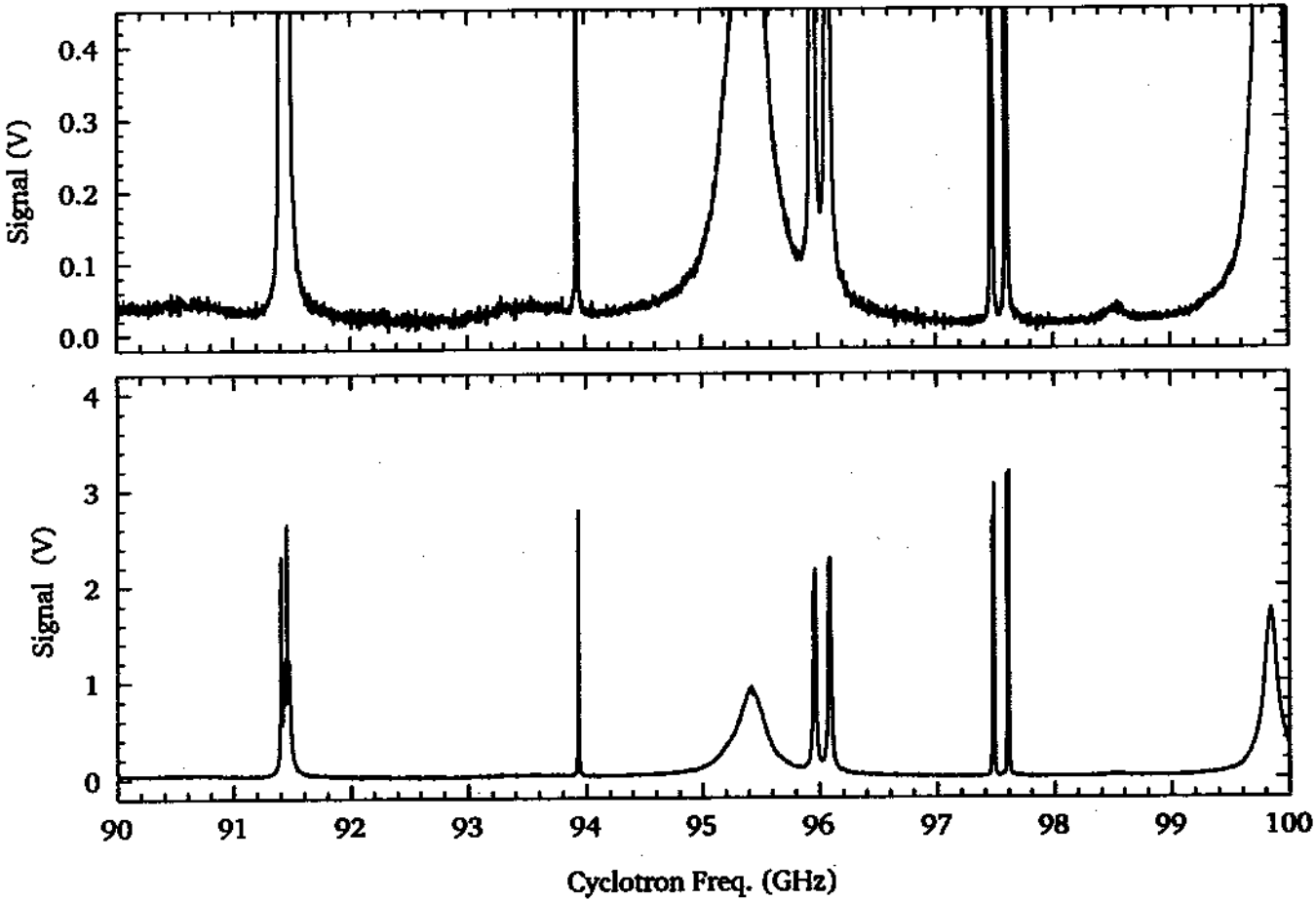
Signal (V)
0.0
0.1
0.2
0.3
0.4
Signal (V)
0
1
2
3
4
90
91
92
93
94
95
96
97
98
99
100
Cyclotron Freq. (GHz)

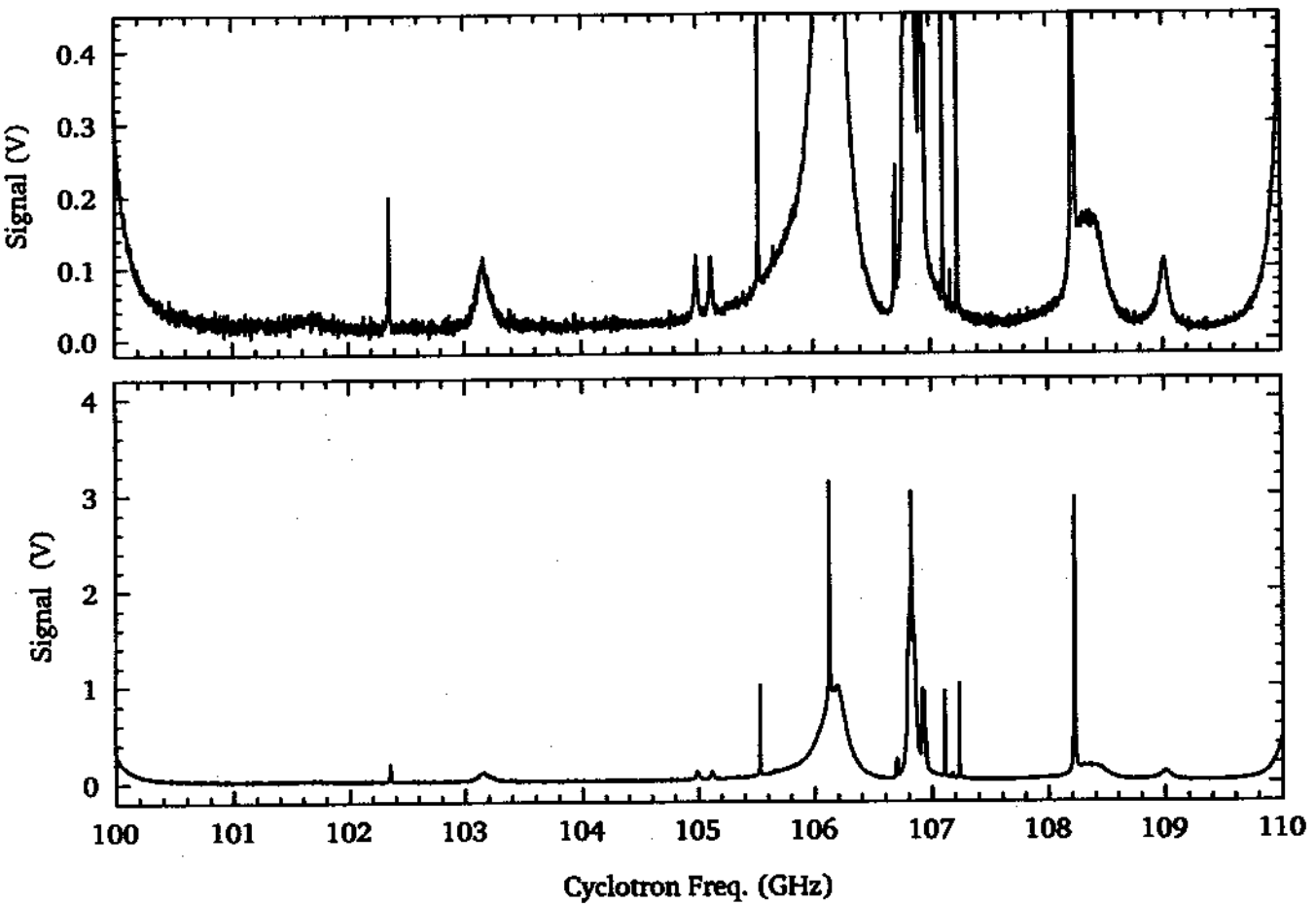
Signal (V)
0.4
0.3
0.2
0.1
0.0
Signal (V)
4
3
2
1
0
100
101
102
103
104
105
106
107
108
109
110
Cyclotron Freq. (GHz)

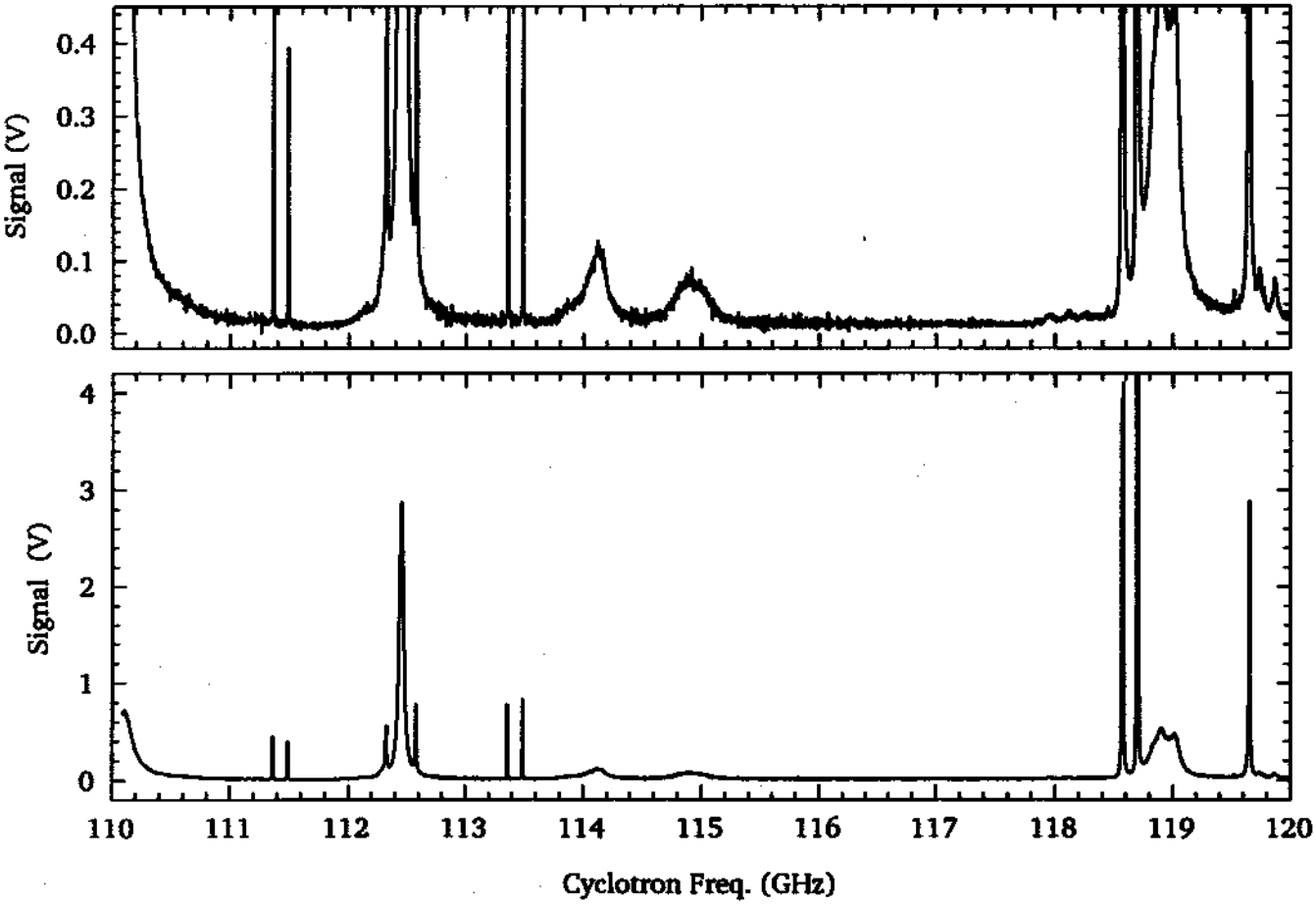
Signal (V)
0.0
0.1
0.2
0.3
0.4
Signal (V)
0
1
2
3
4
110
111
112
113
114
115
116
117
118
119
120
Cyclotron Freq. (GHz)

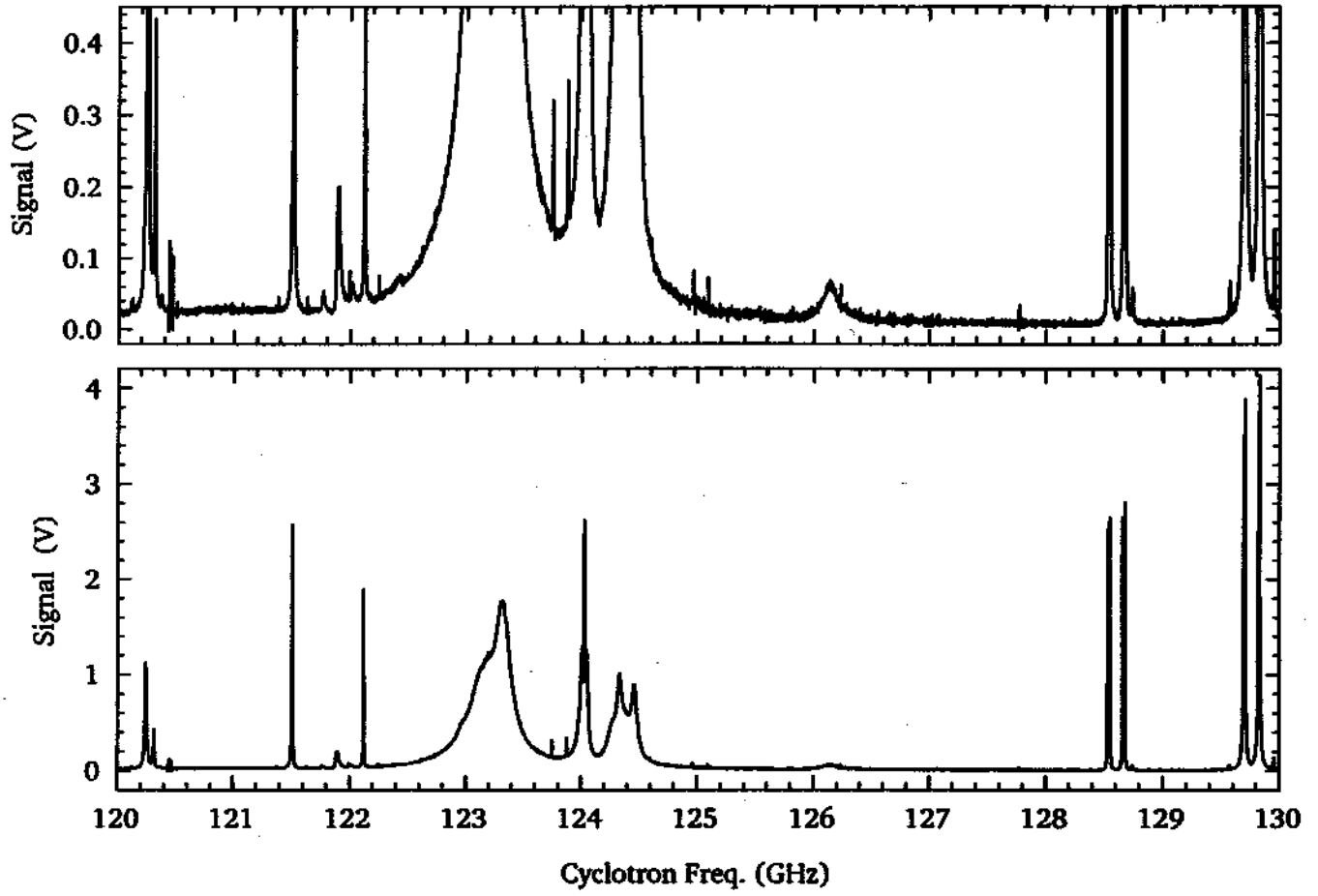
Signal (V)
0.0
0.1
0.2
0.3
0.4
Signal (V)
0
1
2
3
4
120
121
122
123
124
125
126
127
128
129
130
Cyclotron Freq. (GHz)

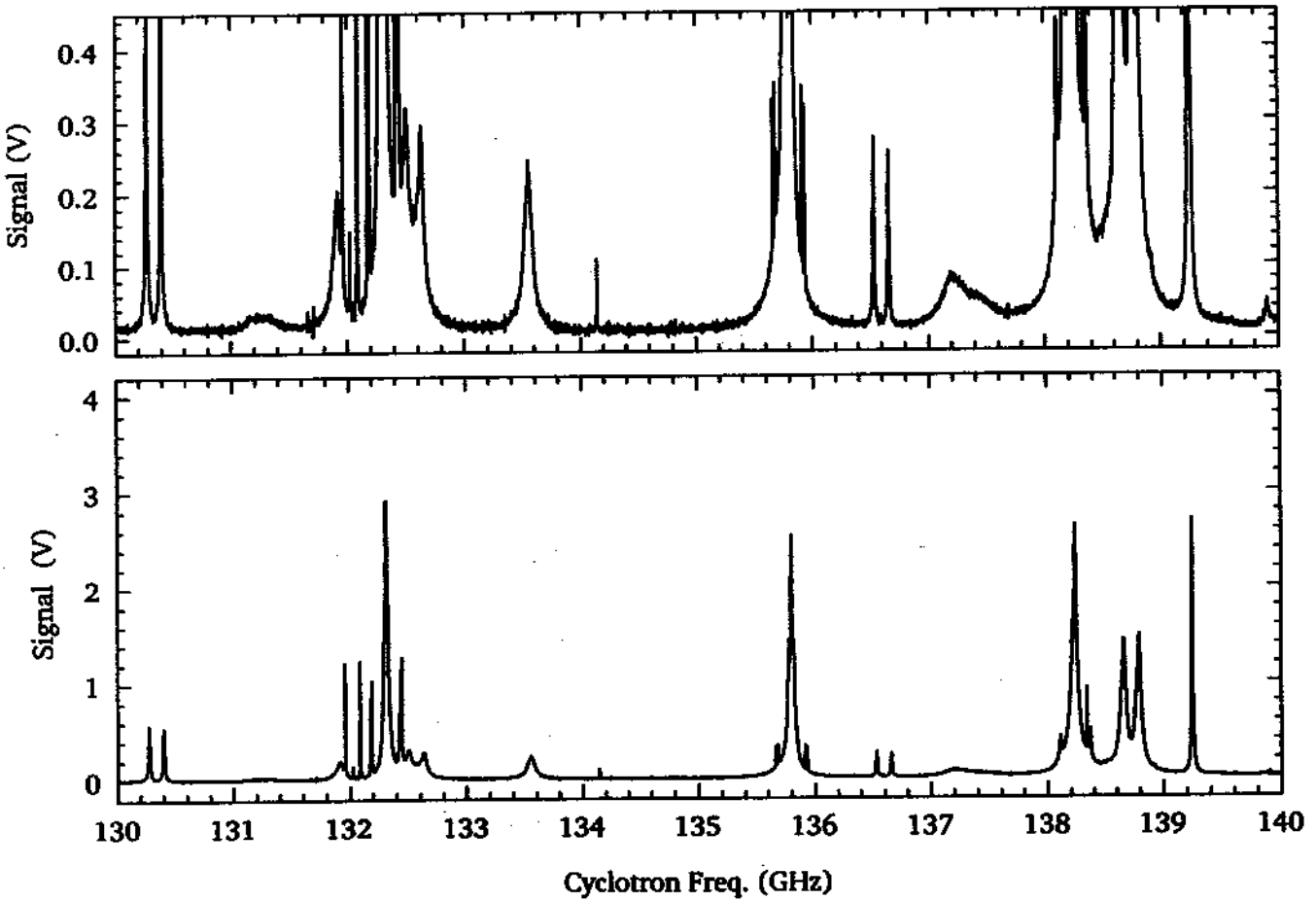
Signal (V)
0.0
0.1
0.2
0.3
0.4
Signal (V)
0
1
2
3
4
130
131
132
133
134
135
136
137
138
139
140
Cyclotron Freq. (GHz)

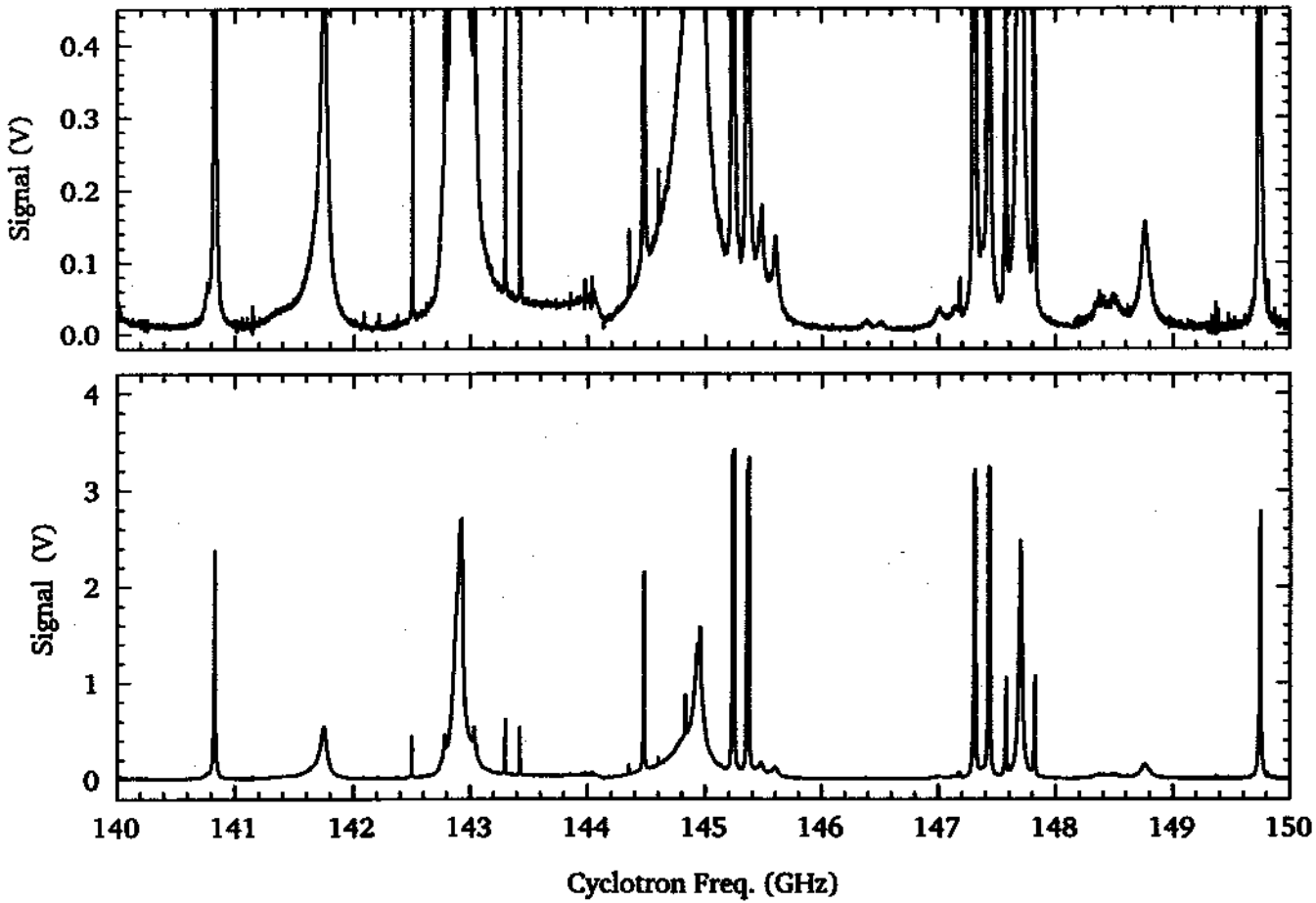
Signal (V)
0.0
0.1
0.2
0.3
0.4
Signal (V)
0
1
2
3
4
140
141
142
143
144
145
146
147
148
149
150
Cyclotron Freq. (GHz)

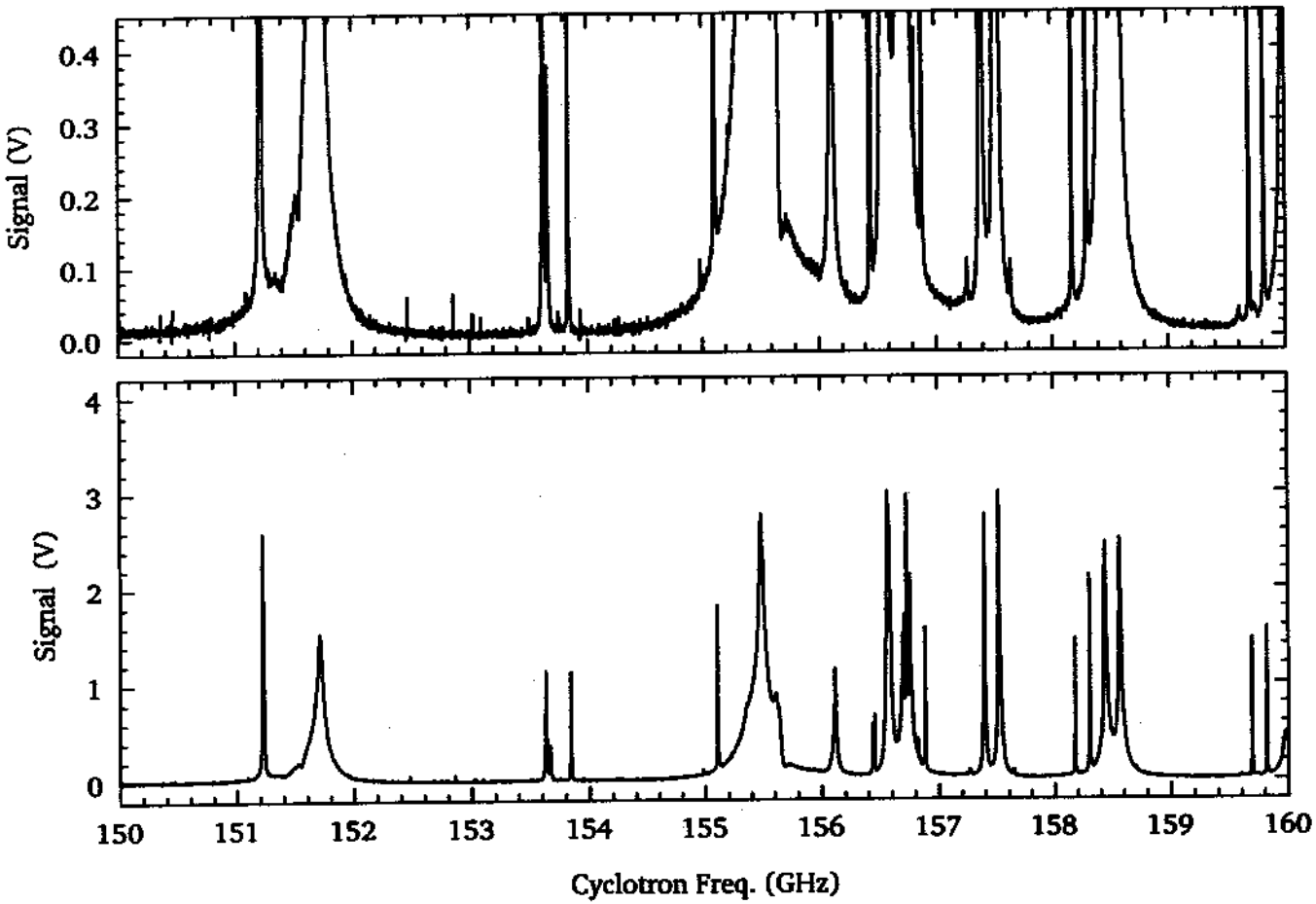
Signal (V)
0.0
0.1
0.2
0.3
0.4
Signal (V)
0
1
2
3
4
150
151
152
153
154
155
156
157
158
159
160
Cyclotron Freq. (GHz)

Signal (V)
0.4
0.3
0.2
0.1
0.0
Signal (V)
4
3
2
1
0
160
161
162
163
164
165
166
Cyclotron Freq. (GHz)

4.6 Summary

The observation that spontaneous emission from the cyclotron motion of an electron in a Penning trap cavity [32] is inhibited and subsequent calculations of the corresponding frequency shifts [8,9,11,12] signalled that the most accurate tests of quantum electrodynamics were seriously interrupted by modifications to the QED vacuum. Experiments with synchronized electron oscillators in a new cylindrical trap cavity [78,79] show how to change the cavity-modified vacuum from a serious interruption into an advantage. A new technique for probing electron-cavity interaction employs the sensitivity of the coherent motions of parametrically-pumped oscillators to radiative cooling, allowing the frequencies and quality factors for radiation modes of a trap cavity to be cleanly observed and measured for the first time. Frequencies of more than 100 observed modes below 166 GHz correspond to those of an ideal cavity to typically 1% or better. This makes it possible to identify observed standing wave fields using familiar classifications [49] (e.g. TE_{115}). The interaction with standing waves is so well controlled that motional sidebands and splittings are observed due to the axial oscillation of electrons in the electric field gradient of the cavity mode. Modification of resonance lineshape (broadening and splitting) is also observed for strong electron-cavity coupling.

Among identified cavity standing waves are some which couple to an electron's cyclotron motion at the trap center. Others should allow rapid change of cyclotron damping, sideband cooling of an electron to very low (mK) temperatures and directly driven spin flips. The cavity-modified vacuum is an advantage insofar as measured linewidths are narrowed when the electron cyclotron oscillator radiates less than in free space. This is arranged by tuning the magnetic field so that the electron cyclotron frequency is not resonant with the resonant frequency of a cavity mode which couples to the electron. Simple theory yields damping rates (eg. Fig. 1.1a) and frequency shifts (eg. Fig. 1.1b) which can be experimentally confirmed and used to avoid attendant frequency shifts, making possible a new generation of measurements of the electron magnetic moment.

Chapter 5

Fluctuations and Related Phenomena

In Chapter 3, the effects of stochastic, internal motions are minimized because the parametrically-pumped electron oscillators are resonantly cooled by a standing wave mode of the cavity. Important observed features of coherent motions could be understood using an ordinary differential equation for rigid axial motion of N electrons, a limit which is approached by cooling the internal motions to their zero-point energy. In Chapter 4, however, we observed that the parametric resonance was modified as the electron cyclotron motion was detuned from resonance with a cavity mode. The extraordinary sensitivity of non-rigid, synchronized motions to radiative cooling proved to be a very useful tool for probing standing wave modes in a cavity. A rigid model can not explain the Lorentzian lineshapes of observed cavity mode resonances or even why the parametric axial resonance is at all sensitive to cyclotron damping. Even when cavity cooling of internal motions is maximized, there are interesting non-rigid behaviors in synchronized motions of electron oscillators. We now explore the ways that parametrically-pumped electron oscillators are only partially synchronized above threshold, with observable fluctuations in both amplitude and phase due to internal motions.

Near threshold ($h \approx h_T$, $\omega_d = 2\omega_z$), the character of the quiescent state changes rather dramatically with small change in the pump strength. Fluctuations in the CM motion grow as the pump strength increase toward the threshold, as

shown on magnified scale in Fig. 5.1a, but the coherence time remains short. To observe fluctuations in the signal directly, a storage scope captures the IF signal, externally triggered by a precision frequency synthesizer at the same frequency. Fluctuations persist above the threshold in the synchronized CM motion, with

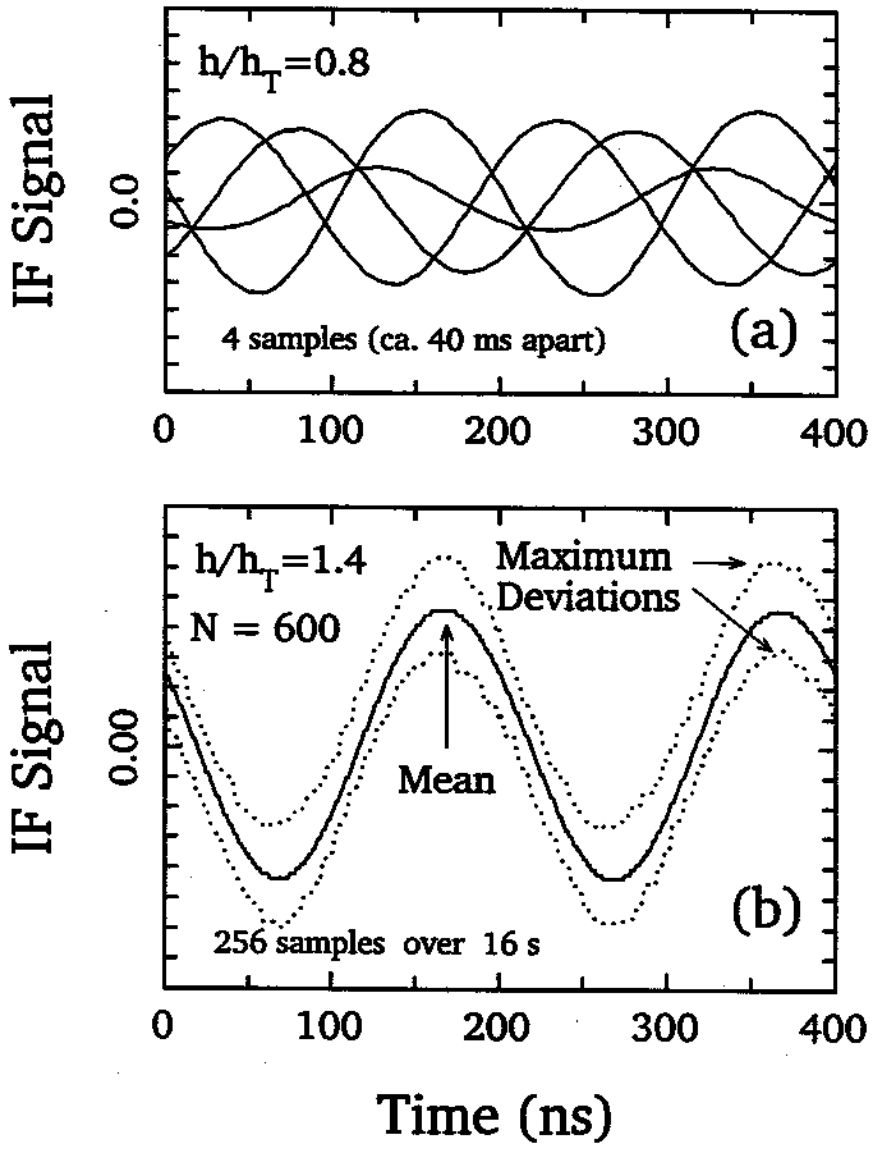

Figure 5.1: Sampled IF signal (5 MHz) illustrates (a) incoherent response for $h < h_T$ and (b) long-term coherence for $h > h_T$. Dotted lines in (b) show maximum deviations from mean coherent motion.

observable deviations (dotted lines in Fig. 5.1b) from a mean coherent oscillation (solid line in Fig. 5.1b) and interesting consequences for this phase bistable system.

5.1 Transitions between Phase Bistable States

Since the system (Fig. 2.17) is invariant under a time translation of one pump period ν_d^{-1}, any coherent response at half the pump frequency must be phase

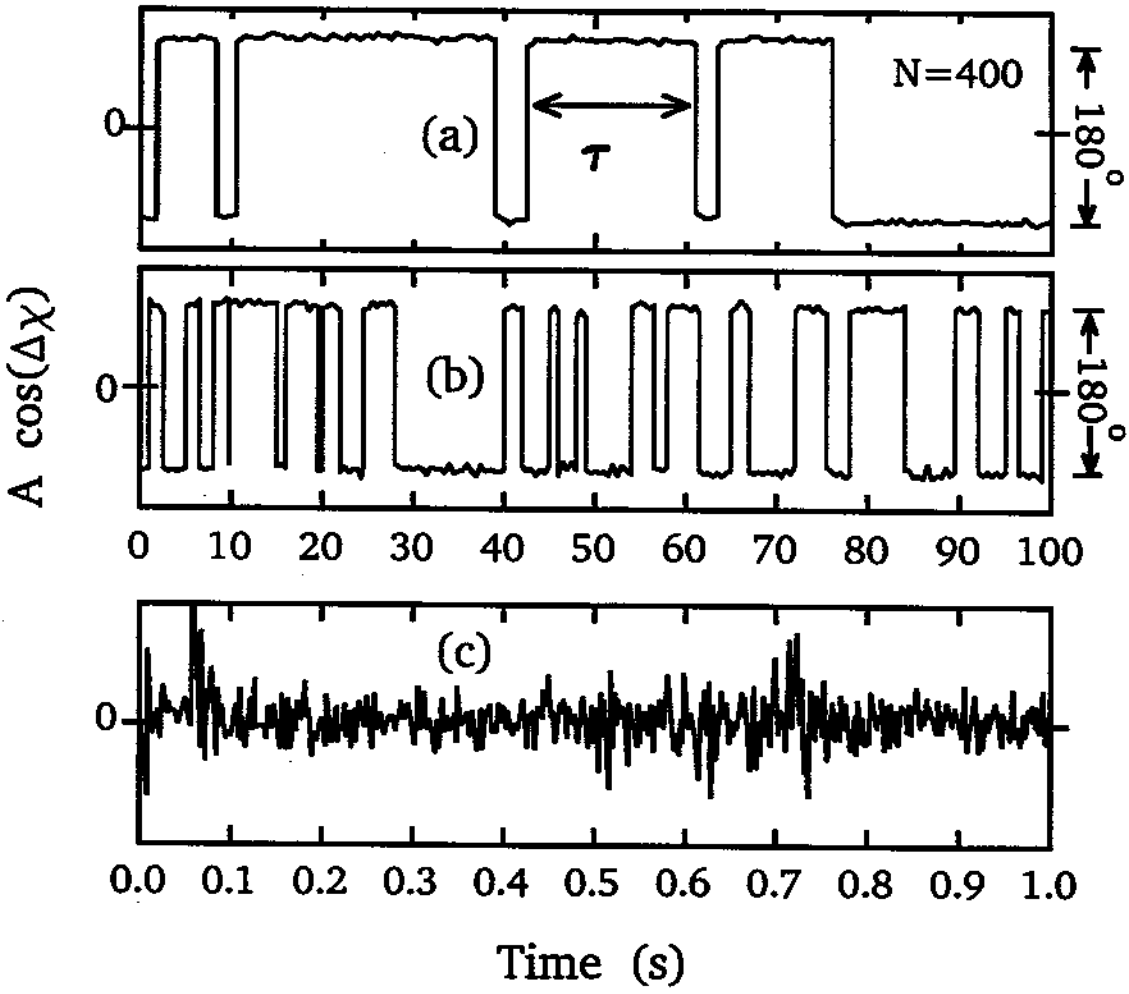

Figure 5.2: Random transitions between phase-bistable states (a)-(b) . Disordered motions (c) result if cyclotron cooling is weak. Residence time τ, illustrated in (a), on average becomes shorter (b) with increasing detuning between cyclotron and cavity mode frequencies.

bistable, with equal likelihood of having either of two steady-state phases which differ by 180°. Fluctuations cause random transitions between these phase states, reminiscent of a two-level system coupled to a heat bath or brownian motion of a particle in a double-well potential. We observe abrupt transitions between the two phases, as illustrated in Fig. 5.2a & b (similar to those attributed to collisions in a much poorer vacuum in an early experiment with only one electron [92]). The time between two consecutive transitions, or the residence time in one phase state, is denoted by τ (Fig. 5.2a). Thousands of flips observed over many hours show the flips to be random with typical distribution of the residence times τ (times between flips) shown in Fig. 5.3a for N = 750 electrons. The distribution fits well to an exponential form (Fig. 5.3b) and is consistent with a two-level model with constant transition probability, except for the shortest times. The first 50-second time bin receives 30 percent of counts from flips occurring within 5 seconds apart. This "over-abundance" of short residence times may be a clue to the mechanism activating the phase-flipping transitions, which is not understood yet.

In more detail, a phase sensitive detector is employed to distinguish between the phase-bistable states. As illustrated in Fig. 2.17, the voltage induced by the synchronized motion across the resistor in the simplified diagram is mixed with a local oscillator at $\nu_d/2$ and the phase of the local oscillator ϕ is adjusted so that the filtered output (near DC) is proportional to

$$A \cos(\Delta\chi) \quad . \tag{5.1}$$

Fluctuations in amplitude A and phase χ of the coherent response (Fig. 5.1) can be observed with a fast storage oscilloscope (after the signal is mixed down to a conveniently lower frequency). The phase fluctuation relative to one phase state χ_{ss} is denoted by

$$\Delta\chi = \chi(t) - \chi_{ss} \quad . \tag{5.2}$$

A transition of the synchronized motion from one phase state to the other ($\chi_{ss} \longrightarrow$

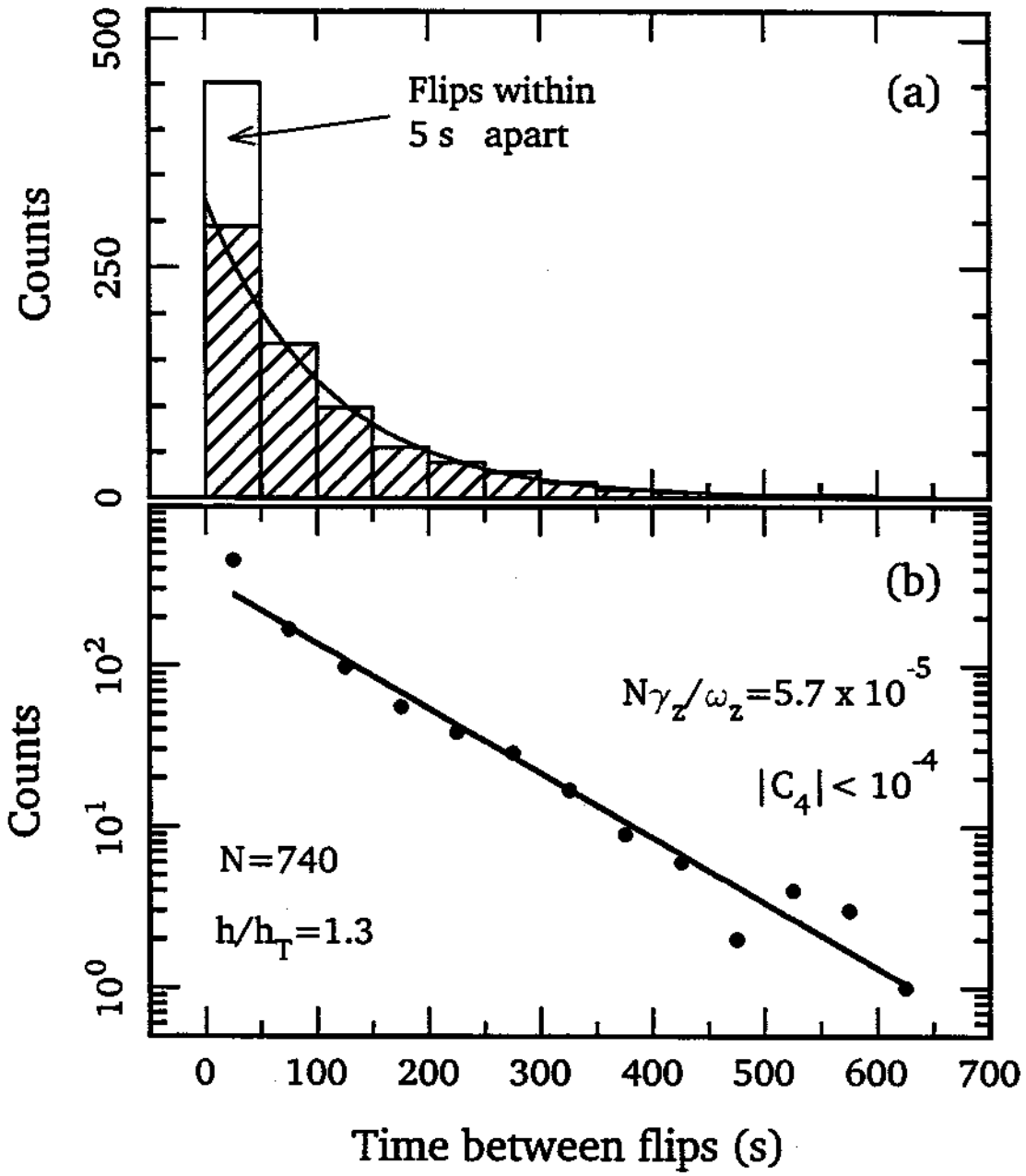

Figure 5.3: (a) Distribution of residence times, and (b) good fit to an exponential form.

$\chi_{ss} + \pi$) is observed as a change in sign of the detected signal

$$A\ \cos(\Delta\chi + \pi) = -A\ \cos(\Delta\chi)\ . \tag{5.3}$$

This signal is related to the projection of the CM "state vector" onto the x-axis in Fig. 3.8 (adjustment of the phase of the local oscillator corresponds to rotating the coordinate system so that the x-axis passes through the steady-states when $\Delta\chi = 0$).

To examine the abrupt transitions from one phase state to the other in great detail, a digital storage oscilloscope is armed to capture the signal when a phase jump occurs. Magnified time resolution on a digital oscilloscope reveals an interesting diversity of phase jump "trajectories" in the synchronized CM motion. Several samples are shown in Fig. 5.4 for $N = 700$ electrons. We observed that in many cases a transition is initiated with a collapse of the CM motion. This is illustrated in Fig. 5.4a. The CM motion is then re-excited to the other phase-state after a being in the "quiescent" state for a "dead time." This dead time can be as long as 100 ms but tends to decrease with increasing pump strength. In some cases, a transition is preceded by a period of observable increased fluctuations (Fig. 5.4 b). Completion of a phase jump may take many attempts in rapid succession (Fig. 5.4c-e). Fig. 5.4f shows a rare event in which the CM motion appears to be oscillating in the "basin" (Fig. 3.8) of one phase-state, switching over to (and then returning from) the other basin with unabated oscillation. (Fig. 5.4a-f were sampled under the same control parameters.) The duration of a phase jump τ_J (defined in Fig. 5.4a), is observed to be roughly in the range 10-100 ms with distributions that depend upon pump strength, anharmonicity and number of electrons (Fig.5.5).

The mean residence time $\bar{\tau}$ in a phase state is observed to vary greatly with control parameters. It increases rapidly with the number of electrons since the fluctuating motions of a larger number of electrons average to a smaller sized fluctuation of their CM motion (Fig. 5.6a). For $N > 2500$, no transition is observed over hours when ω_C' is resonant with a cavity mode (such as TE_{115}). Mean

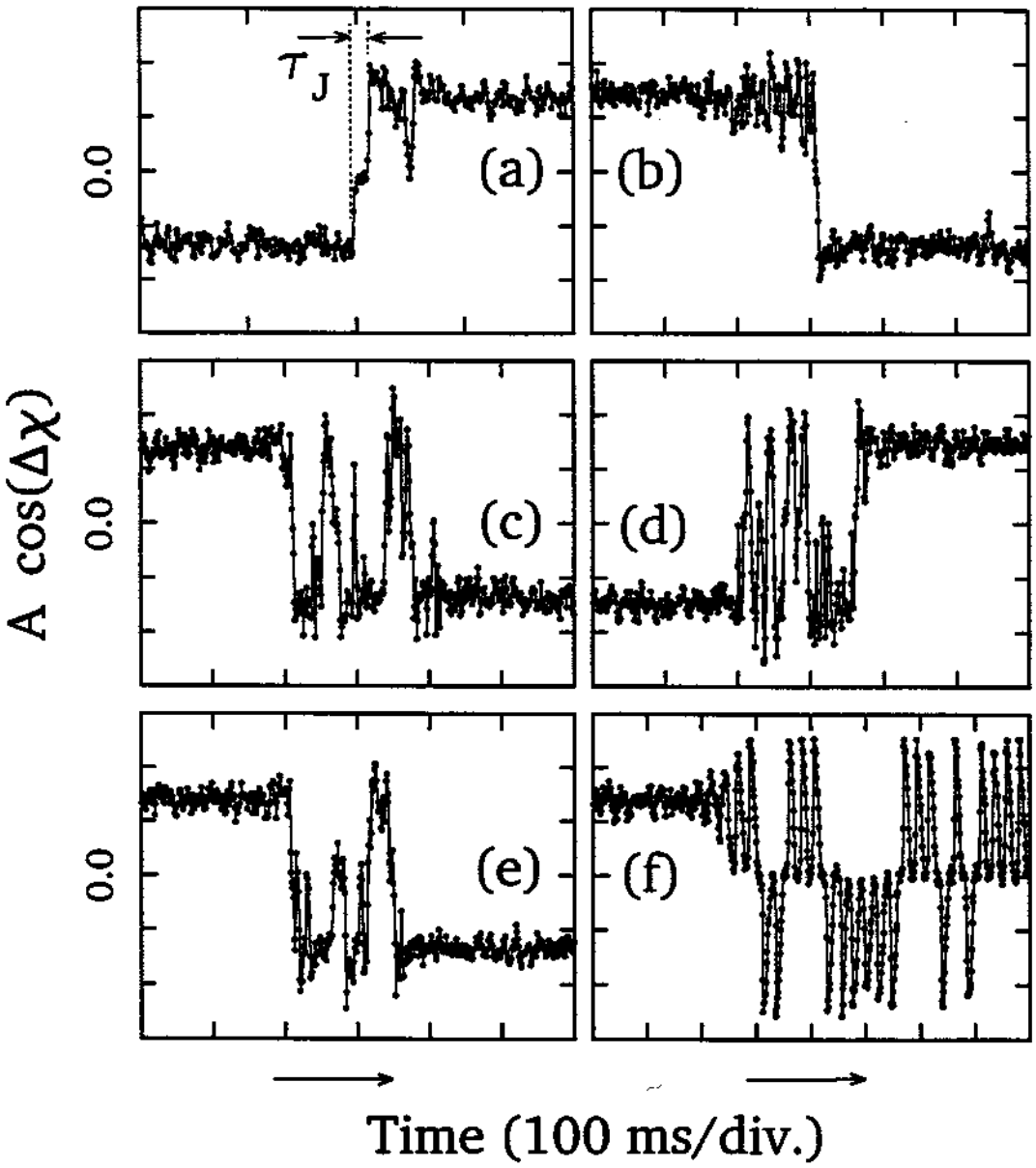

Figure 5.4: Examples of phase jump "trajectories" observed with 600 electrons parametrically driven at $h = 1.4h_T$ ($C_4 \sim -6 \times 10^{-4}$ and $N\gamma_z/\omega_z = 1.2 \times 10^{-5}$).

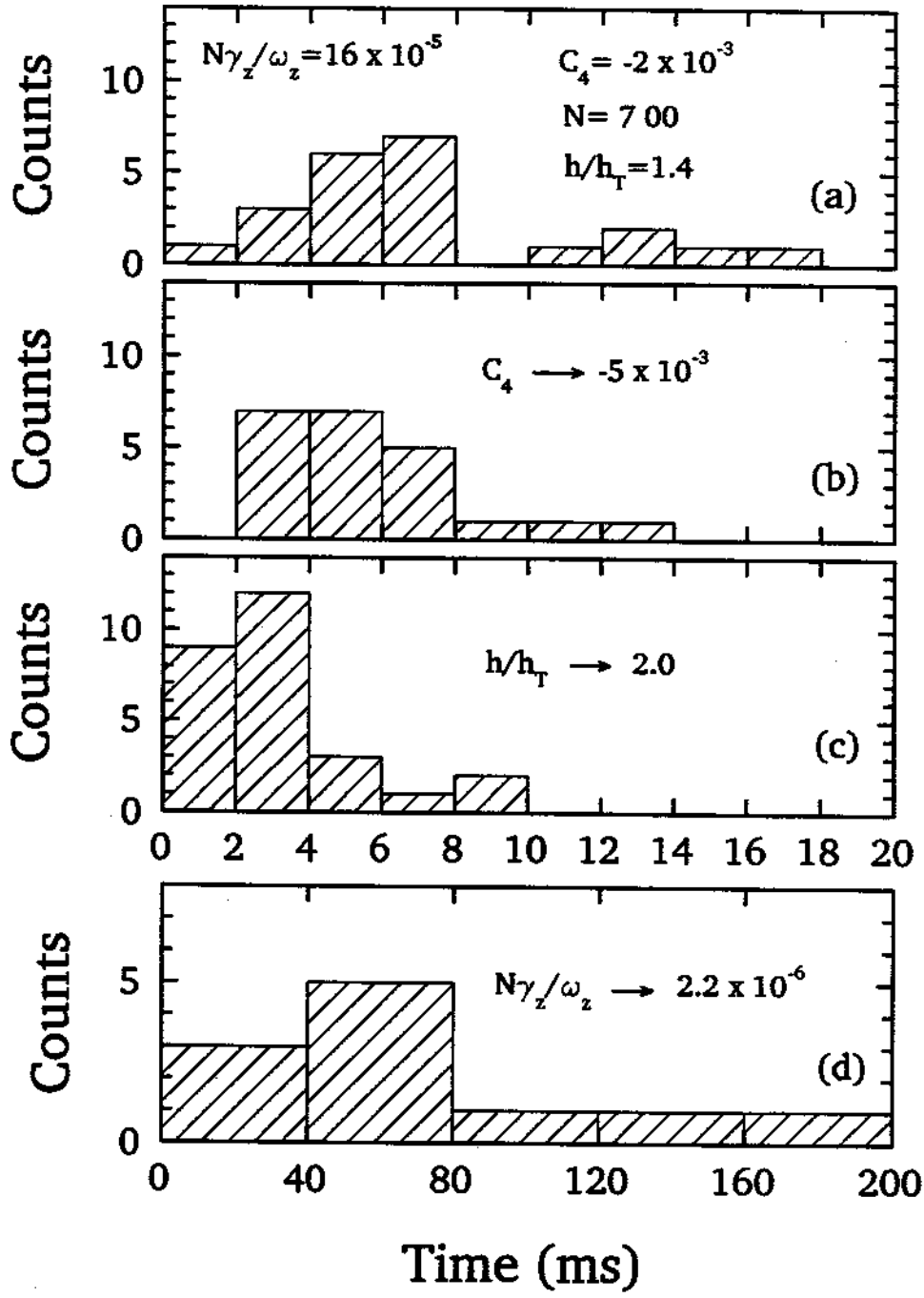

Figure 5.5: Distribution of jump times and variation with control parameters.

residence time is also observed to be longer for larger C_4 (Fig.5.6 b), presumably because a more anharmonic trap reduces internal energy. The internal energy may be lower since the amplitudes of de-synchronized oscillations would be smaller and the cooling via the LCR circuit is more efficient with larger anharmonicity. Phase switching rate increases rapidly with increasing internal energy. Consistent with this interpretation, an increase in the pump power or a stochastic modulation of the spring constant ω_z^2 (by applying a broadband noise potential to the ring) diminishes the mean residence time. The internal energy is conveniently controlled via the electron-cavity interactions. Fig. 5.6d shows the rapid decrease in mean residence time $\overline{\tau}$ for a cloud of $N = 400$ electrons as the frequency ω_c' is detuned from resonance with the TE_{115} cavity mode in Fig. 4.10. Transitions occur least frequently very near to resonance with a cavity mode (Fig. 5.2a) where the internal motion is most strongly cooled. The switching rate $\overline{\tau}^{-1}$ increases (Fig.5.2b) when a slight detuning of ω_c' from the mode resonance allows the internal energy to rise. As the decreasing residence times τ become comparable with the phase jump times τ_J, the CM motion can be expected to become "turbulent." Indeed, observed signals of the two phase-states are weaker and punctuated by random periods of incoherence. Further off resonance (cross-hatched region in Fig. 5.6d), the internal energy increases sufficiently so that the random, desynchronized motions of the electrons keep a detectable coherent CM motion from developing (Fig. 5.2c) because of the nonlinear couplings. Although a large anharmonicity can be introduced to increase cooling by the tuned circuit (presumably causing the dependence in Fig. 5.6b), we find that, in this "turbulent" region, long term coherent oscillation can not be restored by making the trap more anharmonic (increasing $|C_4|$).

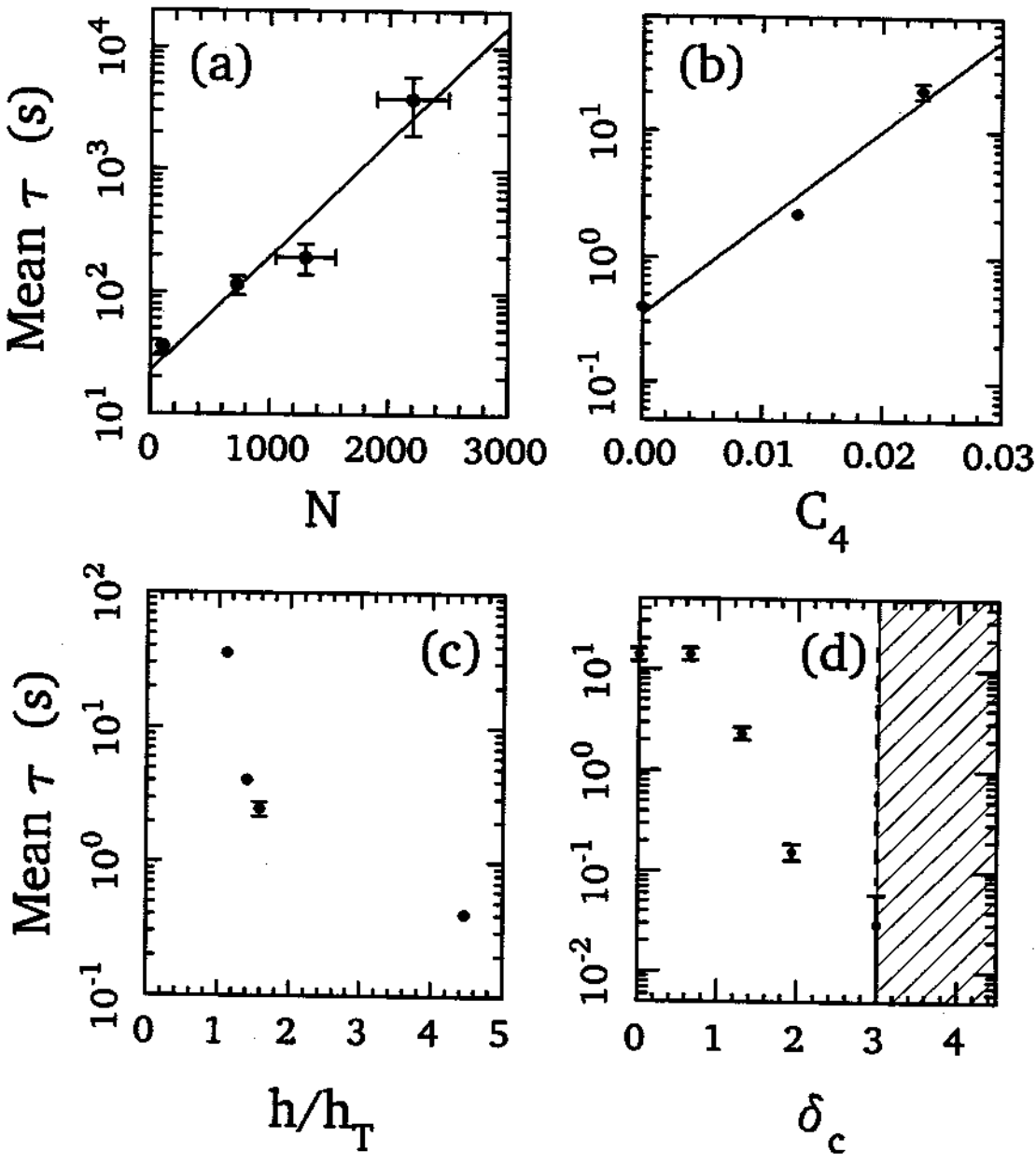

Figure 5.6: Dependences of mean residence time $\bar{\tau}$ on control parameters. Mean time between phase flips versus (a) number of electrons, (b) anharmonicity coefficient $|C_4|$, (c) pump strength h and (d) detuning between cyclotron frequency and a cavity mode eigenfrequency.

5.2 Partial Synchronization

The simplicity of the rigid model provides some understanding of the collective behavior in parametrically-pumped electron oscillators. But the model is inadequate in other important aspects. Parametrically-pumped electron oscillators are only partially synchronized. We now discuss observations of both the coherent and stochastic components of the CM motion, examining the frequency distribution of observed signal with a spectrum analyzer. The electron oscillators are pumped by a frequency synthesizer with very high spectral purity, suitable for high precision radio-frequency spectroscopy. We study changes in the spectrum brought about by varying a system parameter, such as the magnetic field (Fig. 5.8) to control

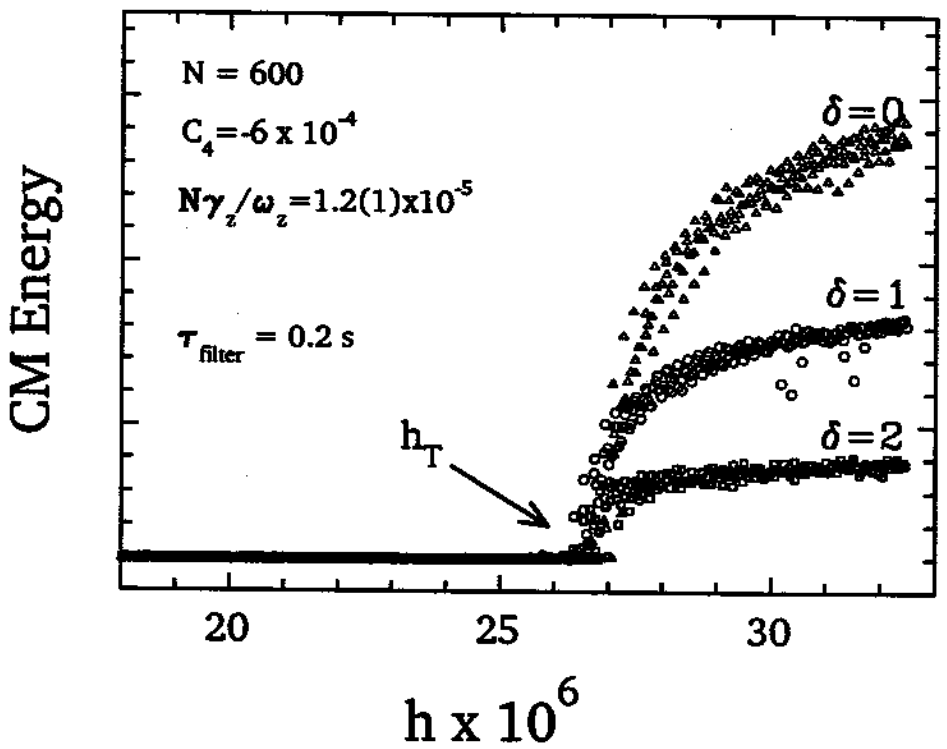

Figure 5.7: CM Energy versus pump strength for various detunings between cyclotron frequency and TE_{115} eigenfrequency. Saturation level is clearly limited by cyclotron cooling of internal motions.

radiative cooling of internal motions. The Fourier spectrum of the response above threshold consists of a broad "pedestal" due to fluctuations and a sharp peak which is orders of magnitude stronger due to the coherent motion. To have good signal for the the fluctuation spectrum, observed spectra are averaged over 100 samples. The highest three points in Fig. 5.8 (log-linear plot) shows the coherent component at $\nu_d/2$ decreasing as the internal energy is increased by detuning the ω_c from a cavity mode. Ignoring the coherent component, we observe that the spectrum of the fluctuations broadens with increasing detuning from a cavity mode (or internal energy).

The threshold of instability h_T is observed to be independent of internal energy, as illustrated in Fig. 5.7 (obtained by sweeping the pump strength for identical set of detunings used in Fig. 5.8), except for a small fluctuation at the 1% level. The energy in the coherent CM motion increases as the cyclotron frequency is tuned closer to the cavity eigenfrequency (for TE_{115}). It is noteworthy that Fig. 5.7 shows less noise in the measured mean squared amplitude for larger detunings from the cavity mode. It appears that the frequency spectrum broadens but amplitude noise is reduced when the cyclotron frequency is detuned from cavity mode resonance. A more detailed study of the amplitude and phase fluctuation as a function of cavity cooling would be interesting.

More evidence points to the limitations of the rigid model even when the radiative cooling of internal motions is maximized. With the electrons resonantly cooled by the mode TE_{115}, the Fourier spectrum is observed to change dramatically with increasing pump strength, as shown in Fig. 5.9 (Each spectrum is an average of 100 samples.). Only the broad, fluctuation spectrum is present below threshold (Fig. 5.9a). Observed width is of order $N\gamma_z/2\pi$ but becomes narrower as the pump strength approaches the threshold. When the pump strength exceeds h_T, a sharp peak (much narrower than the detection bandwidth of 5 Hz in Fig. 5.9a and 25 Hz in Fig. 5.9b) emerges from a larger pedestal. The pump strength is increased first in increments of +1 dB in Fig. 5.9 a, and then in increments

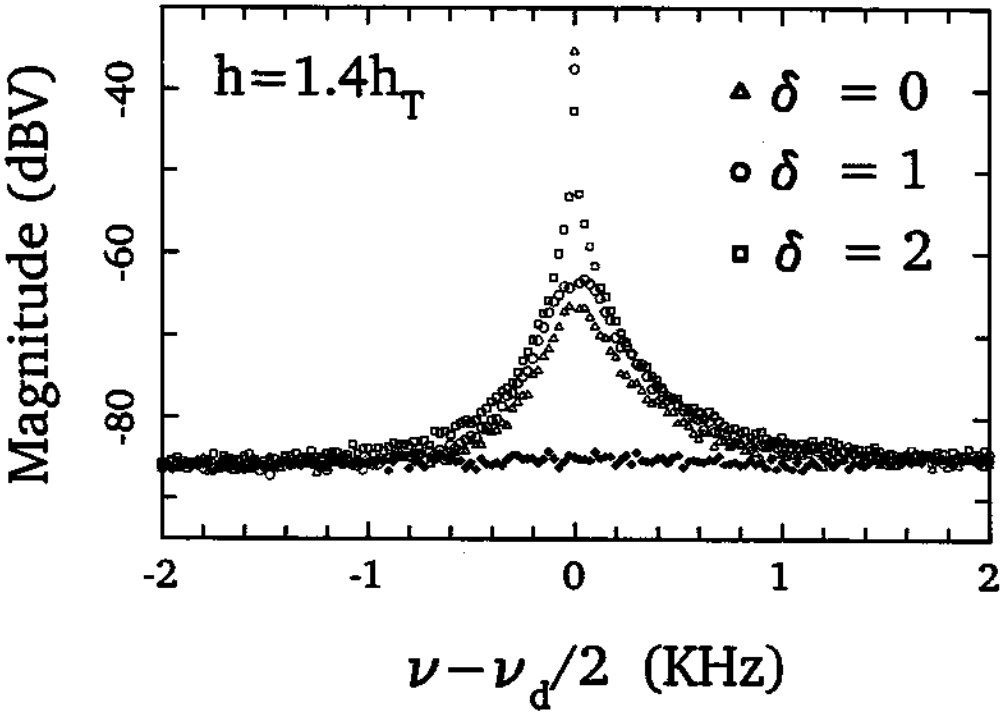

Figure 5.8: Fourier spectra of responses for various detunings from a cavity mode. Coherent response (peak) diminishes as cyclotron frequency is detuned from cavity mode eigenfrequency, but fluctuation spectrum broadens. Other system parameters are given in preceding figure.

of +2dB in Fig. 5.9 b. The fluctuation spectrum broadens as the pump strength increases and is skewed for high pump strengths (Fig. 5.9 b).

An important non-rigid feature with maximized cavity cooling is shown when the variation of signal size is plotted for a wide range of pump strengths. Fig. 5.10 plots the power in the peak (square) and the integrated power in the fluctuation spectrum (circle) versus pump strength for the data set shown in Fig. 5.9 . The integrated power of the fluctuation spectrum is the sum of contributions from each frequency bin with the white-noise background subtracted and the peak removed

by omitting the central bin. Above threshold, the coherent component grows with pump strength but saturates at $h \approx 1.6h_T$ and slowly decreases for $1.6h_T < h < 6h_T$. This is an important disagreement with the rigid model, which predicts the

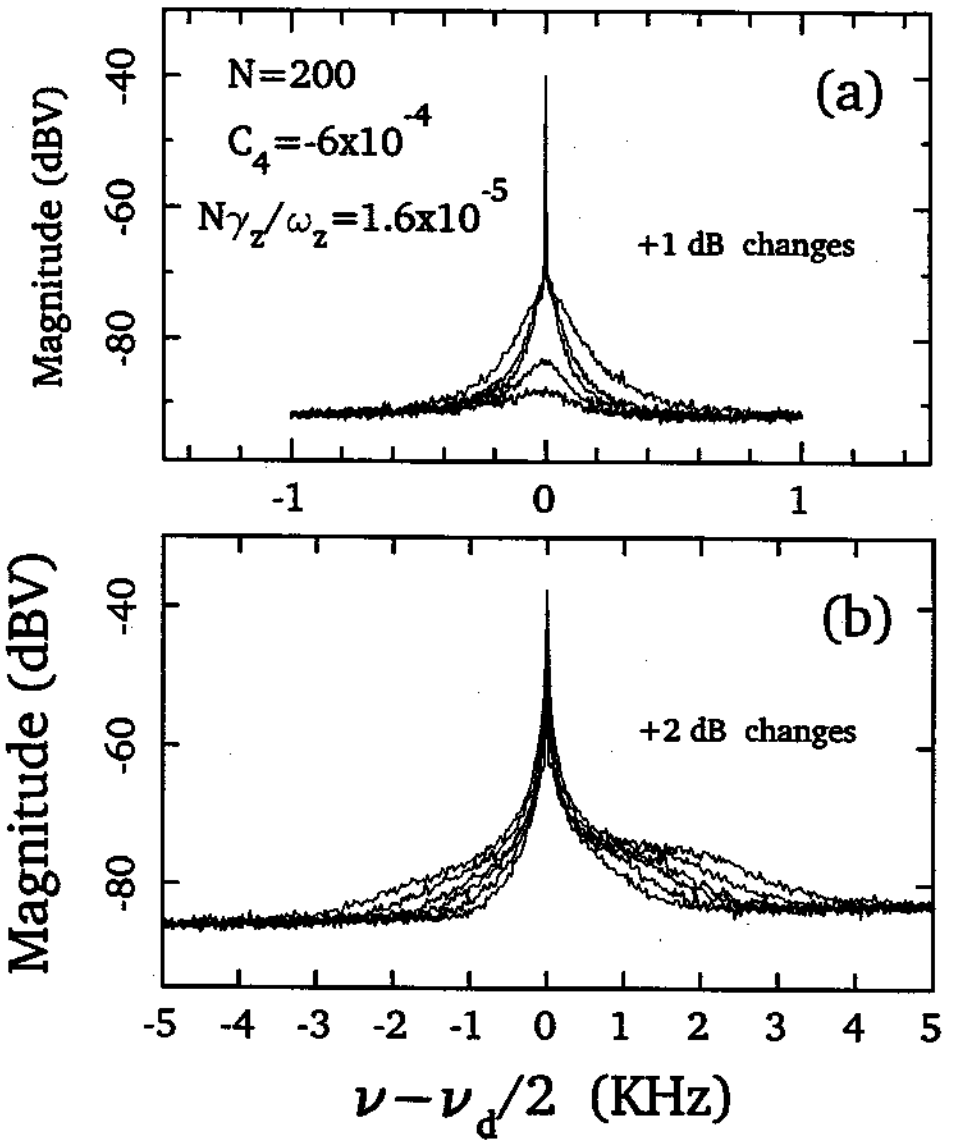

Figure 5.9: Fourier spectra for various pump strengths. A sharp peak emerges as pump strength exceeds threshold (a), with only broadband spectrum appearing below threshold. Fluctuation spectrum continues to broaden with increasing pump strength (b), becoming skewed for very strong pumping.

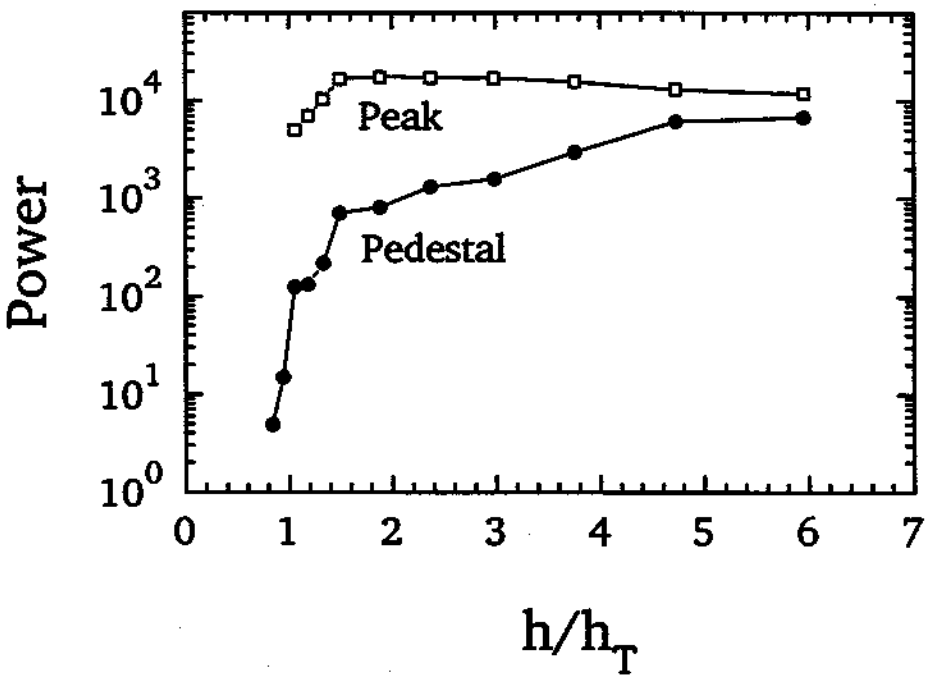

Figure 5.10: Comparison of power in the peak (square) with the integrated power in the fluctuation spectrum (circle) for the data set shown in preceding figure.

CM energy to be a monotonically increasing function of the drive strength (Sec. 3.3.1). For example, if the leading anharmonicity λ_4 is dominant, then the squared amplitude of the steady-state rigid motion goes as

$$A^2 \propto \sqrt{h^2 - h_T^2} \tag{5.4}$$

when drive frequency is $\omega_d = 2\tilde{\omega}_z$. On the other hand, Fig. 5.7 shows that observed energy in coherent CM motion is limited by cooling via radiation into the cavity, not by anharmonicity as would be the case for rigid motion. In spite of the disagreement, the observed lineshapes (Fig. 3.5) agree qualitatively with the rigid model (Fig. 3.4). Taking a linear lineshape like in Fig. 3.5a as an example, the lineshape is well preserved but the slope is observed to decrease when radiative cooling is reduced. The CM energy decreases also if the cyclotron oscillators are

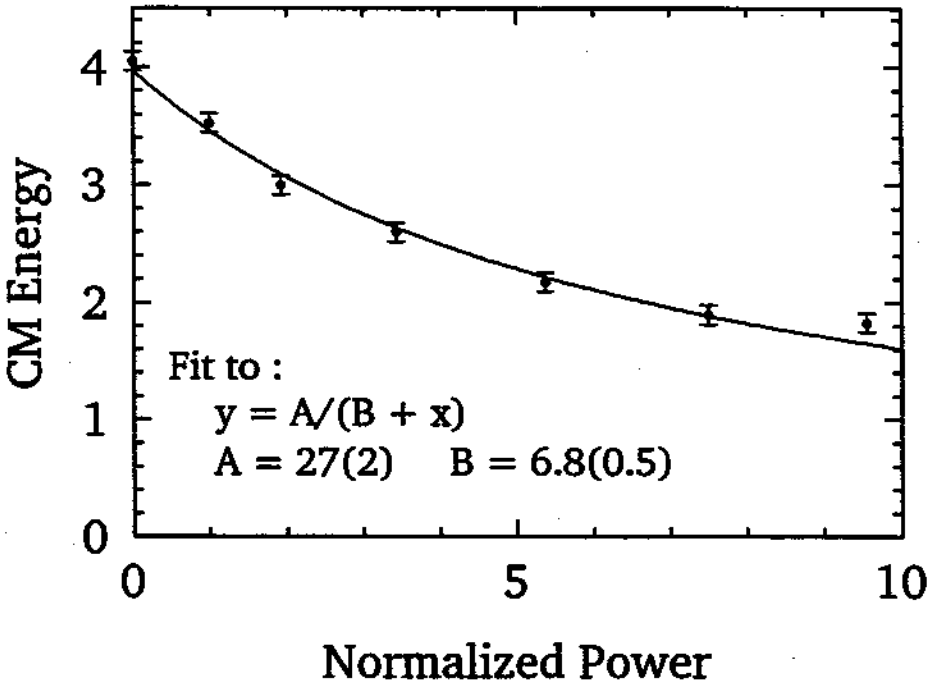

Figure 5.11: Decrease in coherent response to parametric excitation when cyclotron motions are heated with a microwave drive. Measured energy in axial CM energy with parametric drive at lower corner frequency $\nu_d = 2\nu_-$, is plotted versus normalized microwave drive power (dots). A simple form (solid) fits well to it.

heated up with a microwave drive, as illustrated in Fig. 5.11.

The mechanism causing the observed response to be so sensitive to both cyclotron cooling and anharmonicity is not understood. It appears that individual electron oscillators are excited to large amplitudes that are limited by anharmonicity, and that the observed coherent response is generated by their synchronized component which is controlled by a thermal process involving energy exchange between the axial and cyclotron motions. It is this sensitivity of partially synchronized motion to cooling of the internal motions (Fig. 5.7a) which has been very useful for probing the electron-cavity interactions (Fig. 4.1) so important for other radiative studies. We also find that the root-mean-squared (rms) saturation signal

scales linearly with the number of electrons (Fig. 5.12 a). The rms signal below threshold appears consistent with a linear dependence on the number of electrons, but the slope is about 50 times smaller (Fig. 5.12 b).

In contrast to the saturation and decline in power of the peak, we observe

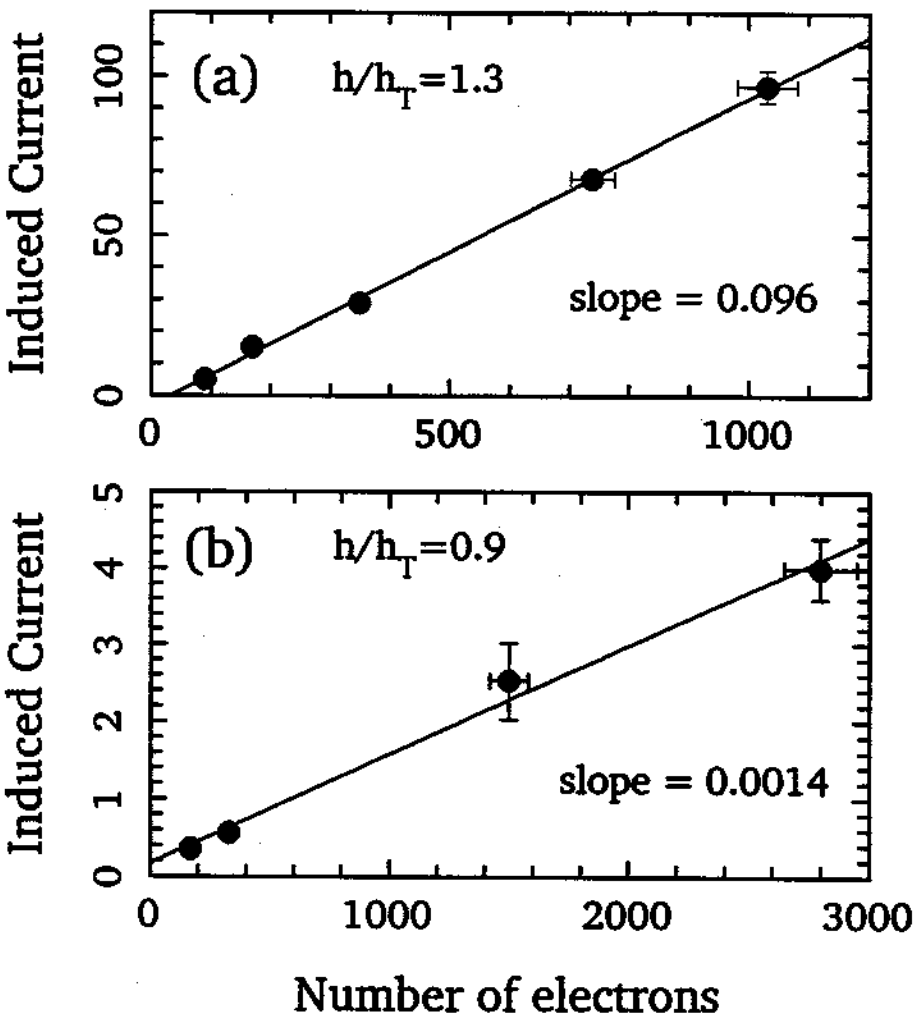

Figure 5.12: Scaling of rms induced current with number of electrons (a) above threshold and (b) below threshold.

that the power in the fluctuation spectrum increases monotonically for $h < 6h_T$ (Fig. 5.10) . The rate of growth in fluctuation power decreases with pump strength. There are a few step-like structures where the fluctuation spectrum changes very little with incremental rise in pump strength, but more data is needed to confirm this and to improve the resolution. The powers in the peak and pedestal are converging for $h < 6h_T$. It is not known if this convergence should continue for even higher pump strengths. Here again, the rigid model provides no clue.

5.3 Internal Motions: Slow Relaxations

A parametric drive excites not only the collective, CM motion of N electron oscillators but also internal degrees of freedom. Even for small systems (< 100 electrons), the full dynamics is difficult to analyze. In the past, a "bolometric" model [18,93] was developed for the disordered, thermal motions of trapped electrons or ions (summarized in Appendix B) and a simplified set of rate equations was thoroughly tested in experiments with electrons at $T \sim 80K$ [93]. In those early experiments, pulsed excitation showed that internal degrees of freedom come into thermal equilibrium so fast that they essentially form a single reservoir, with equilibration time shorter than other relaxation times. Since our apparatus is submerged in LHe, simplifying assumptions used in earlier studies may not apply at the lower temperatures. A few pulsed excitation experiments were carried out in our apparatus. For example, Fig. 5.13a shows the response when electrons initially at 4K are heated with a parametric drive below threshold in periodic 10-ms pulses. A storage oscilloscope captures the response from each pulse and gives an output averaged over 256 pulses to improve signal-to-noise. Fig. 5.13a shows the smooth relaxation which is characteristic of the response in a bolometric model [93] and, as expected, relaxation time is observed to be shorter when anharmonicity is increased ($|C_4|$ is made larger). This indicates that energy is transferred between internal reservoir and CM motion via the non-linear couplings. However, when the pump strength is above threshold, new features are observed. Fig. 5.13b

shows the substantially larger response of the partially coherent response to a single 250-ms pump pulse above threshold. This response has a rapid initial growth overshooting the steady state, characteristic of parametric resonance discussed in Chapter 3. Rapid growth stops abruptly and is followed by a much slower relaxation to a mean steady level with fluctuations. "Ring down" to the steady level (expected in rigid model, Fig. 3.2) is not observed, presumably because they are "washed out" by internal fluctuations. The slow relaxation to steady level is about 30 times longer than the typical rise time of the initial rapid growth, or observed relaxation times below threshold. Preliminary results from available data show that this new time constant is not very sensitive to changes in anharmonicity and pump strength. A more systematic study would extend over the full range of control parameters, including dependences on number of electrons and on detuning of cyclotron frequency from cavity mode resonance, etc.

To see that Fig. 5.13b is a difficulty for a bolometric model, we now give a simplified set of rate equations describing energy transfer between axial CM motion and internal reservoir. Another experimental evidence of its limitations follows. Below threshold, the bolometric model provides

$$C_z\dot{T}_z = -g_{zo}(T_z - T_o) + g_{iz}(T_i - T_z) + \dot{H}_z \tag{5.5}$$

$$C_i\dot{T}_i = -g_{io}(T_i - T_o) + g_{zi}(T_z - T_i) + \dot{H}_i \tag{5.6}$$

where, for simplicity, the tuned circuit and cavity are assumed to be at the same temperature T_o. The axial CM oscillator has temperature T_z with heat capacity C_z. A reservoir formed from all internal oscillations has temperature T_i with heat capacity C_i. Damping of the CM motion due to a tuned circuit is characterized by conductivity g_{zo}. Internal motions decay to T_o at a rate g_{io}/C_i. Energy transfer between CM motion and the internal reservoir is characterized by conductivity $g_{iz} = g_{zi}$. For sufficiently high temperatures, the thermal conductivities g_{ij} and heat capacities C_i are approximately independent of temperature. A set of linear, first-order differential equations, such as Eq. (5.5) and Eq. (5.6), cannot generate a response like in Fig. 5.13b.

Although this set of equations has been shown to be valid for temperatures above or near 80K for weak pumping of trapped electrons, [93] a more general system of equations would be necessary for electrons cooled to near LHe temper-

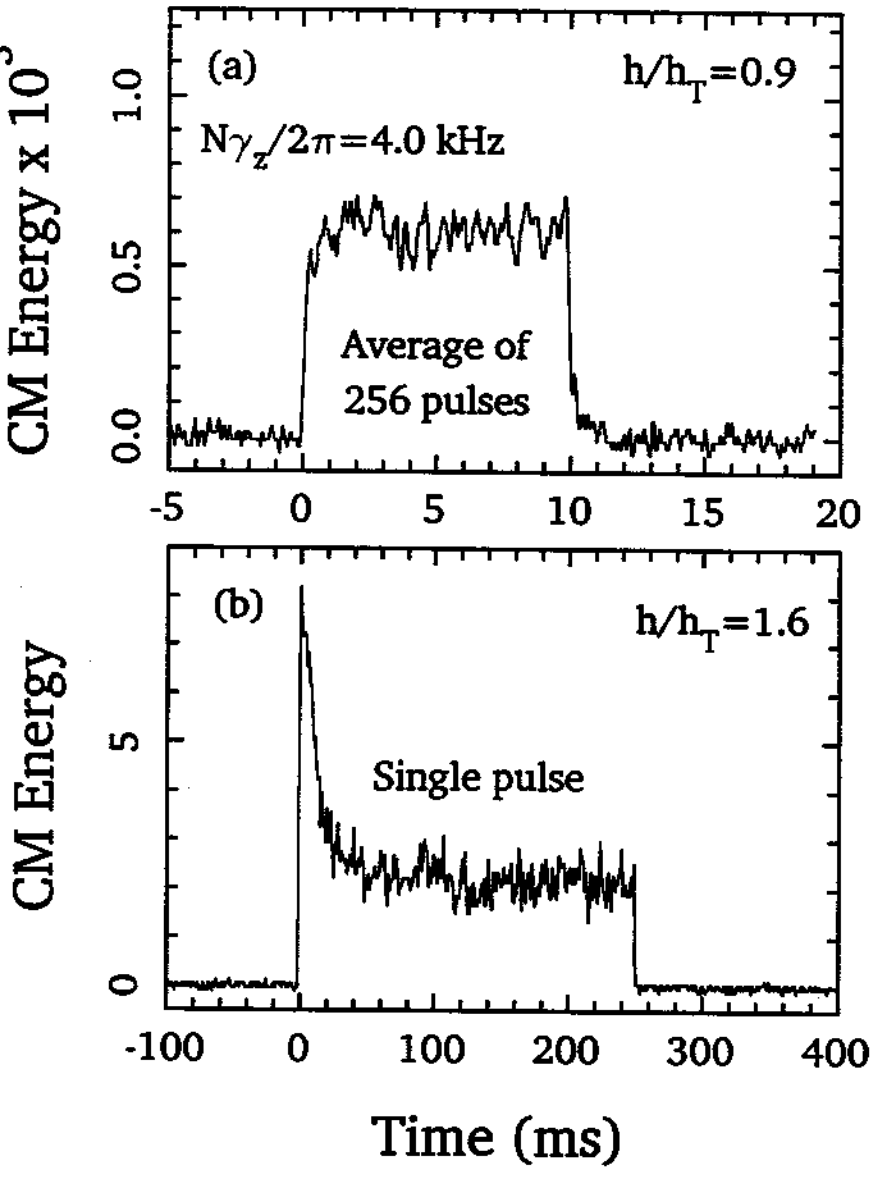

Figure 5.13: Characteristic responses to pulsed parametric pumping (a) below threshold and (b) above threshold. Averaging over 256 pulses improves the S/N below threshold (a), but only a single pulse is used above threshold (b). Slow relaxation (b) follows initial rapid growth, above threshold.

ature if the temperatures of the axial internal motions $T_{\|}$ and transverse internal motions $T_{\perp}$ do not equilibrate faster than other relaxation rates. Theoretical analysis of binary collisions in a strongly magnetized electron gas indicates a strong temperature dependence in this equilibration rate at very low temperatures, dropping rapidly as $T \longrightarrow 0$. [68] In our study, pulsed cyclotron excitations show some evidence for this. In Fig. 5.14, the energy in the axial CM motion of $N = 1600$ electrons is monitored with a storage scope as a square wave actives a microwave drive to excite the cyclotron motions for 10 s, and then deactivates the drive for the next 10 s. The output is averaged over many drive cycles. (Parametric drive is disconnected.) If the equilibration rate is significantly smaller at lower temperature, then the rise time in the energy of the axial CM motion when cyclotron heating

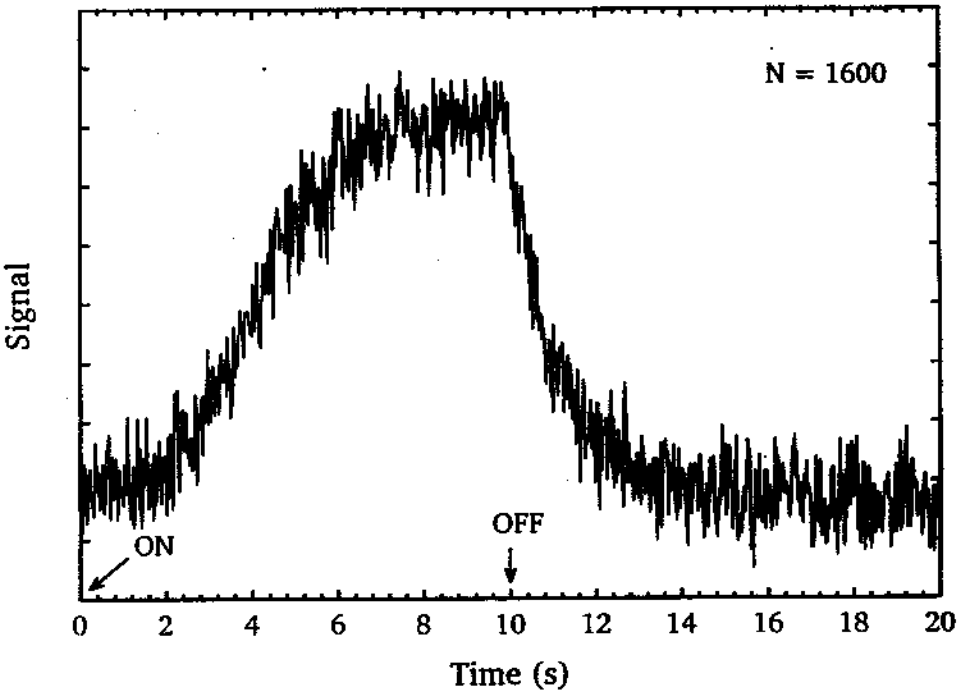

Figure 5.14: Pulsed cyclotron excitation. Slow growth and fast decay indicates temperature dependence of equilibration process.

is turned on would be much longer than the decay time when heating is turned off. Observed relaxation is clearly non-exponential with the rise time significantly longer than the decay time, indicating a slower relaxation at low temperatures. As shown in Fig. 5.14, nearly 2 seconds after the microwave drive was applied, observed axial CM energy increased by less than 10%, but faster growth followed. In contrast, axial CM energy has dropped by over 80% within 2 seconds after the drive was turned off. More detailed experimental study near 4K (at which 90% of cyclotron oscillators are in the ground state) may reveal other interesting features due to temperature dependent collisional processes and may establish a generalized set of rate equations for low temperatures.

5.4 Summary

A rigid model, in spite of its usefulness, does not provide a complete picture. A variety of interesting observations involve fluctuations due to internal motions, which are entirely omitted in a rigid model. Random transitions occur between the phase bistable states of partially synchronized CM motion. Except for very short times, observed residence times fit well to an exponential distribution (consistent with a two-level model with constant transition probability). Prompted by the "over-abundance" of rapid phase flips, observations on magnified time scales show interesting phase jump "trajectories," including a rare event showing synchronized CM motion oscillating in the basins of attraction for the two phase states. Measurements of mean time between flips are made for a wide range of conditions.

Partial synchronization is also examined in the Fourier transform of the observed response using a spectrum analyzer. A typical spectrum has a very sharp, narrow peak corresponding to synchronized motion, and a broadband, random distribution corresponding to fluctuations. As radiative cooling via coupling to a cavity standing wave is reduced, the sharp peak in the spectrum is reduced but the fluctuation "pedestal" is broadened. Even with radiative cooling maximized

(by tuning cyclotron motion into resonance with TE_{115}), the observed spectrum changes dramatically with pump strength. Power in the peak is observed to saturate as pump strength is increased above threshold and then decrease slowly for $h > 1.6h_T$, contradicting the monotonically increasing dependence expected of rigid motion. Only broadband, fluctuation spectrum is observed below threshold. The fluctuation pedestal broadens as the pump strength is increased above threshold, becoming skewed at high pump strengths. Integrated power in the pedestal grows monotonically with pump strength below $6h_T$, and may be converging to the same limit as the peak power.

Pulsed excitations give more evidence of limitations of a "bolometric" model developed for disordered, thermal motions below threshold. As expected, relaxation below threshold is observed to depend on anharmonicity, indicating energy exchange between center-of-mass and internal motions. Above threshold, however, response to pulsed excitation is characterized by a rapid growth which is abruptly stopped and followed by slow relaxation to a lower, mean coherent oscillation with fluctuations. Furthermore, for our apparatus at $\sim 4K$, pulsed cyclotron excitation (with parametric drive switched off) indicates strong temperature dependence in equilibration process for internal motions, requiring a more complicated, generalized model at low temperatures.

These interesting observations in parametrically-pumped electron oscillators demonstrate the fine control over a wide range of system parameters which is available for precise, quantitative studies of fluctuation phenomena. A more detailed theoretical treatment of this system, hopefully, will give a better understanding of the observations and measurements presented, which may lead to new experiments.

Chapter 6

Conclusion

A new cylindrical Penning trap has been demonstrated to be a good approximation to an ideal microwave cavity. Anywhere from 1 to more than 10^5 electron oscillators can be isolated near the center of the trap cavity, localized in the simple standing wave patterns of the cavity modes. A single electron has been observed with good signal-to-noise ratio, demonstrating that precise measurements with one electron, such as measurements of the electron magnetic moment and of inhibited spontaneous emission, etc., can be performed in a cylindrical Penning trap, with the added advantages of a well-characterized microwave cavity.

Resonant cooling of electron oscillators by a cavity standing wave has made possible this first study of cooperative phenomena in parametrically-pumped electron oscillators. Phase bistable CM oscillations with long-term coherence emerge from weak, disordered fluctuations as the pump strength is increased through a sharp threshold, producing extraordinarily large coherent signals. Detailed experimental studies of the (h, ω_d) space of the parametric pump establish a hyperbolic region of instability, in which the quiescent state becomes unstable, with a threshold h_T which is proportional to the number of electrons and to the damping rate by the tuned circuit per electron. Analysis of a rigid model corroborates that this observed instability corresponds to the lowest order ($n = 1$) Mathieu instability in the presence of damping. Phase bistability and hysteresis are also observed and well approximated by an ordinary differential equation for rigid motions. Hys-

teresis in one parametrically-pumped electron oscillator may make it possible to detect relativistic cyclotron excitation [31] without perturbing the excitation during crucial stages.

A rigid model, however, is an oversimplification since internal motions and electron-cavity interaction are also important. Observed energy in the coherent CM motion is limited by cavity cooling of internal motions. For example, the slope of a linear lineshape (obtained when $|C_4|$ is large) increases as the internal motions are cooled. This extreme sensitivity to cavity cooling in partially synchronized motion provides a new technique for probing the radiation field modes of a Penning trap cavity, *in situ* at 4K, without a microwave drive. Measured eigenfrequencies agree well with those of an ideal cylindrical cavity. Interaction with a cavity standing wave is so well characterized that motional sidebands and splittings are observed in cavity mode resonances.

Furthermore, interesting fluctuation phenomena are observed in great detail. The center-of-mass of partially synchronized, parametric electron oscillators makes random transitions between degenerate phase states which differ by 180°, at a rate which increases with increasing internal energy. Detailed observations of phase jumps show a variety of "trajectories." A phase jump is often initiated by a collapse of one CM phase state to the "quiescent" state, followed by re-excitation to the other phase state. In some cases, increased fluctuation is observed as precursor to a phase jump. In a rare event, oscillations in the basins of attraction of the two phase states have also been seen.

Although some insight has been gained, many interesting questions remain to be explored. Are there other collective states which are excited by the parametric pump? Why does observed coherent CM motion above threshold saturate? Is there a simple explanation for the convergence of power in the peak and fluctuation pedestal of the response spectrum? Above threshold, how are the amplitude and phase fluctuations related, and how do they vary with system parameters? As shown in this work, simple notions of synchronization, a rigid model, and electron-cavity interaction have been useful but are inadequate for further investigation.

Unfortunately, a better treatment is not available. The underlying simplicity suggested by our observations of Lorentzian lineshapes of cavity mode resonances, an exponential distribution of residence times, etc. will hopefully prompt a detailed theoretical analysis of parametrically-pumped electron oscillators. Below threshold, perhaps a simple, generalized set of rate equations can be obtained for the energy transfer processes within the cryogenic micro-plasma [68,67].

As an initial application, partially synchronized electrons are used to identify the radiation modes of a trap cavity for the first time. A thousand-fold decrease in an electron's axial temperature now seems feasible, as does a new generation of electron magnetic moment measurements which avoid previous limitations from damping linewidth and cavity shifts of measured frequencies. Extraordinary control over a wide range of parameters in this well-characterized system provides an ideal environment for such precision measurements, and for new experiments in nonlinear dynamics with few electrons, cooperative behavior in increasingly larger systems, radiative effects due to strong coupling of many electrons localized within a fraction of a wavelength of a cavity standing wave, and fluctuation phenomena.

Appendix A

Self-shielding Superconducting Solenoids

For high precision experiments, fluctuations in the ambient magnetic field must be shielded out or otherwise compensated to obtain a region with a strong magnetic field which is stable in time. Flux conservation in superconducting circuits makes it is possible to design superconducting solenoid systems which produce large magnetic fields and also react to shield the high-field region from ambient fluctuations [33]. This may be realized in many specific solenoid geometries and circuit configurations; the choices depend upon the desired field properties for particular applications. Shielding the fluctuations in the ambient field is crucial for achieving the highest precision measurements. However, even for less precise experiments, good shielding makes it possible to make measurements much nearer to sources of fluctuating magnetic fields.

We have demonstrated that an extra superconducting coil added to a standard, 6 Tesla solenoid results in a self-shielding solenoid system which utilizes flux conservation to passively shield an interior volume from changes in the ambient field, such as those from solar activities and from neighboring MBTA (cambridge) subways, particle accelerators, or elevators [38]. Such self-shielding solenoids could be very useful for mass spectroscopy of trapped particles, nuclear magnetic resonance experiments and magnetic resonance imaging. As an example, an antiproton ICR measurement with a fractional accuracy of 4×10^{-8} was recently done in a 6 T

superconducting solenoid located near a large particle accelerator [36]. Without the shielding, the magnetic fluctuations in this environment would have limited the measurement accuracy to 1 ppm.

In this section, we discuss the general shielding principles and important considerations in the design and tests of self-shielding superconducting magnets. In the first trial, the large shielding factor of 156 for fluctuations of the uniform ambient magnetic field has been attained without compromising the spatial homogeneity of the field produced by the basic solenoid. Passive shielding using flux conservation applies in principle to external field fluctuations which are arbitrarily fast. High-field solenoids, however, are typically wound on copper or aluminum cylinders which readily support eddy currents, especially when cold. External field fluctuations more rapid than 1 Hz typically are already severely screened by the cylinder.

A.1 Ambient Fluctuations in the Magnetic Field

For precision mass spectroscopy, we are particularly concerned about spatially uniform fluctuations in the ambient field, the sources of which are frequently beyond the experimenter's control. For example, to compare the masses of a proton and antiproton to a desired precision of 1 part in 10^9 in a 6 Tesla magnet field requires a time stability better than 6 nT per hour. Unfortunately, depending upon location, variations of 10 nT (100 μG) to 100 nT (1 mG) are observed, and larger variations are possible during magnetic storms which are related to solar activity [75].These fluctuations limit the time stability which can be realized in a high field region, even though the high field solenoid system itself produces a more stable field. Fig.A.1 shows the typical situation in our laboratory as measured with a fluxgate magnetometer. During a window of a few hours at night (Fig.A.1a), when the MBTA (Cambridge) subway is not running, the fluctuations are of order 1 nT (100 μG) with occasional steps of order 60 nT (600 μG). By day (Fig.A.1b), much larger fluctuations up to 300 nT (3 mG) are typical. Simultaneous measurements

of the fluctuating ambient field, with probes separated by several meters, showed that the fluctuating ambient field is typically spatially uniform.

Many techniques are available for shielding out such fluctuations in the presence of small magnetic fields, but it is much more difficult to shield them out of a region of high magnetic field. One reason is that highly permeable materials like iron and "mu metal" are severely saturated and hence useless for shielding within the high-field region. Another is that shields made of type I superconducting materials like lead and niobium cannot be used because the large field is above the critical field for type I superconductors. Finally, a type II superconductor has been used to screen external fluctuations from a very small high-field region [24] , but there was trouble with flux jumps associated with the shield.

In typical NMR and ICR experiments, the superconducting solenoids do not and need not shield the components of the fluctuating, ambient field which are perpendicular to the strong field B_o. A fluctuating transverse field $B_\perp$ provides only a quadratic correction to the magnitude of the strong field:

$$B = B_o\sqrt{1+\left(\frac{B_\perp}{B_o}\right)^2} \tag{A.1}$$

Even an extremely large transverse field $B_\perp = 6\mu T$ (60 mG) thus results in an extremely small fractional change in the field, $\delta B/B < 10^{-14}$. Only the z-components of the magnetic field contributions are relevant if we choose the z-axis to coincide with the axis of symmetry of the solenoid system.

A.2 Single Superconducting Solenoid Circuit

We now present an alternative approach, whereby the geometry of the superconducting solenoids that produce the large magnetic field is chosen so that external fluctuations are canceled at the location of the experiment by extra currents induced in the solenoids. As is well known, magnetic flux through a closed superconducting circuit is conserved. We discuss how to configure coupled superconducting circuits so that this flux conservation insures that external field

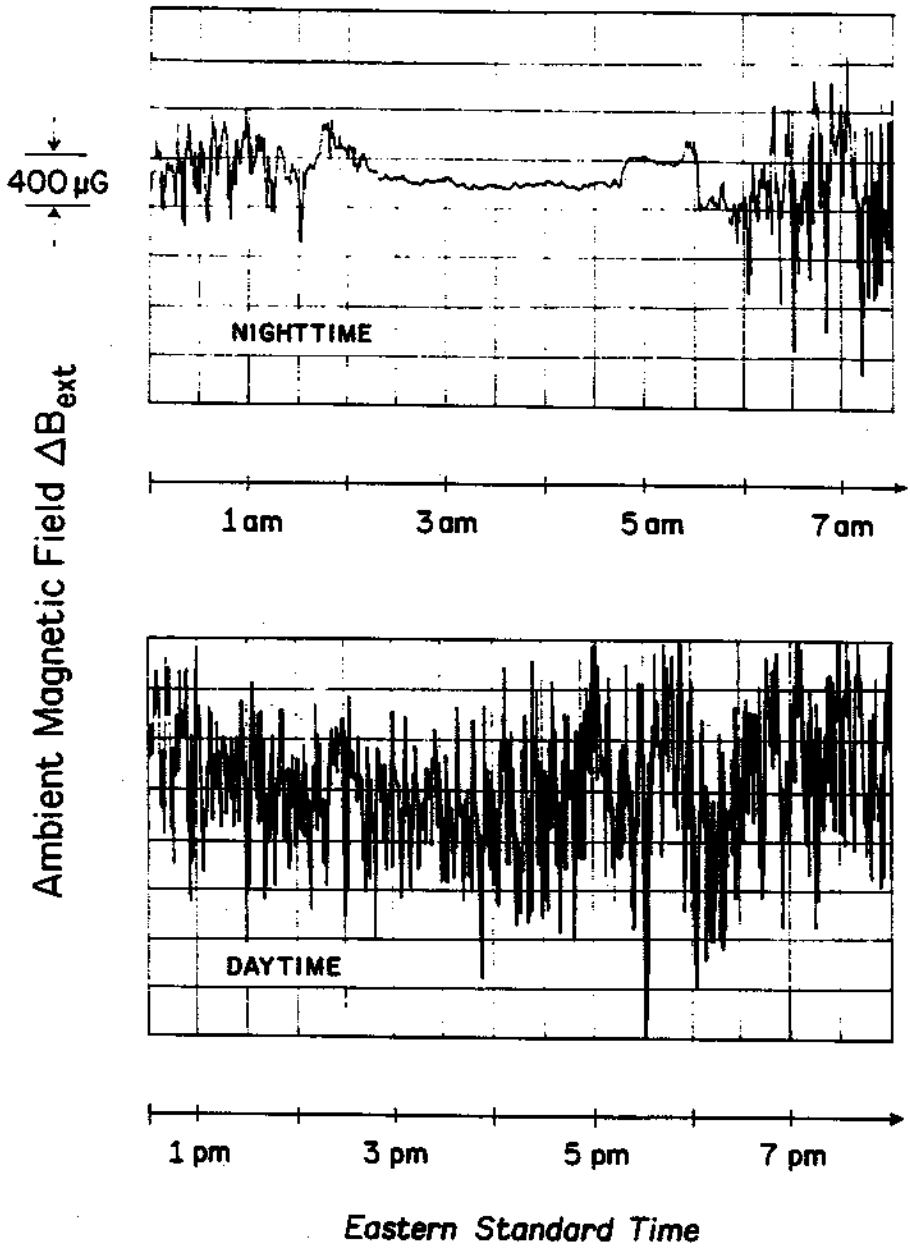

Figure A.1: Typical fluctuations in the magnetic field in our laboratory as measured using a fluxgate magnetometer and a detection bandwidth of 0.01 Hz. The quiet window during the night occurs when the MBTA (Cambridge) subway is shut down.

fluctuations are screened from a selected region of interest. For simplicity, the focus here is on superconducting circuits composed of solenoids which are axially symmetric about a z axis. The z component of the external field B_e is reduced by a shielding factor S to B_e/S and the objective is to make S as large as possible.

A self-shielding solenoid system (a system for which S is large) can be constructed using a wide variety of circuit configurations. Therefore, self-shielding systems can be designed to preserve a variety of other properties. For example, a high degree of spatial homogeneity is often also required in the high-field region in order that very narrow resonance linewidths can be obtained. Time stability is then required to allow measurement of the narrow lines, several hours being required for some mass spectroscopy experiments of interest. We thus choose our examples of self-shielding solenoid systems to suggest ways that these can be designed with minimal distortions of the field homogeneity. Real solenoid systems are more complicated than our examples, but may be analyzed in the same way.

To illustrate the basic shielding scheme, consider a single, axially symmetric solenoid i. The solenoid shown in Fig.A.2 is made of superconducting wire and its ends are connected to make a closed circuit. The potential difference around the shorted solenoid is zero. By Faraday's law, an externally applied field B_e induces a current I_i in the solenoid which in turn produces a magnetic field B_i sufficient to keep the flux through the solenoid from changing, ie.

$$\int_i [B_e + B_i] dA = 0. \tag{A.2}$$

We take the conserved value of the flux to be 0 so that we can focus on fluctuations from some steady state. The subscript on the integral indicates integration over the area of the solenoid. The induced current persists since the resistance around the superconducting circuit is zero.

In what follows, we shall use cylindrical coordinates ρ and z, so that $B_i = B_i(\rho, z)$, for example. The net field at the center of the solenoid $B_e(0,0) + B_i(0,0)$

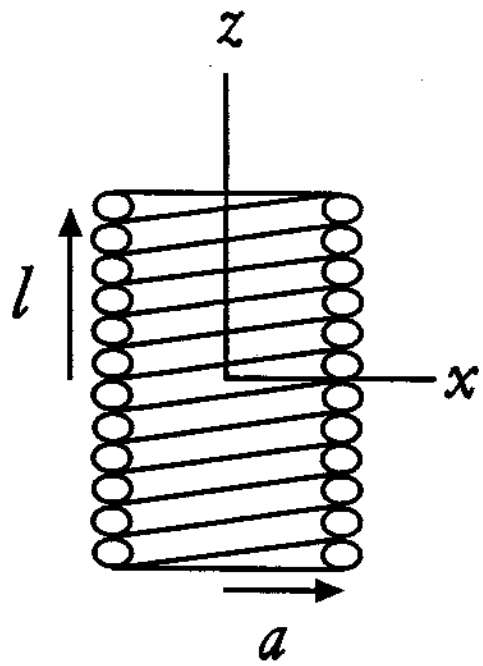

Figure A.2: Simple, single-layer solenoid.

can be written in terms of the shielding factor S as $B_e(0,0)/S$ so that

$$S^{-1} = 1 + \frac{B_i(0,0)}{B_e(0,0)}. \tag{A.3}$$

In light of the flux conservation criterion Eq.(A.2), this can be written

$$S^{-1} = 1 - \frac{\int_i B_e dA / B_e(0,0)}{\int_i B_i(\rho,z) dA / B_i(0,0)} \tag{A.4}$$

To aid intuitive interpretation, we note that S^{-1} is linear in the ratio of two averaged fields

$$S^{-1} = 1 - \frac{\overline{b_e}}{\overline{b_i}} \tag{A.5}$$

defined by

$$\overline{b_e} = \frac{\int_i B_e dA}{B_e(0,0) \int_i dA} \tag{A.6}$$

$$\overline{b_i} = \frac{\int_i B_i(\rho, z) dA}{B_i(0,0) \int_i dA}. \tag{A.7}$$

Here $\int_i dA$ is the total area involved in the flux integration for circuit i. Perfect shielding requires a solenoid for which the normalized average values of the external field and solenoid field are equal, $\overline{b_e} = \overline{b_i}$.

Without explicit calculation, one can immediately see that complete shielding of spatially uniform fields is possible with a single superconducting solenoid circuit, even if the solenoid has many layers of windings. For spatially uniform external field B_e we have $\overline{b_e} = 1$ and the shielding is given by

$$S^{-1} = 1 - \frac{1}{\overline{b_i}}. \tag{A.8}$$

For a short solenoid, the magnetic field near the windings is larger than the magnetic field near the center. The average value in the bore $\overline{b_i}$ is thus greater than 1 so that S^{-1} is positive. For a long solenoid, the volume average of the magnetic field produced by the solenoid within the bore is slightly less than the field at the center because of the fringing field at its ends. Thus, $\overline{b_i}$ increases to a value of 1 with increasing length. This corresponds to S^{-1} increasing to a limit of 0. Since S^{-1} must cross zero between these two limits, complete shielding is obtained with an appropriate choice of dimensions.

To facilitate explicit calculation, we eliminate the induced current from the expression for the shielding factor using factors g_i and L_{ii} which depend only upon the geometry of the solenoid circuit. The field at the center is proportional to the current

$$B_i(0,0) = g_i \, I_i, \tag{A.9}$$

as is the flux through the solenoid

$$\int_i B_i(\rho, z) dA = L_{ii} \, I_i. \tag{A.10}$$

The latter proportionality factor L_{ii} is the self-inductance for solenoid i. Substituting these two expressions in Eq. (A.4) yields

$$S^{-1} = 1 - \frac{g_i A_i}{L_{ii}}. \tag{A.11}$$

For a spatially uniform external field, A_i is the total area $\int_i dA$ used to calculate the flux through circuit i. More generally, A_i is an effective area

$$A_i = \frac{\int_i B_e dA}{B_e(0,0)}, \tag{A.12}$$

which depends on the spatial distribution of B_e.

In Fig. A.3 we plot S^{-1} as a function of the solenoid aspect ratio l/a for a single layer, densely wound solenoid. The necessary techniques for calculating inductances are well known [41] and efficient calculation techniques have been discussed [39]. The qualitative features discussed above are readily apparent. The self-shielding is complete (i.e. $S^{-1} = 0$) at the aspect ratio [13]

$$l/a = 0.88 \tag{A.13}$$

for a densely wound solenoid in the limiting case of vanishing wire diameter.

In general, the shielding produced by a persistent superconducting solenoid is far from complete. To illustrate, we use a solenoid represented in Fig. A.4, which is not unlike many high-field solenoids which are commercially available. The large solenoid is wound uniformly with n_1 turns and its dimensions and characteristics are given in Table A.1. This solenoid would produce a field of 6 T at its center for a reasonable current of approximately 40 A. By itself, we calculate that this solenoid will screen external field fluctuations by a factor of $S = -2.9$, which is typical for commercial superconducting solenoid systems. Improving the self-shielding requires more than a simple reshaping of the solenoid. A self-shielding solenoid of the same radial dimensions, for example, would be reduced in length by more than a factor of 9. Such a squat solenoid would have properties very different from the solenoid in Fig. A.4. More practical modifications involve two or more coupled superconducting circuits, which will be discussed next.

Dimensions	Calculated parameters
$a_1 = 7.62\ cm$	$L_1 = 232.3\ H$
$a_2 = 12.70\ cm$	$A_1 = 2219\ m^2$
$l_1 = 25.40\ cm$	$g_1 = 0.1469\ T/A$
$n_1 = 64000$	$S = -2.95$

Table A.1: Basic solenoid

A.3 Coupled Superconducting Circuits

Practical solenoid systems typically contain several circuits, one to produce the large field and the others as shims to make the field near the center as homogenous

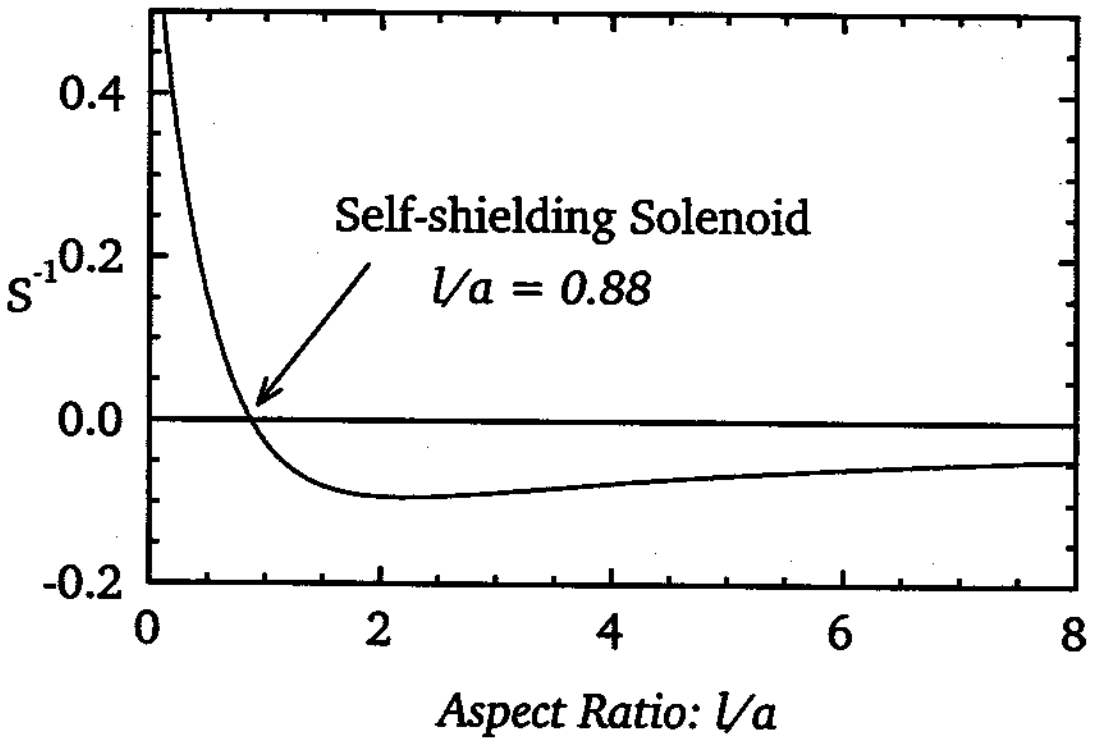

Figure A.3: Shielding of a densely would, single-layer solenoid as a function of its aspect ratio, the ratio of its half length l to its radius a.

as possible. We therefore generalize to a system of N closed superconducting circuits, each of which is axially symmetric. The subscript i now becomes an index $i = 1, ..., N$ which labels the N circuits. A current I_i in circuit i produces the field $B_i(\rho, z)$. The currents can be represented by a column vector **I** and a related column vector **g** relates the field at the center to the currents with components defined by

$$B_i(0,0) = g_i \; I_i. \tag{A.14}$$

The areas of the circuits are represented by column vector **A** with components

$$A_i = \int_i dA \tag{A.15}$$

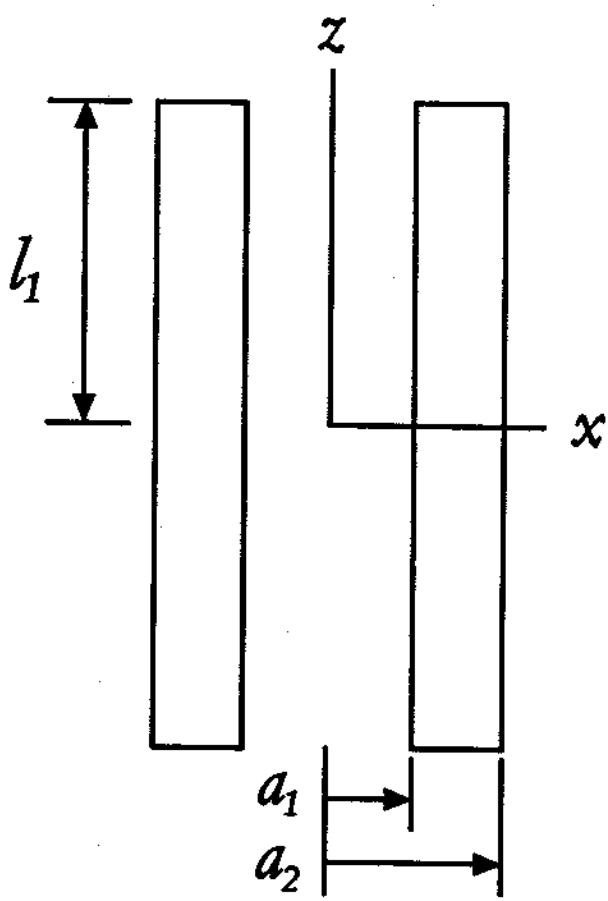

Figure A.4: Large solenoid to illustrate typical properties of high-field persistent solenoids.

which may be generalized for the case of non-uniform B_e as was done in Eq.(A.12). The familiar symmetric inductance matrix L has components given by

$$\int_i B_j(\rho, z) dA = L_{ij}\ I_j. \tag{A.16}$$

A diagonal element L_{ii} is the self-inductance associated with circuit i and off-diagonal elements are the mutual inductances between circuits. The shielding factor is

$$S^{-1} = 1 - \mathbf{g}^T \mathbf{L}^{-1} \mathbf{A}, \tag{A.17}$$

with the superscript T indicating transposition so that $\mathbf{g}^T$ is a row vector. For a single circuit Eq. (A.17) reduces immediately to Eq. (A.11). Complete shielding occurs when

$$\mathbf{g}^T \mathbf{L}^{-1} \mathbf{A} = 1. \tag{A.18}$$

This is the condition for a self-shielding solenoid system.

As an illustration, consider a system of 2 superconducting circuits. One solenoid circuit is characterized by L_1, A_1 and g_1 and the other by L_2, A_2 and g_2. The mutual inductance between the two circuits is M. One circuit could be a commercially constructed NMR solenoid to produce a $6T$ magnetic field, for example, and the other circuit could be a solenoid added to make a self-shielding system. From Eq. (A.17), the shielding factor is

$$S^{-1} = 1 - \left[\frac{g_1 A_1}{L_1} + \frac{g_2 A_2}{L_2} - \frac{M}{L_1 L_2}(g_2 A_1 + g_1 A_2)\right] \left[1 - \frac{M^2}{L_1 L_2}\right]^{-1}. \tag{A.19}$$

For $M \to 0$, comparison with Eq. (A.11) shows that each coil contributes independently to the shielding. In general, however, the mutual inductance significantly modifies the shielding.

Computing S^{-1} is rather involved and lengthy, even in this simple two-circuit system. Many of the needed quantities, however, can be measured. This may be useful when modifications or additions to commercially constructed solenoid systems are contemplated, since their internal designs are often difficult to obtain.

The self-inductance L_2 can be measured in conventional ways, most easily for a large solenoid by measuring the increase of current with time for an applied charging potential V_2

$$V_2 = -L_2 \frac{dI_2}{dt}. \tag{A.20}$$

For two coupled superconducting circuits, the mutual inductance can be measured by introducing a current I_1 in circuit 1. A current I_2 is induced in the second circuit to conserve flux through circuit 2. Thus M may be determined from

$$MI_1 + L_2 I_2 = 0 \tag{A.21}$$

when L_2 is already known. Circuit areas A_1 and A_2 can be determined by measuring the shielding factor S for each coil individually.

Finally, we note that this approach is related to a technique wherein two concentric, coplanar superconducting loops were used to make a tunable gradient in a large magnetic field. [86] The two loops were connected in series such that the current flowed in the same direction. The radii of the loops were chosen to minimize the shift of the magnetic field at the center of the loops which occured when the gradient was tuned. Accordingly, external field fluctuations were expected to cancel by perhaps a factor of 10 at the center of the loops, albeit at the expense of changing the field gradient. This configuration is not generally useful for shielding because of the gradients introduced. Still, it could be analyzed by treating each loop as a "solenoid", with the two loops connected in series to form a circuit. A complete analysis would also include the mutual inductances between these loops and the superconducting solenoid used to produce the large magnetic field being stabilized.

A.4 Commercial Solenoid Circuits

In practical solenoid systems, the closed superconducting circuits are generally composed of individual solenoids connected in series. It is convenient to relate

the column vectors $\mathbf{g}$ and $\mathbf{A}$ and the inductance matrix $\mathbf{L}$ for the circuits to the analogous quantities for the solenoids $\tilde{\mathbf{g}}$, $\tilde{\mathbf{A}}$ and $\tilde{\mathbf{L}}$. We define the $N \times \tilde{N}$ matrix $\mathbf{\Omega}$ such that the currents in the solenoids $\tilde{\mathbf{I}}$ are given by

$$\tilde{\mathbf{I}}^T = \mathbf{I}^T \mathbf{\Omega}. \tag{A.22}$$

For N circuits there are $\tilde{N}$ solenoids with $\tilde{N} \geq N$ since at least one solenoid is in given circuit. In simple cases wherein solenoids are connected in series with their currents flowing in the same rotational sense about the z axis, we have $\Omega_{ik} = 1$ if circuit i includes solenoid k and $\Omega_{ik} = 0$ otherwise. Negative elements may be used to represent currents flowing with opposite helicity with respect to the z axis. The transformation rules are

$$\mathbf{g} = \mathbf{\Omega} \tilde{\mathbf{g}}, \tag{A.23}$$

$$\mathbf{A} = \mathbf{\Omega} \tilde{\mathbf{A}}, \tag{A.24}$$

and

$$\mathbf{L} = \mathbf{\Omega} \tilde{\mathbf{L}} \mathbf{\Omega}^T. \tag{A.25}$$

We have found that it is convenient to set up the computation in terms of the solenoid quantities, since each solenoid typically has a different geometry, and then carry out the contractions as above using $\mathbf{\Omega}$ to get the circuit parameters needed to evaluate the screening.

Simple geometries and dimensions which seemed theoretically promising were described in [33]. However, high-field NMR solenoids with state-of-the-art spatial homogeneity are generally constructed commercially, with complicated geometries which vary from manufacturer to manufacturer. We have analyzed in detail a commercial NMR solenoid system (Nalorac 6.0/100/118) which involves 2 superconducting circuits with several solenoids making up each circuit. For the first trial, Nalorac Cryogenics provided us with the (proprietary) internal dimensions

of their standard, high-homogeneity solenoid made for NMR applications. This system has a calculated shielding factor of

$$S = -4.45 \pm 0.10 \tag{A.26}$$

which agrees with the measured value. Other calculated properties of this system are given in Table A.2. (This comparison is discussed further towards the end of

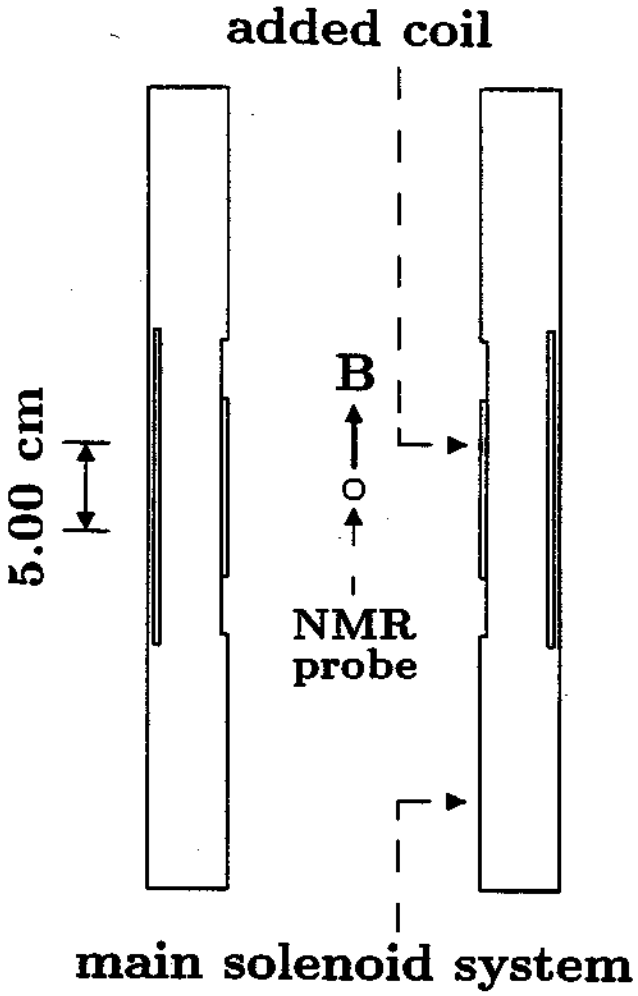

Figure A.5: Cross section of the windings of the high-field solenoid which produces a vertical magnetic field. The innermost solenoid was added to make the solenoid system cancel external fluctuations.

the next section.) The uncertainty reflects some imprecision in our knowledge of the location of the windings and inaccuracy in our inductance calculation. Our detailed calculations for finding a practical geometry which satisfies the shielding condition in Eq.(A.18) indicated that a small, persistent, interior solenoid could be added to make a solenoid system which cancels external fluctuations. No other modification of the standard system was needed to preserve the high degree of spatial homogeneity ($\delta B/B < 10^{-8}$ over a sphere 1 cm in diameter). A cross section of the solenoid and the added interior coil (to scale) is shown in Fig. A.5. The strong field produced within the solenoid is along the symmetry axis of the solenoid. The large outer coil produces the large magnetic field and contains shaped correction coils to obtain a high degree of spatial homogeneity. Without the added interior solenoid, this cross section is typical of a high-field NMR solenoid. The inductance matrix for this system is calculated to be

$$\mathbf{L} = \begin{pmatrix} 0.1310 & 0.2508 & 2.3434 \\ 0.2508 & 2.4161 & 16.1924 \\ 2.3434 & 16.1924 & 173.4107 \end{pmatrix} \text{ H} , \qquad \text{(A.27)}$$

where the smallest diagonal element is the inductance of the added interior solenoid and the remaining diagonal elements are the inductances of the two solenoids forming the standard system. Table A.3 includes other calculated properties of the first system designed and constructed to be self-shielding.

A.5 Measured Shielding

To measure the shielding, we insert an NMR probe with an acetone sample into the high-field region. The sample is a sphere with a diameter of 1 cm. We apply an external magnetic field to the solenoid using large square Helmholtz coils,which are 2.81 m on a side and are separated by 1.53 m. These coils produce a magnetic field which varies over the solenoid by less than 0.3 % .

By opening the circuit of the inner shielding coil, we measure a shielding which is typical of a high-homogeneity, high-field NMR solenoid. Fig. A.6a shows the

Parameter	Value	Unit
A_1	135.88	m^2
A_2	1662.01	m^2
L_1	2.386	H
L_2	177.5	H
M	16.25	H
$L = L_1 + L_2 + 2M$	212 H	H
g_1	14.483	mT/A
g_2	134.910	mT/A
$(e/m)(g_1 + g_2)/2\pi$	4.182(3)	GHz/A
S	-4.45 ± 0.10	—

Table A.2: Calculated properties of a Nalorac superconductive magnet (JOB43).

Parameter	Value	Unit
A_s	17.53	m^2
A_1	136.72	m^2
A_2	1644.02	m^2
L_1	2.416	H
L_2	173.4	H
M	16.19	H
$L = L_1 + L_2 + 2M$	208 H	H
g_s	7.231	mT/A
g_1	14.565	mT/A
g_2	133.109	mT/A
$(e/m)(g_1 + g_2)/2\pi$	4.134(3)	GHz/A

Table A.3: Calculated properties of a new Nalorac superconductive magnet designed to be self-shielding (JOB51). Subscript s indicates the added interior solenoid.

field change within the central volume of the solenoid (from the measured shift in NMR frequency) as a function of the external field applied with the Helmholtz coils. The measured shielding factor is

$$S = -4.27 \pm 0.07 \quad . \tag{A.28}$$

This means that external field fluctuations are reduced by this factor, and we expect that this number is rather typical of high-field solenoids of reasonable geometry since it is rather insensitive to the details of the geometry. The negative sign is also typical. It indicates that the solenoid overcompensates the external fluctuation, so that the fluctuation experienced in the center region is actually oppositely directed to the applied external field. The measured value compares well with the calculated value $S = -4.5 \pm 0.1$ given above.

When the inner solenoid is allowed to go persistent, the shielding improves dramatically, as indicated in Fig.A.6b. The measured shielding factor is

$$S = -156 \pm 6 \quad . \tag{A.29}$$

We interpret this as the shielding for a spatially uniform field, after increasing the uncertainty from 3 (the measurement precision) to 6 to include effects of possible inhomogeneities in our applied field. We observe the same linewidth in the NMR signal with the shielding coil as without, indicating that the spatial homogeneity is not compromised over the 1 cm diameter of the spherical NMR probe.

A.6 Field Homogeneity of Shielded Region

It is extremely important that modifications to make a high-homogeneity solenoid system self-shielding do not spoil the spatial homogeneity. Fortunately, the condition for a self-shielding system in Eq. (A.18) allows for many possible self-shielding configurations. The approach taken in Fig.A.5 has minimal effect on field homogeneity. The basic solenoid, optimized to provide the desired level of homogeneity,

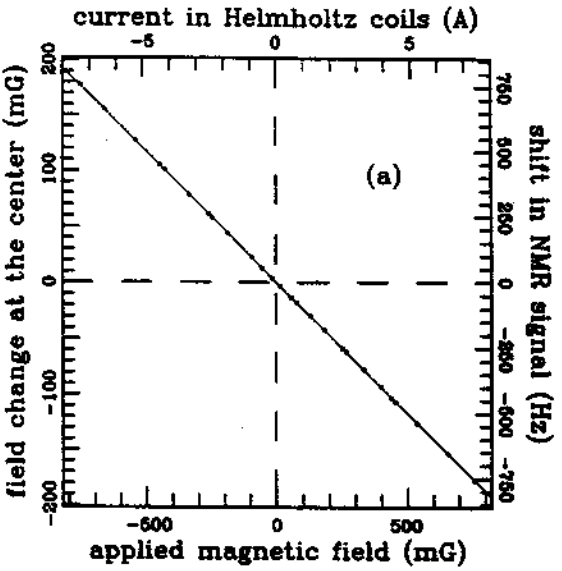

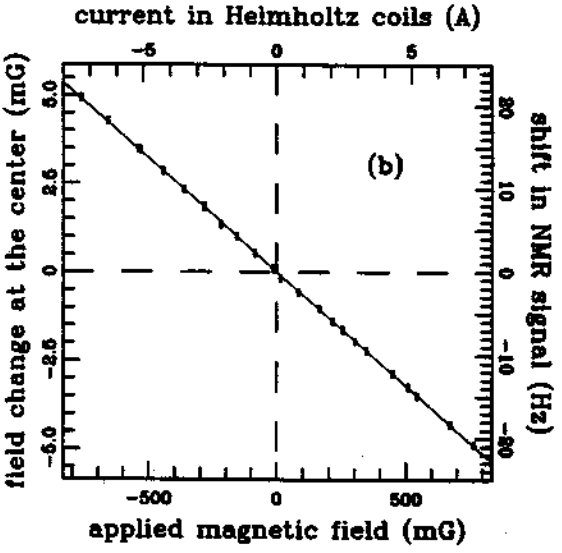

Figure A.6: Change in the magnetic field measured within the solenoid (deduced from the change in NMR frequency of an acetone sample) as a function of the external magnetic field applied over the solenoid, without (a) and with (b) the added inner solenoid.

is left unchanged. A separate additional solenoid is added which would carry no current if the ambient field was stable. Since it only carries the very small current required to cancel out the changes in the external field, it produces only a small field gradient. Suppose, for example, that fluctuations of the ambient field B_e as large as 6 μT are encountered. This means that the added solenoid at most must produce a field which is 10^{-6} of the 6 T field produced by the system used for mass spectroscopy. The fractional homogeneity requirement on the center solenoid is thus reduced by this factor. For the inner solenoid in Fig.A.5, the field at a distance d from the center varies from the field at the center by $(d/l)^2$ which is approximately 10^{-2} so that a homogeneity of 10^{-8} over a sphere 1 cm in diameter would not be compromised by the addition of such a coil.

A.7 Shielding for Nonhomogeneous Fields

Spatial homogeneity of applied field is important in measuring shielding factors. Larger than expected shielding factors were obtained by applying an external field using a single loop around the solenoid, for example, or using Helmholtz coils which are too small (Fig. A.7). An early measurement used a pair of square coils (side length of 2m) to apply an external magnetic field to an unmodified, Nalorac solenoid system. Although the coils were separated by 2 meters, we calculated that the spatial inhomogeneity in the applied external field over the volume of the solenoid system reduces the shielding from $S = -4.45$ in Eq. (A.26) to $S = -4.10$ which is what agrees with our measurements. To calculate the modified shielding factors, the generalized definition of effective areas in Eq. (A.12) must be used, taking B_e to be the nonuniform field of the external coils.

Field fluctuations due to distant sources typically are spatially uniform. The system which has been tested was specifically designed to shield out fluctuating fields which are spatially uniform. There are cases, however, wherein the high-field region can be shielded from nonhomogeneous ambient fluctuations. For example,

a linear gradient in the applied field averages to zero over the solenoid, making no contribution to $\overline{b}_e$ and to the shielding factor. As another example, the highest magnetic fields are produced using multi-strand superconducting wire. Solenoids so constructed often are not completely persistent but have a field which decays in time very slowly. If the spatial distribution of this decaying field is known near the center, it may be taken as B_e and used to calculate the effective area of a small, single-strand superconducting coil located near the center. The dimensions of this interior coil is then suitably chosen to compensate the drift in the field.

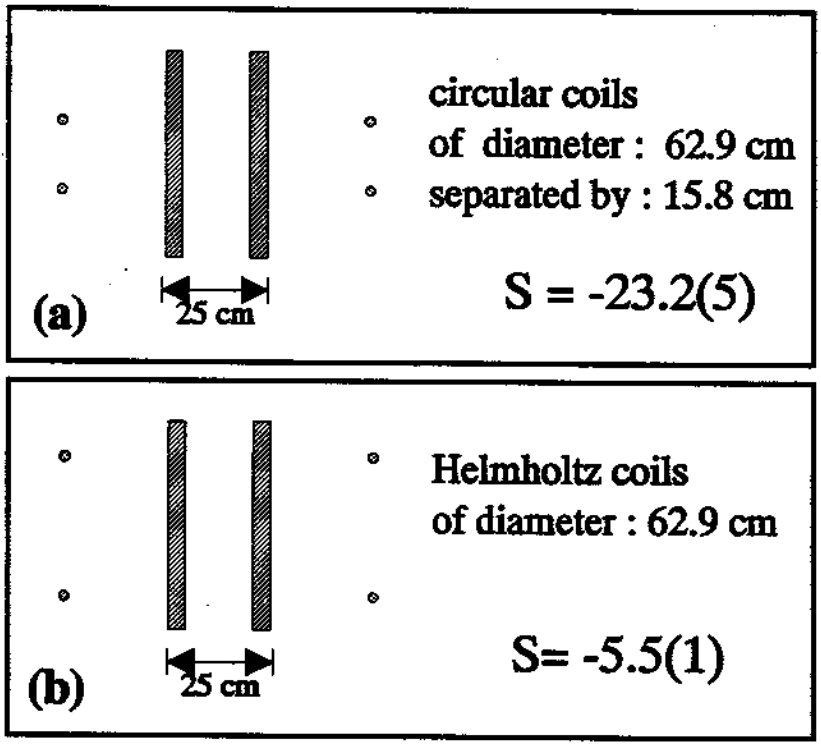

Figure A.7: Examples of larger than expected shielding factors due to gradients in the applied magnetic field.

Nearby magnetic materials distort the fluctuating ambient (otherwise uniform) field and significantly modify the shielding. For example, steel reinforcements in concrete blocks located beside the solenoid at CERN distort the fluctuating field from the nearby storage rings. For the CERN PS, we observe a shielding factor of $S = -100$. The field from the closer LEAR magnets is shielded by a factor of $S = -50$. These shielding factors are significantly lower than the shielding factor of $S = -156$ observed for uniform magnetic fields, but are still large reductions in the fluctuations of the magnetic field in the volume within the solenoid where experiments are located.

Appendix B

Linear Coupled Oscillators with Thermal Noise

Trapped electrons are coupled to a tuned circuit for detection and eventually come into equilibrium with it. The trap electrodes and tuned circuit are in thermal contact with a LHe bath. Thermal motions are observable even near 4 K. For example, the precision of the measured magnetic moment of the electron using a magnetic"bottle" [83] may ultimately be limited by the substantial linewidth broadening caused by the thermal axial motion of an electron in the magnetic field gradient, unless a variable bottle [86] can be used. The thermal motion of an electron oscillator has been thoroughly analyzed [7,10]. In this section, we describe the Johnson noise in the tuned circuit and a square-law detection technique [18,93] used in observing thermal agitations. Some interesting and useful features arising from the interaction between the tuned circuit and trapped electrons are discussed. A simplified explanation is provided for heat transfer in an electron/ion cloud which are sufficiently gradual (quasi-static). Finally, the basic features of a "bolometric" model [18,93] of disordered motions in trapped electrons/ions are summarized.

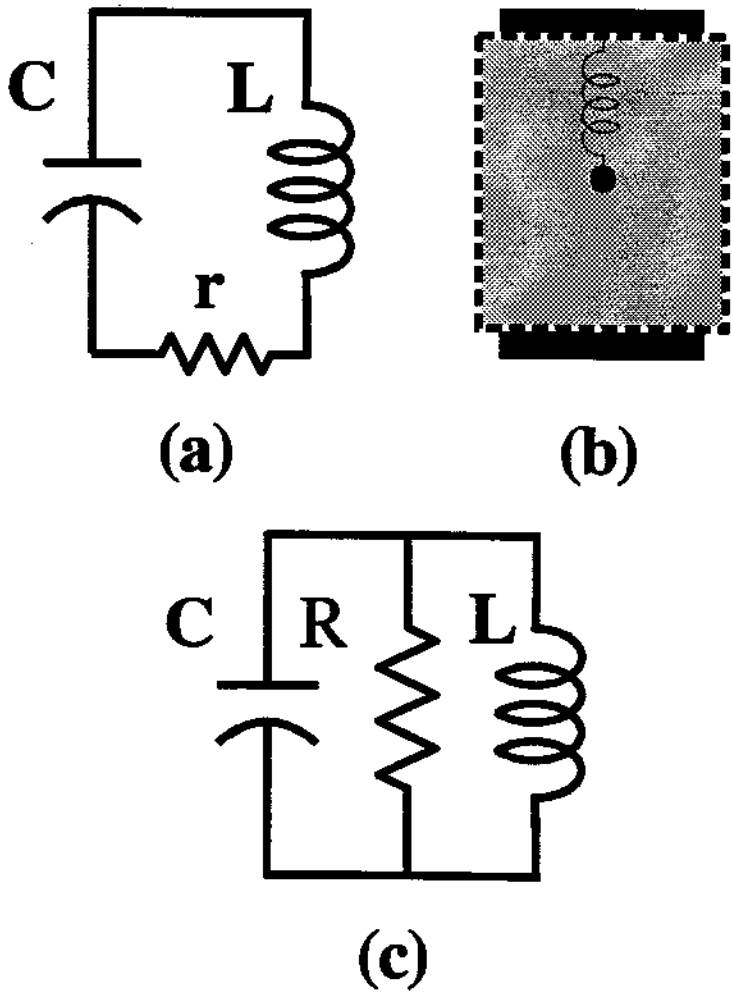

Figure B.1: Harmonic oscillators: (a) series LCr network, (b) damped, ideal spring-mass system, (c) parallel LCR network .

B.1 Detection Circuit: Harmonic Oscillator

The simplest representation of the detection circuit is a series LCr network (represented in Fig. B.1a, where L is the inductance of the helical resonator, C is the trap capacitance, and r represents radio frequency losses in the circuit).

This network is exactly analogous to a damped, harmonic oscillator illustrated in Fig. B.1b consisting of a mass attached to an ideal, massless spring surrounded by a viscous medium. The observed signal is derived from the voltage across the inductor $V_L = L\dot{I}(t)$ where $I(t) = \dot{Q}(t)$ is the current through the inductor. Since thermal agitations produce $\langle V_L(t) \rangle = 0$, only the mean squared value is measured. (The symbol $\langle ... \rangle$ denotes ensemble average.) The mean squared fluctuation in a small frequency bandwidth $\Delta\omega$ can be measured using a square-law detection technique (Fig. 2.15). The theory of square-law detection is briefly discussed in this section.

The voltage across the inductor is amplified, filtered and squared to produce a signal proportional to mean noise power. The signal is obtained by the sum of Fourier amplitudes in the bandpass $[\omega - \Delta\omega/2, \omega + \Delta\omega/2]$of the filter

$$S_N = \int_{-\infty}^{+\infty} dt F(t) V_L(t) \tag{B.1}$$

where the function $F(t)$ which restricts the observation bandwidth,$\Delta\omega$, is given by [10]

$$F(t) = 2 \int_{-\Delta\omega/2}^{+\Delta\omega/2} \frac{d\omega'}{2\pi} cos\left[(\omega_F + \omega')t - \phi\right]. \tag{B.2}$$

The phase ϕ is adjusted by a phase-shifter. Observed output of squarer is proportional to

$$\langle S_N^2 \rangle = \int_{-\infty}^{+\infty} dt_1 \int_{-\infty}^{+\infty} dt_2 F(t_1) F(t_2) \langle V_L(t_1) V_L(t_2) \rangle \ . \tag{B.3}$$

The correlation function for $V_L(t)$ is related to the impedance $\underline{Z}(\omega)$ of the network by [90]

$$\langle V_L(t_1) V_L(t_2) \rangle = 2k_B T r \int_{-\infty}^{+\infty} \frac{d\omega}{2\pi} (\omega L)^2 \left[\underline{Z}^{-1}(\omega) \underline{Z}^{-1}(-\omega)\right] e^{i\omega(t_2 - t_1)} \ . \tag{B.4}$$

For a series LCr network (e.g., Fig. B.1a), the circuit impedance is given by

$$\underline{Z}(\omega) = r + i\omega L + 1/(i\omega C). \tag{B.5}$$

Hence, in the limit of narrow observation bandwidth $\Delta\omega \ll r/L$, we get the familiar result for Johnson noise

$$\langle S_0^2 \rangle = 4k_B T_r \left[\frac{\Delta\omega}{2\pi}\right] R(\omega) \tag{B.6}$$

where the effective resistance $R(\omega)$ is given by

$$R(\omega) = \left[\frac{L}{rC}\right] \frac{\left(\frac{1}{2}\Gamma_M\right)^2}{(\omega_M - \omega)^2 + \left(\frac{1}{2}\Gamma_M\right)^2} \quad . \tag{B.7}$$

The subscript 0 in (S_0^2) indicates that there are no trapped particles. Observed noise power is maximum when the bandpass filter is centered at the resonance frequency ω_M of the tuned circuit. A "noise resonance" is obtained by sweeping the bandpass center frequency, producing a Lorentzian lineshape with resonant frequency $\omega_M = 1/\sqrt{LC}$ and a full width at half-maximum of $\Gamma_M = r/L$. Observed noise-driven resonance for our apparatus is shown in Fig. B.2a, when the trap is empty.

A helical resonator has often been represented by a parallel LCR network shown in Fig.(B.1c) in earlier works [93]. In practice, because the quality factor is fairly high ($Q > 600$), the difference between these two representations is negligible (of order $1/Q$) provided the resistances r and R are related by

$$R = \frac{L}{rC} \quad . \tag{B.8}$$

While the parallel LCR representation is very convenient when $\omega^2 \simeq 1/(LC)$, the series LCr circuit more readily provides a detailed study in general, particularly when the circuit is coupled to trapped particles.

B.2 Coupled oscillators

An electron bound in the trap interacts with the tuned circuit. For a pure electrostatic quadrupole potential, the axial motion of an electron is represented by a spring oscillator. Fig. B.3 illustrates the coupling of the tuned circuit to a trapped electron. In general, the electron may be surrounded by a fluid medium consisting of background gas (e.g., in a poor vacuum) or consisting of simultaneously trapped ions.

The coupling between an electron and the tuned circuit is described by the interaction potential

$$V_{int} = \left[\frac{\kappa q}{dC}\right] ZQ \tag{B.9}$$

where $Z(t)$ is the displacement from the trap center along the symmetry axis and $Q(t)$ is the charge accumulated in the capacitor. The dimensionless geometric

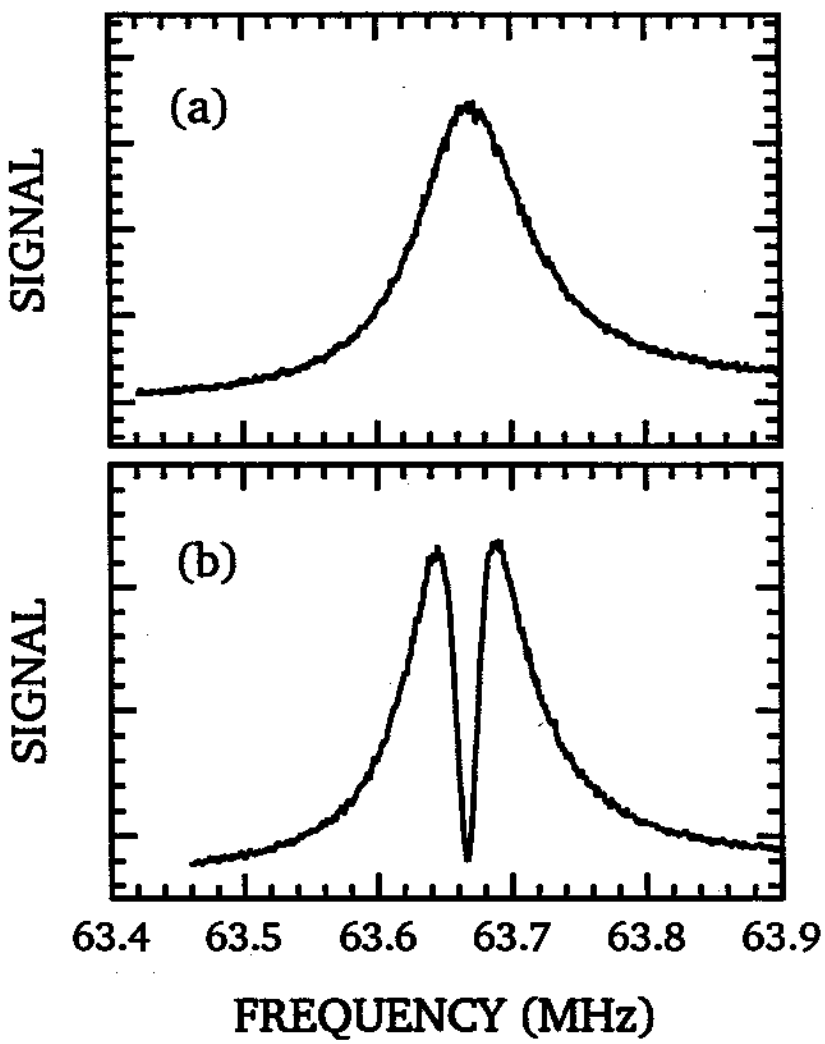

Figure B.2: Observed "noise resonance" of the tuned circuit obtained by sweeping the center frequency of bandpass filter (a) when the trap is empty and (b) when the trap has a small electron cloud with the same resonant frequency.

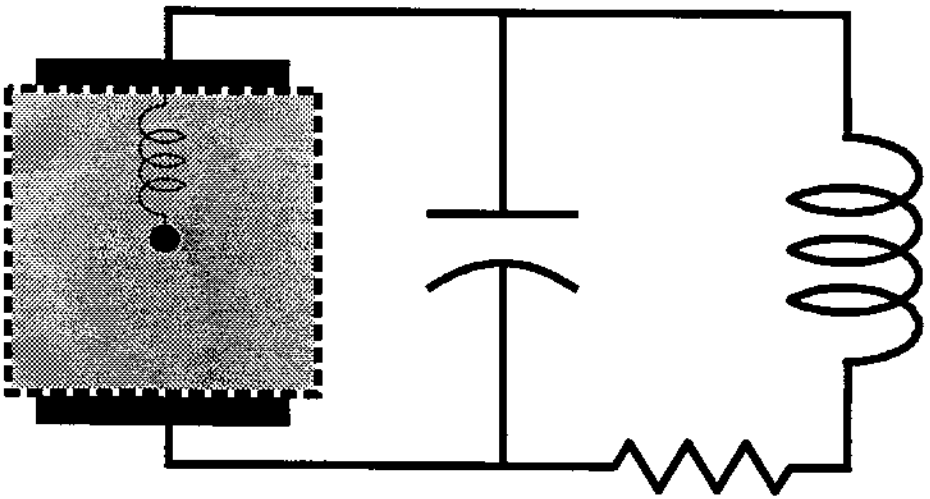

Figure B.3: Simplified representation of a tuned circuit coupled to an charged particle oscillating in a background gas.

factor κ is equal to 1 for an infinite parallel plate capacitor. Thus, the Langevin equations for the coupled oscillators are

$$\begin{aligned} L\left[\frac{d^2}{dt^2}+\Gamma_M\frac{d}{dt}+\omega_M^2\right]Q(t)+\left[\frac{\kappa q}{dC}\right]Z(t) &= V(t), \\ m\left[\frac{d^2}{dt^2}+\gamma_{col}\frac{d}{dt}+\omega_o^2\right]Z(t)+\left[\frac{\kappa q}{dC}\right]Q(t) &= F(t), \end{aligned} \tag{B.10}$$

which appear similar to Eq. (2.39) and Eq.(2.40) except that the "Langevin forces" on the right hand side (and hence $Z(t)$ and $Q(t)$ as well) are stochastic processes. These random forces have Gaussian distributions with $\langle F(t)\rangle = \langle V(t)\rangle = 0$ and are characterized by the correlation functions:

$$\begin{aligned} \langle V(t)F(t')\rangle &= 0, \\ \langle F(t)F(t')\rangle &= 2k_BT_G(m\gamma_{col})\delta(t-t'), \end{aligned}$$

$$\langle V(t)V(t')\rangle \;=\; 2k_BT_r(L\Gamma_M)\delta(t-t'). \tag{B.11}$$

They are uncorrelated, "white" noise sources. In this section, we examine the characteristic features of the observed signal when the system of coupled oscillators is driven by white noise.

Consider first the case of an electron harmonically bound in an ultra-high vacuum envelope held at temperature T. In this case, collisions with background gas is completely negligible, so that $\gamma_{col} = 0$. The output of the squarer given by Eq.(B.6) must be modified to read

$$\langle S_N^2\rangle = \langle S_0^2\rangle \frac{(\omega_z^2-\omega^2)^2}{((\tilde{\omega}_z)^2-\omega^2)^2+(\omega\gamma_z)^2} \tag{B.12}$$

where the $\tilde{\omega}_z$ is the shifted resonant frequency of the electron oscillator and γ_z is its damping rate due to coupling with the circuit , given by Eq.(2.49). The damping and frequency shift caused by the tuned circuit are discussed in Sec. 4, where they are shown to depend in a simple way on the detuning from the tuned circuit.

Features due to this coupling are more easily observed with many electrons since the center-of-mass (CM) motion is also coupled to the tuned circuit in the same way. The description given above remains valid for N electrons suspended near the trap center, provided $q \longrightarrow Nq$, $m \longrightarrow Nm$, and $Z(t)$ becomes the CM coordinate. Illustrative cases calculated from Eq.(B.12) are shown in Fig. B.4.

If the resonant frequencies of the spring oscillator and LCr circuit are tuned to the same value $\omega_z = \omega_M$, a "dip" appears at the center of the signal. An example of observed dip in the noise resonance of the tuned circuit due to trapped electrons is shown in Fig. B.2b. For small number of electrons, $N\gamma_z \ll \Gamma_M$, the signal in a small frequency range about ω_z simplifies to read

$$\langle S_N^2\rangle = 4k_BTR\left(\frac{\Delta\omega}{2\pi}\right)\left[1-\frac{(\Gamma_o/2)^2}{(\omega_z-\omega)^2+(\Gamma_o/2)^2}\right] \quad . \tag{B.13}$$

Thus, the electrons produce an inverted Lorentzian with linewidth $\Gamma_o \equiv \Gamma_z(0) = N\gamma_{zo}$ (i.e., N times wider than the maximum linewidth of one electron). The signal

is "shorted out" at the resonant frequency as shown in Fig.(B.4b). For large N, the signal maxima $\langle S_N^2 \rangle_{max}$ occur at frequencies

$$\omega^{\pm} = \omega_M \pm \frac{1}{2}\sqrt{\Gamma_M \Gamma_o} \quad , \tag{B.14}$$

which are separated by the geometric mean of the widths Γ_o and Γ_M, as can be easily shown by demanding the derivative of Eq.(B.12) with respect to ω to be equal to zero. Thus, $\Gamma_o = (\omega^+ - \omega^-)^2)/\Gamma_M$ can be used to determine N for large systems.

In general, the observed signal is "shorted out" at the unperturbed resonant frequency of the particle oscillator ω_z even when $\omega_z \neq \omega_M$. This feature could be useful for high precision mass spectroscopy which compares ions of nearly the same mass (such as protons and antiprotons) without being limited by shifts caused by the detection circuit. It should be noted that the sharp peak near the ω_z has its maximum slightly farther away from the tuned circuit resonant frequency than $\tilde{\omega}_z$. In the narrowband limit, this maximum occurs at

$$\omega_{max} = \tilde{\omega}_z + \frac{N\gamma_z}{2}\left[\frac{\Gamma_M/2}{\omega_z - \omega_M}\right] \quad . \tag{B.15}$$

The order in the frequencies is given by

$$\begin{aligned} &\omega_M < \omega_z < \tilde{\omega}_z < \omega^+ \quad for \quad \omega_z > \omega_M \quad , \\ &\omega^- < \tilde{\omega}_z < \omega_z < \omega_M \quad for \quad \omega_M > \omega_z \quad , \end{aligned} \tag{B.16}$$

as illustrated in Fig. B.4c.

B.3 Electron Cooling of Trapped Antiprotons

Fig. B.3 provides a simple model for the process of cooling antiprotons captured in a Penning trap using simultaneously trapped electrons sharing the same trapping volume. [35] Consider one electron trapped together with a hot cloud of anti-protons. If spontaneous emission is completely suppressed, then the electron couples only to the LCr circuit connected to the trap electrodes. Without

the tuned circuit, the electron comes into equilibrium with the antiproton gas at temperature T_G and undergoes brownian motion. When the tuned circuit is connected to the electrodes, the electron couples and transfers energy to the tuned circuit which dissipates the energy in the resistor. This process gradually cools the antiproton gas surrounding the electron.

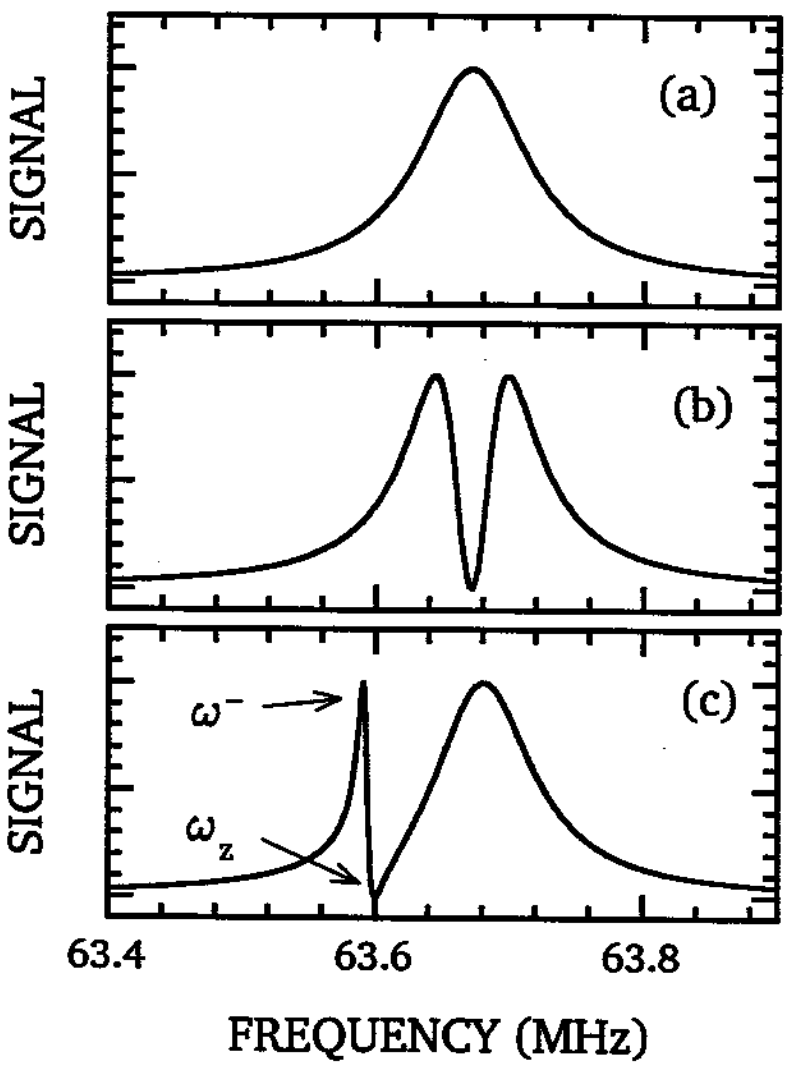

Figure B.4: Calculated noise power from tuned circuit coupled to (a) no electron, (b) small electron cloud at $\omega_z = \omega_M$, and (c) small electron cloud at $\omega_z > \omega_M$

The rate of cooling is equal to the power dissipated in the resistor. If the process is quasi-static, then we can write

$$C_G \frac{d}{dt} T_G = -\langle \dot{Q}(t)^2 \rangle r, \tag{B.17}$$

where C_G is the heat capacity of the gas. Joule heating (right hand side) can be calculated from the fluctuating current in the tuned circuit induced by the Brownian motion of the electron oscillator (which is driven by the heat bath of antiprotons). This has a simple form when $\gamma_{col} + \gamma_z \ll \Gamma_M$:

$$\langle \dot{Q}(t)^2 \rangle r = \left(\frac{\gamma_{col}\gamma_z}{\gamma_{col} + \gamma_z} \right) k_B T_G \ , \tag{B.18}$$

where γ_z is the decay rate of electron oscillation due to the tuned circuit. At sufficiently high temperature, the heat capacity C_G is independent of temperature. Hence, the temperature of the antiprotons gas drop exponentially with a damping constant τ given by

$$\frac{1}{\tau} = \frac{k_B}{C_G} \left(\frac{\gamma_{col}\gamma_z}{\gamma_{col} + \gamma_z} \right). \tag{B.19}$$

Typically,the damping rate γ_z of an electron by a tuned circuit is sufficiently fast near resonance, and hence the cooling rate of the antiprotons is essentially determined by the collision constant γ_{col} and the heat capacity. That is, for $\Gamma_M \gg \gamma_z \gg \gamma_{col}$, the cooling rate is $\tau^{-1} = \gamma_{col}(k_B/C_G)$. If now we sweep the cyclotron frequency into resonance with a cavity mode, then a factor of 2 in cooling rate is gained from synchrotron radiation provided energy transfer to the electron cyclotron motion has the same time constant. On the other hand, unavoidable anharmonicity in real Penning traps makes large axial motions very anharmonic. This would cause the electron oscillator to be greatly detuned from the cold, LCr circuit so that $\gamma_z \ll \gamma_{col}$, thus making the cooling process much less efficient. Since the heat capacity is proportional to the number of gas particles, a large number of electrons is necessary to get useful cooling rates.

This description of electron cooling of trapped antiprotons , although qualitatively useful, is oversimplified in some important aspects. For example, the equilibration time constant between electrons and anti-protons is a function of tempera-

ture and density. Furthermore, the heat capacity of a cloud of harmonically-bound antiprotons is different from that of a gas. Careful consideration of such issues is given in Ref. [72].

B.4 Bolometric model

In addition to the coupling between CM motion and tuned circuit, an electron cloud has many internal degrees of freedom which can be heated separately with an RF or microwave drive. The electron cloud gyrates in the strong magnetic field of the Penning trap and thus can radiate via cavity modes which couple to the cyclotron motion, just as the axial CM motion is damped by the tuned circuit. A full description of the dynamics is difficult. The problem is significantly simplified if the disordered, internal motions of a given type (e.g., axial oscillations) form a thermal reservoir characterized by a temperature. A "bolometric" model [18,93] of trapped electrons/ions has been developed which essentially focuses on the temperatures of such reservoirs. To illustrate the main features of the bolometric model, we first consider a simple example, which can be generalized.

The simplified system is made up of only the axial motions of the electrons ($B \rightarrow \infty$ limit). For a pure electrostatic quadrupole potential, the axial CM motion is completely decoupled from the thermal reservoir formed by the internal motions. In practice, however, deviations from the pure electrostatic quadrupole couple the CM motion to the internal reservoir. Fig. B.3 can be used for illustration if the "gas" now represents the internal (axial) degrees of freedom of the electron cloud. The tuned circuit is assumed to be held at a temperature T_r, and an amount of power $\dot{H}$ flowing through the container heats or cools this "gas".

Under quasi-static conditions, energy conservation requires that

$$C_G \frac{d}{dt} T_G = \dot{H} + (m\gamma_{col})\langle \dot{Z}^2 \rangle - \langle \dot{Q}(t)^2 \rangle r. \qquad \text{(B.20)}$$

where we have added two more terms to Eq.(B.17) . The term $(m\gamma_{col})\langle \dot{Z}^2 \rangle$ accounts for the heat dissipated in the gas by the axial oscillation $Z(t)$, which is driven by

the Johnson noise in the tuned circuit. Joule heating in the tuned circuit is given by $\langle \dot{Q}^2 \rangle r$. The term $\dot{H}$ is due to heat exchange between the gas and the external world. Mean squared terms on the right hand side can be calculated to give

$$C_G \frac{d}{dt} T_G = g(T_r - T_G) + \dot{H}. \tag{B.21}$$

The thermal conductivity between the internal reservoir and the resistor r via the brownian motions of the coupled oscillators is given by

$$g = 2k_B \gamma_{col} \Gamma_o (\Gamma_M \omega_M)^2 \int \frac{d\omega}{2\pi} \left| \frac{\omega}{\Delta} \right|^2 \tag{B.22}$$

where

$$\Delta \equiv (\omega_M^2 - \omega^2 - i\Gamma_M \omega)(\omega_z^2 - \omega^2 - i\gamma_{col}\omega) - \Gamma_M \omega_M^2 \Gamma_o \ . \tag{B.23}$$

This integral has a simple limit if $\Gamma_M \gg \gamma_{col} + \Gamma_z$, yielding $g = k_B \gamma_{col} \Gamma_z / (\gamma_{col} + \Gamma_z)$ with Γ_z being the damping rate of the CM motion due to the tuned circuit. This is one of the simplest case of the bolometric model.

We summarize here the basic features of the bolometric model, represented electro-mechanically in Fig.(B.5). Two internal reservoirs are used to account for both axial and cyclotron motions. For parallel motions, a tuned circuit is coupled to the axial CM motion , which in turn interacts with the gas representing the internal axial motions of the electron cloud. For transverse motions, a cavity mode (represented by an LCr circuit) is coupled to the cyclotron CM motion, which in turn interacts with another reservoir representing the cyclotron internal motions . Heat exchange between the internal reservoirs occurs via electron-electron collisions. External sources can raise the temperatures of these motions independently.

Assuming that equilibration time between the internal reservoirs is shorter than other relaxation times, further simplification is obtained by combining all internal motions into one reservoir at temperature T_i. The two temperatures of interest are those of the axial CM motion T_z and the temperature of the combined internal reservoir T_i. Energy conservation gives a system of first-order ordinary differential equations [18,93]

$$C_z \frac{d}{dt} T_z = g_{rz}(T_r - T_z) + g_{iz}(T_i - T_z) + \dot{H}_z,$$

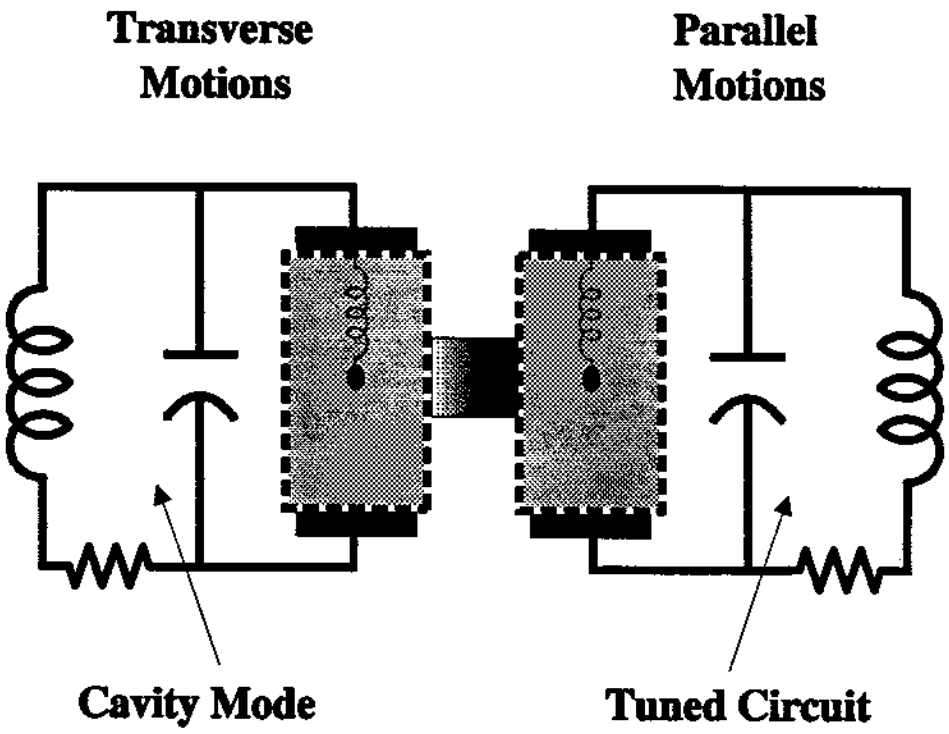

Figure B.5: The bolometric model

$$C_i \frac{d}{dt} T_i \quad = \quad g_{Mi}(T_M - T_i) + g_{zi}(T_z - T_i) + \dot{H}_i, \tag{B.24}$$

where T_r and T_M are the temperatures of the detection circuit and cavity, respectively. (Typically, $T_r \approx T_M$.) The terms $\dot{H}_z$ and $\dot{H}_i$ denote energy flowing into the axial CM motion and internal reservoir, respectively. The heat capacities C_z and C_i are those for harmonic oscillators (k_B per oscillator). The thermal conductivities g_{ij} are determined experimentally. This set of rate equations has been thoroughly investigated with trapped electrons cooled to $\sim$ 80K, for which the equilibration time between internal reservoirs is observed to be very fast. [93] The

equilibration rate, however, can decrease dramatically at much lower temperatures [68] and a more general set of rate equations may be necessary. Finally, the bolometric model is useful only if the system is not driven so strongly that collective behaviors emerge.

Bibliography

[1] "Mathieu Functions," p.722 in **Handbook of Mathematical Functions**, edited by M. Abramowitz and I.A. Stegun (Dover, New York, 1970).

[2] Barut, A.O., and J.P. Dowling, "Quantum Electrodynamics Based on Self-Field, Without Second Quantization: Apparatus Dependent Contributions to $g-2$", Phys. Rev. A **39**, 2796 (1989).

[3] It is customary in microwave electronics to present information in the form of equivalent circuits. See for example Beringer, R., "Resonant Cavities as Microwave Circuit Elements", in **Principles of Microwave Circuits** pp. 207- 239, edited by C.G. Montgomery, R.H. Dicke, and E.M. Purcell (MIT Rad. Lab. Series) (McGraw, NY, 1948).

[4] Boulware, D.G., and L.S. Brown, "Comment on 'Mass and Anomalous Magnetic Moment of an Electron Between Two Conducting Plates' ", Phys. Rev. Lett. **55**, 133 (1985).

[5] Boulware, D.G., L.S. Brown and T. Lee, "Apparatus-dependent contributions to $g-2$?", Phys. Rev. D **32**, 729 (1985).

[6] Brown, L.S., "Line Shape for a Precise Measurement of the Electron's Magnetic Moment", Phys. Rev. Lett. **52**, 2013 (1984).

[7] Brown L.S., "Geonium Lineshape", Annals of Phys. **159**, 62 (1985).

[8] Brown, L.S., G. Gabrielse, K. Helmerson and J. Tan, "Cyclotron Motion in a Microwave Cavity: Possible Shifts of the Measured Electron g Factor", Phys.

Rev. Lett. **55**, 44 (1985).

[9] Brown, L.S., G. Gabrielse, K. Helmerson, J. Tan, "Cyclotron Motion in a Microwave Cavity: Lifetime and Frequency Shifts", Phys. Rev. A **32**, 3204 (1985).

[10] See review by Brown, L.S., and G. Gabrielse, "Geonium Theory: Physics of an Electron or Ion in a Penning Trap", Rev. Mod. Phys. **58**, 233 (1986).

[11] Brown, L.S., K. Helmerson and J. Tan, "Cyclotron Motion in a Spherical Microwave Cavity", Phys. Rev. A. **34**, 2638 (1986).

[12] Brown, L.S., G. Gabrielse, J. Tan and K.C.D. Chan, "Cyclotron Motion in a Penning-trap Microwave Cavity", Phys. Rev. A **37**, 4163 (1988).

[13] This result has been confirmed by L.S. Brown (private communication) for the case of a cylindrical, uniform current sheet using the line-integral of the vector potential around the solenoid circuit to define the flux produced by the solenoid itself.

[14] Conti, R., D. Newman, A. Rich and E. Sweetman, "Experimental Determinations of the Anomalous Magnetic Moments of the Free Leptons", p. 207, in **Precision Measurements and Fundamental Constants II**, edited by B.N. Taylor and W.D. Phillips (Nat'l. Bur. Stand. (U.S.) Spec. Publ. 617, 1984).

[15] Daido, H., "Lower Critical Dimension for Populations of Oscillators with Randomly Distributed Frequencies: A Renormalization-Group Analysis," Phys. Rev. Lett. **61**, 231 (1988).

[16] See, for example, Davidson, R.C., **Physics of Non-neutral Plasma**, (Addison Wesley, Redwood, 1990), p.65; and references therein.

[17] Degiorgio, V.,"The laser instability," Physics Today, October 1976, page 42.

[18] Dehmelt, H.G., and F.L. Walls, " 'Bolometric' Technique for the RF Spectroscopy of Stored Ions," Phys. Rev. Lett. **21**, 127 (1968).

[19] Dehmelt, H.G., and P. Ekstrom, "Proposed g-2/$\delta\omega_z$ Experiment on a Single Stored Electron or Positron," Bull. Am. Phys. Soc., **18**, 727 (1973).

[20] Dehmelt, H.G., "g-Factor of Electron Centered in a Symmetric Cavity", Proc. Nat. Acad Sci. U.S.A. **81**, 8037 (1984). See also the erratum in Proc. Nat. Acad. Sci. U.S.A. **82**, 6366 (1985).

[21] Diedrich, F., E. Peik, J. Chen, W. Quint, and H. Walther, "Observation of a Phase Transition of Stored Laser-cooled Ions," Phys. Rev. Lett. **59**, 2931 (1987).

[22] Cavity-like effects were observed earlier with fatty acid molecules near the surface of a conducting plate. K.H. Drexhage, "Interaction of Light with Monomolecular Dye Layers", 165, Prog. in Optics **XII**, 165 (1974).

[23] Dubin, D., "Theory of Electrostatic Fluid Modes in a Cold Spheroidal Non-Neutral Plasma," Phys. Rev. Lett. **66**, 2076 (1991).

[24] Dutta, A., and C.N. Archie,"High Field Nuclear Magnetometer," Rev. Sci. Instrum. **58**, 628 (1987)

[25] Fabiny, L., and K. Wiesenfeld, "Clustering Behavior of Oscillator Arrays," Phys. Rev. A **43**, 2640 (1991).

[26] Fishbach, E., and N. Nakagawa, "Is $(g_e - 2)$ Apparatus Dependent?", Phys. Lett. **149 B**, 504 (1984).

[27] Fishbach, E., and N. Nakagawa, "Apparatus-Dependent Contributions to $g-2$ and Other Phenomena", Phys. Rev. D **30**, 2356 (1984).

[28] Gabrielse, G., "Relaxation calculation of the electrostatic properties of compensated Penning traps with hyperbolic electrodes," Phys. Rev. A **27**, 2277 (1983)

[29] Gabrielse, G., "Detection, damping, and translating the center of the axial oscillation of a charged particle in a Penning trap with hyperbolic electrodes," Phys. Rev. A **29**,462 (1984).

[30] Gabrielse, G., and F.C. MacKintosh, "Cylindrical Penning Traps with Orthogonalized Anharmonicity Compensation", Int. J. of Mass Spec. and Ion Proc. **57**, 1 (1984).

[31] Gabrielse, G., H. Dehmelt and W. Kells, "Observation of a Relativistic, Bistable Hysteresis in the Cyclotron Motion of a Single Electron", Phys. Rev. Lett. **54**. 537 (1985).

[32] Gabrielse, G., and H.G. Dehmelt, "Observation of Inhibited Spontaneous Emission", Phys. Rev. Lett. **55**, 67 (1985).

[33] Gabrielse, G., and J. Tan,"Self-shielding Superconducting Solenoid Systems," J. Appl. Phys. **63**, 5143 (1988); U.S. Patent # 4,974,113.

[34] Gabrielse, G., L. Haarsma and S.L. Rolston, "Open-endcap Penning Traps for Precision Experiments", Intl. J. of Mass Spec. and Ion Proc. **88**, 319 (1989).

[35] Gabrielse, G., X. Fei, L.A. Orozco, R.L. Tjoelker, J.Haas, H. Kalinowsky, T.A. Trainor, and W. Kells, "Cooling and slowing of trapped antiprotons below 100meV," Phys. Rev. Lett. **63**, 1360 (1989).

[36] Gabrielse, G., X. Fei, L. Orozco, R. Tjoelker, J. Haas, H. Kalinowsky,T. Trainor, W. Kells, "Thousandfold improvement in the measured antiproton mass," Phys. Rev. Lett. **65**, 1317 (1990).

[37] Gabrielse, G., J. Tan, and L.S. Brown, "Cavity Shifts of Measured Electron Magnetic Moments," in **Quantum Electrodynamics**, p.389 ff, edited by T. Kinoshita (World, Singapore, 1990).

[38] Gabrielse, G., J. Tan, P. Clateman, L.A. Orozco, S.L. Rolston, C.H. Tseng, and R.L. Tjoelker,"A Superconducting Solenoid System which Cancels Fluc-

tuations in the Ambient Magnetic Field," J. Magnetic Resonance **91**, 564 (1991).

[39] Garrett, M.W., "Calculation of Fields, Forces, and Mutual Inductances of Current Systems by Elliptic Integrals," J. Appl. Phys. **34**, 2567 (1963)

[40] Gilbert, S.L., J.J. Bollinger and D.J. Wineland, "Shell-Structure Phase of Magnetically Confined Strongly Coupled Plasmas," Phys. Rev. Lett. **60**, 2022 (1988).

[41] Grover, F.W., **Inductance Calculations**, (Van Nostrand, New York, 1946).

[42] Haken, H., "Cooperative phenomena in systems far from thermal equilibrium and in nonphysical systems," Rev. Mod. Phys. **47**, 67 (1975).

[43] Hansen, J.B., and P.E. Lindelof,"Static and dynamic interactions between Josephson junctions," Rev. Mod. Phys. **56**, 431 (1984).

[44] Reviewed by Haroche, S., and D. Kleppner,"Cavity Quantum Electrodynamics", Physics Today, Jan. 1989, p. 24.

[45] Reviewed by E.A. Hinds, "Cavity Quantum Electrodynamics", p. 231, in Adv. At. Mol. Opt. Phys. **28** (1990).

[46] Reviewed by E.A. Hinds, "Cavity Quantum Electrodynamics", p. 231, in Adv. in Atom. Mol. Opt. Phys. **28** (1990).

[47] Hoffnagle, J., R.G. DeVoe, L. Reyna, and R.G. Brewer, "Order-Chaos Transition of Two Trapped Ions," Phys. Rev. Lett. **61**, 255 (1988).

[48] Hulet, R.G., E.S. Hilfer and D. Kleppner, "Inhibited Spontaneous Emission by a Rydberg Atom", Phys. Rev. Lett. **55**, 2137 (1985).

[49] See for example, Jackson, J.D., **Classical Electrodynamics**, 2nd ed. (Wiley, New York, 1975), pp. 353-356.

[50] Jackson, J.D., **Classical Electrodynamics**, 2nd ed. (Wiley, New York, 975), p. 108.

[51] Kasevich, M., and S. Chu, "Atomic Interferometry Using Stimulated Raman Transitions," Phys. Rev. Lett. **67**, 181 (1991).

[52] **Quantum Electrodynamics**, edited by T. Kinoshita (World Scientific, Singapore, 1990).

[53] The most recent and accurate calculation is by Kinoshita, T., "Theory of the Anomalous Magnetic Moment of the Electron - Numerical Approach", in **Quantum Electrodyanics**, edited by T. Kinoshita (World Scientific, Singapore, 1990).

[54] Kleppner, D., in **Atomic Physics and Astrophysics**, edited by M. Chretien and E. Lipworth (Gordon & Breach, NY, 1971).

[55] Kleppner, D., "Inhibited Spontaneous Emission", Phys. Rev. Lett. **47**, 233 (1981).

[56] Kreuzer, M., and K. Svozil, "QED Between Conducting Plates: Corrections to Radiative Mass and $g-2$", Phys. Rev. D **34**, 1429 (1986).

[57] Kreuzer, M., "Mass and Magnetic Moment of Localized Electrons Near Conductors", J. Phys. A **21**, 3285 (1988).

[58] Kuramoto, Y., and I. Nishikawa,"Statistical Macrodynamics of Large Dynamical Systems. Case of a Phase Transition in Oscillator Communities," J. Stat. Phys. **49**, 569 (1987).

[59] Landau, L.D., and E.M. Lifshitz, **Mechanics**, 3rd ed., (Pergamon, New York, 1976).

[60] Lukens, J., "Josephson Arrays as High Frequency Sources", in **Superconducting Devices**,pp. 135-167, edited by S.T. Ruggiero and D.A. Rudman, (Academic Press, Boston, 1990).

[61] Malmberg, J.H., and T.M. O'Neil, "The Pure Electron Plasma, Liquid and Crystal," Phys. Rev. Lett. **39**, 1333 (1977).

[62] Matthews, P.C., and S.H. Strogatz, "Phase Diagram for the Collective Behavior of Limit-Cycle Oscillators," Phys. Rev. Lett. **65**, 1701 (1990).

[63] McLachlan, N.W., **Theory and Application of Mathieu Functions**,(Clarendon Press, Oxford, 1947).

[64] Nayfeh, N.H., and D.T. Mook, **Nonlinear Oscillations**, (Wiley, New York, 1979), pp. 338-348.

[65] Nicolis, G., and I. Prigogine, **Self-Organization in Nonequilibrium Systems**, (John Wiley and Sons, New York, 1977).

[66] Niebur, E., H.G. Schuster and D.M. Kammen,"Collective Frequencies and Metastability in Networks of Limit-Cycle Oscillators with Time Delay," Phys. Rev. Lett. **67**, 2753(1991).

[67] O'Neil, T.M., "Cooling of a pure electron plasma by cyclotron radiation," Phys. Fluids **23**, 725 (1980).

[68] O'Neil, T.M., and P.G. Hjorth, "Collisional Dynamics of a Strongly Magnetized Pure Electron Plasma," Phys. Fluid **28**, 3241 (1985).

[69] See, for example, Panovsky, W., and M. Phillips, **Classical Electricity and Magnetism**, 2nd edition, (Addison-Wesley, Reading, MA., 1962) chapters 21 and 22; or J.D. Jackson, *op. cit.*, Chapter 17.

[70] Purcell, E.M., "Spontaneous Emission Probabilities at Radio Frequencies", Phys. Rev. **69**, 681 (1946).

[71] Raizen, M.G., R.J. Thompson, R.J. Brecha, H.J. Kimble, and H.J. Carmichael,"Normal-Mode Splitting and Linewidth Averaging for Two-State Atoms in an Optical Cavity," Phys. Rev. Lett. **63**, 240 (1989).

[72] Rolston, S.L., and G. Gabrielse, "Cooling antiprotons in an ion trap," Hyperfine Int. **44**, 233 (1988).

[73] Shockley, W., "Currents to Conductors Induced by a Moving Point Charge," J. Appl. Phys. **9**, 635 (1938).

[74] Strogatz, S.H., and R.E. Mirollo,"Collective synchronization in lattices of non-linear oscillators with randomness," J. Phys. A **21**, L699 (1988).

[75] Sugiura, M., and J.P. Heppner, in **American Institute of Physics Handbook**, 3rd ed., pp. 5-264 ff., McGraw-Hill, New York, 1972.

[76] Svozil, K., "Mass and Anomalous Magnetic Moment of an Electron between Two Conducting Parallel Plates", Phys. Rev. Lett. **54**, 742 (1985).

[77] Tan, J., and G. Gabrielse, "One Electron in an Orthogonalized Cylindrical Penning Trap," Appl. Phys. Lett. **55**, 2144 (1989).

[78] Tan, J., and G. Gabrielse, "Synchronization of Parametrically-pumped electron oscillators with Phase Bistability," Phys. Rev. Lett. **67**, 3090 (1991).

[79] Tan, J., and G. Gabrielse, "Parametrically-pumped Electron Oscillators," to be published.

[80] Tang, A.C., "Comments on the Electron Anomalous Magnetic Moment Between Conducting Plates", Phys. Rev. D **36**, 2181 (1987).

[81] Mentioned by Van der Pol, B., "Forced Oscillations in a Circuit with Nonlinear Resistance," Phil. Mag. **3**, 65 (1927).

[82] Van Dyck, R.S., Jr., D.J. Wineland, P.A. Ekstrom and H.G. Dehmelt, "High mass resolution with a new variable anharmonicity Penning trap," Appl. Phys. Lett. **28**, 446 (1976).

[83] Van Dyck, R.S., Jr., P.B. Schwinberg, and H.G. Dehmelt, in **New Frontiers in High Energy Physics**, edited by B. Kursunoglu, A. Perlmutter, and L. Scott (Plenum, New York ,1978).

[84] Van Dyck, R.S., Jr.,P.B. Schwinberg and H.G. Dehmelt, in **Atomic Physics 9**, edited by R.S. Van Dyck, Jr. and E.N. Fortson, p.53 (World Scientific, Singapore,1984).

[85] Van Dyck, R.S., Jr., F.L. Moore, D.L. Farnham and P.B. Schwinberg, "New Measurement of the Proton-Electron Mass Ratio," Int. J. Mass Spectrom. Ion Processes, **66**, 327 (1985).

[86] Van Dyck, R.S., Jr., F.L. Moore, D.L. Farnham, and P.B. Schwinberg,"Variable magnetic bottle for precision geonium experiments," Rev. Sci. Instrum. **57**, 593 (1986).

[87] Van Dyck, R.S., Jr., F.L. Moore, D.L. Farnham, P.B. Schwinberg and H.G. Dehmelt, "Microwave-cavity Modes Directly Observed in a Penning Trap", Phys. Rev. A **36**, 3455 (1987).

[88] Van Dyck, R.S., Jr., P.B. Schwinberg and H.G. Dehmelt, "New high-precision comparison of electron and positron g factors," Phys. Rev. Lett. **59**, 26 (1987).

[89] Van Dyck, R.S., Jr., "Anomalous Magnetic Moment of Single Electrons and Positrons: Experiment", p. 322 in **Quantum Electrodynamics**, edited by T. Kinoshita (World Scientific, Singapore, 1990).

[90] Reviewed by Wang, M.C., and G.E. Uhlenbeck,"On the Theory of the Brownian Motion II", in **Selected Papers on Noise and Stochastic Processes**, edited by N. Wax (Dover, New York, 1954).

[91] Wiesenfeld, K., and P. Hadley,"Attractor Crowding in Oscillator Arrays," Phys. Rev. Lett **62**,1335 (1989).

[92] Wineland, D.J., P. Ekstrom, and H.G. Dehmelt, "Monoelectron Oscillator," Phys. Rev. Lett. **31**, 1279 (1973).

[93] Wineland, D.J., and H.G. Dehmelt,"Principles of the stored ion calorimeter," J. Appl. Phys. **46**, 919 (1975).

[94] Wineland, D.J., and H. Dehmelt, "Line Shifts and Widths of Axial, Cyclotron and $g-2$ Resonances in Tailored, Stored Electron (Ion) Cloud", Int. J. Mass Spectrom. Ion Phys. **16**, 338 (1975); Erratum, **19**, 251 (1975).

[95] Wineland, D.J., J. Bergquist, W. Itano, J. Bollinger, and C. Manney, "Atomic-Ion Coulomb Clusters in an Ion Trap," Phys. Rev. Lett. **59**, 2935 (1987).

[96] Yamaguchi, Y., and H. Shimizu, "Theory of self-synchronization in the presence of native frequency distribution and external noise," Physica **11D**, 212 (1984).

[97] Zhu, Y., D.J. Gauthier, S.E. Morin, Qilin Wu, H.J. Carmichael, and T.W. Mossberg, "Vacuum Rabi Splitting as a Feature of Linear-Dispersion Theory: Analysis and Experimental Observations," Phys. Rev. Lett. **64**, 2499 (1990).

[98] This is the definition of $(\lambda_M)^2$ used in Ref. [9]. It is smaller than the dimensionless $(\lambda_M)^2$ used in Ref. [12] by a factor $\omega_M^2 r_e/z_o$.